The Dissertation Committee for Tara Catherine LaForce certifies that this is the approved version of the following dissertation:

MATHEMATICS OF PARTIALLY MISCIBLE THREE-PHASE FLOW

Committee:

Russell T. Johns, Supervisor

Steven L. Bryant

Clint N. Dawson

Larry W. Lake

William R. Rossen

MATHEMATICS OF PARTIALLY MISCIBLE THREE-PHASE FLOW

by

Tara Catherine LaForce, B. S.; M. S.

Dissertation

Presented to the Faculty of the Graduate School of

the University of Texas at Austin

in Partial Fulfillment

of the Requirements

for the Degree of

Doctor of Philosophy

The University of Texas at Austin

May 2005

Dedication

This dissertation is dedicated to my husband, Greg. I never would have made it without you!

Acknowledgements

First and foremost I would like to thank my advisor, Dr. Johns for his guidance and constructive criticism throughout my research. I would also like to thank Dr. Cinar and Dr. Orr of Stanford University for allowing me to use their core flood data in my research.

I would especially like to thank my husband, Greg, for hanging with me through all the ups and downs of graduate school and helping me to keep it all in perspective. Thank you also to my parents, Bob and Beverly, for always believing I could accomplish anything I set my mind to.

Financial support for this research came from Donors of the Petroleum Research Fund, administered by the American Chemical Society and the Department of Energy. The Thrust 2000 Endowed Graduate Fellowship Program also provided financial support for my graduate work. Their support is gratefully acknowledged.

MATHEMATICS OF PARTIALLY MISCIBLE THREE-PHASE FLOW

Publication No. _____

Tara Catherine LaForce, Ph. D.

The University of Texas at Austin, 2005

Supervisor: Russell T. Johns

Partially miscible flow of several components in three or more phases occurs in both enhanced oil recovery and remediation of contaminated aquifers. There is insufficient understanding of how the formation of multiple phases affects subsurface flow. The main objective of this work is to develop compositional solution routes using the method of characteristics (MOC) for one-dimensional, dispersion-free flow where up to three partially miscible flowing phases may be present; a problem that is poorly understood. Analytical solutions provide insight into the behavior of multi-phase flow and can be used as benchmarks for numerical simulation.

Unique composition routes are found for a ternary system that can form three flowing phases and is analogous to carbon dioxide and methane injection into an oil reservoir. A single-component, single-phase initial composition is assumed and injection of the other two components is studied. A ternary system modeling surfactant-enhanced remediation of a non-aqueous phase contaminant is also studied for a two-phase initial composition and a series of injection compositions. Analytical solutions are found for three different relative permeability models. Finally, the analytical solutions are compared to core floods and simulations.

The results show that recovery of oil or contaminant often declines with surfactant enrichment for a range of injection compositions. Multiple-contact miscibility (MCM) is developed at the critical point of the alcohol/oleic two-phase region and on the boundary of the three-phase region for the single-phase initial composition. When the initial composition is two-phase miscibility is not developed; a substantial divergence from two-phase flow.

Analytical composition routes match the experimental data in most cases. Numerical dispersion may cause simulated routes to differ from analytical routes at shock fronts, but as dispersion is minimized the simulated routes converge to the analytical solutions. Numerical dispersion causes a decrease in recovery, particularly near MCM and may not adequately model the true physical dispersion in the core floods.

Two-phase partially miscible flow is also studied for the case when the initial composition has two hydrocarbon phases. The flow in MCM condensing and condensing/vaporizing drives is dependent on the relative permeability curves and recovery of heavy hydrocarbons may be substantially delayed.

Table of Contents

List of Tables

List of Figures

Chapter 1 Introduction

Subsurface flow of two or more phases occurs in enhanced oil recovery (EOR) as well as in cleanup of aquifers when surfactant enhanced remediation (SEAR) techniques are used. In both EOR and SEAR the goal is to efficiently displace hydrocarbons or contaminants by injection of fluids that solubilize and/or mobilize the oleic phase, allowing it to flow to production wells.

In oil recovery, water and surfactant or gas are injected into the reservoir to create miscible or partially miscible flow fronts. One-phase flow is the most efficient and is often the goal of EOR, but two-phase or three-phase flow may be necessary intermediates to developing single-phase flow in the case of multi-contact miscibility (MCM).

In SEAR, water and surfactant are injected into the contaminated aquifer to solubilize non-aqueous phase liquid (NAPL) contaminants. Unlike EOR processes, complete miscibility is undesirable in SEAR since complete mobilization of the NAPL phase could cause a dense NAPL (DNAPL) to sink, increasing the contaminated aquifer volume (Dwarakanath, 1997).

Analytical solutions for simultaneous flow of two partially miscible phases in porous media have been studied in detail and are well understood. Extensive research has been done on mathematical models of one- and two-phase one-dimensional flow in three component (oil/water/surfactant, heavy oil/light oil/CO_2 and contaminant/water/ surfactant) systems. Modeling one-dimensional flow of three-component fully immiscible systems such as oil/water/gas flow problems has also been extensively studied. There are few theoretical results on partially miscible flow of three phases. For a three-component system, analytical solutions for three-phase partially miscible flow require combining the three-phase immiscible problem together with the two-phase partially miscible problem. Developing these analytical solutions is the subject of most of this work.

This chapter provides a review of past research in the areas of partially miscible two and three-phase flow through porous media. First the situations in which three-phase flow through porous media occurs are presented. Next is a literature review of analytical theory for two-phase partially miscible flow, three-phase immiscible flow, steam injection, and finally three-phase partially miscible flow through porous media. Compositional simulation and the effect of dispersion are also briefly discussed.

1.1 THE OCCURRENCE OF THREE-PHASE PARTIALLY MISCIBLE FLOW

In porous media flow it is possible to have any number of components in three or more flowing phases. Of interest in this work are systems that have three components or can be represented as three pseudo-components. Additionally, each component has some miscibility with the other two components so that when the components are mixed each of the phases contains some of each component, however several phases may persist. In three-phase partially miscible systems there are overall compositions which have one, two, or three-phases. An example ternary figure for a three-component three-phase partially miscible system is shown in Fig. 1.1. There are three two-phase regions, one on each boundary of the three-phase region. In Fig 1.1 two of the two-phase regions have critical points where the phase compositions merge and the two-phase region disappears. The other two-phase region extends all the way to the edge of composition space, because C_1 and C_2 are nearly immiscible fluids. There are a variety of situations in which three-phase flow occurs in porous media.

1.1.1 Three-Phase Flow in CO_2 Injection

Formation of three-phases is believed to be undesirable in gas flooding. Injection of CO_2 can cause the formation of three hydrocarbon phases under realistic reservoir temperature and pressure conditions. Many laboratory experiments of CO_2 mixed with real and synthesized oils have shown three-phase behavior (Coutinho *et al.*, 1999; Creek and Sheffield, 1993; Henry and Metcalfe, 1983; Larsen, 1984; Larson *et al.*, 1989; Orr and Jensen, 1984; Orr *et al.*, 1980; Turek *et al.*, 1980; Turek *et al.*, 1988). The three phases are a hydrocarbon liquid phase, a CO_2-rich liquid phase, and a dense CO_2 gas phase. Development of three phases has an adverse effect on overall mobility, and so may cause a decrease in injectivity of CO_2 (Henry and Metcalfe, 1983). It has also been demonstrated in laboratory experiments that in systems in which three-phases may form, the minimum miscibility pressure (MMP) occurs at the lower pressure boundary of the three-phase region (Creek and Sheffield, 1993). This indicates that three-phases may form in miscible or near-miscible CO_2 floods.

1.1.2 Three-phase Flow in SEAR and Surfactant Flooding

Surfactants in laboratory experiments can substantially improve the effectiveness of remediation of both dense and light NAPLs (e.g. Dwarakanath *et al.*, 1999; Gupta and Mohanty, 2001; Martel and Gélinas, 1996). Three flowing phases are desirable in surfactant injection as three phases occur in water/hydrocarbon/surfactant systems at optimal salinity (Dwarakanath, 1997). The three liquid phases that form in SEAR projects are an aqueous phase, an oleic phase, and a microemulsion phase and are described by Winsor type III phase behavior (Winsor 1954). Winsor type III phase behavior solubilizes hydrocarbons by transferring them into the microemulsion phase (Dwarakanath, 1997). The ultra-low interfacial tension (IFT) between the microemulsion phase and the other two phases also mobilizes the NAPL by reducing the oleic phase residual (Baran *et al.*, 1994a). Surfactant floods with Winsor type III microemulsions have been shown to be highly effective in SEAR in laboratory experiments (Dwarakanath, 1997; Dwarakanath et al., 1999; Jayanti *et al.*, 2002; Shotts, 1996).

1.1.3 Three-Phase Flow in Steam Injection

Steam injection also involves three phases in situ and is used in both EOR or NAPL remediation projects. In this case gas, water and oleic phases are present. Steam injection is substantially different than surfactant and CO_2 injection problems because there are thermal mechanisms at work in displacement of the oleic phase, as well as thermodynamic mechanisms. Additionally it is typical to assume a modified black-oil type model in steam injection.

1.2 TWO-PHASE PARTIALLY MISCIBLE DISPLACEMENT THEORY

Buckley and Leverett (1941) developed the first analytical solutions for one-dimensional flow through porous media. They constructed solutions for two-phase two-component fully immiscible displacements. Fayers and Perrine (1959) extended two-phase immiscible analytical theory to include sorption. In 1979 Helfferich presented a general analytical theory using the method of characteristics (MOC) for multi-component multi-phase displacements.

MOC has been used extensively to study two-phase partially miscible gas and surfactant injection for oil field applications. MOC solutions were initially limited to ternary systems (e.g. Helfferich, 1982; Hirasaki, 1981; Larson, 1979; Wachman, 1964; Zanotti *et al.*, 1983). Partially miscible MOC theory has also been extended to include the adsorption of a surfactant or polymer component on to the solid (e.g. Larson and Hirasaki, 1978; Pope, 1980).

More recently the MOC has been used to find analytical solutions to gas displacements of an arbitrary number of components (e.g. Johns, 1992; Dindoruk *et al.*, 1992; Yuan, 2003; Wang 1998; Jessen *et al.*, 1999; Pires *et al.,* 2004a; Yuan and Johns, 2002). Most research has focused on single-phase reservoir oil. Displacements of two-phase initial reservoir compositions have also been studied (Lake, 1989; Jessen and Orr, 2003; Bedrikovetsky *et al.*, 1996). However the effect of in situ two-phases on miscible flood recovery has not been explored.

MOC theory has been used in other remediation and enhanced oilfield applications as well. Sleep (1995) uses MOC to model SEAR in two-phase three-component displacements of a two-phase NAPL/water initial aquifer composition. Pires *et al.* (2004b) apply MOC to solve the problem of two-phase water and polymer injection when the polymer sorbs onto the rock with an arbitrary number of components present. Rossen and Bruining (2004) apply MOC to find foam injection profiles when the foam strength is a function of the water saturation.

1.2.1 Development of Miscibility in Ternary Systems

In ternary systems there are two key tie lines: the injection gas tie lie and the initial oil tie line. Multi-contact miscibility (MCM) is achieved when the length of either tie line goes to zero i.e. the composition lies on the tie-line extension through the critical point. Thus there are two ways to achieve MCM. The first is to inject enough intermediates so that the length of the gas tie line goes to zero and is shown in Fig. 1.2. This enrichment is the minimum miscibility enrichment (MME) and the recovery mechanism is a condensing gas drive. In a condensing drive the components in the gas phase are condensed into the oleic phase. The second way to achieve MCM is to increase the pressure of the system until the length of the oil tie line goes to zero and is shown in Fig. 1.3. This pressure is the minimum miscibility pressure (MMP) and the recovery mechanism is a vaporizing gas drive. In a vaporizing drive the components in the oleic phase are vaporized into the gas phase (Lake, 1989).

In oilfield applications miscibility is desirable because miscible fluids flow as a single phase. Residual saturations are eliminated and a piston-like or quasi-piston-like displacement occurs, which results in optimal oil recovery (Johns, 1992; Bedrikovetsky *et al.*, 1996).

1.2.2 Development of Miscibility in Multi-component Systems

In displacement of an oil with n_c components the composition route must traverse n_c-1 key tie lines between the injection and initial compositions. The intermediate tie lines between the gas and the oil tie lines are called crossover tie lines. MCM is achieved when the length of any of the key tie lines goes to zero. Multi-component displacements may achieve MCM through condensing or vaporizing drives, however there is a third possible mechanism for the development of miscibility. If the length of one of the crossover tie lines goes to zero then the gas drive will have both condensing and vaporizing (C/V) behavior and is shown in Fig. 1.4 for a quaternary system. This third mechanism for the development of MCM flow is typically achieved by raising the pressure to the MMP (Yuan, 2003).

1.3 THREE-PHASE IMMISCIBLE DISPLACEMENT THEORY

Fully immiscible three-phase three-component displacements have also been extensively studied in the oilfield literature. Three-phase immiscible flow is common in water-alternating-gas (WAG) EOR projects. Three-phase MOC composition routes are constructed in much the same way as two-phase composition routes. Falls and Schulte (1992a, 1992b) and Guzman (1995) contain detailed discussions of construction of composition routes in three-phase immiscible flow.

The current issues in modeling three-phase immiscible displacements can be summed up as a combination of the following two issues; first, there is concern as to whether MOC solutions to three-phase immiscible problems are unique, and second, three-phase relative permeabilities are hard to measure accurately and models that fit the data typically result in elliptic characteristics. Both of these concerns are addressed below.

1.3.1 The Question of Existence and Uniqueness

There has been considerable mathematical research dedicated to understanding non-unique solutions in MOC of three-phase immiscible flow (Azevedo and Marchesin, 1995; Azevedo *et al.*, 1996, 1999, and 2002). Lax and Liu entropy conditions often fail to provide a composition route in three-phase fully immiscible problems and transitional shocks must be introduced into the solution (Isaacson *et al.*, 1990). Schecter *et al*. (1996) discusses the formation and construction of transitional shocks in detail. Non-uniqueness in the composition route is the result of transitional shocks in the composition route (Azevedo *et al*, 1996).

The question of uniqueness arises for the general form of the diffusion term. This means that mass-balance equations with different dispersion tensors may have different zero-dispersion limits. However, by assuming a form of the diffusion term it is possible to generate unique solutions (Isaacson *et al*., 1990; Marchesin *et al*., 1997 and 1999). The primary concern is that composition routes simulated with numerical dispersion may converge to a different zero-dispersion limit than the mass-balance equation with true physical dispersion (Marchesin *et al*., 1997).

The existence of MOC solutions has also been questioned for initial compositions in the elliptic region or routes that must traverse the region of imaginary characteristics. However, Bell *et al*. (1986) show by simulation study that even if a compositional simulation is started at a composition in the elliptic region the simulated solution does not grow without bound, but exits the elliptic region. Compositional simulations with boundary conditions outside of the elliptic region do not enter it (Bell *et al*., 1986). It has traditionally been thought that the loss of uniqueness is a consequence of the mass-balance equation having elliptic or parabolic points, however Azevedo *et al.* (1999) have proposed that the non-uniqueness is a consequence of linearized instability and may occur even in mass-balance equations with no elliptic or parabolic points.

1.3.2 Relative Permeabilities

Choice of relative permeability model has a substantial influence on the equations used in MOC in immiscible three-phase flow. The mass-balance equations governing flow may be hyperbolic, non-strictly hyperbolic, or mixed hyperbolic and elliptic depending on the relative permeability model used (e.g. Guzman, 1995). Shearer and Trangenstein (1989) showed that for most physically meaningful relative permeability models hyperbolicity must fail at least one interior point. Moreover, only relative permeability models in which each phase permeability is a function only of that phase saturation are guaranteed not to have elliptic mass-balance equations (Trangenstein, 1989). Even in models where non-strictly hyperbolic behavior is guaranteed, hyperbolicity may fail at more than one interior point (Guzman and Fayers, 1994).

1.3.2.1 Measurement of Relative Permeabilities

In 1941, Leverett and Lewis first studied three-phase relative permeabilities. Johnson *et al*. (1959) first proposed a method for finding relative permeabilities from core flood experiments. Since then there has been extensive study of three-phase relative permeabilities and how to model them mathematically. A detailed discussion of relative permeability models is beyond the scope of this work; however a brief overview of research on modeling relative permeabilities is given below.

Grader and O'Meara (1988) studied three-liquid phase relative permeabilities in bead packs and concluded that the relative permeability of all three phases were functions of all three phases. Siddiqui *et al.* (1996) studied the flow of three immiscible liquids in glass bead packs and also concluded that the relative permeability of each phase was a function all three phase saturations.

In the water/oil/gas system studied by Leverett and Lewis (1941) the aqueous-phase relative permeability was a function of its own saturation, while the oleic- and gaseous-phase relative permeabilities were dependent on the saturation of all three phases in sand packs. DiCarlo *et al*. (2000) studied relative permeabilities in water-wet, mixed-wet and oil-wet sand packs and found that oil relative permeability was only sensitive to the other phase saturations at low oil saturations, while the gaseous phase permeability was sensitive to all three phase saturations. Corey *et al*. (1956), Saraf and Fatt (1967), and Saraf *et al*. (1982) studied the flow of water, oil, and gas through sandstones and concluded that only the oil-phase relative permeability was affected by saturation of the other two phases.

Dria *et al*. (1993) studied gas/oil/brine relative permeabilities in a carbonate core and concluded that the relative permeability of each phase was a function of only that phase saturation. Clearly there is no consensus on whether phase relative permeabilities are functions of only the saturation of their own phase, or all three phases.

1.3.2.2 Relative Permeability Models

Given the array of conflicting results on relative permeabilities in core floods, it is not surprising that there is also an array of relative permeability models for use in simulation and MOC. The Corey-type three-phase relative permeability model assumes each phase permeability is dependent only on the saturation of that phase (Lake, 1989). Because of the difficulties in obtaining relative permeabilities from three-phase core floods, Stone (1970, 1973) introduced a three-phase relative permeability model based on interpolation of two-phase data. These two models are the most widely used.

Holden (1990) proposed a method of manipulating relative permeability parameters to avoid elliptic regions. Juanes and Patzek (2002 and 2003a) went one step further and proposed relative permeability curves that are strictly hyperbolic at every point in the interior of the three-phase region. Many other relative permeability models have been proposed (e.g Blunt, 2000; Grader and O'Meara, 1988; Delshad and Pope, 1989; Fayers, 1987; Gonzalez and Araujo, 2002; Svirsky *et al.,* 2004). Miller *et al*. (1998) provides a more detailed look at many of the relative permeability models used in ground water contamination.

Delshad and Pope (1989) compared the fit of seven relative permeability models to core flood data from three experiments and concluded the Baker (1988) and Pope models were superior for the data sets considered. Spiteri and Juanes (2004) found that the Stone I model was superior to Stone II and Baker's models on three-phase data from Oak (1990). Fayers and Matthews (1984) compared Stone's models I and II and concluded that the Stone I model fit their data more accurately. In contrast, Saraf *et al*. (1982) compared Stone's models I and II and concluded that the Stone II model fit their data more accurately. Sahni *et al.* (1996) assumed Corey-type relative permeabilities and showed that they were sufficient to match core flood composition path and recovery data accurately.

Hicks and Grader (1996) studied the fit of four relative permeability models to three-immiscible liquid relative permeability data in glass bead packs. In their research the Stone I and II models did not fit the data as well as extended Corey relative permeabilities. All of the models had elliptic regions. One relative permeability model was then chosen to construct MOC solutions for comparison with core flood data.

Hysteresis is also an important effect in three-phase immiscible displacements, but a discussion of hysteresis is beyond the scope of this work. See Spiteri and Juanes (2004) for a discussion of the importance of hysteresis in relative permeability modeling.

1.4 STEAM INJECTION DISPLACEMENT THEORY

Steam injection is one of the most important and successful EOR techniques. Until now, all MOC solutions discussed have applied to mass transport problems. In steam injection it is necessary to consider the coupled transport and energy balance equations.

In a conventional black oil model the aqueous phase contains only water, the gaseous phase contains only gas, and the oleic phase contains gas and oil components (Lake, 1989). In steam flooding a modified black oil model is used and, it is assumed that oil exists only in the oleic phase, gas exists only in the gas phase, and water partitions between the gas and aqueous phases.

In aquifer remediation problems where the concentration of contaminant is small enough that its mass may be neglected it is possible to model steam injection as a single-component, two-phase problem. Unique analytical solutions exist for one component steam injection into porous media (Bruining *et al.*, 2003; Bruining *et al.*, 2004). Analytical solutions also exist for two component, two-phase injection of steam and another gas (Bruining and Marchesin, 2004).

Oil recovery by steam injection is typically solved as a two-component (non-volatile oil and water) problem coupled with three-phase flow. MOC solutions for steam injection have been found, but some aspects of the non-isothermal phase behavior must be omitted to find analytical solutions (Wingard and Orr, 1989; Bruining and van Duijn, 2000).

1.5 THREE-PHASE PARTIALLY MISCIBLE DISPLACEMENT THEORY

There has been relatively little research done on three-phase partially miscible displacements. This is in part because three partially miscible phases form under a much smaller set of oilfield conditions than two-phase partially miscible and three-phase immiscible flow, but is also a consequence of the complexity of the displacements.

There is very little in the literature on the development of MOC solutions to three-phase partially miscible flow. Giordano and Salter (1984) compared numerical simulations, core floods, and one MOC solution for a partially miscible three-phase water/NPA/DMP system. The MOC and simulated composition routes agreed well, although the match to core floods was only qualitative. The development of this one MOC solution was not thoroughly explained in their paper.

In the literature there are three studies of relative permeabilities in three-phase partially miscible systems. Delshad *et al.* (1987) measure two- and three-phase relative permeabilities for a partially miscible brine, n-decane, and IBA alcohol mixture. The three-phase relative permeabilities appear to be functions of their own phase saturations and are fitted to a Hirasaki relative permeability model (also known as a Corey or extended Corey model).

Kvanivik *et al*. (1992) measure two- and three-phase relative permeabilities in a partially miscible brine, heptane, and sodium dodecylbenzene sulfonate mixture. The aqueous and microemulsion phase relative permeabilities are dependent on the saturations of all three phases. Kvanivik *et al*. (1992) also observed relative permeability hysteresis in all three phases. The data are fitted to Hirasaki (Corey), Lake, Delshad's modified Lake, and Stone I and II models. Only the Stone models match the data accurately. In both works the micellar phase-relative permeability has Corey exponent is less than one, a result that has substantial implications when applying MOC theory to partially miscible displacements.

Cinar and Orr (2004) measured three-phase relative permeabilities in a four component three-phase partially miscible system containing hexadecane, n-butanol, water, and isopropanol in an oil wet porous media. The purpose of their study was to demonstrate the effect of interfacial tension (IFT) on relative permeability. The relative permeability of the wetting phase was largely unaffected by the decrease in IFT caused by adding isopropanol, while the other two phase relative permeabilities increased substantially. Cinar *et al.* (2004) expanded on the work of Cinar and Orr (2004) and measured three-phase relative permeabilities in two water-wet media as a function of IFT for the same quaternary system and a hexadecane, n-butanol, water, and sodium system.

1.6 SIMULATION OF MULTI-COMPONENT MULTI-PHASE DISPLACEMENTS

Simulators are the primary tool reservoir engineers use in evaluating oil reservoirs and production strategies. Compositional simulators must be used whenever multiple partially miscible phases occur in situ. Any SEAR process or EOR technique such as miscible gas or surfactant injection must be simulated compositionally. Compositional simulation is a vast topic, so discussion will be limited to compositional simulation results that provide insight into analytical solutions and the effects of relative permeability or dispersion.

1.6.1 Simulation of Three-Phase Immiscible Displacements

Several researchers have compared MOC and simulated composition routes, profiles and recoveries favorably. Juanes and Patzek (2003) compare one-dimensional simulations to analytical solutions for a strictly hyperbolic mass-balance equation and show that even coarse mesh simulations match the MOC solutions closely. Marchesin *et al*. (1999) show that the composition path and profiles in WAG injection are nearly identical to the MOC solution for the averaged injection composition once the oscillations in the composition route die out. Both of the studies show very little effect of numerical dispersion.

Guzman *et al.* (1994) showed the importance of relative permeability model in three-dimensional WAG flood performance simulations using Stone I and normalized Stone II relative permeabilities fitted to the same data set. The simulations showed substantial differences in predictions of iso-permeabilities, oil recovery, and gas oil ratio (GOR) after water break through. Hicks and Grader

(1996) compare the results of core flood experiments to one-dimensional simulations. Several relative permeability models were fitted to data and the model with the best fit was used in simulations. Their work demonstrates that simulations can very accurately capture the experimental profiles and production of the components when an appropriate relative permeability model is used.

1.6.2 Simulation of Partially Miscible Displacements in SEAR

Relatively little compositional simulation has been done on partially miscible flow in SEAR. Roeder and Falta (2001) matched simulations from UTCHEM (Delshad *et al.,* 1996) to unstable core floods of DNAPL remediation by alcohol and water slug injection. Ouyang *et al.* (2002) used UTCHEM to model the formation and flow of microemulsions. Both of these papers demonstrate that simulators can accurately model partially miscible flow when correct parameters are used.

Finite difference simulations at field scale can introduce large numerical dispersion that obscures the physical mechanisms at work. This is particularly a concern in remediation of DNAPL as a pool may be much smaller than a grid block. Falta (2003) showed the importance of accurately modeling DNAPL pool dissolution at the sub-grid block scale. Ignoring the sub-grid block flux of the contaminant resulted in a serious under-estimate of the time required for remediation as compared with core flood data.

1.6.3 Simulation of Three-Phase Partially Miscible Displacements in EOR

Numerical simulation of three-phase partially miscible flow has been a topic of interest in the oilfield literature since the late 1970's. Gardner *et al.* (1979) obtained an excellent match to slim-tube experiments with one-dimensional simulations using pseudo-ternary representations of CO_2 injected into Wasson crude. Moreover, Gardner *et al.* (1979) showed that the simulated composition route is dependent on the level of numerical dispersion.

Orr (1980) developed numerical simulator that allows for partially miscible flow of up to four components and four phases. Pongpitak (1980) used this simulator to model three-phase water flooding for cores saturated with the alcohol n-butanol (NBA) and C_{16}. The simulations significantly under-estimated the oil recovery compared with core flood experiments. Fanchi (1987) showed the relative unimportance of small three-phase regions using a similar simulator on pseudo-ternary representations of CO_2 injection with crude and synthetic oils, though a larger three-phase region corresponded to a slight increase in recovery. Ngheim and Li (1986) also demonstrated the small effect of ignoring the three-phase region in CO_2 injection in simulating slim tube experiments when using a simulator that incorporated a three-phase flash algorithm. Jabbour *et al.* (1996) also found that three-phase flow effects enhanced oil recovery in their experiments of steam and hot nitrogen injection into sand packs saturated with water and non-distillable oil at its residual.

Giordano and Salter (1984) performed a detailed comparison of MOC, simulations, and core floods in water/alcohol/oil analogue systems that formed two or three-phases. One-dimensional simulations and MOC routes matched well and also fit the experimental data qualitatively. In core floods the alcohol broke through earlier and tailed to the injection composition, rather than having a shock out of the multi-phase region as predicted by the simulator. Giordano and Salter (1984) verified that the trailing shock had an unfavorable mobility ratio and was subject to viscous fingering by examination of one core used in the floods. The instability of the shock accounted for the difference between the one-dimensional simulations and the core floods.

1.6.4 Simulation of Two-Phase Partially Miscible Displacements in EOR

Numerical simulation of two-phase partially miscible flow has been studied extensively. For example, Trangenstein and Bell (1989) compared simulated and MOC results favorably for partially miscible simulations, but the simulator failed to accurately capture the miscible front in a MCM flood. Since many floods are designed to be MCM it is critical to build simulators that can be accurate at or near miscibility.

Simulation studies have shown that dispersion causes two-phase flow in multi-component MCM floods. Even a small amount of dispersion causes the composition route to enter the two-phase region near a critical point (Johns *et al.*, 1992). The region of two-phase flow causes a decline in recovery and is more severe for systems with a large number of components (Johns *et al.*, 2004; Johns *et al.*, 1992). C/V displacements that are mostly condensing are also more sensitive to the effects of dispersion (Johns *et al.*, 2004).

In two-phase partially miscible flow MOC can be used to determine the MMP and MME of a displacement. MOC predictions of miscibility are based on one-dimensional dispersion-free flow; assumptions that do not hold in oil reservoirs. In the presence of gravity and reservoir heterogeneities displacements that are predicted to be MCM by MOC often develop regions of lost miscibility. Moulds *et al*. (2003) simulate the injection of miscible gases in C/V drives. Re-saturation of swept regions has a significant effect on residual oil. Rich gases are much more efficient at displacing oil than the poor gases, though this is thought to be a consequence of enhanced phase behavior of the denser gas, rather than interfacial tension effects on relative permeability as miscibility is approached.

In compositionally graded reservoirs the question of miscible gas injection is complicated by the fact that the MMP/MME is a function of depth and the drive mechanism may change from vaporizing to C/V with increasing depth (Hoier and Whitson, 2001). Hoier *et al.* (2004) show that when the gas-oil contact (GOC) in a compositionally graded reservoir is a super-critical fluid any injection gas will result in a miscible displacement. This is caused by the fact that the injection gas will be miscible with the gas cap of the reservoir. Miscible one-dimensional displacements simulated showed the formation of a leading-edge oil bank that miscibly displaces all downstream compositions (Hoier and Whitson, 2001; Hoier *et al.* 2004).

Seto *et al.* (2003) used MOC composition routes in streamline simulation of gas injection for condensate recovery. In the simulator streamlines are found by solving the pressure equation in a two- or three-dimensional reservoir and

MOC solutions are applied down tie lines. This is a first example of using MOC in compositional simulation. The simulator is unable to account for viscous cross-flow so recovery is consistently under-estimated.

1.7 OUTLINE OF THIS WORK

In this work, the analytical theory using MOC is extended to three-component three-phase partially miscible flow. In Chapter 2 the mathematical details of three-component three-phase partially miscible MOC solutions are outlined. In Chapter 3 unique solutions are found for three-phase partially miscible flow problem with a large three-phase region and a single-phase initial reservoir composition in an EOR application. In Chapter 4 MOC is applied to a miscible gas injection problem with a two-phase initial composition. In Chapter 5 the unique MOC solutions for three relative permeability models are compared for a two-phase initial composition in SEAR of a DNAPL. In Chapter 6 the MOC solutions are compared with core flood data and finite-difference solutions to study the effects of physical and numerical dispersion on composition routes and recoveries in three-phase partially miscible flow.

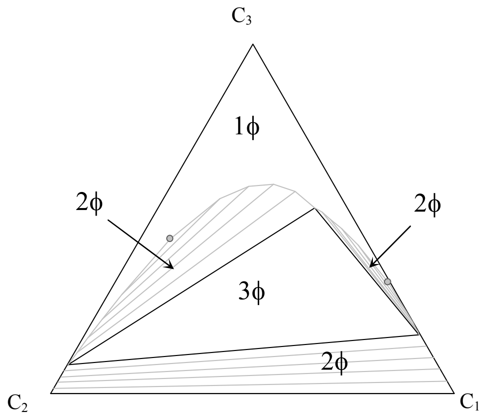

Figure 1.1 Example of a ternary system with three partially miscible phases. Large circles indicate critical points of the two-phase regions.

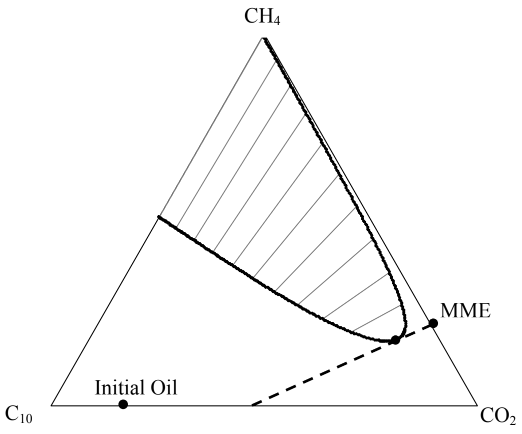

Figure 1.2 A condensing gas drive at the minimum miscibility enrichment. The MME is the same for any initial oil. The injection gas is on the tie-line extension through the critical point, shown as a dashed line.

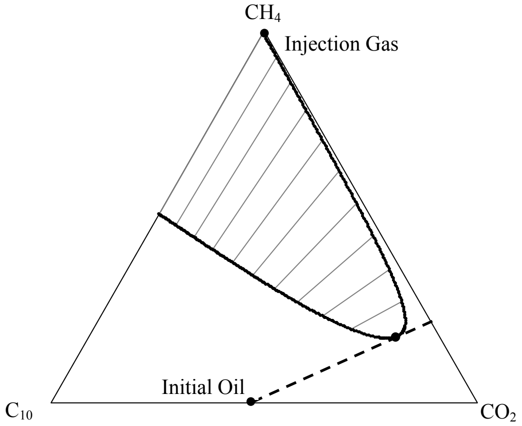

Figure 1.3 A vaporizing gas drive at the minimum miscibility pressure for the initial oil composition shown. The MMP is the same for any CO_2 and CH_4 injection gas mixture. The initial oil is on the tie-line extension through the critical point, shown as a dashed line.

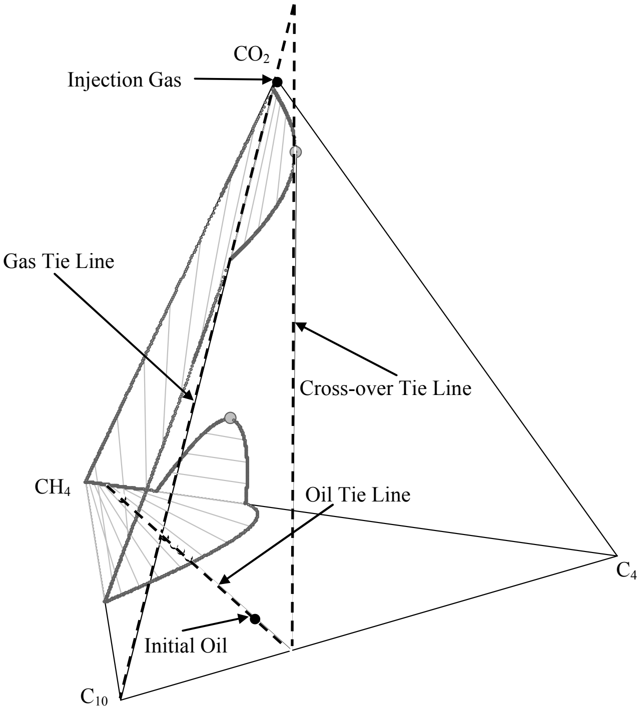

Figure 1.4 A combined vaporizing and condensing drive at the minimum miscibility pressure for CO$_2$ injection. The MMP is the same for any CO$_2$ and C$_{10}$ injection gas mixture. The crossover tie line is the limiting tie line at the critical point. All tie lines are shown as dashed lines.

Chapter 2 Mathematical Model

In this chapter the mathematical results necessary to solve a system of mass-balance equations representing one-dimensional partially miscible flow by the method of characteristics are presented. First, an appropriate system of mass-balance equations is derived from a general continuity equation for reservoir flow. Second, the mass-balance equations are solved by MOC for the paths through composition space and the basic features of the characteristics in the two- and three-phase regions are discussed. Third, the shock jump conditions satisfying the weak form of the mass-balance equations are derived and the characteristics of the Hugoniot loci of shocks between phases are explored. Finally, the constraints for physically valid shocks are discussed.

2.1 The One-Dimensional Dispersion Free Mass-balance Equation

The general continuity equation or conservation of total mass for each component in isothermal flow is (Lake, 1989)

$$\begin{aligned}&\frac{\partial}{\partial t}\left(\phi\sum_{j=1}^{n_p}\rho_j S_j x_{ij}+(1-\phi)\rho_s x_{is}\right)+\nabla\cdot\left(\sum_{j=1}^{n_p}\left(\rho_j x_{ij}u_j-\phi S_j\rho_j K_{ij}\nabla\cdot x_{ij}\right)\right)\\&=\phi\sum_{j=1}^{n_p}S_j r_{ij}+(1-\phi)r_{is}\qquad i=1,\ldots,n_c\end{aligned}\tag{2.1}$$

where n_c is the number of components, n_p is the number of phases present, ϕ is the porosity, ρ_j is the molar density of phase j, S_j is the saturation of the j^{th} phase, x_{ij} is the mole fraction of component i in the j^{th} phase, u_j is the superficial velocity of phase j, K_{ij} is the dispersion tensor, and r_{ij} is the reaction rate of reactions in which component j is created or destroyed. To obtain a system of mass-balance equations that can be solved by MOC, the following standard assumptions are made:

- One-dimensional and isothermal flow
- Constant porosity with time
- No gravity effects
- No chemical reactions or adsorption
- Thermodynamic equilibrium
- Laminar and incompressible flow

With these assumptions Eqs. (2.1) simplifies to

$$\phi \frac{\partial}{\partial t}\left(\sum_{j=1}^{n_p} \rho_j S_j x_{ij}\right) + u \frac{\partial}{\partial x}\left(\sum_{j=1}^{n_p} \rho_j x_{ij} f_j\right) = 0 \qquad i = 1, \ldots, n_c \tag{2.2}$$

where f_j is the fractional flow of the j^{th} phase and is defined as $f_j = u_j / u$ where u is the total velocity $u = \sum_{j=1}^{n_p} u_j$. The fractional flow is given by

$$f_j = \frac{\lambda_j}{\sum_{j=1}^{n_p} \lambda_j} \quad \text{and} \quad \lambda_j = \frac{k_{rj}}{\mu_j} \tag{2.3}$$

where λ_j is the mobility, k_{rj} is the relative permeability, and μ is the viscosity of phase j. This assumes Darcy's law for multiple phases without capillary pressure. Ideal mixing is assumed so that we can divide by the pure component density ρ_i^{o} and substitute in $c_{ij}=\rho_j x_{ij}/\rho_1^{\circ}$

$$\frac{\partial}{\partial t}\left(\sum_{j=1}^{n_p} S_j c_{ij}\right)+\frac{u}{\phi}\frac{\partial}{\partial x}\left(\sum_{j=1}^{n_p} f_j c_{ij}\right)=0 \qquad i=1,\ldots,n_c. \tag{2.4}$$

The dimensionless distance is defined as $x_D = x/L$ and the dimensionless time $t_D = u/\phi L$ is pore volumes injected (PVI). C_i, and F_i are also defined to be

$$C_i=\sum_{j=1}^{n_p} S_j c_{ij},\ \ F_i=\sum_{j=1}^{n_p} f_j c_{ij}\ \ . \tag{2.5}$$

The final mass-balance equation (or conservation law) is

$$\left(\frac{\partial C_i}{\partial t_D}\right)_{x_D}+\left(\frac{\partial F_i}{\partial x_D}\right)_{t_D}=0\ \ i=1,\ldots,n_c. \tag{2.6}$$

The assumptions of no gravity effects and no volume change on mixing may be relaxed; however they simplify the eigenvalue problem. There are four additional auxiliary relations in which $\sum_{i=1}^{n_c} C_i,\ \sum_{i=1}^{n_c} F_i,\ \sum_{j=1}^{n_p} S_j,\ \sum_{j=1}^{n_p} f_j,$ and equilibrium volume and equilibrium volume fractions $\sum_{j=1}^{n_p} c_{ij}$, in each phase are unity. In this work component 1 is water, component 2 is oil or NAPL contaminant, and component 3 is surfactant or alcohol. Similarly, phase 1 is defined as the aqueous phase, phase 2 is the oleic phase (NAPL), and phase 3 is the alcohol or microemulsion phase.

2.2 RELATIVE PERMEABILITY MODEL

For the purposes of this work an extended Core-type relative permeability is used. The relative permeability of phase *j* is (Delshad and Pope, 1998)

$$k_{rj} = k_{rj}^{o}\left(S_j^*\right)^{n_j} \tag{2.7}$$

and

$$S_j^* = \frac{S_j - S_{rj}}{1 - S_{r1} - S_{r2} - S_{r3}} \tag{2.8}$$

where S_{r1} and S_{r3} are fixed and S_{r2} is a function of S_1 and S_3 such that

$$S_{r2} = \alpha S_{r21} + (1-\alpha) S_{r23} \tag{2.9}$$

and S_{r21} is the residual saturation of phase 2 in the presence of phase 1 and S_{r23} is the residual of phase 2 in component 3. S_{r2} defined in this way allows for the mobilization of the oleic phase by surfactant or other solvent. Similarly, n_2 and k^o_{r2} are defined as

$$\begin{aligned} n_2 &= \alpha n_{21} + (1-\alpha) n_{23} \\ k^o_{r2} &= \alpha k^o_{r21} + (1-\alpha) k^o_{r23} \end{aligned} . \tag{2.10}$$

In order to be consistent on the boundaries of the three-phase region, α must be defined so that α=0 when S_1=0, α=1 when S_3=0, and α increases monotonically from zero to one along lines of constant saturation of phase 2. These conditions require that α be double-valued at the point S_2=1. We will use the function

$$\alpha = \frac{S_1(1-S_3)}{S_1+S_3}, \tag{2.11}$$

which was taken from Kvanik *et al*. (1992). S_{r2} defined as in Eq. (2.8) implies that the relative permeability of every phase is dependent on both of the other phase saturations through S_{r2}. This dependence may result in imaginary characteristics in the three-phase region (Trangenstein, 1989).

2.3 THE METHOD OF CHARACTERISTICS

In this work the number of components n_c = 3 and the number of phases present n_p = 1, 2, or 3, and is dependent on the overall composition. Appendix A explains the MOC solution to the system of quasilinear equations in Eq. (2.6) for three components in detail. In the two- and three-phase region, Eq. (2.6) has the eigenvalues (or characteristic directions)

$$\lambda_{+/-} = \frac{1}{2}\left[(F_{11} + F_{33}) \pm \sqrt{(F_{11} - F_{33})^2 + 4F_{13}F_{31}} \right] \tag{2.12}$$

where F_{ij} denotes the derivative of F_i with respect to component j. The corresponding eigenvectors (or characteristics) are

$$\frac{dC_3}{dC_1} = \frac{\lambda_\pm - F_{11}}{F_{13}} \text{ or } \frac{dC_1}{dC_3} = \frac{\lambda_\pm - F_{33}}{F_{31}}. \tag{2.13}$$

The eigenvectors in Eq. (2.13) are the legal paths through composition space that must be followed by every composition route. The eigenvalues are the dimensionless velocities of the compositions on these paths. Compositions flow down the paths as spreading waves.

2.3.1 One-Phase Flow

All three components can coexist in any number of phases. When all three components mix to form a single phase the flow is miscible and the composition flows with dimensionless velocity one. The fractional flow of each component, F_i is equal to the composition of that component C_i and the compositions may flow in any direction in composition space (Lake, 1989). This can be verified by looking at the eigenvalue problem. In the single phase region both of the eigenvalues are equal to one and every direction is an eigenvector.

2.3.2 Two-Phase Paths

In three-component systems that can form up to three-phases there are multiple two-phase regions, one on each boundary of the tie triangle as shown in Figure 2.1. In order to simplify the phase behavior, boundaries of the two-phase regions are determined by a quadratic fit to the tie lines using the method outlined by Orr (1980). In this method a quadratic function is fit to each bubble point and dew point curve using three tie lines or two tie lines and the critical point from measured data (using mole fractions).

Within each two-phase region the tie lines intersect at a point. When no critical point is present, the intersection point of all tie lines is determined by the intersection of the tie line on the boundary of the three-phase region and the two component tie line on the boundary of the ternary diagram. When a critical point is present, the slope of the limiting tie line at the critical point is defined as the average slope of the quadratics modeling the bubble and dew point curves at the critical point. The intersection of the limiting tie line and the tie line on the boundary of the three-phase region are used to determine the tie-line intersection point (Orr, 1980).

In the two-phase region the eigenvalues are distinguished by the direction in which the eigenvector points. The eigenvector that corresponds to the tie-line eigenvalue, λ_t, points down the tie-line and the non-tie-line eigenvector, which corresponds to the non-tie-line eigenvalue, λ_{nt}, points across the tie lines. Tie lines are paths in the two-phase region. The displacement reduces to a Buckley-Leverett problem (Buckley and Leverett, 1941) on the tie-line path, where phase compositions are fixed and so

$$\lambda_t = \partial f_j / \partial S_j \tag{2.14}$$

which can be used to determine which eigenvalue is the tie-line eigenvalue. The non-tie-line paths are found by numerically integrating Eq. (2.13) using the non-tie-line eigenvalue. As a consequence of the assumption that all of the tie lines intersect in a point, non-tie-line paths are indifferent waves (Johns, 1992).

A singular point may exist in the two-phase region where the eigenvalues become equal (parabolic points). At parabolic points the eigenvectors merge into a single eigenvector that points down the tie line. Composition routes can switch from tie-line paths to non-tie-line paths at singular points (Johns, 1992). Figure 2.1 shows an example of tie-line and non-tie-line paths in the two-phase regions for the three-component system outlined in Table 2.1 with the relative permeability parameters shown in Table 2.2.

2.3.3 Three-Phase Paths

According to the Gibb’s phase rule, in a ternary system at constant temperature and pressure there are zero degrees of freedom. Thus, the three-phase compositions are fixed to the compositions at each apex of the three-phase region. This important result implies that the three-phase region behaves immiscibly and solving the system of equations within the three-phase region

$$\left(\frac{\partial S_j}{\partial t_D}\right)_{x_D} + \left(\frac{\partial f_j}{\partial x_D}\right)_{t_D} = 0 \quad j = 1,\ 2,\ 3 \tag{2.15}$$

is equivalent to solving Eq. (2.6). A derivation of Eq. (2.15) from Eq. (2.6) is shown in Appendix B. The eigenvalues and vectors of (2.15) are given by Eqs. B.7 and B.8 respectively. There are two motivations for solving the mass-balance equations in the form of Eq. (2.15) rather than the original mass-balance equations in Eq. (2.6). The primary reason is that all of the previously developed theory for immiscible three-phase flow applies directly to Eq. (2.15), but not Eq. (2.6) (e.g. Azevedo and Marchesin, 1995; Azevedo *et al.,* 1996, 1999, 2002; Falls and Schulte, 1992a, b; Guzman, 1995; Holden, 1990; Isaacson *et al.,* 1990; Juanes and Patzek, 2002, 2003a; Marchesin *et al.,* 1997, 1999; Schecter *et al.,* 1996; Shearer and Trangenstein, 1989; Trangenstein, 1989). An additional advantage of Eq. (2.15) is that the partial derivatives of the fractional flow curves f_j often can be found analytically, while the derivatives of F_i must be approximated.

In the three-phase region the paths are distinguished by magnitude. The paths resulting from the larger eigenvalue are defined as the fast paths and the paths from the smaller eigenvalue are the slow paths. Both types of path are found by numerically integrating Eq. (2.13) using the appropriate eigenvalue (Guzman, 1995).

In the three-phase region it is possible to have one, two, or three phases flowing simultaneously. In a region that is below the residual saturation of one phase the velocity of the slow path is always zero and the fast paths are lines of constant saturation of the phase that is below residual. The velocity of the slow path is zero at the edge of the three-phase flow region, even when residuals are not present. A fast path follows the boundary of the tie triangle, hence it is not possible to enter or exit the three-phase region without a shock. In the corners of the three-phase region there may be only one mobile phase if two phases are below their residual saturations. In this case both eigenvalues are zero and every direction is a characteristic path.

Figure 2.1 shows an example of fast and slow paths in the three-phase region for the three-component system outlined in Table 2.1 with the relative permeability parameters shown in Table 2.2. In the interior of the three-phase region, the mass-balance equation is one of three types of partial differential equation (Shearer and Trangenstein, 1989; Greenberg, 1998):

- Strictly hyperbolic (SH): At every point in composition space the mass-balance equations have two distinct eigenvalues and vectors as given by Eqs. (2.12) and (2.13).
- Non-strictly hyperbolic (NSH): There is one or more isolated points in composition space at which the square root term in Eq. (2.12) goes to zero. The points at which strict hyperbolicity fails are referred to as umbilic points. At umbilic points Eq. (2.12) has a single eigenvalue and all directions are eigenvectors.

- Mixed hyperbolic and elliptic (MHE): There is one or more regions in composition space for which the square root term in Eq. (2.12) is less than zero, resulting in imaginary eigenvalues. Compositions with imaginary eigenvalues have no legal paths through composition space.

The eigenvectors of Eq. (2.13) were derived under the assumption that the mass-balance equations were hyperbolic (see Appendix A). Obviously neither the NSH nor the MHE cases satisfy this assumption. This may cause non-uniqueness of the solution as has been observed by Azevedo and Marchesin (1995) and Azevedo *et al.,* (1996) among others.

Figures 2.2, 2.3, and 2.4 show the composition paths through the three-phase region for a SH, NSH, and MHE mass-balance equation, respectively. The density, viscosity and phase behavior for the three-component system in Figs. 2.2-2.4 is outlined in Table 2.3 and the relative permeability parameters are in Table 2.4.

2.4 SHOCKS IN COMPOSITION

Shocks in composition space must be introduced to satisfy the weak form of Eq. (2.6) when upstream compositions flow faster than downstream compositions so that spreading waves become multi-valued. Shocks are always necessary to travel between the one-, two-, and three-phase regions because the compositional paths are discontinuous at phase boundaries. The velocity of any shock must satisfy the Rankine-Hugoniot shock conditions for three components (Guzman 1995):

$$\frac{F_1^d - F_1^u}{C_1^d - C_1^u} = \frac{F_2^d - F_2^u}{C_2^d - C_2^u} = \frac{F_3^d - F_3^u}{C_3^d - C_3^u} = \Lambda \,. \qquad (2.16)$$

In Eq. (2.16), Λ is the shock velocity, superscript d denotes the downstream composition, u denotes upstream composition, and the subscripts denote component number as before. Equation (2.16) is under-determined, and hence, there are many compositions that satisfy the jump conditions. These compositions make up the Hugoniot locus.

2.4.1 Shocks Between One-Phase and Two-Phase Regions

One- to two-phase shocks are well understood (ex. Johns, 1992; Yuan, 2003) and are only briefly discussed here. Larson (1979) proved that a shock from a single-phase composition into the two-phase region must occur along a tie-line extension in order to satisfy Eq. (2.16). Unfortunately, the entire tie line satisfies Eq. (2.16), so the Rankine-Hugoniot shock condition doesn't provide any additional information. However, one- to two-phase shocks are often tangent to the tie-line path, meaning that $\Lambda = \partial f_i / \partial S_i$ for either of the two phases present. There are two possible shocks tangent to the tie-line path, one with velocity less than one, and one with velocity greater than one.

2.4.2 Intra-Two-Phase Shocks

It may be necessary to shock down a tie line or between tie lines to prevent a solution from becoming double valued. Shocks between tie lines occur if the non-tie-line path is a sharpening wave or if the non-tie-line velocity is slower than upstream velocities. The construction of these shocks is explained in detail in Johns (1992). Shocks between tie lines rarely occur in the solutions for the three-phase partially miscible systems studied in this work because all non-tie-line paths are indifferent waves when all of the tie lines intersect in a point.

2.4.3 Shocks Between One-Phase and Three-Phase Regions

One to three-phase shocks must also satisfy Eqs. (2.16). In the one-phase region $F_i = C_i$ for all of the components, this simplifies the numerical problem considerably. The locus of one to three-phase shocks for a given one-phase composition is typically two curves through the three-phase region in composition space. Shocks may be tangent either to the fast or the slow path through composition space, or they may result in a constant state. Tangent shocks occur when the shock velocity is the same as one of the eigenvalues within the three-phase region. Tangent shocks occur only at isolated points, but several tangent shocks may exist. In this work all shocks are approximated by Newton's method for systems of equations (Burden and Faires, 1997) on the equations $\Lambda_1 - \Lambda_2 = 0$ and $\Lambda_1 - \Lambda_3 = 0$ where Λ_i is the shock velocity calculated with component *i*.

Figures 2.5 and 2.6 show an example of how the locus of shocks and the tangent shocks evolve when the one-phase composition is moved through composition space from pure C_{16} to pure NBA. The ternary system in Fig. 2.5 is the water/NBA/C_{16} system outlined in Tables 2.1 and 2.2. One-phase compositions A_1-L_1 compositions are outlined in Table 2.5. The behavior of the locus of one to three-phase shocks and tangent shocks has not been previously been explored.

2.4.3.1 Behavior of the Locus of One- to Three-Phase Shocks

The behavior of the locus of one to three-phase shocks has not been previously been explored. In shocks between one and three-phases the one phase composition is always known and the three-phase compositions on the locus of shocks from that composition must be found. As shown in Fig. 2.5, one-phase composition A_1 is pure C_{16} and the locus of shocks consists of two curves, one with high aqueous phase saturation, and one with low aqueous phase saturation. Moving from composition A_1 to B_1, both of the curves on the locus of shocks migrate toward the C_{16} apex of composition space. Between compositions B_1 and C_1 the curves that make up the Hugoniot locus continue to migrate towards each other until they intersect in the locus of shock from one-phase composition C_1. At C_1 the locus bifurcates and for one-phase compositions C_1-G_1 there is a curve with high alcohol phase saturation and a curve with low alcohol phase saturation. Composition D_1 is on the tie-line extension of the three-phase boundary, so the entire water/C_{16} boundary of the three-phase region is on the locus of shocks, as discussed in the section on one to two-phase shocks. In this extreme case, the curve with low alcohol phase saturation is made up of two-phase compositions in the water/C_{16} two-phase region.

For one-phase compositions with more NBA than D_1, the two curves in the locus move toward the center of the three-phase region until at G_1 they intersect. At G_1 the Hugoniot Locus again bifurcates and the new loci are a curve with high oleic phase saturation and one with low oleic phase saturation. The curve with low oleic phase saturation moves toward the water/NBA boundary of the three-phase region with increasing NBA in the one-phase composition. One-phase composition I_1 is on the tie-line extension of the water/NBA boundary of the three-phase region. The curve of the Hugoniot locus with low oleic phase saturation consists of two-phase compositions in the water/NBA two-phase region.

The two curves in the locus of shocks migrate toward the NBA apex of the three-phase region with increasing NBA in the one-phase composition, such as J_1. For one-phase composition K_1 the curves again intersect and the locus bifurcates into a curve with high aqueous phase saturation and with low aqueous phase saturation. This trend continues to the one-phase composition L_1, which is pure NBA.

In conclusion, the locus of one to three-phase shocks for this example always consists of two curves through the three-phase region. At three different one-phase compositions the curves of the Hugoniot locus intersect and bifurcate.

2.4.3.2 Behavior of One- to Three-Phase Tangent Shocks

Figures 2.5 and 2.6 show that for most of the one-phase compositions (A_1-C_1, E_1-H_1 and J_1-L_1) there are three compositions in the three-phase region for which the shock is tangent to either the fast or the slow path through composition space. For one-phase compositions D_1 and I_1 there are four tangent shocks. It is impossible to tell in advance how many tangent shocks may exist.

For each of the one-phase compositions at which the Hugoniot locus bifurcates there are tangent shocks near the intersection point of the two curves of the Hugoniot locus. A shock tangent to the slow path coincides with the intersection point of the curves (shown in Table 2.6) for one-phase compositions C_1, G_1, and K_1. For one-phase compositions C_1 and K_1 there are two tangent shocks are extremely close to each other and the intersection point. For one-phase composition G_1 there is only one tangent shock near the intersection point.

2.4.4 Shocks Between Two-Phase and Three-Phase Regions

For one- to three- and one- to two-phase shocks the single-phase composition is typically known (either the injection or initial composition). For two- to three-phase shocks, however, the upstream, downstream, or both compositions may be unknown. Two to three-phase shocks must also satisfy Eqs. (2.16). Shocks may be tangent either to the fast or the slow path in the three-phase region, or they may result in a constant state in the three-phase region. Additionally, shocks may be tangent to either the tie-line or the non-tie-line path in the two-phase region, or result in a constant state in the two-phase region.

Rarely shocks are tangent to a path at the three-phase composition and the two-phase composition in a dual tangent shock. Tangent shocks occur only at isolated points, however several tangent shocks may exist. The behavior of the locus of two to three-phase shocks and tangent shocks has not been previously been explored.

2.4.4.1 Behavior of the Locus of Two- to Three-Phase Shocks

It is often the case that the two-phase composition is known because either the injection or the initial composition is two-phase. Figures 2.7-2.8 show how the locus of tangent shocks changes for two-phase compositions along the water/NBA axis of the ternary diagram. Table 2.7 gives the two-phase saturations and compositions.

Two-phase composition A_2 is 100% aqueous phase and is on one apex of the three-phase region. As a consequence A_2 is on both the water/NBA and the C_{16}/NBA tie lines that make up the boundary of the three-phase region. As a consequence, both tie lines are in the Hugoniot locus of shocks for A_2. There is also a line of compositions through the center of the three-phase region on the Hugoniot locus. The central line intersects the water/NBA boundary of the three-phase region near A_2.

Composition B_2 has slightly more NBA than A_2, which results in 7% alcohol phase saturation. The locus of shocks consists of two curves; a curve with high aqueous phase saturation near the water apex of the three-phase region, and a curve through the center of the three-phase region with lower aqueous phase saturation. With increasing NBA in the two-phase composition, such as C_2, the aqueous phase-rich curve moves toward the center of the three-phase region, while the aqueous-phase poor curve retreats toward the C_{16}/NBA axis. By two-phase composition D_2 the aqueous phase-poor branch of the Hugoniot locus has disappeared completely, however between D_2 and E_2 the curve with low aqueous phase saturation reappears and begins to move toward the center of the three-phase region.

At two-phase composition F_2 the curves of the Hugoniot locus intersect and the locus bifurcates into a curve with high alcohol phase saturation and one with low alcohol phase saturation. Composition G_2 shows both branches of the locus moving back towards the boundaries of the three-phase region with increased NBA in the two-phase composition. By composition H_2 the curve with low alcohol phase saturation has disappeared and the curve with high alcohol phase saturation is an oval in the interior of the three-phase region and does not touch the two to three-phase boundary. At I_2 the locus of shocks touches the boundary and it bifurcates into a 'U' shape. Between I_2 and J_2 a curve of the Hugoniot locus with high alcohol phase saturation is advancing toward the center of the three-phase region and a curve with low alcohol phase saturation reappears. At K_2 the curves intersect and the locus bifurcates back into a curve with high aqueous phase saturation and one with low aqueous phase saturation. The curves of the locus both migrate back towards the boundaries of the three-phase region with increasing NBA in the two-phase composition. Composition L_2 shows an example of curves with high and low aqueous phase saturation on the Hugoniot locus. L_2 is on the boundary of the two-phase region with 100% alcohol phase present.

In conclusion, the locus of two to three-phase shocks for this example consists of one or two curves through the three-phase region. The locus of two to three-phase shocks becomes an oval in the three-phase region and does not touch the two to three-phase boundary for some two-phase compositions. This behavior was not observed in the locus of one to three-phase shocks. At three different two-phase compositions the curves of the Hugoniot locus intersect and the locus bifurcates.

2.4.4.2 Behavior of Two- to Three-Phase Tangent Shocks

Figures 2.7 and 2.8 show that there are between two and five compositions in the three-phase region for which the shock is tangent to either the fast or the slow path through composition space. Typically each curve in the Hugoniot locus has one or two shocks tangent to a three-phase path, but it is impossible to tell in advance how many of these tangent shocks may exist. For each of the two-phase compositions at which the locus bifurcates (F_2, I_2, and K_2) there is a shock tangent to one of the three-phase paths at the intersection point of the two curves of the Hugoniot locus as shown in Table 2.8.

Figures 2.7 and 2.8 also show between zero and six compositions in the three-phase region for which the shock is tangent to either the tie-line or the non-tie-line path at the two-phase composition. At the boundaries of the two-phase region (compositions A_2 and L_2) the non-tie-line path has velocity one and so shocks to the boundaries of the three-phase region are all tangent to the non-tie-line path. That is why these compositions have so many two-phase tangent shocks.

Unlike tangents to the three-phase path, there is frequently no shock tangent to a path at the two-phase composition. At composition C_2 all of the shocks in the curve rich in aqueous phase have velocity less than the tie-line path velocity while all of the shocks in the curve poor in aqueous phase have shocks greater than the tie-line path velocity. All of the shocks in the locus have velocity smaller than the non-tie-line path velocity. For compositions D_2 and F_2-H_2 there are no two-phase tangent shocks because all of the shocks in the locus are much slower than the tie-line and the non-tie-line path velocities. For J_2 and K_2 all of the shocks are faster than the tie-line path and slower than the non-tie-line path.

Often for shocks between the two- and three-phase regions, the path a composition route is flowing down is known, but the exact upstream and downstream compositions must be found to construct shocks in the composition route. Fortunately, the correct shocks are often tangent to a path on one or both sides of the shock, so the number of possible compositions on the Hugoniot locus can be significantly reduced by only looking at compositions that result from tangent shocks from the known path. Equation (2.16) gives the locus of tangent shocks when C^u or C^d are constrained to a path and Λ constrained so that $\Lambda = \lambda_{t/nt}$ or $\lambda_{+/-}$.

An example of the locus of tangent shocks where the shock originates somewhere the two-phase tie-line path down the water/NBA axis is shown in Fig.

2.9. In this case the shocks shown are all tangent to the fast or slow path in the three-phase region. There are five compositions on the locus of tangent shocks for which the shock is simultaneously tangent to a path in the two and three-phase regions, four of which occur at compositions on the oval of tangent shocks in composition space.

2.4.4.3 Three- to Two-Phase Shocks

In all of the examples studied in this work the initial and injection compositions have one or two components and a maximum of two phases. As a consequence three-phase compositions in shocks are always unknown and must be found by finding two to three-phase shocks from a known two-phase composition or from the locus of tangent shocks. Thus there is little purpose in analyzing the locus of shocks from a known three-phase composition into the two-phase region as was done for one to three-phase shocks and two to three-phase shocks. Figure 2.10 shows the Hugoniot locus of shocks into the two-phase region for a given three-phase composition. In each two-phase region the locus is either a single curve or a pair of curves. There is only one tangent shock in one of the two-phase regions.

2.4.5 Intra-Three-Phase Shocks

The construction of legally valid shocks within the three-phase region is discussed in detail by Guzman (1995) and by Falls and Schulte (1992a, b). Much like shocks from two to three-phases, intra-three-phase shocks may be tangent to a path at either or both three-phase compositions, or may result in a constant state on both sides. There is no way to determine in advance the structure of the Hugoiniot locus of shocks within the three-phase region or where the tangent shocks will lie for an arbitrary three-phase composition. If one phase is below its residual saturation shocks between compositions in that same region must lie on the same fast path. A proof of this result is presented in Appendix C.

2.5 THE ENTROPY CONSTRAINT

In two-phase partially miscible MOC Lax (1957) and Liu (1974) entropy constraints are sufficient to build unique continuous solutions for given initial and boundary conditions. Shocks between tie lines in the two-phase region satisfy the form of the entropy condition derived by Wang (1998). In three-phase partially miscible and immiscible MOC the Lax and Liu entropy constraints may fail to provide a solution and so the entropy constraint must be relaxed and the viscous profile criterion must be used. The viscous profile criterion states that a solution is admissible if it is limit of the parabolic equation

$$\left(\frac{\partial C_i}{\partial t_D}\right)_{x_D} + \left(\frac{\partial F_i}{\partial x_D}\right)_{t_D} = \varepsilon \frac{\partial}{\partial x_D}\left(K_{ij}\frac{\partial C_i}{\partial x_D}\right) \quad i = 1, \ldots, n_c \tag{2.17}$$

as ε → 0 (Isaacson *et al.*, 1992).

Schecter *et al.* (1996) explains the development of the viscous profile criterion and classification of shocks in detail. Their development is summarized here. Suppose two or three-phase compositions C^u and C^d with eigenvalues $\lambda^u_{+/-}$

and $\lambda^{d}_{+/-}$ are connected by a shock satisfying Eq. (2.16). The equilibria at C^u and C^d are defined as $\eta^{u/d}_{+/-} = \lambda_{+/-} - \Lambda$. Equilibria can be classified as a repeller ($\eta_{+/-} > 0$), a repeller-saddle ($\eta_{+} > 0, \eta_{-} = 0$), a saddle ($\eta_{+} > 0$, $\eta_{-} < 0$), a saddle-attractor ($\eta_{+} = 0$, $\eta_{-} < 0$) or an attractor ($\eta_{+/-} < 0$) at each composition C^u and C^d.

Shocks are classified as fast, slow, overcompressive, or transitional, depending on the equilibria at C^u and C^d. Table 2.9 shows the classification of shocks.

Fast and slow shocks are the only two types of shocks allowed under the Lax and Liu entropy constraints and are called classical shock waves. The viscous profile criterion allows transitional and classical shock waves in the solutions of Riemann problems. Transitional shocks are non-self-sharpening, but not all non-self-sharpening waves are transitional. For example an indifferent wave down a non-tie-line path in the two-phase region is non-self-sharpening, but is not classified as a transitional shock.

Tangent shocks between two and three-phase compositions may be classified as transitional since the classification depends on both eigenvalues of the upstream and downstream compositions. Assume two-phase composition B_2 is an upstream composition. The shock from B_2 to $(C_1,C_2,C_3) = (0.6754,0.1619, 0.1627)$ on Fig. 2.7 is tangent to the slow path in three-phases, but it is also a saddle to a repeller-saddle transitional shock (see Tables 2.7 and 2.10). Alternately, the shock from two-phase composition B_2 to $(C_1,C_2,C_3) = (0.2932,0.5378,0.1690)$ on Fig. 2.7 is tangent to the non-tie-line path in two-phases, but it is a saddle-attractor to a saddle transitional shock (see Tables 2.7 and 2.10).

All shocks connecting two constant states are not transitional shocks. For example a slow shock that connects a repeller and a saddle must have a constant state on both sides since the shock is slower than both of the upstream paths and the shock velocity is in between the downstream path velocities. A similar argument applies to fast shocks connecting a saddle and an attractor. Most transitional shocks in solutions to Riemann problems are tangent on either the upstream or downstream side, though saddle-to-saddle shocks do occur.

Transitional shocks are not self-sharpening and yet they are stable in the presence of dispersion. Figure 2.11 compares a transitional shock and a classical self-sharpening shock in simulated solutions. The simulator used is one-dimensional, explicit in time and uses single point upstream weighting. Numerical dispersion is used to represent physical dispersion where $D_{num} = 0.5(\Delta x - \Delta t)$. The simulator and numerical dispersion are discussed in detail in Chapter 5. The Peclet number is a dimensionless measure of dispersion and is defined as $N_{Pe} = 1/D_{num}$ (Lake, 2002).

The water/decane/ethylene-glycol ternary system outlined in Table 2.3 is used along with the relative permeability parameters outlined in Table 2.4 that give a SH mass-balance equation. In both cases the initial condition is 30% decane and 70% water by volume. The classical shock results from injection of 70% water and 30% ethylene glycol. The transitional shock results from injection of 36% water and 64% ethylene glycol. Both shocks are upstream tangent to a slow path in the three-phase region and shock to the tie line on the water/decane boundary of composition space. The classical shock is a slow shock and the transitional shock is of saddle-attractor to saddle type. Clearly the transitional shock is stable in the presence of dispersion for all of the Peclet numbers considered and experiences no more spreading than the classical shock.

2.6 CONSTRUCTION OF SOLUTIONS TO RIEMANN PROBLEMS

Composition routes can be constructed once all physical parameters and boundary conditions are specified. The boundary conditions for a Riemann problem consist of a constant initial composition along the entire length of the system and a constant injection composition implemented at $x_D = 0$ for all t_D. There are four criteria that must be met for all valid composition routes in partially miscible flow (Hadamard, 1952).

2.6.1 Mass-Balance Constraints

The composition route must connect the boundary conditions by following the paths from Eq. (2.13). The construction and behavior of these paths is discussed in Section 2.3. Spreading or rarefaction waves in the solution form along these allowable paths. If shocks are introduced into a solution, they must also preserve mass, i.e. they must satisfy the shock jump conditions given by Eq. (2.16).

2.6.2 Velocity Constraint

All physically meaningful solutions must be single-valued functions of x_D/t_D. It is rarely possible to construct solutions exclusively by following paths because composition velocities along paths are not monotonic within the two- or three-phase regions and are discontinuous at the phase boundaries. Shocks are introduced when necessary to prevent multi-valued solutions. Construction of shocks is discussed in section 2.4

2.6.3 Entropy Constraint

The entropy constraint requires that solutions must be stable in the presence of diffusion. This is because the physically meaningful solutions to Eq. (2.6) are the zero-dispersion limit of the more general equations including dispersion. The viscous profile criterion outlined in Section 2.5 is the entropy constraint for shocks in composition. The entropy condition combined with the velocity condition often requires tangent shocks.

2.6.4 Continuity Condition

The continuity condition requires that small perturbations in injection composition or any other input parameter lead to small changes in composition and saturation profiles. Multiple solutions may exist which preserve mass and obey the velocity constraint but only one satisfies all four conditions.

2.6.5 A Well-Posed Problem

Given the complexity of the composition routes in three-phase partially miscible flow, it is possible to construct any number of possible solutions for a given initial and injection composition. The vast majority of potential composition routes can be eliminated using the mass-balance, velocity and entropy conditions, but occasionally more than one solution will exist that satisfies these three conditions.

A partial differential equation is well-posed only if it has the following three properties: existence, uniqueness, and stability (Strauss, 1992). Existence of the solution is verified by construction of one or more possible solutions. In all of the examples studied it is possible to use the stability (or equivalently continuity) condition to build a unique solution.

Consider the ternary system in Fig. 2.1 with an initial reservoir composition of 100% C_{16}. The solution for pure water injection is a two-component, two-phase displacement and is well understood. Similarly, pure NBA injection results in a first-contact miscible displacement, which is also well understood. Starting with pure water injection, the problem is perturbed by addition of a small amount of NBA into the injection composition. Continuity ensures that the solution to the perturbed problem must be near the solution to the original problem. In this way it is possible to build solutions for all injection compositions between 100% water and 100% NBA that are continuous with nearby injection compositions. Moreover, the solutions constructed in this way are continuous with known solutions for 100% water and 100% NBA injection.

By enforcing continuity, a single solution is found for each set of injection and initial compositions. While this does not rigorously prove the uniqueness of solutions, there was only one possible set of continuous solutions for each of the cases studied in this work.

2.6.6 Example Solution Construction

MOC composition routes are constructed for partially-miscible three-phase flow for the first time. Solutions are constructed in the same way as the solutions for three-phase immiscible flow (e.g. Falls and Schulte, 1992b; Isaacson *et al.*, 1992; Marchesin *et al.*, 1999). However, the solution structure in three-phase partially miscible flow is typically more complex than in immiscible flow.

Sometimes the Lax entropy constraint is sufficient to build a solution (Lax, 1957). In this case, the solution consists of a slow wave group from the injection composition and a fast wave group from the initial composition. The slow wave group may be a spreading wave along a slow path, a slow shock, or a combination of slow shocks and spreading waves. The fast wave group is defined in the same way (Marchesin *et al.*, 1999). In many cases the Lax entropy condition fails to provide a solution and a transitional wave group must be introduced to connect the fast and slow wave groups. The transitional wave group may consist of a transitional shock or a combination of a shock and a fast spreading wave (Isaacson *et al.*, 1992).

An example composition route is shown in Fig. 2.12 for an initial and injection composition pair that can be connected using classical shock waves.

The ternary system outlined in Table 2.3 is used along with the relative permeability parameters outlined in Table 2.4 that give a NSH mass-balance equation. The initial composition is 70% water and 30% decane by volume and the injection composition is 61% water and 39% surfactant.

The slow wave group is a slow shock from the injection composition to a_1 on the slow path in the three phase region. The composition route takes the slow path in a spreading wave to a_2, followed by a slow shock to a_3 on the water/decane tie line. Both of the shocks are tangent to the slow path, so there are no constant states within the slow wave group. The fast wave group is a fast shock wave from a_3 to the initial composition.

It is not possible to connect the fast and slow wave groups for the initial and injection composition pair shown in Fig. 2.13. The ternary system outlined in Table 2.3 is used along with the relative permeability parameters outlined in Table 2.4 that give a SH mass-balance equation. The initial composition is 70% water and 30% decane by volume and the injection composition is 38% water and 62% surfactant.

Fig 2.13 shows the slow wave group in the composition route is a slow shock to g_1 in the three-phase region, followed by a spreading wave down the slow path to g_2. The transitional wave group is a spreading wave down the fast path from g_2 to g_3 followed by a transitional shock from g_3 to g_4 on the water/decane tie line. The fast wave group is a fast shock from g_3 to the initial composition.

2.7 SUMMARY

In this chapter the equations for method of characteristics were derived from the general equation for conservation of mass for isothermal flow. A relative permeability model based on extended-Corey relative permeabilities was described. The characteristics in a three-component system were derived in a general form that applies to one, two or three-phase flow regimes. The behavior of the characteristics in each of the flow regimes was discussed. In the three-phase region it is sufficient to use the characteristics and MOC theory derived for three-phase fully immiscible flow. The mass-balance equations may be hyperbolic, strictly hyperbolic, or elliptic in the three-phase region, depending on the relative permeability parameters used.

The Hugoniot locus of shocks was defined for finding shocks between compositions that cannot be connected by spreading waves. The locus of shocks and the tangent shocks into the three-phase region were studied for a series of fixed one-phase compositions and two-phase compositions. The locus of tangent shocks was also introduced for shocks in which neither the upstream nor the downstream composition is known, but the compositional path of one composition is fixed. The entropy condition was defined to be the viscous profile criterion and stability of transitional shocks in the presence of numerical dispersion was demonstrated. Finally, the conditions for construction of a unique solution between any initial and injection compositions are described and two example solutions are constructed.

Pure Component Information	Water	C_{16}	NBA
Density, ρ_i (g/cm^3)	0.9971	0.8061	0.7701
Viscosity, μ_i (cp)	0.8937	3.0500	2.5600
Three-phase region	c_{1i}	c_{2i}	c_{3i}
Phase 1	0.9127	0.0000	0.0872
Phase 2	0.0066	0.8604	0.1330
Phase 3	0.1060	0.1716	0.7224
Water/alcohol rich two-phase region			
Alcohol phase	c_{1i}	c_{2i}	c_{3i}
Tie line 1	0.1751	0.0000	0.8249
Tie line 2	0.1276	0.0925	0.7799
Tie line 3	0.1060	0.1716	0.7224
Aqueous phase	c_{1i}	c_{2i}	c_{3i}
Tie line 1	0.9127	0.0000	0.0873
Tie line 2	0.9127	0.0000	0.0873
Tie line 3	0.9127	0.0000	0.0873
Water/oil rich two-phase region			
Oleic phase	c_{1i}	c_{2i}	c_{3i}
Tie line 1	0.0005	0.9995	0.0000
Tie line 2	0.0040	0.9240	0.0720
Tie line 3	0.0066	0.8604	0.1330
Aqueous phase	c_{1i}	c_{2i}	c_{3i}
Tie line 1	1.0000	0.0000	0.0000
Tie line 2	0.9170	0.0000	0.0830
Tie line 3	0.9127	0.0000	0.0873
Alcohol/oil rich two-phase region			
Alcohol phase	c_{1i}	c_{2i}	c_{3}
Critical point	0.0221*	0.5279*	0.4500*
Tie line 2	0.0057	0.8448	0.1495
Tie line 3	0.0066	0.8604	0.1330
Oleic phase	c_{1i}	c_{2i}	c_{3i}
Tie line 2	0.0930	0.1908	0.7162
Tie line 3	0.1060	0.1716	0.7224

Table 2.1 Pure component viscosities, densities and three-phase region water/C_{16}/NBA system at 25°C and atmospheric pressure. Density, viscosity, and phase composition data are from Pongpitak (1980). *Approximate.

	S_1	S_2	S_3
Residual Saturation, S_{rj}	0.09	0.00	0.05
Relative Permeability, k_{rj}^o	1.00	1.00	1.00
Corey exponent, n_j	2.00	2.00	2.00

Table 2.2 Relative permeability parameters for water/C_{16}/NBA ternary system. In this example S_{r2}, k_{r2}^o, and n_2 are constants.

Pure Component Information	Water	C_{10}	Ethylene Glycol
Density, ρ_j (g/cm^3)	1.027	0.896	0.728
Viscosity, μ_j (cp)	0.911	0.752	0.740
Three-phase region	c_{1i}	c_{2i}	c_{3i}
Phase 1	0.8280	0.0028	0.1692
Phase 2	0.0029	0.9159	0.0812
Phase 3	0.3900	0.0795	0.5304
Water/alcohol rich two-phase region			
Alcohol phase	c_{1i}	c_{2i}	c_{3i}
Critical Point	0.6745	0.0056	0.3199
Tie line 2	0.4589	0.0520	0.4891
Tie line 3	0.3900	0.0795	0.5304
Aqueous phase	c_{1i}	c_{2i}	c_{3i}
Tie line 2	0.8116	0.0028	0.1856
Tie line 3	0.8280	0.0028	0.1692
Water/oil rich two-phase region			
Oleic phase	c_{1i}	c_{2i}	c_{3i}
Tie line 1	0.0000	1.0000	0.0000
Tie line 2	0.0000	0.9829	0.0171
Tie line 3	0.0029	0.9159	0.0812
Aqueous phase	c_{1i}	c_{2i}	c_{3i}
Tie line 1	1.0000	0.0000	0.0000
Tie line 2	0.9386	0.0000	0.0614
Tie line 3	0.8280	0.0028	0.1692
Alcohol/oil rich two-phase region			
Alcohol phase	c_{1i}	c_{2i}	c_{3}
Critical point	0.0735	0.4826	0.4438
Tie line 2	0.3375	0.0952	0.5673
Tie line 3	0.3900	0.0795	0.5304
Oleic phase	c_{1i}	c_{2i}	c_{3i}
Tie line 2	0.0036	0.9092	0.0872
Tie line 3	0.0029	0.9159	0.0812

Table 2.3 Pure component viscosities, densities and three-phase region water/C_{16}/NBA system at 25°C and 1.0 atm. Density and viscosity data are from the Chemical Properties Handbook (Yaws, 1999). Phase composition data are from Negahban *et al.* (1986).

	NSH	SH	MHE
S_{r1}	0.117	0.117	0.117
S_{r2}	0.033	0.033	$S_{r21}=0.3$, $S_{r23}=0.033$
S_{r3}	0.082	0.082	0.082
k_{r1}^{o}	0.85	0.85	0.85
k_{r2}^{o}	0.95	0.95	$k_{r21}=0.9$, $k_{r23}=0.95$
k_{r3}^{o}	1.0	1.0	1.0
n_1	1.5	1.5	1.5
n_2	1.98	1.98	$n_{21}=1.4$, $n_{23}=1.98$
n_3	1.98	0.48	1.98

Table 2.4 Relative permeability parameters for three different relative permeability models: NSH denotes non-strictly hyperbolic mass-balance equation, SH strictly hyperbolic, and MHE mixed hyperbolic-elliptic. Parameters are based in part on measured three-component, three-phase partially miscible data from *Delshad et al.* (1987).

One-Phase Composition	Water	C_{16}	NBA
A_1	0.0000	1.0000	0.0000
B_1	0.0000	0.8800	0.1200
C_1	0.0000	0.8692	0.1308
D_1	0.0000	0.8667	0.1333
E_1	0.0000	0.7500	0.2500
F_1	0.0000	0.5500	0.4500
G_1	0.0000	0.5338	0.4662
H_1	0.0000	0.5000	0.5000
I_1	0.0000	0.1941	0.8059
J_1	0.0000	0.1800	0.8200
K_1	0.0000	0.1286	0.8714
L_1	0.0000	0.0000	1.0000

Table 2.5 One-phase compositions for Hugoniot loci shown in Figs. 2.5-2.6.

One-Phase Composition	S_1	S_2	Water	C_{16}	NBA	Λ	λ_+	λ_-
C_1	0.0979	0.8338	0.1021	0.7291	0.1688	0.0677	0.0702	0.0677
G_1	0.3810	0.3011	0.3834	0.3136	0.3030	1.4564	2.5275	1.4549
K_1	0.1482	0.1453	0.2111	0.2462	0.5427	0.5530	0.6872	0.5532

Table 2.6 One-phase compositions at which the Hugoniot locus of shocks bifurcates and the intersection point of the two curves.

Two-Phase Composition	Water	C_{16}	NBA	S_2	λ_t	λ_{nt}
A_2	0.9127	0.0000	0.0873	0.0000	0.0000	1.0000
B_2	0.8611	0.0000	0.1389	0.0700	0.0270	1.1505
C_2	0.8021	0.0000	0.1979	0.1500	0.1794	1.3704
D_2	0.6177	0.0000	0.3823	0.4000	1.4205	2.6519
E_2	0.4701	0.0000	0.5299	0.6000	2.4325	0.9129
F_2	0.4440	0.0000	0.5560	0.6355	2.3322	1.4269
G_2	0.4185	0.0000	0.5815	0.6700	2.1301	1.6320
H_2	0.3595	0.0000	0.6405	0.7500	1.3941	1.6879
I_2	0.3161	0.0000	0.6834	0.8089	0.7935	1.5601
J_2	0.2931	0.0000	0.7069	0.8400	0.5077	1.4676
K_2	0.2684	0.0000	0.7316	0.8735	0.2396	1.3595
L_2	0.1751	0.0000	0.8249	1.0000	0.0000	1.0000

Table 2.7 Two-phase compositions for Hugoniot loci shown in Figs. 2.7-2.8.

Two-Phase Composition	S_1	S_2	Water	C_{16}	NBA	Λ	λ_+	λ_-
F_2	0.1781	0.5634	0.1937	0.5291	0.2772	1.3478	1.6401	1.3478
I_2	0.2075	0.0164	0.2717	0.1473	0.5810	1.0978	1.0978	0.0471
K_2	0.1625	0.4791	0.1895	0.4737	0.3368	1.2575	2.3051	1.2575

Table 2.8 Two-phase compositions at which the Hugoniot locus of shocks bifurcates and the intersection point of the two curves.

		Upstream Composition			
		Repeller	Repeller-Saddle	Saddle	Saddle-Attractor
Downstream Composition	Repeller-Saddle	slow	slow	trans.	trans.
	Saddle	slow	slow	trans.	trans.
	Saddle-Attractor	over-comp.	over-comp.	fast	fast
	Attractor	over-comp.	over-comp.	fast	fast

Table 2.9 Classification of shocks based on upstream and downstream equilibria from Schecter *et al.* 1996. transitional shock wave (trans.) over compressive shock wave (over-comp.)

Tangent Side	S_1	S_2	C_1 Water	C_2 C_{16}	C_3 NBA	Λ	λ_+	λ_-
3ϕ	0.1972	0.7184	0.1937	0.6326	0.1737	1.2711	1.2711	0.1641
3ϕ	0.1612	0.4683	0.1895	0.4665	0.3440	1.2391	2.3552	1.2391
3ϕ	0.7264	0.1669	0.6754	0.1619	0.1627	0.1205	0.3286	0.1205
3ϕ	0.9104	0.0308	0.8373	0.0366	0.1261	0.0111	0.0311	0.0111
3ϕ	0.9251	0.0036	0.8519	0.0153	0.1328	0.0034	0.0262	0.0034
2ϕ	0.0650	0.5219	0.1066	0.5199	0.3735	1.1505	2.2021	0.0000
2ϕ	0.2449	0.4217	0.2617	0.4201	0.3183	1.1505	2.6011	2.1537
2ϕ	0.3070	0.6082	0.2932	0.5378	0.1690	1.1505	2.5094	0.1785
2ϕ	0.0650	0.8510	0.0738	0.7466	0.1795	1.1505	0.1234	0.0000

Table 2.10 Tangent shocks into the three-phase region for two-phase composition B_2.

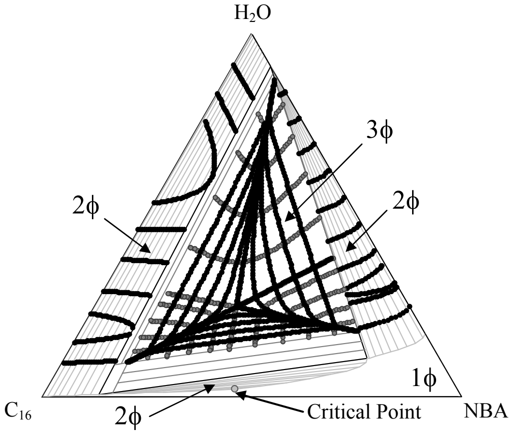

Figure 2.1 Composition paths in the two and three-phase regions for the water/C_{16}/NBA system outlined in Table 2.1 using the relative permeability parameters from Table 2.2. The gray lines are slow paths and black lines are fast paths. Non-tie-lie paths are also shown in black.

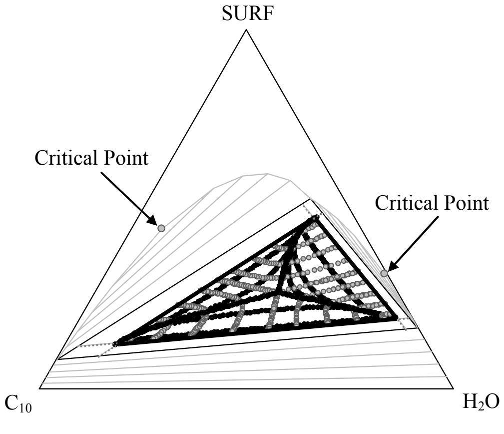

Figure 2.2 Composition paths for the water/decane/surfactant ternary system outlined in Table 2.3. The mass-balance equation is NSH. Relative permeability parameters are in Table 2.4. The gray lines are slow paths and black lines are fast paths.

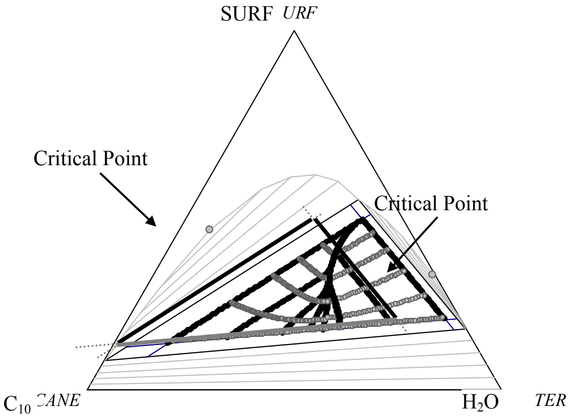

Figure 2.3 Composition paths for the water/decane/surfactant ternary system outlined in Table 2.3. The mass-balance equation is SH. Relative permeability parameters are in Table 2.4. The gray lines are slow paths and black lines are fast paths.

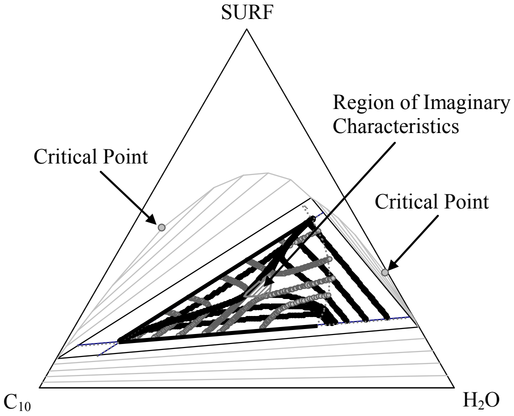

Figure 2.4 Composition paths for the water/decane/surfactant ternary system outlined in Table 2.3. The mass-balance equation is MHE. Relative permeability parameters are in Table 2.4. The gray lines are slow paths and black lines are fast paths. The area stripped gray is the region of imaginary characteristics.

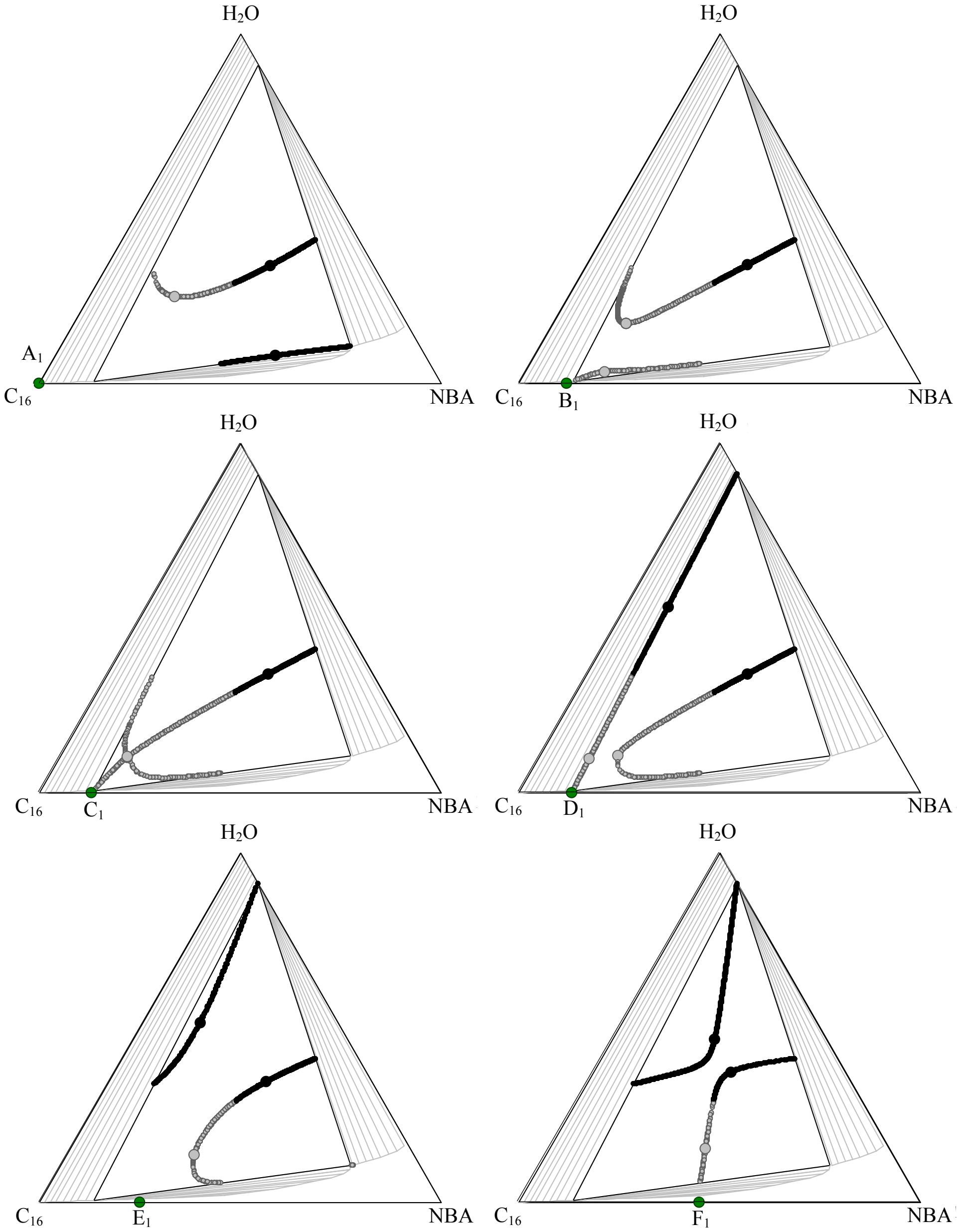

Figure 2.5 Hugoniot loci of shocks between one- and three phase-regions for one-phase compositions on the NBA/C_{16} axis. A gray circle shows one-phase compositions. In the three-phase region black indicates compositions for which the shock velocity is greater than one; gray indicates the shock velocity is less than one. Large circles denote tangent shocks.

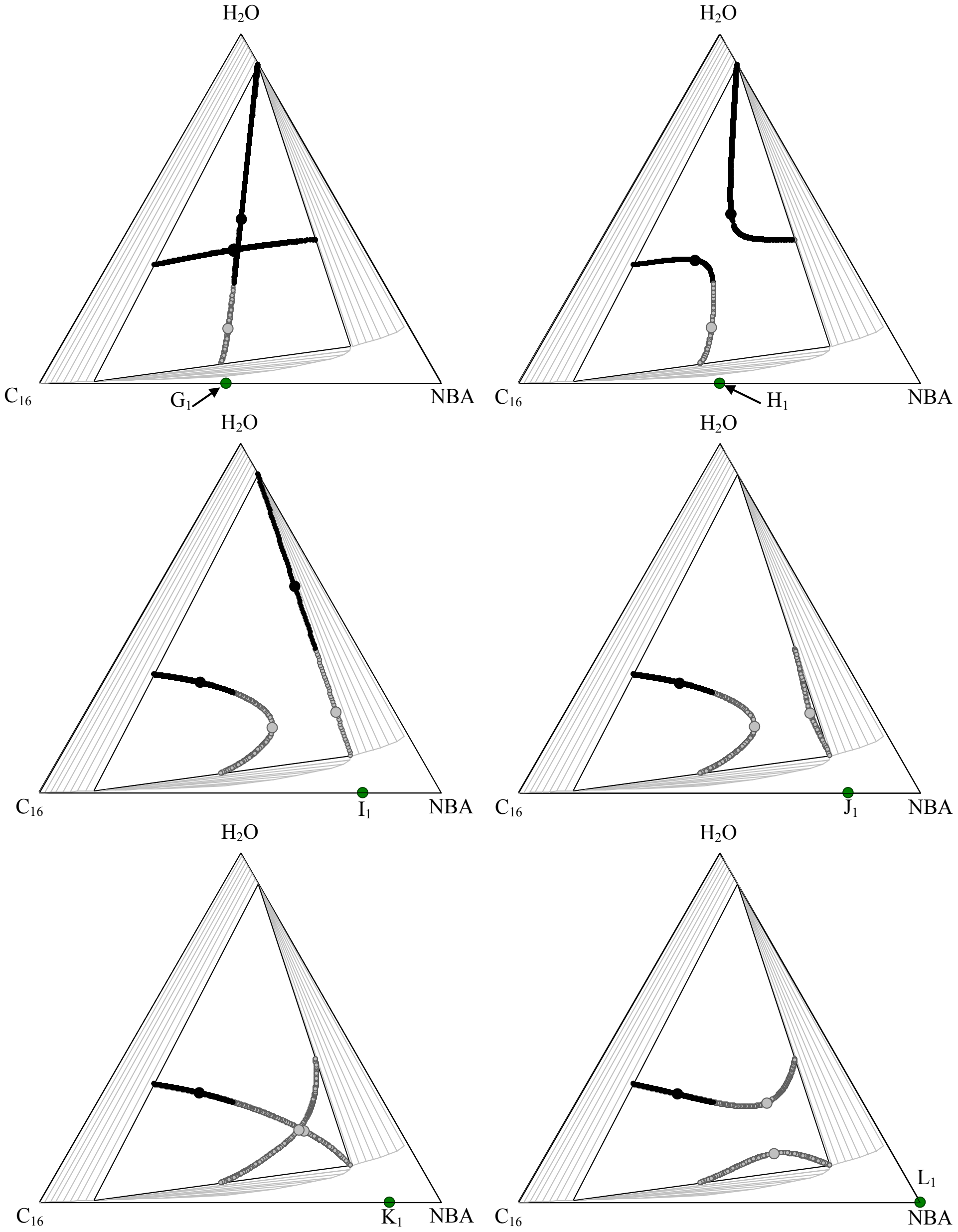

Figure 2.6 Hugoniot loci of shocks between one- and three-phase regions for one-phase compositions on the NBA/C_{16} axis. A gray circle shows one-phase compositions. In the three-phase region black indicates compositions for which the shock velocity is greater than one; gray indicates the shock velocity is less than one. Large circles denote tangent shocks.

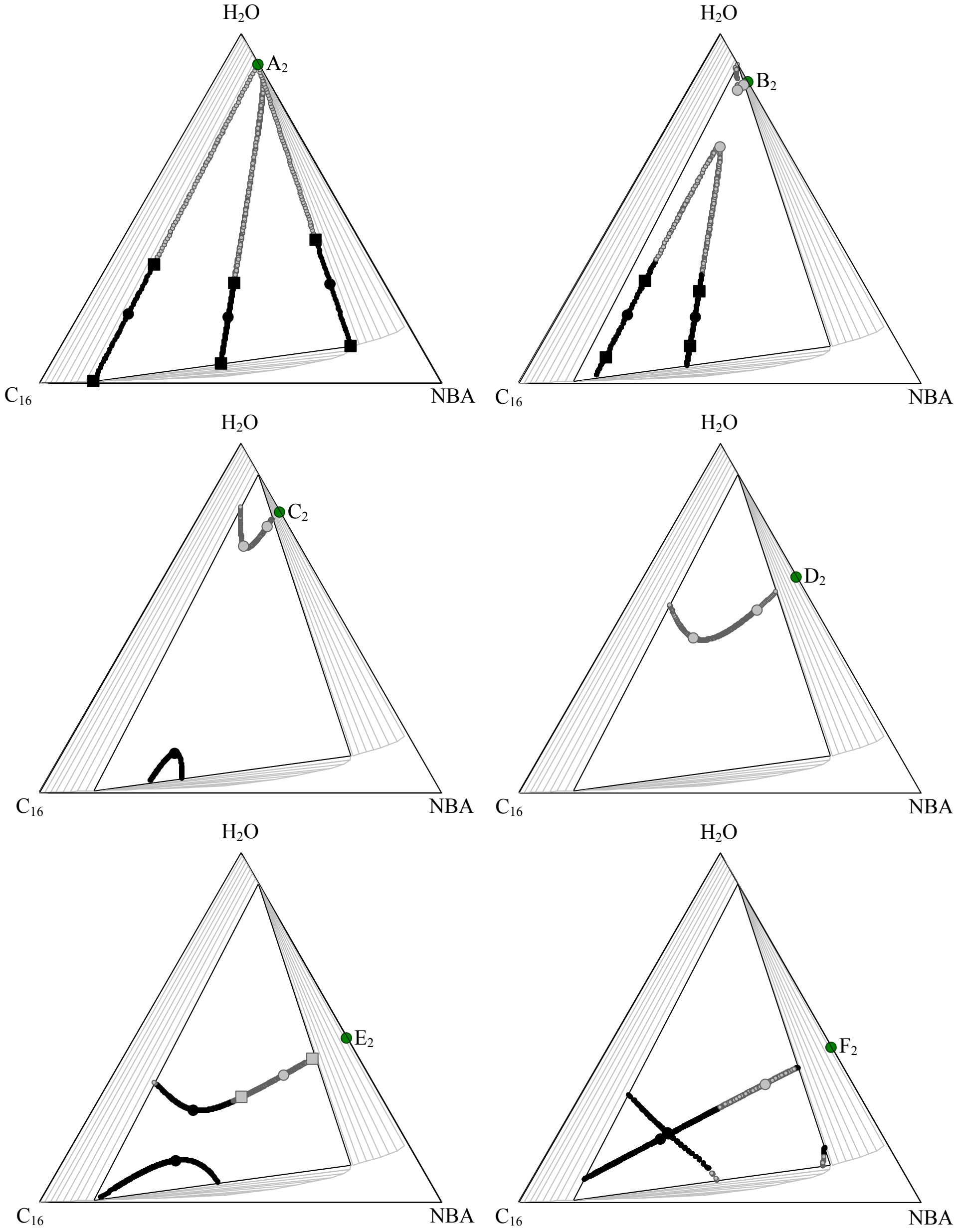

Figure 2.7 Hugoniot loci of shocks between two- and three-phase regions. A gray circle shows two-phase compositions on the water/NBA axis. Black indicates compositions for which the shock velocity is greater than one; gray indicates the shock velocity is less than one. Large circles denote shocks tangent to a path in the three-phase region. Large squares denote shocks tangent to path in the two-phase region.

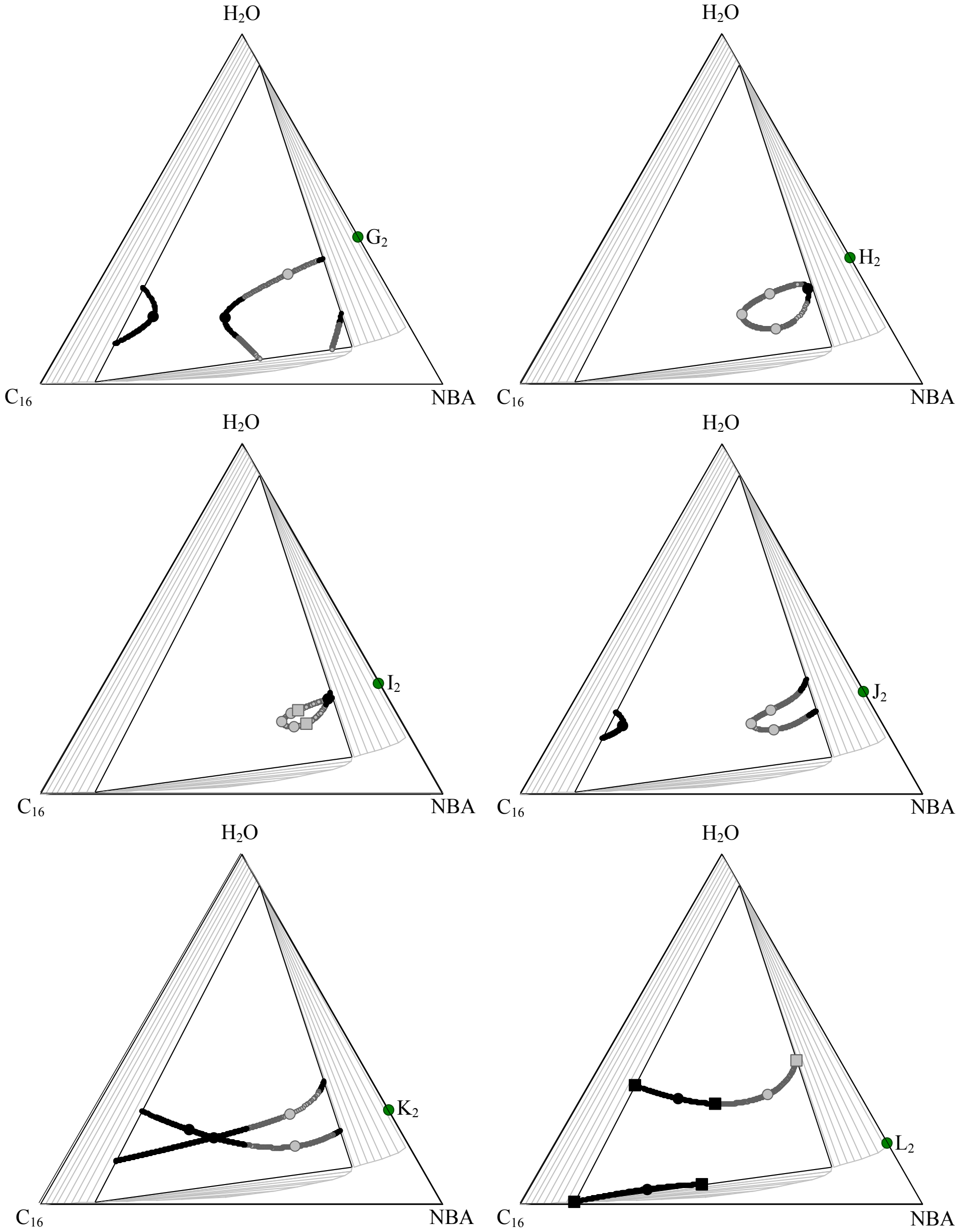

Figure 2.8 Hugoniot loci of shocks between two- and three-phase regions. A gray circle shows one-phase compositions on the water/NBA axis. Black indicates compositions for which the shock velocity is greater than one; gray indicates the shock velocity is less than one. Large circles denote shocks tangent to a path in the three-phase region. Large squares denote shocks tangent to path in the two-phase region.

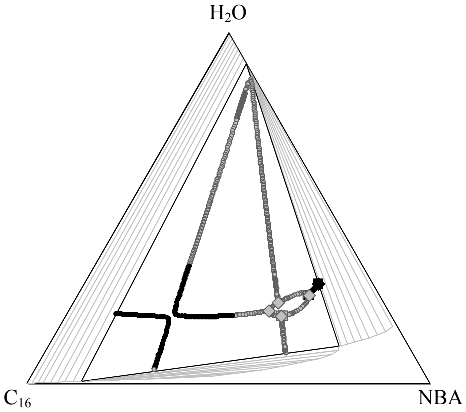

Figure 2.9 Locus of tangent shocks between two- and three-phase regions for two-phase compositions on the tie-line path down the water/NBA axis of composition space. Black indicates compositions for which the shock velocity is greater than one; gray indicates the shock velocity is less than one. Large circles denote shocks tangent to both a path in the three-phase region and a path in the two-phase region.

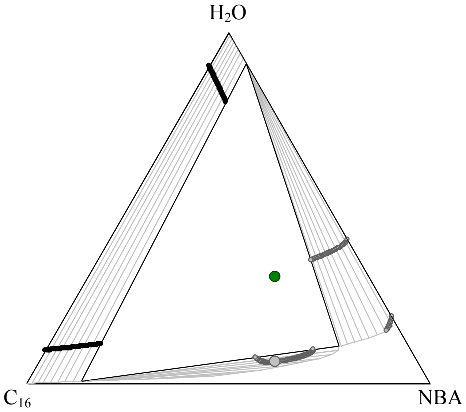

Figure 2.10 Hugoniot locus of shocks into the two-phase region from a known three-phase composition. A gray circle shows the three-phase composition. Black indicates compositions for which the shock velocity is greater than one; gray indicates the shock velocity is less than one. Large circle denotes a shock tangent to a three-phase path.

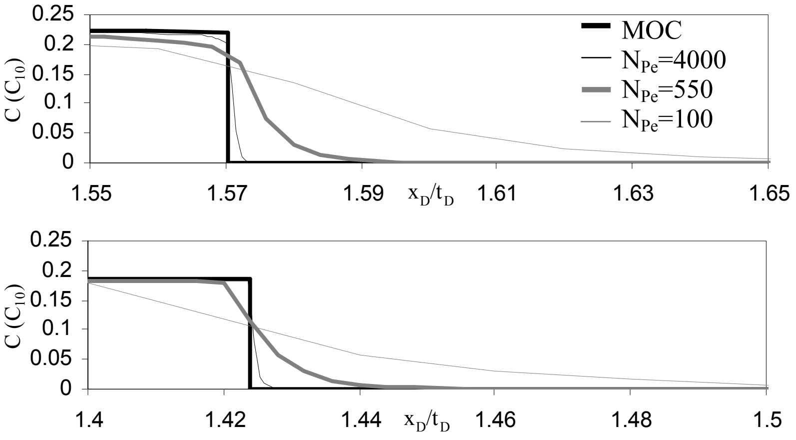

Figure 2.11 The behavior of a self sharpening (top) and transitional (bottom) shock in the presence of numerical dispersion. Both shocks experience about the same amount of spreading with dispersion.

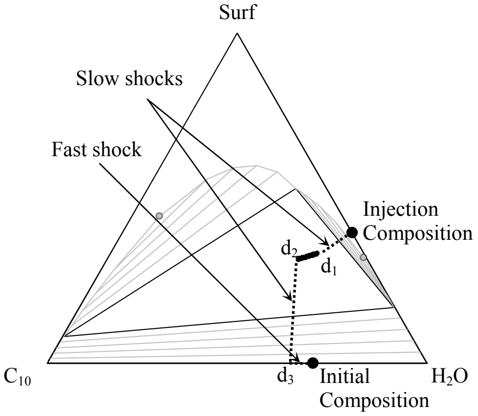

Figure 2.12 Example of a composition route that has only classical shocks.

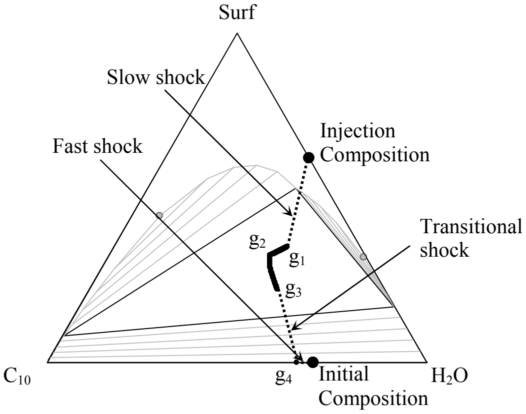

Figure 2.13 Example of a composition route that has a transitional wave set.

Chapter 3 MOC for Three-Phase Partially Miscible Flow in Hydrocarbon Recovery

In this chapter complete MOC compositional routes are built for a ternary system in which three phases may flow. In each route a single-component initial composition is used and the other two components are injected. Three-phase partially miscible flow occurs in CO_2 flooding at low temperature and pressure. Laboratory experiments on west Texas oils have shown the formation of a second, CO_2-rich liquid phase at reasonable reservoir temperature and pressures (Gardner *et al.*, 1979; Orr et al., 1980; Orr and Jensen, 1984; Turek *et al.*, 1988). Formation of three-phases has also been observed in ternary systems containing only light hydrocarbons (Merrill *et al.*, 1983). Moreover, the $L_1/L_2/V$ three-phase behavior is observed near the MMP (Creek and Sheffield, 1993). Hence the formation of three-phases in situ is likely in miscible-gas injection projects at low temperature.

It is unclear whether the formation of three phases is beneficial to recovery in partially miscible gas injection. In simulation experiments an enlarged region of three-phase flow resulted in slightly increased recovery of the heavy hydrocarbon pseudo-component (Fanchi 1987). Ngheim and Li (1986) showed that three-phase flow had little effect on simulated recoveries. However, the formation of three-phases causes an increase in pressure, likely as a consequence of a reduction of overall mobility (Henry and Metcalfe, 1983). The increased pressure may reduce injectivity, and the reduced mobility could delay CO_2 breakthrough. The level of numerical dispersion in simulations changes the route through composition space, thus analytical results are critical to correctly interpreting in situ phase behavior (Gardner *et al.* 1979).

In this chapter the MOC solutions are found for a water/C_{16}/NBA analogue system where the three-components represent light, intermediate or CO_2, and heavy oil fractions, respectively. The compositional paths are found for injection of various mixtures of water and NBA into pure component oil. Analytical routes are compared with simulated results for fine-grid finite-difference simulations. Oil recovery is studied as a function of NBA enrichment and compared to the simulated recovery. The resistance to flow for all injection compositions is also studied.

3.1 COMPOSITION ROUTES

In this section, the MOC composition routes are found for the displacement of C_{16} by mixtures of H_2O and NBA varying from 100% water to 100% NBA. The ternary system is shown in Fig. 2.1. The equilibrium phase compositions (volume fractions) and molar density are taken from Pongpitak (1980) while the pure component viscosities are from the Chemical Properties Handbook (Yaws, 1999). The properties are outlined in Table 2.1. Boundaries of the two-phase regions are modeled by a quadratic fit to the tie lines. For simplicity, we assume that all tie lines in a two-phase region intersect at a single point (Orr, 1980). One of the two-phase regions has a critical point at C =

(0.0221, 0.5279, 0.4500) but two-phases exist in the binary water/C_{16} and water/NBA systems as shown in Fig. 2.1.

The aqueous and alcohol phases are assumed to have small residual saturations, while the oleic phase residual saturation is zero. Residual saturations and other relative permeability parameters are given in Table 2.2. The resulting compositional paths are shown in Fig. 2.1.

To ensure that the selected composition routes satisfy the continuity condition, we first consider known MOC solutions for two-phase displacements where the injection composition is pure water. Subsequent composition routes are determined for injection compositions where NBA is incrementally added to the water. This ensures that the solutions satisfy the continuity condition. The initial condition is pure C_{16} for all displacements. The MOC solutions can be categorized into six types of composition routes, where each type has a unique feature that impacts cumulative oil recovery.

3.1.1 Type 1 Routes (Injection Compositions A and B)

Type 1 composition routes are two-phase partially miscible displacements. They are well understood and do not enter the three-phase region. As shown in Fig. 3.1, compositions A and B and the initial composition are on tie-line extensions from the same two-phase region. Figure 3.2 gives the composition and saturation profiles for these simple cases and Table 3.1 shows the velocities of key compositions in the composition routes.

Injection composition A is pure water and so the displacement of C_{16} by A is a two-component displacement down the tie line that extends through the initial and injection conditions. The displacement by composition B, however, has two key tie lines in the displacement (the tie lines that extend through the initial and injection compositions). The tie line that extends through B is also on the boundary of the three-phase region and thus represents a limiting case before the possible onset of three-phase flow. The composition route for the displacement by B has a spreading wave down the tie line from B to b_1, which is the equal-velocity point. (In the model B is on the boundary of the two-phase region, so there is no shock from B into the two-phase region.) At the equal-velocity point, the composition route switches to the non-tie-line path and travels to b_2, on the tie line that extends through the initial condition. All non-tie-line paths are indifferent waves (a consequence of all tie lines intersecting the same point), so all compositions from b_1 to b_2 travel at the same velocity. At b_2 a constant state occurs because the shock to the initial condition from that point is not a tangent shock.

This type of solution route continues for injection compositions where the amount of NBA is increased slightly from B but the alcohol saturation is still below its residual saturation. Although not shown here, a shock of zero velocity occurs from the injection composition to composition B so that the three-phase region is avoided. The composition route subsequently follows the two-phase route of composition B. Similar behavior was observed below the residual of two-phases for three-component fully immiscible behavior for systems by Falls *et al*. (1992a, b).

3.1.2 Type 2 Routes (Injection Compositions C-G)

As the volume fraction of NBA is increased further, the alcohol saturation becomes greater than its residual value, and the composition routes enter the three-phase region. The defining characteristic of type 2 composition routes is a spreading wave along a slow path in the three-phase region. The composition routes for these injection compositions are shown in Fig. 3.1 and are outlined in Tables 3.2-3.3. Figure 3.3 gives the composition and saturation profiles.

First consider the injection of composition C as shown in Figs. 3.1 and 3.3. Injection composition C is a two-phase composition on the water/NBA tie line. The composition route shocks from the injection condition directly into the three-phase region to point c_1, which is on a slow path. The shock is tangent to the slow path at c_1. Next, the route takes a spreading wave down the slow path from c_1 to c_2. At c_2 there is another shock tangent to the slow path (upstream side) to c_3 on the boundary of the three-phase region. A constant state occurs at c_3 because the shock is not tangent there. From c_3 the route takes the tie-line spreading wave and subsequently follows the same route as for injection composition B. Compositions c_1 and c_2 contain less water than compositions C and c_3, which causes the dip in the water fraction and corresponding spike in the C_{16} fraction on the profile in Fig. 3.3.

The path construction for composition D is exactly the same as for composition C. For D the three-phase spreading wave is wider on the composition profiles and richer in C_{16}, and the constant state on the boundary tie line is longer. When the displacement from composition D shocks out of the three-phase region, the upstream tangent shock lands at b_1, the umbilic point. The composition route has a constant state since the shock is not tangent to the non-tie-line path. The composition route then follows the non-tie-line path without having a spreading wave on the tie-line path. Injection composition D is a key composition because it corresponds to the last route that is similar to the displacement with injection composition B. Subsequent routes, such as that with composition E follow different non-tie-line paths in the water/C_{16} two-phase region.

The route corresponding to injection composition F is important because the route from F is the transition to the next route sub-type. The composition route shocks from the injection condition at F to f_1 and follows a slow path to f_2. From f_2 there are two possible composition routes, which give the same composition and saturation profiles. First, the route could shock directly to f_3, followed by an indifferent wave along the non-tie-line path to f_4. There is no longer a constant state at f_3 because the shock from f_2 to f_3 is tangent to both the three-phase slow path and the non-tie-line path. Second, the route could take a more direct route with a single shock from f_2 to f_4. This shock is also a tangent shock along the three-phase slow path and the non-tie-line path as shown in Fig. 3.1. Although both routes give the same composition and saturation profiles, the simpler route provides the transition to the next route sub-type. Composition routes with more NBA in the injection condition cannot shock to a non-tie-line path because such shocks would violate the velocity constraint.

As the NBA fraction in the injection composition is increased, the composition route takes higher velocity slow paths near the center of the three-phase region. At injection composition G the two-phase constant state at g_4 disappears. The vanishing constant state allows for three possible composition routes from g_2, (shown in Fig. 3.1) all of which give identical composition and saturation profiles. First, the route can shock from g_2 to g_4 as discussed above, followed by a shock of the same velocity to the initial condition. Second, the route can shock directly from g_2 to the initial condition, again with the same velocity as the alternate shocks. Third, the route can shock from g_2 to g_3, followed by a shock of the same velocity to the initial condition. Composition g_3 lies on the Hugoniot locus for shocks from the initial condition to the three-phase region. All of these shocks have the same velocity so that the composition and saturation profiles are identical even though the composition routes are not. The route through g_3 provides a transition to the next route type.

3.1.3 Type 3 Routes (Injection Compositions H-K)

Further enrichment of the injection condition with NBA causes a constant state to develop in the three-phase region. All routes with a constant state in the three-phase region are type 3 routes and for this system three subtypes exist. The composition routes for injection compositions H through K are shown in Fig. 3.4.

Figure 3.5 gives the corresponding composition and saturation profiles and Table 3.4 shows the velocity of key compositions on the routes.

The displacement of C_{16} by H is a type 3a route. The composition route takes a tangent shock from H to a slow path at h_1. A spreading wave along the slow path occurs until it is possible to take a shock (again tangent to the slow path) from h_2 to h_3. A non-tangent shock then occurs to the initial condition from composition h_3, whose aqueous phase saturation is below residual. A constant state exists at h_3 because the shock is not a tangent shock. A shock directly from h_2 to the initial condition or to the tie-line that extends through the initial condition is not possible because they would violate the velocity condition.

The velocity of the leading (upstream) shock to the initial condition is faster than the similar shock from g_3 for the composition route associated with injection composition G. The leading shock velocity continues to increase with NBA enrichment. As will be discussed in the next section, this is significant because oil recovery decreases as the result of the faster leading shock.

For composition I there are two possible routes, both of which give exactly the same saturation and composition profiles. The first route has a tangent shock to the slow path at i_1 and another tangent shock from i_1 to the constant state at i_2, without a spreading wave down the slow path. The second route is a shock (with the same velocity) directly from I to i_2, followed by a non-tangent shock to the initial condition. In both cases a constant state exists on the downstream side of the shock. The second route is a transition to type 3b routes.

The route for the displacement by injection composition J consists of only two shocks separated by a constant state. However, the shock from point j_1 to the initial condition is now a tangent shock to the fast path on the downstream side (see Fig. 3.4). The trailing shock is non-tangent, and results in a constant state on the upstream end of the fast path.

Last, the displacement by injection composition K gives an example of a composition route that has a constant state and a spreading wave in three-phase region, a type 3c route. The route for the displacement by injection composition K shocks from the injection condition to a constant state at k_1. A spreading wave occurs along the same fast path as the route from injection composition J in the residual aqueous phase region, followed by the tangent shock from j_1 to the initial condition. Since the fast path containing j_1 is below the residual saturation of the aqueous phase, it follows the line of constant saturation of the aqueous phase given by $S_w = 0.0025$.

3.1.4 Type 4 Routes (Injection Compositions L-P)

The defining characteristic of type 4 composition routes is a spreading wave along a fast path without any constant states in the three-phase region. Figure 3.6 illustrates the composition routes on the ternary diagram, whereas Fig. 3.7 gives the corresponding composition and saturation profiles. Tables 3.5-3.6 show the velocity of important compositions on the routes.

Further enrichment with NBA causes the shock from the injection composition at L to become a tangent shock to the fast path where S_w is 0.0025 at

n_1. From there the route takes the spreading wave along the fast path to n_2, followed by a tangent shock from n_2 to the initial condition (n_2 and j_1 are the same composition).

The composition route from L has an alternate route that consists of two equal-velocity shocks. The first shock is from the injection composition to N on the same two-phase tie line. The second shock from N to n_1 is tangent shock to the fast path. This alternate route is important to subsequent routes with injection compositions richer in NBA. For those routes, there cannot be a shock directly from the injection composition to the fast path where $S_w = 0.0025$ (that shock would violate the velocity condition). Instead, there is a shock to N from the injection composition, i.e. from M, O and P.

The velocity of the shock from the injection composition to N decreases as the injection composition approaches N, as shown by the route with injection composition M. As the injection composition is enriched beyond N, say to O or P, the velocity of the trailing shock increases again. Injection composition O is also the first single-phase injection composition shown. Composition O lies near, but not on the boundary of the aqueous/alcohol two-phase region.

Another route type transition takes place at the single-phase injection composition P. For this route, the shock velocity from P to N is also equal to the velocity of the shock from N to n_1. Thus, a more direct route is a shock from P to the three-phase fast path at n_1. Composition routes for injection compositions richer in NBA than P take a direct shock to a constant state on the fast path in the three-phase region where S_w is 0.0025 and are type 3c routes. The injection conditions that result in these routes exist over a range in NBA enrichment of less than one-thousandth of a volume fraction and so are not shown here.

3.1.5 Type 3 Routes Revisited (Injection Compositions Q-T)

For the injection compositions considered thus far, it has not been possible to meet the velocity constraint with composition routes containing shocks into the alcohol-oleic two-phase region. The injection compositions Q through T, however, allow for routes through the alcohol-oleic two-phase region. These type 3 composition routes are slightly different from the previous type 3 routes because they experience two-phase trailing flow. The route from injection compositions Q-T are shown in Fig. 3.8, along with their corresponding composition and saturation profiles in Fig. 3.9. Tables 3.7-3.8 show the velocity of important compositions on these routes.

Consider the route with injection composition Q. Q is not the first injection condition along a tie line in the alcohol-oleic two-phase region, but it is the first injection composition that results in a route through this two-phase region. Q has two possible composition routes. One route is a direct shock from the injection composition to a constant state in the three-phase region on the fast path where S_w is 0.0025 (at q_2). The second possible route is a tangent shock to q_1 on a two-phase tie line, followed by a shock of the same velocity to q_2. Both routes have a spreading wave from q_2 to q_3 where q_3 is identical to composition n_2 from Fig. 3.6. The route is completed with a tangent shock from q_3 to the initial condition. Thus, injection of composition Q provides the transition to type 3c routes with two-phase trailing flow.

The route for the displacement with injection composition R takes spreading waves in the two- and three-phase regions (see Table 3.7). The route takes a tangent shock to the tie-line path and follows this path until it is possible to shock (tangent to the tie-line path) to the fast path where S_w is 0.0025. As with the composition route from injection composition Q, there is a constant state in the three-phase region before the route proceeds down the fast path.

Injection of composition S results in a route with a tangent shock to the tie-line path at s_1, followed by a spreading wave along the tie line to s_2. From s_2 the route takes a shock (tangent to the tie-line path) to the constant state at q_3. From q_3 the route shocks to the initial condition. The route from injection composition S has no spreading wave in the three-phase region and it is the last composition route that can shock to the fast path where $S_w = 0.0025$. The route from injection composition S is the transition to type 3b routes with two-phase trailing flow. All subsequent composition routes with greater NBA enrichment in the injection condition shock from a tie line in the alcohol/oleic two-phase region to a constant state in the three-phase region. The route for injection composition T illustrates this type of route.

3.1.6 Type 5 Routes (Injection Composition U)

Multi-contact miscibility (MCM) is achieved at injection composition U. As the injection condition is enriched with NBA beyond T, the velocity of the trailing shock to the two-phase region increases, while the velocity of the leading shock to the initial condition decreases. With increasing enrichment, the constant state region in the three-phase region becomes narrower (see Figs. 3.7-3.8 and Tables 3.8-3.9), and the constant state composition approaches the border of the three-phase region.

The onset of miscibility occurs at injection composition U, which lies on the extension of the limiting tie line at the critical point of the alcohol-oleic two-phase region. This is analogous to how miscibility is developed in a condensing drive process. The composition route shocks to the critical point at u_1, follows the equal velocity curve from u_1 to the edge of the three-phase region at u_2 (alternatively it could shock directly from the critical point to u_2). From u_2 the composition route shocks directly to the initial condition. Figure 2.5 shows that the Hugoniot locus from the initial condition contains u_2.

The initial condition is not on a tie-line extension of the alcohol/oleic two-phase region. Thus, MCM flow is not developed in exactly the same way as for partially miscible two-phase systems. Instead the path for MCM flow takes a shock from the boundary of the three-phase region. The composition on the boundary is on the Hugoniot locus in the three-phase region, but not in the two-phase region.

3.1.7 Type 6 Routes (Injection Composition V)

First contact miscibility (FCM) is obtained at injection composition V when the mixing line between the injection and initial compositions does not intersect two- or three-phase regions. The route and profile are shown in Figs. 3.8-3.9 and outlined in Table 3.9. In this case the mixing line between composition V and the initial condition is just tangent to the boundary of the alcohol/oleic two-phase region.

3.2 COMPARISON WITH NUMERICAL SIMULATION

The analytical solutions are compared to fine-grid finite-difference simulations to show that the simulated results and the MOC solutions have the same dispersion-free limit. A more detailed analysis of the effect of dispersion on simulated routes is in Chapter 5. A single-point upstream weighting method that is explicit in time is used for the simulations. The simulations have a Peclet number of about 2000.

Figures 3.10 and 3.11 show a comparison of the simulated and the MOC routes for a variety of injection compositions. The MOC and simulated routes are nearly identical in the ternary diagram, except near route type transitions where alternate solutions are possible. Diffusion causes the simulated route from injection composition I to take the alternate route (thin dotted MOC route shown in Fig. 3.10) through composition space instead of the more direct route (heavy dotted MOC line.) A slight enrichment of the injection composition with NBA injection composition past I results in the correct route. Similarly, it is apparent that the route from composition G is drawn toward an alternate route. In coarse simulations G will take the alternate route instead of the more direct route. Although the composition routes for the alternate solutions appear different on the ternary diagram, the composition and saturation profiles are identical except for a dip at 0.74 PVI corresponding to the alternate path in the simulated route of injection composition I as shown in Fig. 3.11. A more detailed analysis of the effect of numerical dispersion on routes and recoveries is carried out Chapter 5.

3.3 ENRICHMENT AND OIL RECOVERY

Figure 3.12 shows the oil recovered after one pore-volume of injection for each of the injection compositions for both the MOC and simulated routes. The agreement between the MOC oil recovery and the numerical simulation recoveries are nearly exactly the same until near miscibility.

As is shown in Fig. 3.12, recovery increases with NBA enrichment for type 1 routes (injection compositions A and B). The recovery then becomes constant for type 2 routes with injection composition C and D since these routes have the same leading shock. For injection compositions E through G the recovery improves, primarily because the velocity of the leading shock decreases. Recovery peaks with NBA enrichment at G; therefore G is the optimum injection composition. The leading shock velocity increases for type 3 routes (injection compositions H through K), which causes a decline in recovery.

Decreasing recovery with increasing enrichment is contrary to what is observed in two-phase partially miscible flow. The decrease in recovery is caused by the higher mobility of the three-phase compositions that form in type 3 and type 4 routes. The three-phase compositions in type 3 and 4 routes have very little aqueous phase and the flow behaves like two-phase flow of the oleic and alcohol phases.

The recovery plateaus for L-P since these routes have the same leading shock and increases again once the injection composition is enriched to Q and continues to increase until miscibility is reached at injection composition U.

The recovery approaches 1.0 at the minimum enrichment for miscibility (MME), which corresponds to injection composition U. The recovery from numerical simulation, however, is not 1.0 at the MME owing to numerical dispersion. Numerical dispersion causes the composition route to enter the two-phase region, but does not cause three-phase flow.

3.4 RESISTANCE TO FLOW

In practice it is not always possible to inject fluids at the desired rate because of the resistance to flow. Three-phase flow may adversely affect injectivities because of reduced relative permeability. The total resistance to flow from Darcy's law is

$$R = \int_0^1 \left(\sum_{j=1}^{n_p} \frac{k_{rj}}{\mu_j} \right)^{-1} dx_D. \tag{3.1}$$

Resistance as defined in Eq. (3.1) is the effective viscosity of the multi-phase fluids in the porous medium. Figure 3.13 shows the calculated flow resistance after 1.0 PVI for each of the injection conditions examined. The resistance to flow is greatest just before the transition from type 2 to type 3 routes. This peak coincides with the composition routes that have the widest three-phase regions in the composition profiles at this time. The peak in resistance is just before G, the peak in oil recovery as a function of injection composition (see Fig 3.12). This indicates that it may be difficult to inject composition G in practice. In this case, the occurrence of three-phase flow increased the total flow resistance by a factor of about two.

3.5 CONCLUSIONS

MOC solutions have been developed for dispersion-free one-dimensional displacements for a wide range of injection compositions in three-phase partially miscible flow. The primary conclusions are:

- The composition routes for three-phase partially miscible flow are unique.
- The types of composition routes that develop are much more complicated than for two-phase partially miscible flow. For the displacements examined here, six basic types of routes were defined, although there are subtypes of routes within many of these types as shown in Figs. 3.1, 3.4, 3.6 and 3.8.
- The presence of the three-phase region has a significant effect on oil recovery. Unlike two-phase displacements where oil recovery always increases with enrichment, oil recovery remained constant over large increments in enrichment. For some injection compositions, oil recovery even decreased with NBA enrichment.

- Miscibility is developed at the critical point of the alcohol/oleic two-phase region and along the border of the three-phase region. The shock from the boundary of the three-phase region can go directly to the oil composition even though it does not lie on a two-phase tie-line extension.
- Numerical simulation results are consistent with the calculated MOC routes. Small levels of dispersion, however, can cause the simulated routes to take alternate routes in composition space.
- Flow resistance is increased significantly when three-phase flow occurs. For the system examined here, the flow resistance changed by a factor of two.

	Volume Fraction			Phase Saturations				
Label on Figures	H_2O	C_{16}	NBA	S_1	S_2	S_3	Dimensionless Velocity	Phases present
Injection Composition A								
A	1.0000	0.0000	0.0000	1.0000	0.0000	0.0000	0.0000(s)	1-2
a_1*	0.5618	0.4382	0.0000	0.5615	0.4385	0.0000	1.4203	2
I.C.	0.0000	1.0000	0.0000	0.0000	1.0000	0.0000	1.4203	1
Injection Composition B								
B	0.9127	0.0000	0.0873	1.0000	0.0000	0.0000	0.0000(s)	1-2
b_1	0.6021	0.8156	0.1030	0.6572	0.3428	0.0000	0.8954(i)	2
b_2	0.5327	0.7534	0.0000	0.5924	0.4676	0.0000	0.8954-1.4144	2
I.C.	0.0000	1.0000	0.0000	0.0000	1.0000	0.0000	1.4144	1

Table 3.1 Composition routes and velocities for type 1 composition routes from injection compositions A and B. (s) denotes the start of a spreading wave, (i) denotes the start of an indifferent wave, and (a) denotes the alternate path through composition space. *not labeled in figures

	Volume Fraction			Phase Saturations				
Label on Figures	H_2O	C_{16}	NBA	S_1	S_2	S_3	Dimensionless Velocity	Phases present
Injection Composition C								
C	0.8243	0.0000	0.1757	0.8802	0.0000	0.1198	0.0000-0.0223	2
c_1	0.7949	0.0381	0.1670	0.8564	0.0196	0.1240	0.0223(s)	3
c_2	0.7890	0.0442	0.1668	0.8500	0.0268	0.1232	0.0313	3
c_3	0.8661	0.0443	0.0896	0.9486	0.0514	0.0000	0.0313-0.0485	2-3
b_1	0.6021	0.8156	0.1030	0.6572	0.3428	0.0000	0.8954(i)	2-3
b_2	0.5327	0.7534	0.0000	0.5924	0.4676	0.0000	0.8954-1.4144	2
I.C.	0.0000	1.0000	0.0000	0.0000	1.0000	0.0000	1.4144	1
Injection Composition D								
D	0.6459	0.0000	0.3541	0.6383	0.0000	0.3617	0.0000-0.2326	2
d_1^*	0.5564	0.1336	0.3100	0.5690	0.0866	0.3445	0.2326(s)	3
d_2^*	0.5329	0.1677	0.2993	0.5453	0.1302	0.3245	0.3967	3
b_1	0.6021	0.8156	0.1030	0.6572	0.3428	0.0000	0.3967-0.8954(i)	2-3
b_2	0.5327	0.7534	0.0000	0.5924	0.4676	0.0000	0.8954-1.4144	2-3
I.C.	0.0000	1.0000	0.0000	0.0000	1.0000	0.0000	1.4144	1

Table 3.2 Composition routes and velocities for type 2 composition routes from injection compositions C and D. (s) denotes the start of a spreading wave, (i) denotes the start of an indifferent wave, and (a) denotes the alternate path through composition space. *not labeled in figures

	Volume Fraction			Phase Saturations				
Label on Figures	H_2O	C_{16}	NBA	S_1	S_2	S_3	Dimensionless Velocity	Phases present
Injection Composition E								
E	0.5500	0.0000	0.4500	0.5083	0.0000	0.4917	0.0000-0.4467	2
e_1^*	0.4479	0.1760	0.3761	0.4381	0.1155	0.4463	0.4467(s)	3
e_2^*	0.4231	0.2200	0.3569	0.4145	0.1735	0.4121	0.7817	3
e_3^*	0.4716	0.4189	0.1095	0.5131	0.4869	0.0000	0.7817-0.9234(i)	2-3
e_4^*	0.4701	0.5298	0.0000	0.4699	0.5301	0.0000	0.9234-1.3543	2
I.C.	0.0000	1.0000	0.0000	0.0000	1.0000	0.0000	1.3543	1
Injection Composition F								
F	0.5137	0.0000	0.4863	0.4592	0.0000	0.5408	0.0000-0.5372	2
f_1	0.4094	0.1910	0.3997	0.3915	0.1257	0.4828	0.5372(s)	3
f_2	0.3846	0.2382	0.3772	0.3686	0.1885	0.4429	0.9464	3
f_3	0.4257	0.4625	0.1119	0.4625	0.5375	0.0000	0.9464 (i),(a)	2-3
f_4	0.4307	0.5693	0.0000	0.4304	0.5696	0.0000	0.9464-1.2755	2
I.C.	0.0000	1.0000	0.0000	0.0000	1.0000	0.0000	1.2755	1
Injection Composition G								
G	0.4644	0.0000	0.5356	0.3922	0.0000	0.6078	0.0000-0.6516	2
g_1	0.3584	0.2107	0.4309	0.3300	0.1390	0.5311	0.6516(s)	3
g_2	0.3360	0.2576	0.4064	0.3101	0.2021	0.4878	1.1070	3
g_3	0.0652	0.4637	0.4712	0.0017	0.4244	0.5739	1.1070(a)	3
g_4	0.3755	0.6245	0.0000	0.3752	0.6248	0.0000	1.1070(a)	2
I.C.	0.0000	1.0000	0.0000	0.0000	1.0000	0.0000	1.1070	1

Table 3.3 Composition routes and velocities for type 2 composition routes from injection compositions E-G. (s) denotes the start of a spreading wave, (i) denotes the start of an indifferent wave, and (a) denotes the alternate path through composition space. *not labeled in figures

	Volume Fraction			Phase Saturations				
Label on Figures	H_2O	C_{16}	NBA	S_1	S_2	S_3	Dimensionless Velocity	Phases present
Injection Composition H								
H	0.4400	0.0000	0.5600	0.3592	0.0000	0.6408	0.0000-0.6982	2
h_1	0.3339	0.2201	0.4460	0.3004	0.1453	0.5543	0.6982(s)	3
h_2	0.3221	0.2460	0.4319	0.2901	0.1803	0.5295	0.9479	3
h_3	0.0698	0.4343	0.4960	0.0022	0.3819	0.6160	0.9479-1.1430	3
I.C.	0.0000	1.0000	0.0000	0.0000	1.0000	0.0000	1.1430	1
Injection Composition I								
I	0.4098	0.0000	0.5902	0.3182	0.0000	0.6818	0.0000-0.7429	2
i_1	0.3042	0.2316	0.4642	0.2645	0.1530	0.5824	0.7429(a)	3
i_2	0.0757	0.3953	0.5290	0.0025	0.3254	0.6721	0.7429-1.1681	3
I.C.	0.0000	1.0000	0.0000	0.0000	1.0000	0.0000	1.1681	1
Injection Composition J								
J	0.4033	0.0000	0.5967	0.3094	0.0000	0.6906	0.0000-0.7129	2
j_1	0.0788	0.3739	0.5473	0.0025	0.2943	0.7032	0.7129-1.1714	3
I.C.	0.0000	1.0000	0.0000	0.0000	1.0000	0.0000	1.1714	1
Injection Composition K								
K	0.3968	0.0000	0.6032	0.3006	0.0000	0.6994	0.0000-0.6828	2
k_1	0.0835	0.3414	0.5751	0.0025	0.2472	0.7503	0.6828-0.8905(s)	3
k_2^*	0.0788	0.3739	0.5473	0.0025	0.2943	0.7032	1.1714	3
I.C.	0.0000	1.0000	0.0000	0.0000	1.0000	0.0000	1.1714	1

Table 3.4 Composition routes and velocities for type 3 composition routes from injection compositions H-K. (s) denotes the start of a spreading wave, (i) denotes the start of an indifferent wave, and (a) denotes the alternate path through composition space. *not labeled in figures

	Volume Fraction			Phase Saturations				
Label on Figures	H_2O	C_{16}	NBA	S_1	S_2	S_3	Dimensionless Velocity	Phases present
Injection Composition L								
L	0.3949	0.0000	0.6051	0.2980	0.0000	0.7020	0.0000-0.6742	2
N	0.1985	0.0000	0.8015	0.0317	0.0000	0.9683	0.6742(a)	2
n_1	0.0875	0.3136	0.5989	0.0025	0.2068	0.7906	0.6742(s)	3
n_2	0.0788	0.3739	0.5473	0.0025	0.2943	0.7032	1.1714	3
I.C.	0.0000	1.0000	0.0000	0.0000	1.0000	0.0000	1.1714	1
Injection Composition M								
M	0.3000	0.0000	0.7000	0.1693	0.0000	0.8307	0.0000-0.1578	2
N	0.1985	0.0000	0.8015	0.0317	0.0000	0.9683	0.1578-0.6742	2
n_1	0.0875	0.3136	0.5989	0.0025	0.2068	0.7906	0.6742(s)	3
n_2	0.0788	0.3739	0.5473	0.0025	0.2943	0.7032	1.1714	3
I.C.	0.0000	1.0000	0.0000	0.0000	1.0000	0.0000	1.1714	1
Injection Composition N								
N	0.1985	0.0000	0.8015	0.0317	0.0000	0.9683	0.0-0.6742	2
n_1	0.0875	0.3136	0.5989	0.0025	0.2068	0.7906	0.6742(s)	3
n_2	0.0788	0.3739	0.5473	0.0025	0.2943	0.7032	1.1714	3
I.C.	0.0000	1.0000	0.0000	0.0000	1.0000	0.0000	1.1714	1

Table 3.5 Composition routes and velocities for type 4 composition routes from injection compositions L-N. (s) denotes the start of a spreading wave, (i) denotes the start of an indifferent wave, and (a) denotes the alternate path through composition space.

	Volume Fraction			Phase Saturations				
Label on Figures	H_2O	C_{16}	NBA	S_1	S_2	S_3	Dimensionless Velocity	Phases present
Injection Composition O								
O	0.1600	0.0000	0.8400	0.0000	0.0000	1.0000	0.0000- 0.3921	2
N	0.1985	0.0000	0.8015	0.0317	0.0000	0.9683	0.3921 0.6742	2
n_1	0.0875	0.3136	0.5989	0.0025	0.2068	0.7906	0.6742(s)	3
n_2	0.0788	0.3739	0.5473	0.0025	0.2943	0.7032	1.1714	3
I.C.	0.0000	1.0000	0.0000	0.0000	1.0000	0.0000	1.1714	1
Injection Composition P								
P	0.1267	0.0000	0.8733	0.0000	0.0000	1.0000	0.0000- 0.6742	1
N	0.1985	0.0000	0.8015	0.0317	0.0000	0.9683	0.6742(a)	2
n_1	0.0875	0.3136	0.5989	0.0025	0.2068	0.7906	0.6742(s)	3
n_2	0.0788	0.3739	0.5473	0.0025	0.2943	0.7032	1.1714	3
I.C.	0.0000	1.0000	0.0000	0.0000	1.0000	0.0000	1.1714	1

Table 3.6 Composition routes and velocities for type 4 composition routes from injection compositions O and P. (s) denotes the start of a spreading wave, (i) denotes the start of an indifferent wave, and (a) denotes the alternate path through composition space.

	Volume Fraction			Phase Saturations				
Label on Figures	H_2O	C_{16}	NBA	S_1	S_2	S_3	Dimensionless Velocity	Phases present
Injection Composition Q								
Q	0.1266	0.0000	0.8734	0.0000	0.0000	1.0000	0.0000-0.6763	1
q_1	0.0825	0.3146	0.6028	0.0000	0.2075	0.7925	0.6763(a)	2
q_2	0.0855	0.3272	0.5873	0.0025	0.2266	0.7709	0.6763-0.7768(s)	3
q_3	0.0788	0.3739	0.5473	0.0025	0.2943	0.7032	1.1714	3
I.C.	0.0000	1.0000	0.0000	0.0000	1.0000	0.0000	1.1714	1
Injection Composition R								
R^*	0.1246	0.0000	0.8754	0.0000	0.0000	1.0000	0.0000-0.6791	1
r_1^*	0.0811	0.3153	0.6037	0.0000	0.2077	0.7923	0.6791(s)	2
r_2^*	0.0792	0.3289	0.5919	0.0000	0.2278	0.7722	0.7838	2
r_3^*	0.0827	0.3471	0.5702	0.0025	0.2554	0.7420	0.7838-0.9380(s)	3
r_4^*	0.0788	0.3739	0.5473	0.0025	0.2943	0.7032	1.1714	3
I.C.	0.0000	1.0000	0.0000	0.0000	1.0000	0.0000	1.1714	1
Injection Composition S								
S	0.1197	0.0000	0.8803	0.0000	0.0000	1.0000	0.0000-0.6881	1
s_1	0.0774	0.3184	0.6042	0.0000	0.2085	0.7915	0.6881(s)	2
s_2	0.0737	0.3460	0.5803	0.0000	0.2499	0.7501	0.9120	2
q_3	0.0788	0.3739	0.5473	0.0025	0.2943	0.7032	0.9120-1.1714	3
I.C.	0.0000	1.0000	0.0000	0.0000	1.0000	0.0000	1.1714	1

Table 3.7 Composition routes and velocities for type 3 composition routes with two-phase trailing flow from injection compositions Q-S. (s) denotes the start of a spreading wave, (i) denotes the start of an indifferent wave, and (a) denotes the alternate path through composition space. *not shown in figures

	Volume Fraction			Phase Saturations				
Label on Figures	H_2O	C_{16}	NBA	S_1	S_2	S_3	Dimensionless Velocity	Phases present
Injection Composition T								
T	0.0901	0.0000	0.9099	0.0000	0.0000	1.0000	0.0000- 0.8114	1
t_1^*	0.0497	0.3923	0.5580	0.0000	0.2228	0.7772	0.8114(s)	2
t_2^*	0.0475	0.4137	0.5388	0.0000	0.2656	0.7344	1.0609	2
t_3^*	0.0682	0.4444	0.4874	0.0020	0.3965	0.6015	1.0609- 1.1323	3
I.C.	0.0000	1.0000	0.0000	0.0000	1.0000	0.0000	1.1323	1

Table 3.8 Composition routes and velocities for type 3 composition routes with two-phase trailing flow from injection composition T. (s) denotes the start of a spreading wave, (i) denotes the start of an indifferent wave, and (a) denotes the alternate path through composition space. *not labeled in figures

	Volume Fraction			Phase Saturations				
Label on Figures	H_2O	C_{16}	NBA	S_1	S_2	S_3	Dimensionless Velocity	Phases present
Injection Composition U								
U	0.0605	0.0000	0.9395	0.0000	1.0000	0.0000	0.0000-1.0000	1
u_1	0.0221	0.5279	0.4500	0.0000	1.0000	1.0000	1.0000 (i)	1-2
u_2	0.0557	0.5204	0.4240	0.0000	0.5064	0.4936	1.0000	2-3
I.C.	0.0000	1.0000	0.0000	0.0000	1.0000	0.0000	1.0000	1
Injection Composition V								
V	0.0442	0.0000	0.9558	0.0000	1.0000	0.0000	0.0000-1.0000	1
u_1	0.0221	0.5279	0.4500	0.0000	1.0000	1.0000	1.0000 (i), (a)	1-2
u_2	0.0557	0.5204	0.4240	0.0000	0.5064	0.4936	1.0000	2-3
I.C.	0.0000	1.0000	0.0000	0.0000	1.0000	0.0000	1.0000	1

Table 3.9 Composition routes and velocities for type 5 (MCM) and type 6 (FCM) composition routes from injection compositions U and V respectively. (s) denotes the start of a spreading wave, (i) denotes the start of an indifferent wave, and (a) denotes the alternate path through composition space.

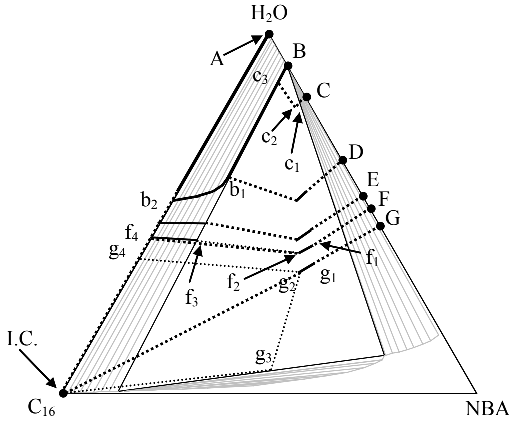

Figure 3.1 Composition paths for injection compositions A-G. Injection compositions A and B result in type 1 composition routes. Injection of the compositions C-G result in type 2 composition routes. Shocks are shown as heavy dotted lines, spreading and indifferent waves as solid lines, and alternate routes are thin dotted lines.

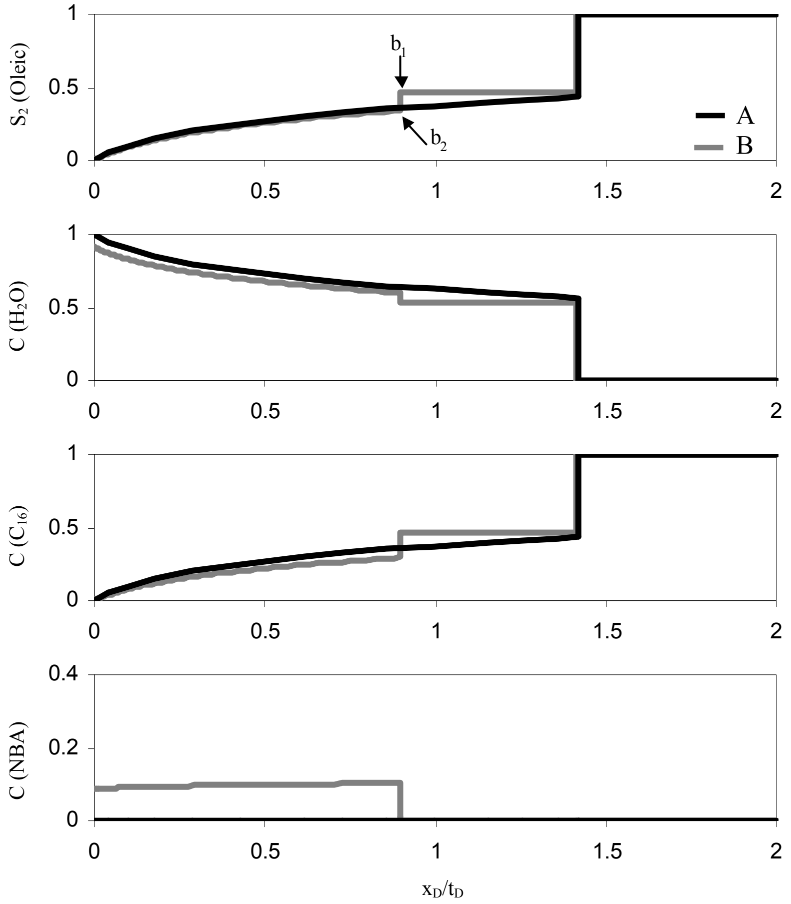

Figure 3.2 Compositions and phase saturations as a function of dimensionless velocity for injection compositions A-B, both are type 1 composition routes.

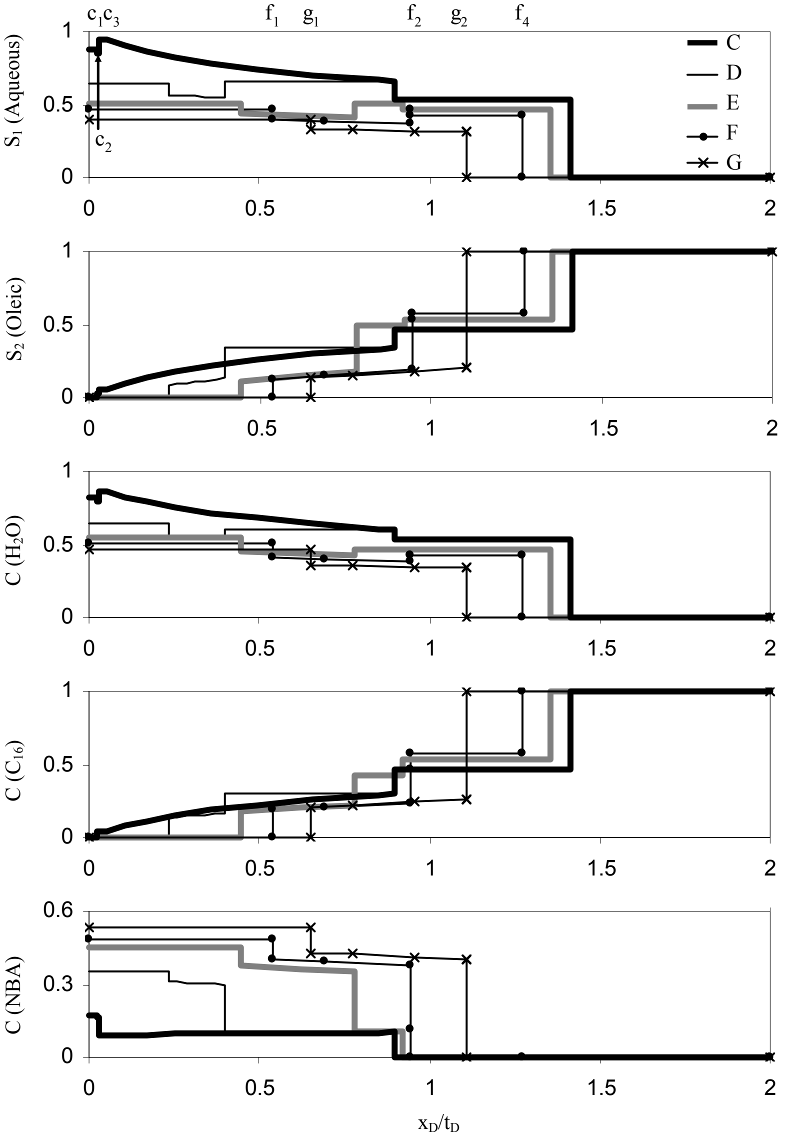

Figure 3.3 Compositions and phase saturations as a function of dimensionless velocity for injection compositions C-G, all of which are type 2 composition routes.

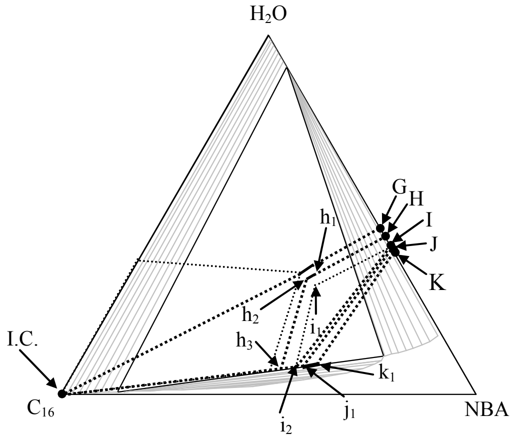

Figure 3.4 Composition paths injection compositions H-K, all of which are type 3 composition routes. Shocks are shown as heavy dotted lines, spreading and indifferent waves as solid lines, and alternate routes are thin dotted lines.

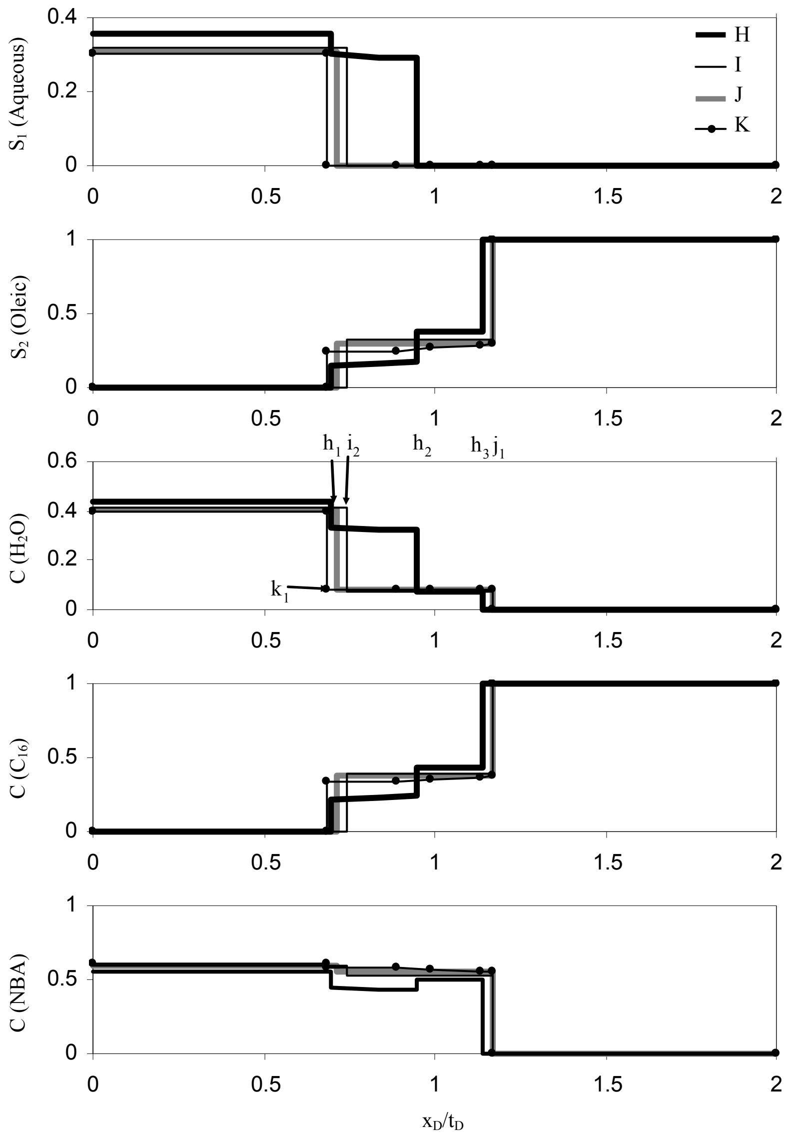

Figure 3.5 Compositions and phase saturations as a function of dimensionless velocity for injection compositions H-K, all of which are type 3 composition routes.

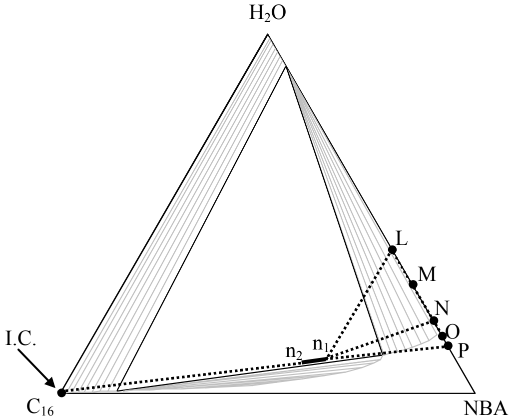

Figure 3.6 Composition paths for injection compositions L-P, all of which are type 4 composition routes. Shocks are shown as heavy dotted lines, spreading waves are shown as solid lines.

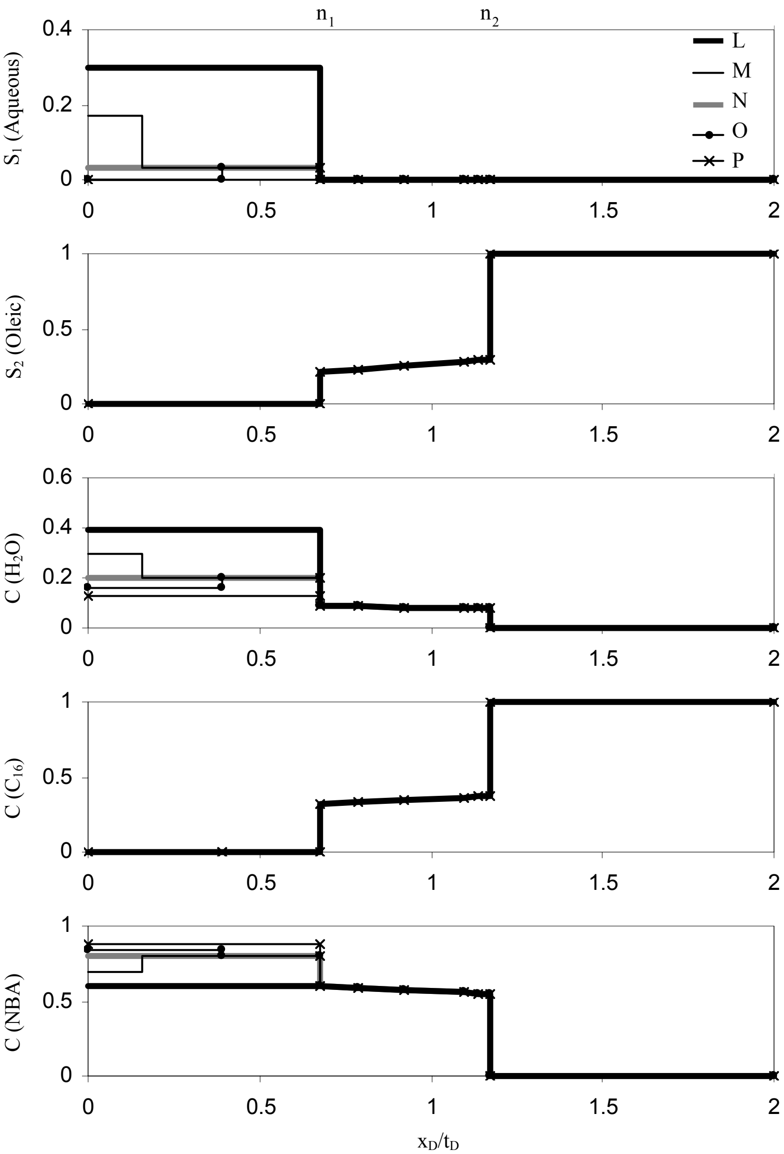

Figure 3.7 Compositions and phase saturations as a function of dimensionless velocity for injection compositions L-P, all of which are type 4 composition routes.

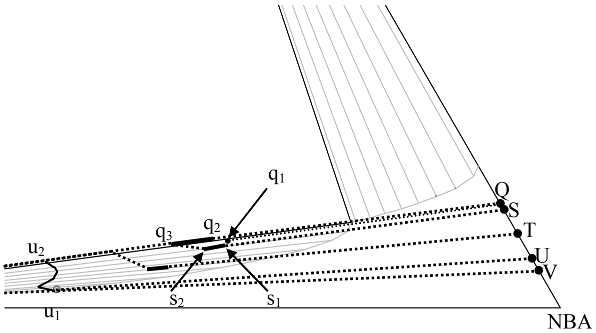

Figure 3.8 Composition routes for injection compositions Q-V. Injection conditions Q-T result in type 3 routes with two-phase trailing flow. Injection condition U results in a type 5 (MCM) route Injection condition V results in a type 6 (FCM) route. Shocks are shown as heavy dotted lines, spreading waves are shown as solid lines.

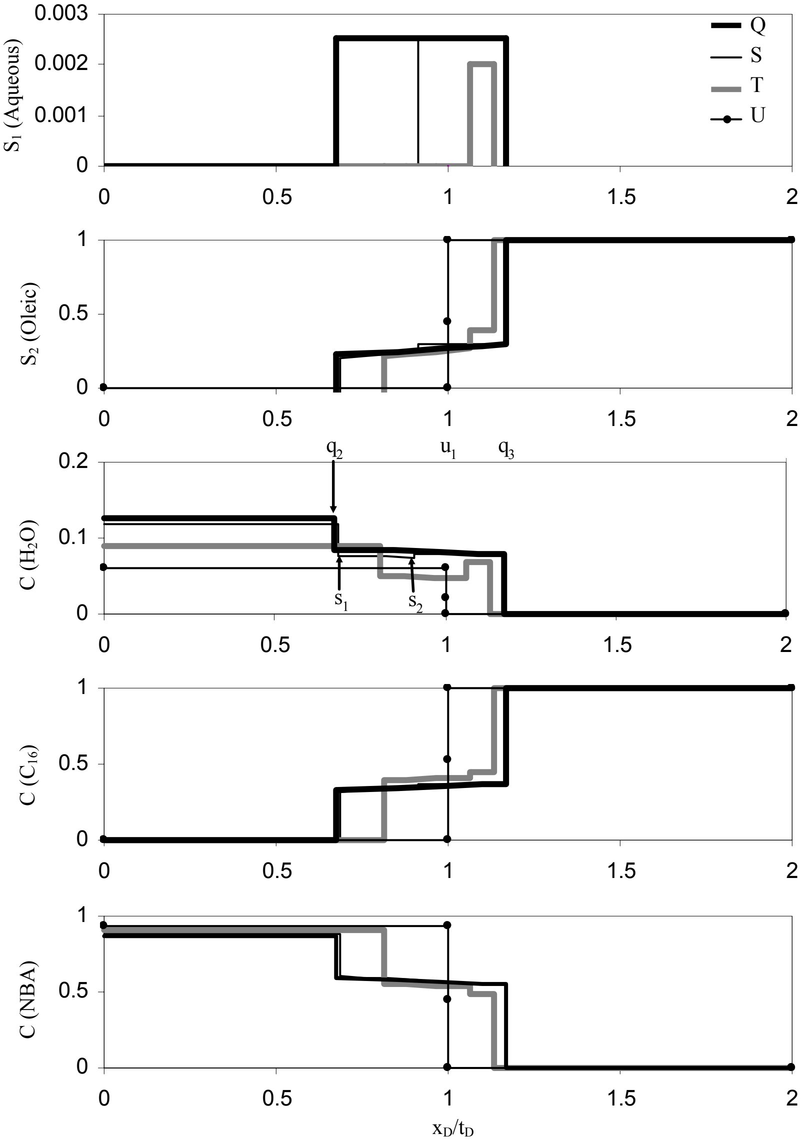

Figure 3.9 Compositions and phase saturations as a function of dimensionless velocity for injection compositions Q-U. Injection conditions Q-T result in type 3 routes with two-phase trailing flow. Injection condition U results in a type 5 (MCM) route.

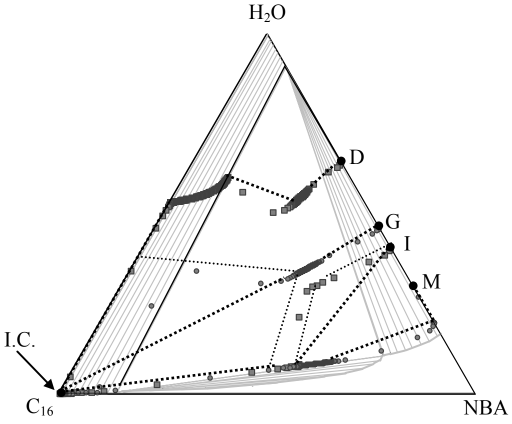

Figure 3.10 Comparison of MOC and numerical solutions for selected composition routes. The thick dotted lines indicate MOC solutions for the routes from injection conditions D, G, I, and M. Thin dotted lines indicate alternate routes for injection compositions G and I. Squares are simulated routes for injection compositions D and I. Circles are simulated routes for injection compositions G and M. Injection composition I follows the alternate route.

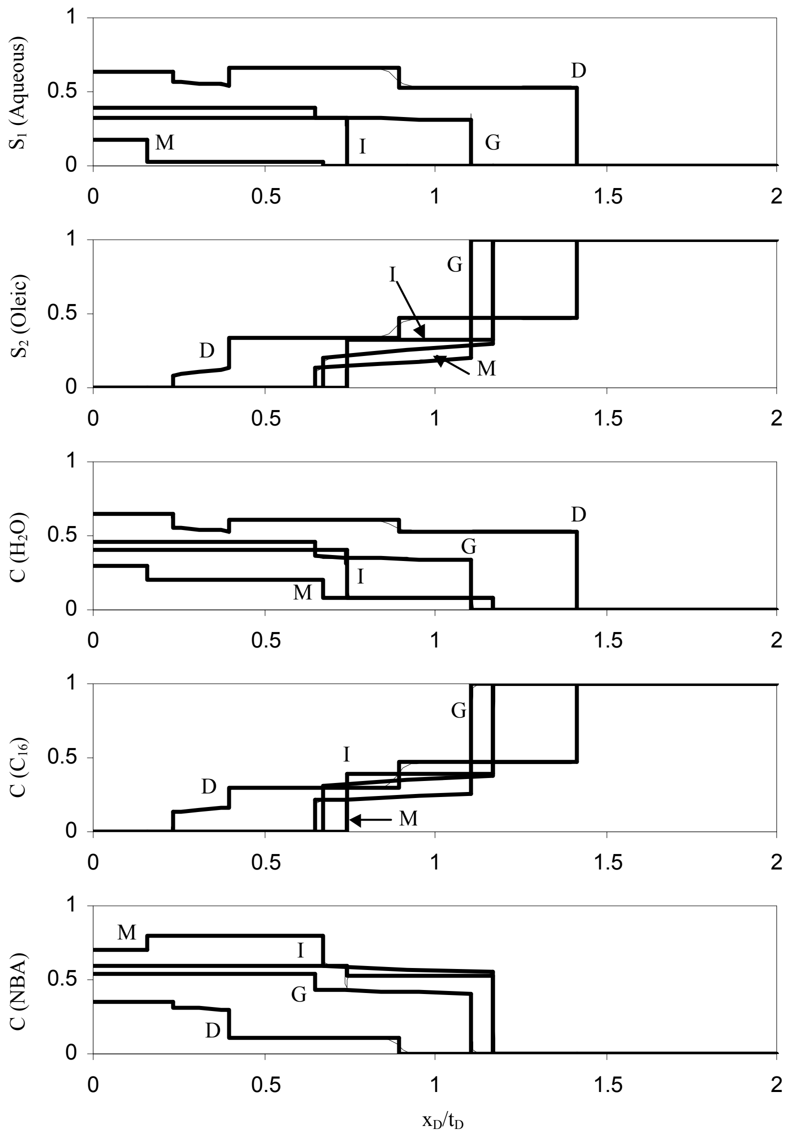

Figure 3.11 Comparison of MOC and numerical solutions for selected composition routes. Thick lines indicate MOC solutions for the routes from injection conditions D, G, I, and M. Thin lines are simulated solutions.

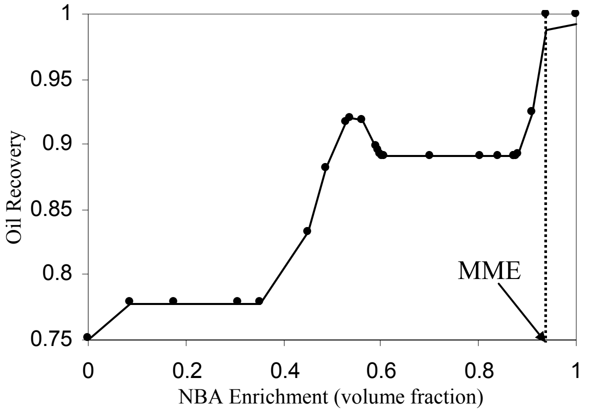

Figure 3.12 Cumulative oil recovery after one pore volume of injection as a function of NBA enrichment in the injection composition. The solid line is the recovery from numerical simulations, and circles are the MOC oil recovery.

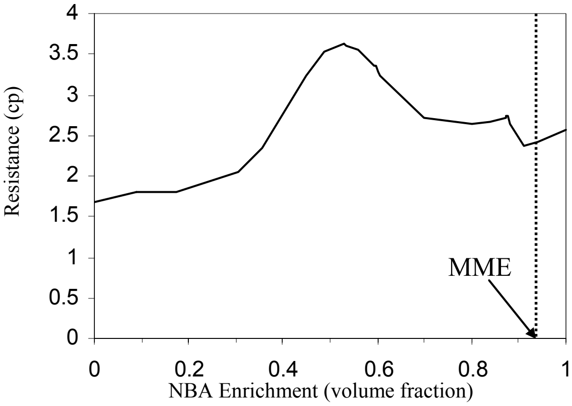

Figure 3.13 Resistance to flow after one pore volume of injection as a function of NBA enrichment in the injection composition.

Chapter 4 MOC for Three-Phase Partially Miscible Flow in SEAR of NAPL

In this chapter method of characteristics composition routes for two-phase initial composition are developed for a three-phase partially miscible ternary system. As with the two-phase system in Chapter 6, the two-phase initial composition effects the development of miscibility. Three different relative permeability curves are also studied in order to demonstrate the existence and uniqueness of solutions for the three different types of mass-balance equation. Comparing relative permeability models also serves to demonstrate the importance of parameter choice on composition routes and recoveries.

Contamination of groundwater with non-aqueous phase liquids (NAPLs) is a worldwide problem. Traditional pump and treat methods are often ineffective or excessively time consuming in recovering NAPLs because of the low solubility of contaminants in water. Remediation of aquifers contaminated with NAPLs is further complicated by the tendency of NAPLs to be unevenly distributed within the aquifer. Dense non-aqueous phase liquid (DNAPL) saturations in particular can also vary greatly within the aquifer because DNAPLs can percolate as fingers below the water table. DNAPL can be hard to detect in situ because of saturations less than a percent or two for most of the contaminated volume, however saturations may be large just above clay or other low permeability layers (Fountain *et al.*, 1996). These high saturation lenses provide a continuing

DNAPL source of contaminant, so their removal is critical to the success of any remediation process.

SEAR can substantially improve the effectiveness of clean-up efforts by solubilizing and/or mobilizing NAPL that would otherwise remain trapped by capillary forces within the aquifer. Laboratory experiments and field demonstrations with surfactants have been very effective in NAPL remediation when the process is properly designed (e.g. Dwarakanath and Pope, 2000; Gupta and Mohanty, 2001; Jayanti et al., 2002). Light (Kilpatrick *et al.*, 1986), heavy (Shotts, 1996), and chlorinated (Baran *et al.*, 1994b) hydrocarbons have all been shown to form three-phases with appropriate surfactants.

The SEAR process is often designed at the optimal salinity where Winsor type III phase behavior exists (Dwarakanath, 1997). In such cases, three partially miscible flowing phases coexist. The formation of a microemulsion phase is advantageous because it greatly enhances contaminant solubility. Moreover, at optimal salinity the interfacial tensions between the micro-emulsion and aqueous phases, and the microemulsion and the NAPL phases are significantly reduced (Dwarakanath, 1997). Residual NAPL can also be mobilized if the interfacial tension and thus the capillary forces are sufficiently lowered.

Miscibility is desirable for EOR applications because all hydrocarbons are mobilized and the displacement is very efficient. In SEAR, however, significant mobilization could result in downward movement of DNAPL, which would increase the contaminated aquifer volume. Thus, a successful remediation process often depends more on increasing the solubility of contaminant in a partially miscible remediation process than on mobilization.

In this chapter a continuous set of unique analytical solutions are developed for one-dimensional dispersion-free flow in SEAR of a NAPL contaminant. Three pseudo-components are used to represent the water, contaminant, and surfactant; where up to three flowing phases may be present. The effect of relative permeability on the composition routes is examined by considering three sets of relative permeability parameters, which lead to strictly hyperbolic, non-strictly hyperbolic, and mixed hyperbolic and elliptic conservation laws. Injection compositions varying continuously from pure water to pure surfactant are modeled for each relative permeability model. The composition routes, profiles and contaminant recoveries are found. The analytical composition routes and recovery curves are compared to those obtained by fine-grid numerical simulations. Finally, the optimal surfactant enrichment that results in the minimum total surfactant injection necessary for complete contaminant recovery are also found.

4.1 EFFECT OF RELATIVE PERMEABILITY ON COMPOSITION PATHS

Consider the phase behavior shown in Fig. 2.2, which is taken from a water/decane/alcohol system that is analogous to water/NAPL/surfactant systems. An analogous system is used because a complete set of phase behavior data was available for this system. Although pure decane forms a light non-aqueous phase liquid (LNAPL), the resulting phase behavior is similar to that for contaminants that form DNAPL. The phase envelopes for the two- and three-phase regions are based on phase-behavior data at 25°C and atmospheric pressure (Negahban *et al.*, 1986) and are outlined in Table 2.3. Density and viscosity data from the Chemical Properties Handbook are used (Yaws, 1999) and are also shown in Table 2.3.

In the three-phase region the relative permeability model determines whether umbilic points exist and whether the eigenvalues are real or imaginary. We use extended Corey relative permeabilities to demonstrate the effect of relative permeability on the composition paths for each possible type of mass-balance equation. Recall from Chapter 2 that the type of mass-balance equation refers to its character as a partial differential equation and that all composition routes are solutions to Eq. (2.6), the equation for conservation of mass in partially miscible flow.

Figures 2.2-2.4 show the legal paths through composition space for various choices of parameters in the relative permeability model. Figure 2.2 shows a case where the NAPL phase residual saturation, endpoint relative permeability, and exponent are independent of the saturations of the other two phases. When the relative permeability of each phase is a function of only the saturation of that phase, the mass-balance equation cannot have imaginary characteristics (Trangenstein, 1989). The microemulsion phase exponent, n_3, is greater than unity. The two eigenvectors merge at a single umbilic point near the center of the three-phase region as shown in Fig. 2.2. Thus, these mass-balance equations are NSH.

In Fig. 2.3 the NAPL phase residual saturation, endpoint relative permeability, and exponent are also independent of the saturations of the other two phases. However, the microemulsion phase exponent, n_3, is less than unity, which matches laboratory data on ternary partially miscible systems (Delshad *et al.*, 1987; Kvanvik *et al.*, 1992). This choice of parameters results in a SH mass-balance equation with two distinct characteristics everywhere as shown in Fig 2.3. See Juanes and Patzek (2002, 2003a) for further discussion of strictly hyperbolic mass-balance equations.

The composition paths in Fig. 2.4 are the result of assuming that the NAPL phase residual saturation, endpoint relative permeability, and exponent are functions of the water and microemulsion phase saturations. This accounts for the reduction in interfacial tension between the oleic and microemulsion phases. Thus, this model accounts for oleic phase mobilization. An exponent $n_3 > 1.0$ is used for the microemulsion phase. The conservation law for this case is mixed type (MHE) and a small region of imaginary eigenvalues occurs near the center of the three-phase region as shown in Fig. 2.4.

4.2 COMPOSITION ROUTES

For all composition routes, the initial composition is 30% decane and 70% water. No surfactant is present initially. As in Chapter 3 the injection composition is varied from 100% water to 100% surfactant to demonstrate the continuity and uniqueness of the composition routes. The composition of each injection condition is given in Table 4.1.

Four of the six types of composition routes that are outlined in Chapter 3 appear in the construction of solutions and three new route subtypes occur. For each of the relative permeability models, there is only one fast path in the three-phase region that is taken by the composition routes. This also occurred for the system in Chapter 3. The correct fast path for the NSH equation is the one that passes through the umbilic point. Though the solutions follow a fast path that passes through the umbilic point, the composition routes do not go near the umbilic point. The correct fast path for the SH equation passes through the center of the three-phase region, but has no defining characteristics. For the MHE mass-balance equation, the correct fast path passes through an umbilic point at the edge of the region of imaginary characteristics, but does not cross into the region of imaginary characteristics. Though the solutions follow a fast path that borders the region of imaginary characteristics, the composition routes do not go near or enter the region of composition space where hyperbolicity fails.

4.2.1 Continuity of Composition Routes for NSH Case

Figure 4.1 shows the progression of route types for the relative permeability model that results in a NSH conservation law. Figures 4.2-4.4 show the composition and saturation profiles for each initial composition outlined in Table 4.1. The exact compositions at which the path type changes are shown in Table 4.2. The progression of route types is very similar to the progression for the system in Chapter 3.

Starting with 100% water injection at A, type 1 routes occur until the injection composition is on the tie-line extension of the tie line that makes up the boundary of the three-phase region at B. The route type then switches to type 2 routes, exactly the same as for the system in Chapter 3. Injection compositions C-D are examples of type 2 routes.

At an injection composition of 57.66% surfactant the composition route follows the slow path in a spreading wave all the way to the fast path. Subsequent enrichment results in compositional routes that follow the slow path only as far as the fast path and then non-tangent shock to the initial composition tie line. This composition route type is defined as a type 3d route and was not encountered in Chapter 3. An example of a type 3d route is from injection composition F shown on Figs. 4.3 and 4.5 and outlined in Table 4.3. The route has a tangent shock to the slow path at f_1, followed by a spreading wave to f_2, where the slow path intersects the fast path. At f_2 there is a constant state followed by a shock to f_3 on the aqueous/NAPL tie line. After a constant state at f_3, the route takes the leading shock to the initial composition, I.C.

After a small region of type 3d routes the composition route changes to another new subtype. For clarity no type 3e routes are shown on Fig. 4.5, but the injection of composition G on Fig. 4.6 and 4.9 and Table 4.4 is also an example of a type 3e route for the SH conservation law. The route tangent shocks from the injection composition G to a slow path at g_1. The slow path is followed in a spreading wave until it intersects the fast path at g_2. After a constant state at g_2, the route flows down the fast path to g_3, where there is a shock (tangent to the fast path) to g_4 on the aqueous/NAPL tie line. After a constant state at g_4 the route shocks to I.C. The transition between type 3d and type 3e routes is continuous because at the transitional injection composition the leading shock is tangent to the fast path, though no spreading wave down the fast path occurs. Subsequent enrichment will result in composition routes that intersect the fast path at compositions richer in surfactant than i_3 and then spread down the fast path to i_3. Hence all type 3e routes will have the same leading shock. The leading tangent shock occurs at i_3 in the NSH conservation law and at g_3 for the SH model as shown in Figs. 4.5 and 4.6 respectively.

At an injection composition enrichment of 64.219% surfactant the composition route changes to another new type 3 route, subtype 3f. At the transition to type 3f routes the tangent shock from the injection composition to a slow path disappears. Type 3f routes have a constant state at the trailing end of the displacement, but are otherwise identical to type 3e routes. Injection composition I has a type 3f route and is shown in Figs. 4.3 and 4.5 and outlined in Table 4.3. As shown on Fig. 4.5, the composition route shocks to the slow path at i_1. The shock to i_1 results in the shortest possible constant state, however it is not a tangent shock. After the constant state at i_1, the route takes the slow path to i_2, where there is a constant state until the route can flow down the fast path to i_3, and then shocks (tangent to the fast path) to i_4 on the aqueous/NAPL tie line. After a constant state at i_4, the route shocks to I.C.

Enrichment past I causes the shock to the slow path to approach the fast path until at 64.221% surfactant concentration the shock to the slow path lands exactly on the fast path and the route changes to a type 3c route, which was outlined in Chapter 3. At this injection composition the routes also begin to have two-phase trailing flow. For clarity no type 3c routes are shown.

At an enrichment of 66.01% surfactant concentration a legal tangent shock from the tie line in two-phases to a slow path appears and the route type changes to another new subtype, type 3g. In type 3g routes it is necessary to shock between the fast and slow paths because it is not possible to follow the slow path all the way to the fast path without violating the velocity constraint. Injection composition K on Fig. 4.1 is a type 3g route for the NSH conservation law, but a clearer example is provided by injection composition K for the SH conservation law and is shown in Figs. 4.6 and 4.10 and outlined in Table 4.4. As shown on Fig. 4.6, the route tangent shocks along the tie line from K to k_1. The composition follows the tie-line path until a shock that is tangent both upstream and downstream occurs between k_2 on the tie line to k_3 on the slow path. The slow path is followed from k_3 to k_4, where a shock (upstream tangent to the slow path) to k_5 on the fast path occurs. From k_5 the composition follows the fast path exactly like a type 3e route.

After a small region of type 3g routes the spreading wave down the fast path disappears and the composition route changes to a type 3a route. Type 3a routes were discussed in Chapter 3. Injection composition M on Fig. 4.6 shows an example for the SH conservation equation. For the NSH model, the constant state on the fast path grows shorter and disappears at an injection composition of

75.17% surfactant, which has the transitional route back to type 2 composition routes. Type 2 routes continue all the way to 100% surfactant injection.

Though there is no practical application for the injection of decane and surfactant, for the purpose of completeness the analysis above is continued through all injection compositions between 100% surfactant and 100% decane. All injection compositions along the surfactant/decane boundary between 100% surfactant and injection composition P at 8.09% surfactant have type 2 routes. Injection compositions N and O on Fig. 4.1 are examples of type 2 routes. Injection composition P is on the extension of the tieline making up the aqueous/NAPL boundary of the three-phase region. At P the route type changes to type 1.

4.2.2 Continuity of Composition Routes for SH Case

Figure 4.7 shows the progression of route types for the relative permeability model that results in a SH conservation law and Figs. 4.8-4.10 show the composition and saturation profiles for each route. Table 4.2 shows the exact compositions at which the path types change. The progression of route types is very similar to the progression for the NSH conservation law described above.

Starting with 100% water injection at A, the route types progress in the same manner as for the NSH case through type 1, 2, 3d, and 3e routes, though the compositions at which the route types chance are quite different, as shown in Table 4.2 and Fig. 4.7. In the SH system the tangent shock to the slow path never disappears, and so the route type progresses directly from type 3e routes to type

3c routes. In the region of type 3c routes trailing two-phase flow begins to appear in the composition route.

At a surfactant enrichment of 64.09% the constant state on the fast path disappears and the route changes to a type 4 route with two-phase trailing flow. Injection composition J on Figs 4.7 and 4.10 is a type 4 route. The constant state on the fast path reappears at a surfactant enrichment of 65.92% and the composition route reverts to a type 3c route. The route type again progresses identically to the NSH conservation law through type 3c, 3g, and 3a routes. Type 3a routes continue all the way to 100% surfactant injection.

4.2.3 Continuity of Composition Routes for MHE Case

Figure 4.11 shows the progression of route types for the relative permeability model that results in a MHE conservation law and Figs. 4.12-4.14 show the composition and saturation profiles for each route. Table 4.2 shows the exact compositions at which the path types change.

No displacement occurs for injection composition A, (100% water injection) because in the MHE model the initial composition is at the oleic phase residual in water, as shown in Table 2.4. After injection composition A, the route types progress in the same manner as for the NSH and SH case for type 1 and 2 routes. For the MHE conservation law it is not possible for compositions to follow the slow path all the way to the fast path in the direction of increasing decane without violating the velocity constraint. Hence the path type must switch to type 3a routes. The route type then progresses to type 3g, 3c, 3e, 3d, and finally type 2 routes, exactly opposite the progression from the NSH model. The only exception is that type 3f routes do not occur because the tangent shock to a slow path never disappears. This was also the case for the SH conservation law.

4.3 EFFECT OF RELATIVE PERMEABILITY ON COMPOSITION ROUTES

Figures 4.1, 4.7, and 4.11 show the composition routes given by injection compositions A-D and K-M for all three of the relative permeability models. The composition routes from injection composition A and B are identical for the NSH and SH mass-balance equations, while the MHE model gives a substantially different route. When three-phase flow occurs the SH model routes take spreading waves down slow paths with small microemulsion phase saturation. In contrast, the NSH and MHE models take slow paths in which a large saturation of microemulsion phase is present. The routes from injection compositions C and D are very different for all of the relative permeability models, while the routes from K-M are similar for the NSH and MHE models.

The progression of composition routes types is similar for all three relative permeability models. The differences in routes and recoveries are likely the result of the changes in parameters, rather than fundamental differences in solution structure for the three types of partial differential equation.

The analytical composition profiles from injection composition D are compared on Fig. 4.15. The MHE model creates a large leading bank rich in decane for injection of composition D. However, the MHE model also has the slowest trailing shock, with a dimensionless velocity of 0.32. The NSH model also results in a leading decane bank and it has the fastest trailing shock, with a dimensionless velocity of 0.46. The SH model has a small decane bank.

The composition and saturation profiles for each of the mass-balance equations from injection composition M are compared on Fig. 4.16. Fig. 4.16 shows the MHE model again mobilizes by far the largest oil bank for injection composition M. However, unlike the routes from injection composition D, the SH model results in the slowest trailing shock with a dimensionless velocity of 0.85.

As shown in Figs. 4.1, 4.7, and 4.11, all of the models predict regions of three-phase flow for injection composition M, and none of the composition routes have reached miscibility. This is unexpected as the surfactant is fully miscible with both pure decane and pure water. Furthermore, M is past the critical tie-line extensions of both the microemulsion/aqueous and the microemulsion/NAPL two-phase regions, which is the criterion for multi-contact miscibility in partially miscible two-phase flow. However, the failure to develop miscibility is consistent with laboratory experiments of surfactant floods of two-phase initial compositions (Giordano and Salter, 1984).

The lack of development of miscibility is a positive result when it is desirable to avoid complete mobilization of the decane. For the relative permeability models chosen, the composition routes enter directly into the three-phase region, except for a small range of injection compositions near K, shown on Figs. 4.1, 4.7 and 4.11. Over-enrichment of the injection composition with surfactant, including the case of 100% surfactant injection, results in routes that shock directly into the three-phase region. When there is no two-phase trailing flow the lowest interfacial tensions that develop are given by the equilibrium phase interfacial tensions of the three-phase region which limits the mobilization of decane.

4.4 COMPARISON WITH NUMERICAL SIMULATION

In Fig. 4.15 the simulated composition and saturation routes for fine-grid finite difference simulations from injection composition D are also shown. The simulations shown have a Peclet number of 4400 to minimize numerical dispersion. A more detailed discussion of the simulator and numerical dispersion is in Chapter 5. The simulated composition route resulting from the NSH model has spikes in water composition at dimensionless velocities of 0.46 and 1.12. These anomalous spikes are a consequence of dispersion spreading the shocks into and out of the three-phase region, and are not a sign of instability in the simulations. Similar spikes are observed for the SH model at a dimensionless velocity of 0.40 and for the MHE model at a dimensionless velocity of 1.18. This was also observed in some simulations in Chapter 3 and is explored further in Chapter 5. All simulated composition profiles for injection composition D are very similar to the analytical routes. In Fig. 4.16 the composition and saturation profiles given by the analytical and numerical solutions for injection composition M are nearly indistinguishable.

4.5 CONTAMINANT RECOVERY

Figure 4.17 shows contaminant recoveries as a function of time for injection compositions C and M for each relative permeability model. The composition routes are shown on Figs. 4.1, 4.7, and 4.11. The SH model recovery for injection composition C is slightly better than NSH recoveries between 1.0 and 2.0 pore-volumes injected (PVI). The MHE model results in almost no contaminant recovery for times less than 0.5 PVI because of the initially immobile NAPL phase. The predicted recovery from the MHE model is substantially poorer than the other two models for all injection times.

For injection composition M, the MHE recoveries are again low until 0.5 PVI because of the initially immobile oleic phase. By 0.75 PVI the recovery predicted by the MHE model is higher than for the SH. This is because of the mobilization of a large decane bank as shown in Fig. 4.16. The SH model recoveries are always smaller than the NSH recoveries. The work of Guzman *et al.* (1994) reported similarly large discrepancies in comparing two relative permeability models on a fully immiscible three-phase system.

Figure 4.18 shows the recovery after 1.0 PVI and 2.0 PVI as a function of surfactant concentration in the injection composition. At both times the NSH model predicts the highest recovery for almost all injection compositions. After 1.0 PVI, both the NSH and SH model recoveries reach a maximum at 55% and 20% surfactant injection, respectively. Recovery then declines with increasing surfactant concentration and plateaus. The fast leading shocks in type 3d routes cause the decline in recovery in the NSH and SH models. The plateau in recovery is a consequence of all type 3c, 3e, 3f, 3g, and type 4 routes having the same leading shock for each of the relative permeability models. Eventually, recovery improves with increasing surfactant concentration. Declining recovery with increasing surfactant concentration followed by a plateau was also observed in Chapter 3. For the MHE model, recovery never declines with increasing surfactant concentration, but plateaus for a short time.

After 2.0 PVI, the recovery from all relative permeability models increases with surfactant concentration, as shown in Fig. 4.18. This is because after 2.0 PVI the amount of contaminant remaining in the subsurface is determined by the trailing shocks in the displacement, rather than the leading fronts.

4.6 OPTIMIZATION OF INJECTED SURFACTANT VOLUME

In practice it is desirable to limit the surfactant volume injected into an aquifer as well as how long the remediation process takes. Here, we determine the minimum volume of surfactant injected in a 1-D displacement to obtain 100% decane recovery. Complete recovery occurs when the trailing shock breaks through the outlet of the 1-D model. The volume V of surfactant necessary for 100% decane recovery is defined as $V = C_3(inj)/\Lambda_t$ where $C_3(inj)$ is the volume fraction of surfactant in the injection composition and Λ_t is the dimensionless velocity of the trailing shock in the displacement. Figure 4.19 shows V as a function of the volume fraction of surfactant injected.

As shown in Fig. 4.19, the minimum total volume of surfactant injected with the NSH model occurs at an injection composition near 30% surfactant concentration and requires a total of 0.82 PVI of surfactant. 2.73 PV of total injection time is necessary to obtain perfect recovery of decane.

The SH model is similar in that the minimum total volume of surfactant injection occurs at an injection composition near 30% surfactant concentration, however a total of 0.95 PVI of surfactant are required, slightly greater than the NSH model result. In this model 3.16 PV of total injection time is necessary to obtain complete recovery of decane.

Finally, for the MHE model, the minimum total volume of surfactant injected is at an injection composition near 75% surfactant concentration. A minimum total of 1.0 PVI of surfactant is required. This required surfactant concentration is significantly greater than for the other two relative permeability models. However, because of the greater surfactant concentration only 1.31 PV of total injection time is required to obtain complete recovery. Surfactant optimization when the MHE model applies allows for much faster clean up of the decane, but more surfactant must be used than when the other two models apply.

The optimal surfactant concentration in practice is dependent on many other factors not examined here. However, this analytical result is important because it demonstrates that increased surfactant concentration in the injection composition is not always advantageous.

4.7 CONCLUSIONS

Three complete sets of MOC solutions have been developed for remediation of a high saturation lens of DNAPL contaminant using surfactant near optimal salinity. The key conclusions are:

- All analytical solutions and composition routes are shown to be unique even when the conservation law is MHE type.
- The relative permeability model can significantly affect the composition routes that develop in situ, and therefore contaminant recovery.
- Miscibility is never developed because of the presence of the three-phase region. Thus, complete mobilization of the contaminant will never occur. Partial mobilization is dependent on the interfacial tensions.
- Analytical composition routes and recoveries are nearly identical to fine-grid finite difference simulations. Anomalies in simulated routes are explained by the effect of dispersion on three-phase flow.
- Contaminant recoveries after 1.0 PVI of surfactant injection decrease with increasing surfactant enrichment in the injection composition for the NSH and SH mass-balance equations.
- Contaminant recovery is substantially affected by choice of relative permeability model. The relative permeabilities that give a NSH mass-balance equation predict the fastest recovery for most injection compositions.

- The optimal surfactant concentration to minimize total surfactant volume injected is significantly impacted by the three-phase relative permeability model.

	Volume Fractions		
Injection Composition	H_2O	C_{16}	Surf
A	1.0000	0.0000	0.0000
B	0.8305	0.0000	0.1695
C	0.8003	0.0000	0.1997
D	0.6050	0.0000	0.3950
E	0.5500	0.0000	0.4500
F	0.4202	0.0000	0.5798
G	0.3796	0.0000	0.6204
H	0.3661	0.0000	0.6339
I	0.3578	0.0000	0.6422
J	0.3591	0.0000	0.6409
K	0.3000	0.0000	0.7000
L	0.1956	0.0000	0.8044
M	0.0000	0.0000	1.0000
N	0.0000	0.5000	0.5000
O	0.0000	0.8805	0.1195
P	0.0000	0.9191	0.0809

Table 4.1 Injection compositions in volume fractions.

NSH				SH				MHE			
Type	Range (Vol. Frac. Surf. Inj.)		Routes on Figs. 4.3-4.6	Type	Range (Vol. Frac. Surf. Inj.)		Routes on Figs. 4.7-4.10	Type	Range (Vol. Frac. Surf. Inj.)		Routes on Figs. 4.11-4.14
1	0.0000	0.1695	A, B	1	0.0000	0.1695	A, B	1	0.0000	0.1695	A, B
2	0.1695	0.5766	C, D	2	0.1695	0.3260	C	2	0.1695	0.5642	C, D, E
3d	0.5766	0.6204	F	3d	0.3260	0.4713	D, E	3a	0.5642	0.5859	-
3e	0.6204	0.64219	-	3e	0.4713	0.6358	G	3g	0.5859	0.6339	-
3f	0.64219	0.64221	I	3c	0.6358	0.6409	-	3c	0.6339	0.6340	H
3c	0.64221	0.6601	-	4	0.6409	0.6592	J	3e	0.6340	0.6923	-
3g	0.6601	0.7068	K	3c	0.6592	0.6595	-	3d	0.6923	0.7242	K
3a	0.7068	0.7517	-	3g	0.6595	0.8251	K, L	2	0.7242	1.0000	L, M
2	0.7517	1.0000	L, M	3a	0.8251	1.0000	M				

Table 4.2 Progression of route types with surfactant enrichment for each relative permeability model.

	Volume Fraction			Phase Saturations				
Label on Figures	H_2O	C_{10}	Surf	S_1	S_2	S_3	Dimensionless Velocity	Phases present
Injection Composition F (type 3d)								
F	0.4202	0.0000	0.5798	0.0000	0.0000	1.0000	0.0000-0.5619	1
f_1	0.4753	0.1511	0.3736	0.2941	0.1126	0.5933	0.5619 (s)	3
f_2	0.4219	0.2266	0.3515	0.2483	0.1987	0.5530	1.2637	3
f_3	0.6008	0.3992	0.0000	0.6008	0.3992	0.0000	1.2637-1.8055	2
I.C.	0.7000	0.3000	0.0000	0.7000	0.3000	0.0000	1.8055	2
Injection Composition I (type 3f)								
I	0.3578	0.0000	0.6422	0.0000	0.0000	1.0000	0.0000-0.5638	1
i_1	0.4124	0.1798	0.4078	0.1708	0.1355	0.6936	0.5638-0.5684 (s)	3
i_2	0.4116	0.1808	0.4076	0.1700	0.1367	0.6933	0.5715-0.6975 (s)	3
i_3	0.4171	0.2097	0.3732	0.2170	0.1756	0.6074	1.2765	3
i_4	0.6026	0.3974	0.0000	0.6026	0.3974	0.0000	1.2765-1.8022	2
I.C.	0.7000	0.3000	0.0000	0.7000	0.3000	0.0000	1.8022	2

Table 4.3 Composition routes and velocities for new composition route types using the NSH conservation law. Routes are also shown on Fig. 4.5 and profiles are in Fig. 4.3. (s) denotes the start of a spreading wave, (i) denotes the start of an indifferent wave, and (a) denotes the alternate path through composition space.

	Volume Fraction			Phase Saturations				
Label on Figures	H_2O	C_{10}	Surf	S_1	S_2	S_3	Dimensionless Velocity	Phases present
Injection Composition G (type 3e)								
G	0.3796	0.0000	0.6204	0.0000	0.0000	1.0000	0.0000-0.5184	1
g_1	0.4567	0.1922	0.3512	0.2951	0.1618	0.5431	0.5184 (s)	3
g_2	0.4242	0.2496	0.3262	0.2805	0.2291	0.4904	0.7834-0.8193	3
g_3	0.4950	0.2838	0.2212	0.4957	0.2897	0.2146	1.5704	3
g_4	0.6578	0.3422	0.0000	0.6578	0.3422	0.0000	1.5704-1.6786	2
I.C.	0.7000	0.3000	0.0000	0.7000	0.3000	0.0000	1.6786	2
Injection Composition K (type 3g)								
K	0.3000	0.0000	0.7000	0.0000	0.0000	1.0000	0.0000-0.6139	1
k_1	0.1873	0.3242	0.4885	0.0000	0.2553	0.7447	0.6139	2
k_2	0.1813	0.3414	0.4773	0.0000	0.2810	0.7190	0.6800	2
k_3	0.3798	0.3041	0.3161	0.2328	0.2899	0.4773	0.6800 (s)	3
k_4	0.4271	0.2809	0.2920	0.3237	0.2705	0.4058	0.9230	3
k_5	0.4400	0.2666	0.2934	0.3393	0.2549	0.4058	0.9230-0.9761	3
g_3	0.4950	0.2838	0.2212	0.4957	0.2897	0.2146	1.5704	3
g_4	0.6578	0.3422	0.0000	0.6578	0.3422	0.0000	1.5704-1.6786	2
I.C.	0.7000	0.3000	0.0000	0.7000	0.3000	0.0000	1.6786	2

Table 4.4 Composition routes and velocities for new composition route types using the SH conservation law. Routes are also shown on Fig. 4.6 and profiles are in Figs. 4.9 and 4.10. (s) denotes the start of a spreading wave, (i) denotes the start of an indifferent wave, and (a) denotes the alternate path through composition space.

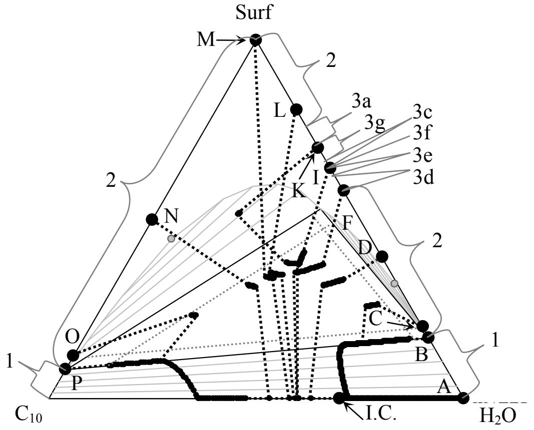

Figure 4.1 Progression of composition route types resulting from the NSH conservation law. Shocks are shown as dotted lines, spreading and indifferent waves as solid lines. Gray dotted lines near the edge of the three-phase region are phase residual saturations.

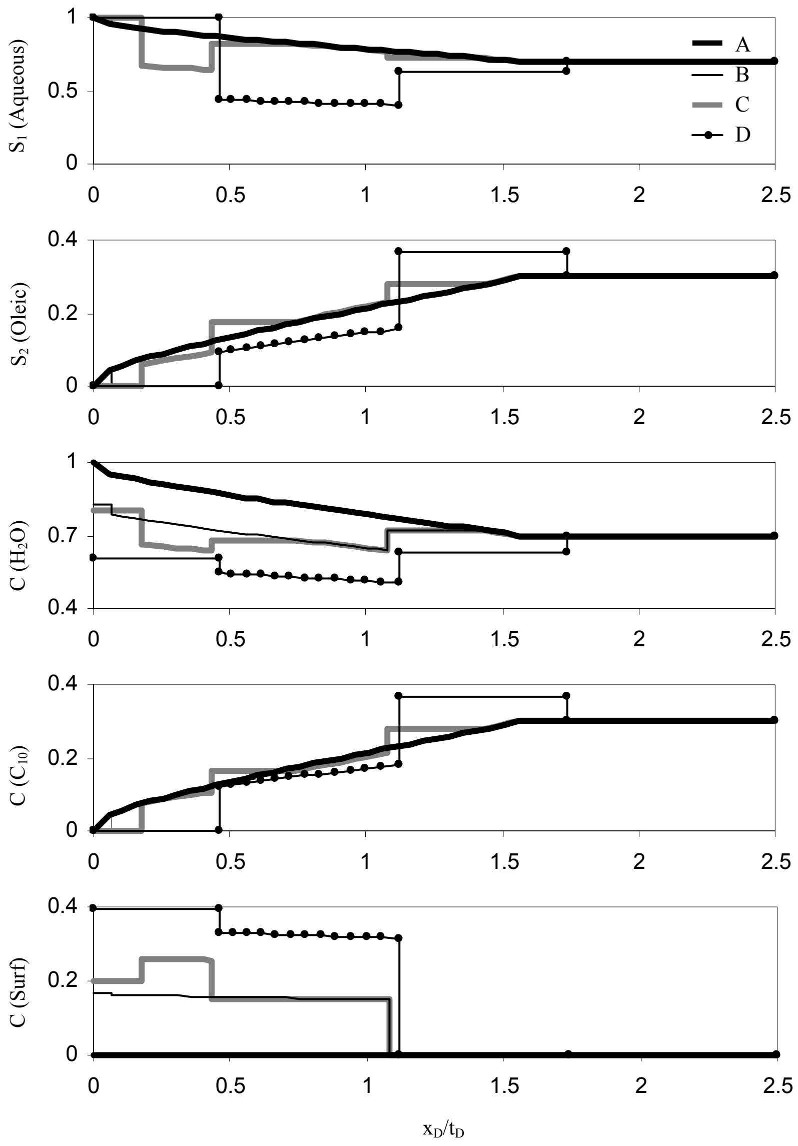

Figure 4.2 Compositions and phase saturations as a function of dimensionless velocity for injection compositions A-D using the NSH conservation law. A and B are type 1 composition routes. C and D are type 2 composition routes.

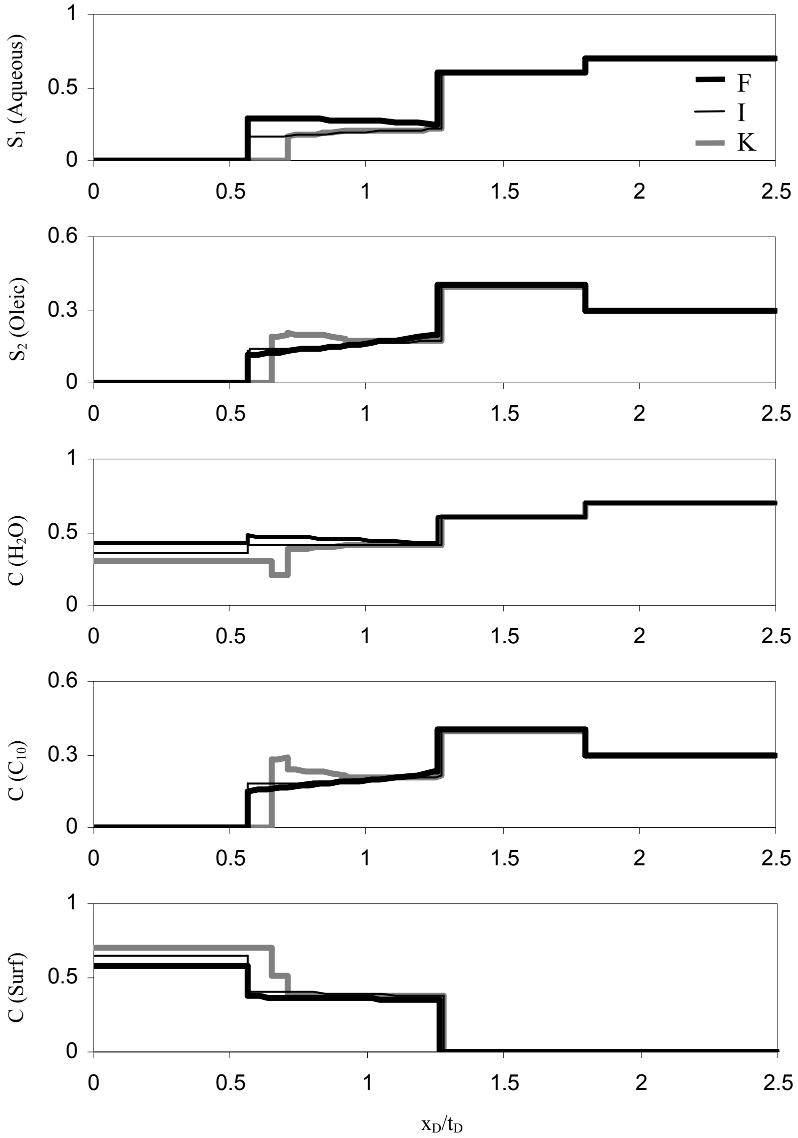

Figure 4.3 Compositions and phase saturations as a function of dimensionless velocity for injection compositions F, I, and K using the NSH conservation law. F, I, and K are type 3d, 3f, and 3g composition routes respectively.

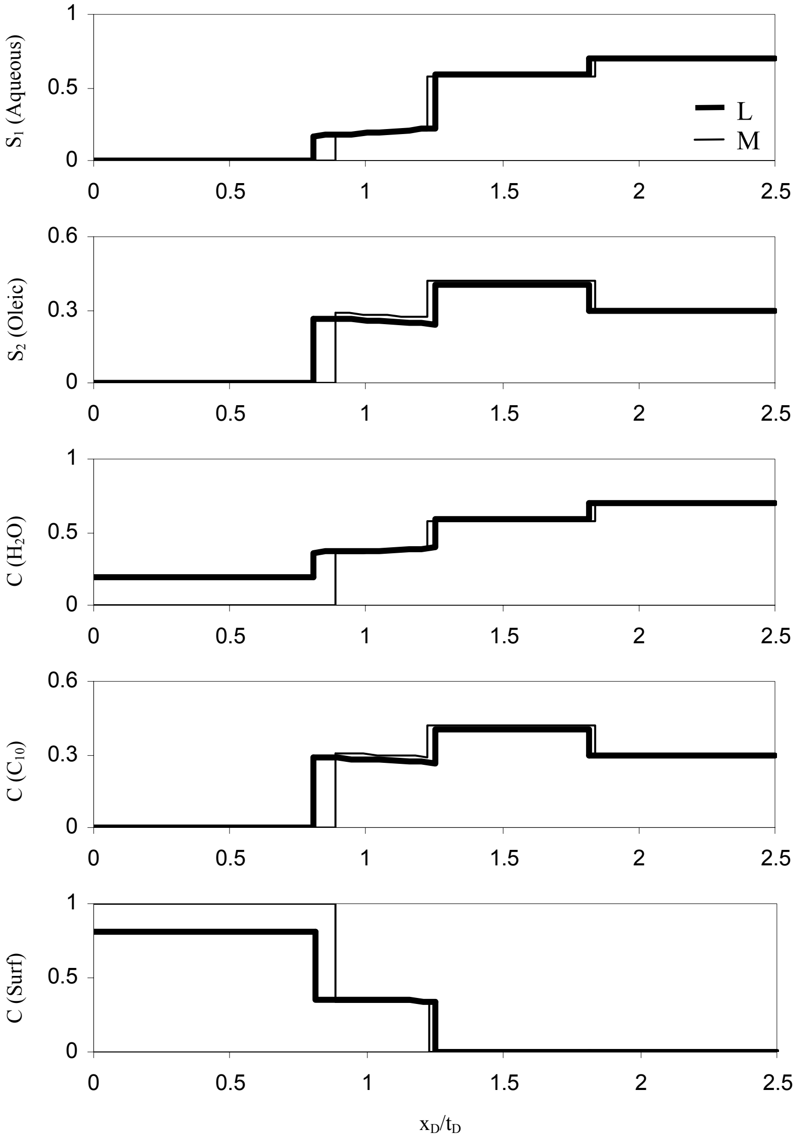

Figure 4.4 Compositions and phase saturations as a function of dimensionless velocity for injection compositions L and M using the NSH conservation law. L and M are both type 2 composition routes.

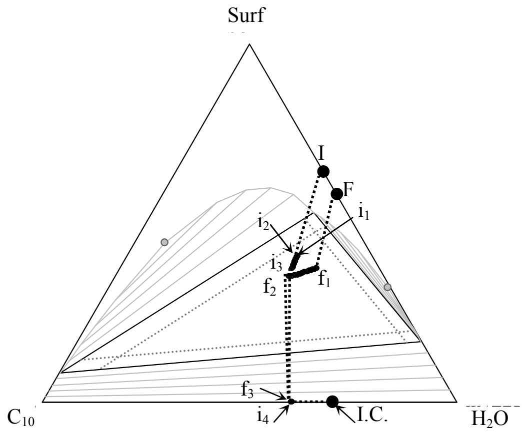

Figure 4.5 Examples of new types of composition routes using the NSH model. I.C. denotes the initial composition. Shocks are shown as dotted lines, spreading waves are solid lines. F is a type 3d composition route and I is type 3f. Gray dotted lines near the edge of the three-phase region are phase residual saturations.

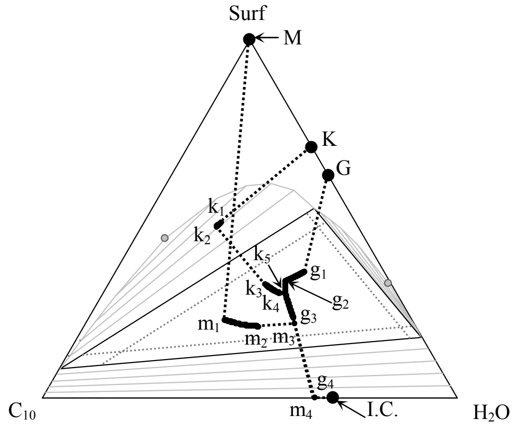

Figure 4.6 Examples of composition routes using the SH model. I.C. denotes the initial composition. Shocks are shown as dotted lines, spreading waves are solid lines. G is a type 3d composition route and K is type 3g neither of which was encountered in Chapter 3. M is a type 3a composition route. Gray dotted lines near the edge of the three-phase region are phase residual saturations.

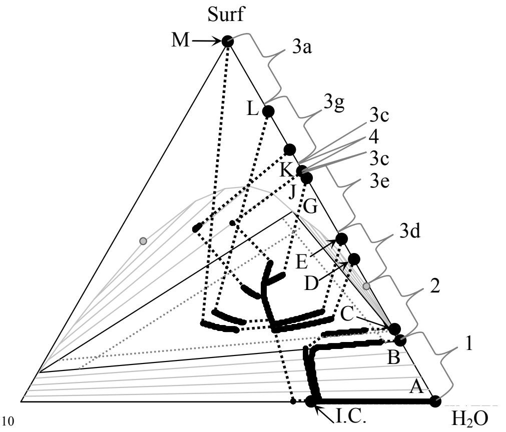

Figure 4.7 Progression of composition route types resulting from the SH conservation law. Shocks are shown as dotted lines, spreading and indifferent waves as solid lines. Gray dotted lines near the edge of the three-phase region are phase residual saturations.

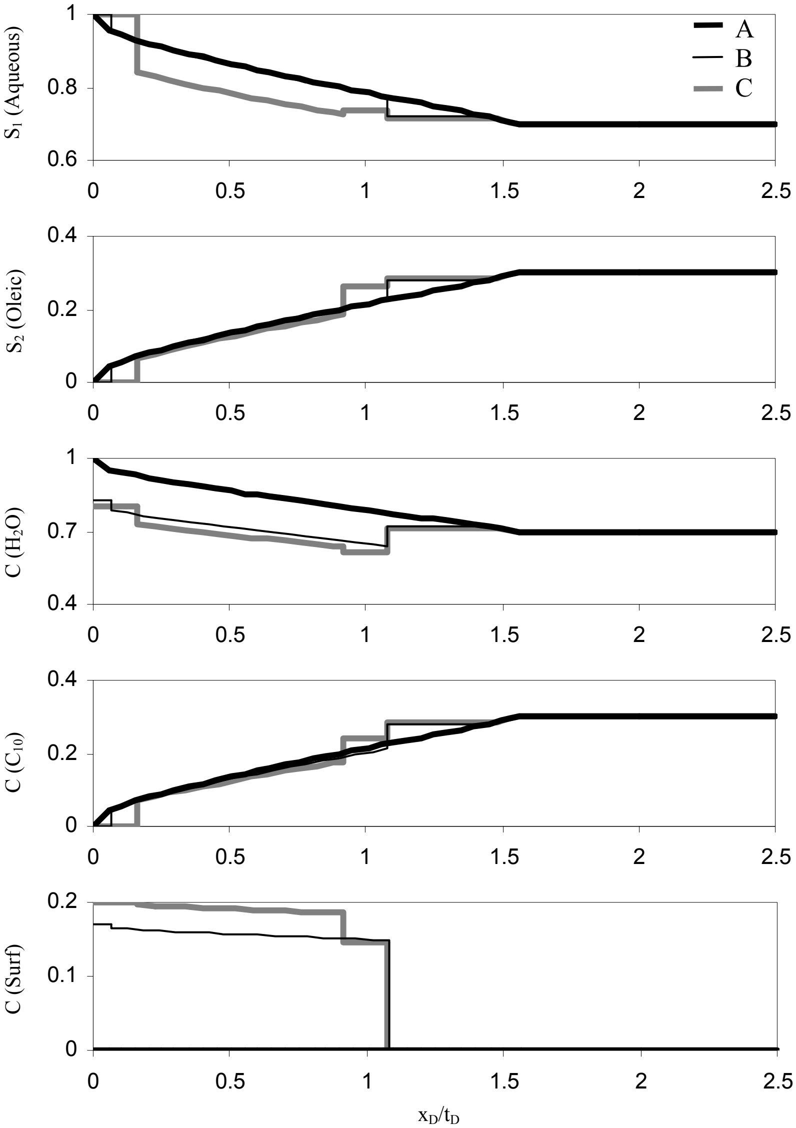

Figure 4.8 Compositions and phase saturations as a function of dimensionless velocity for injection compositions A-C using the SH conservation law. A and B are type 1 composition routes. C is a type 2 composition route.

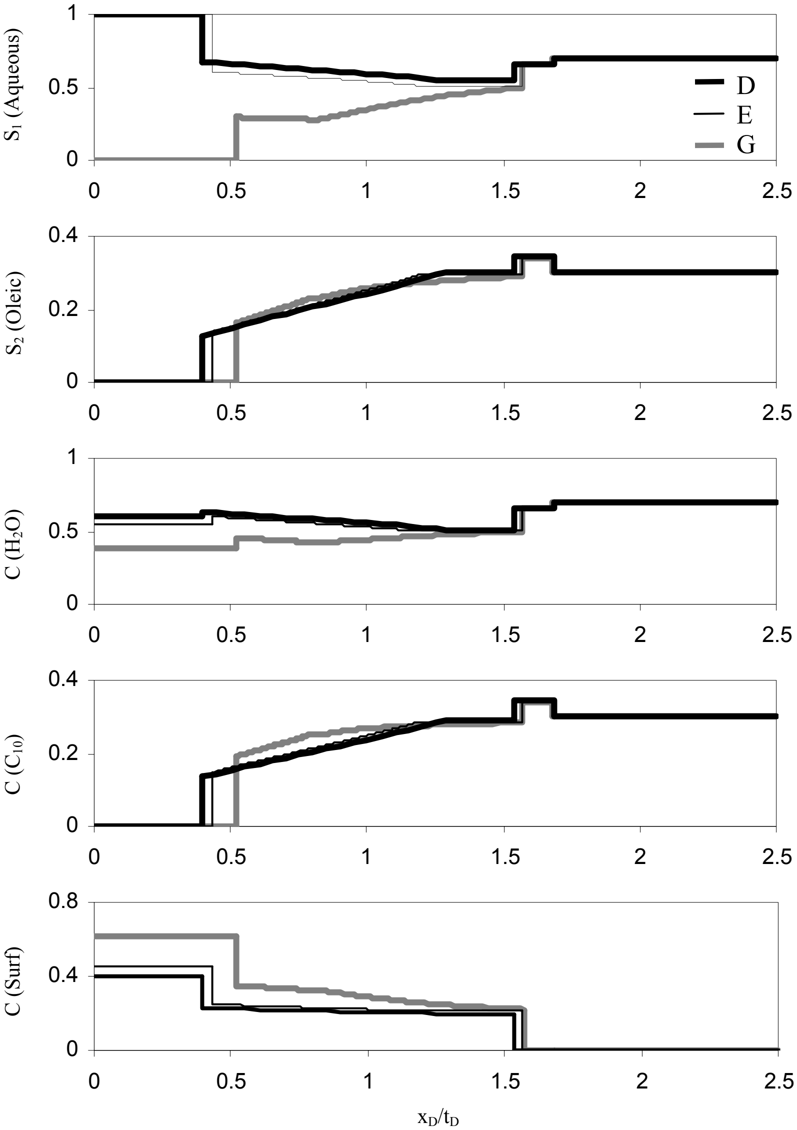

Figure 4.9 Compositions and phase saturations as a function of dimensionless velocity for injection compositions D, E, and G using the SH conservation law. D and E are type 3d composition routes. G is a type 3e composition route.

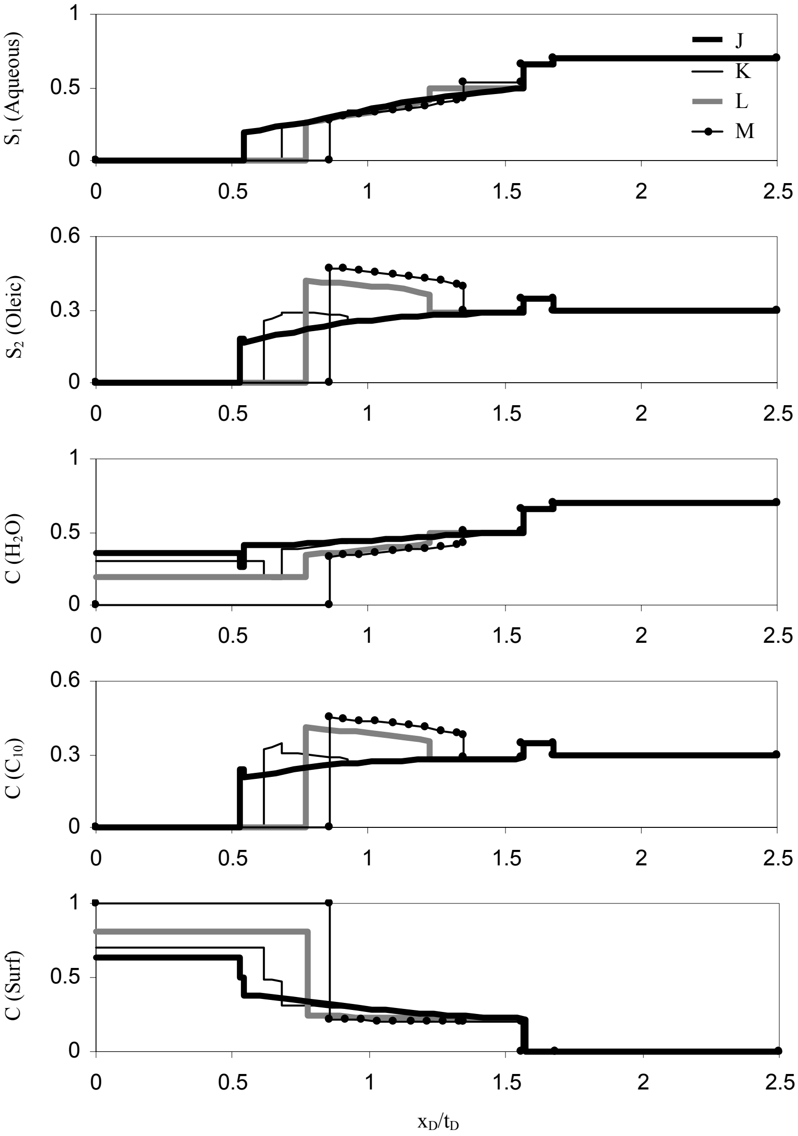

Figure 4.10 Compositions and phase saturations as a function of dimensionless velocity for injection compositions J-M using the SH conservation law. J is a type 4 composition route. K and L are type 3g composition routes. M is a type 3a route.

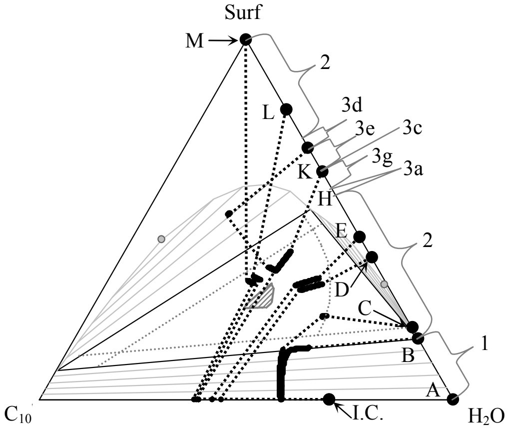

Figure 4.11 Progression of composition route types resulting from the MHE conservation law. Shocks are shown as dotted lines, spreading and indifferent waves as solid lines. Gray dotted lines near the edge of the three-phase region are phase residual saturations.

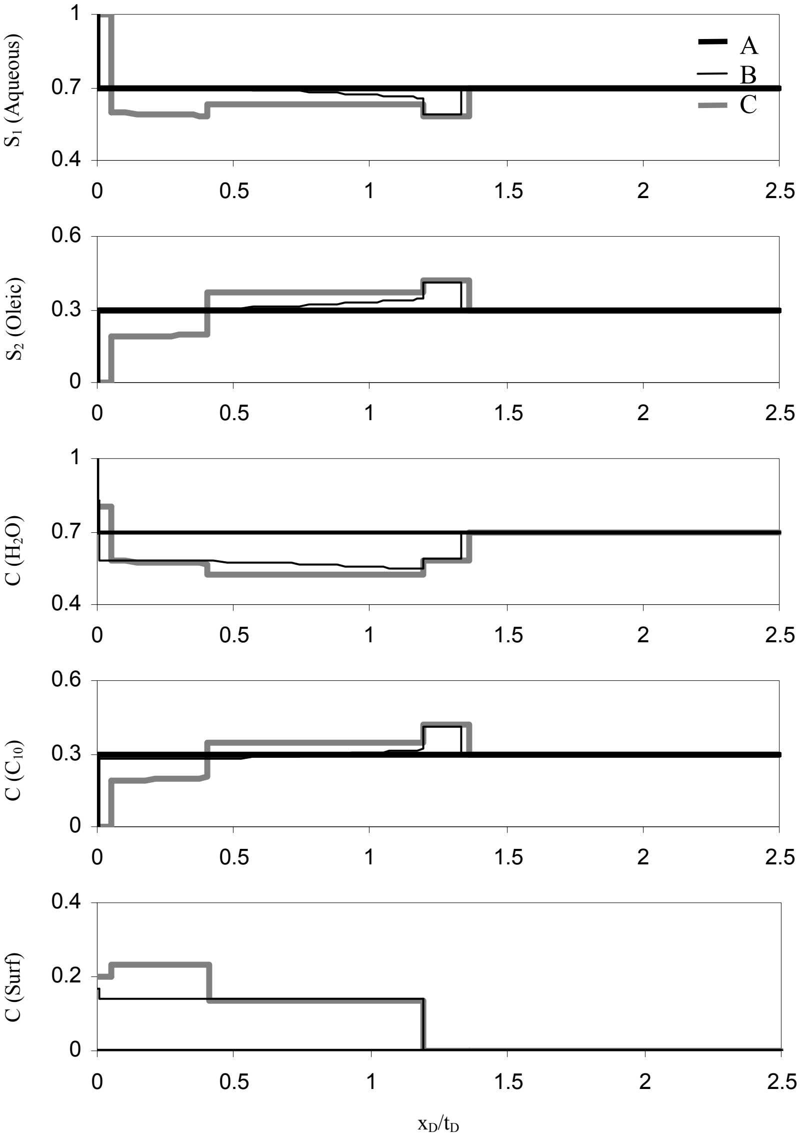

Figure 4.12 Compositions and phase saturations as a function of dimensionless velocity for injection compositions A-C using the MHE conservation law. A and B are type 1 composition routes. C is a type 2 composition route.

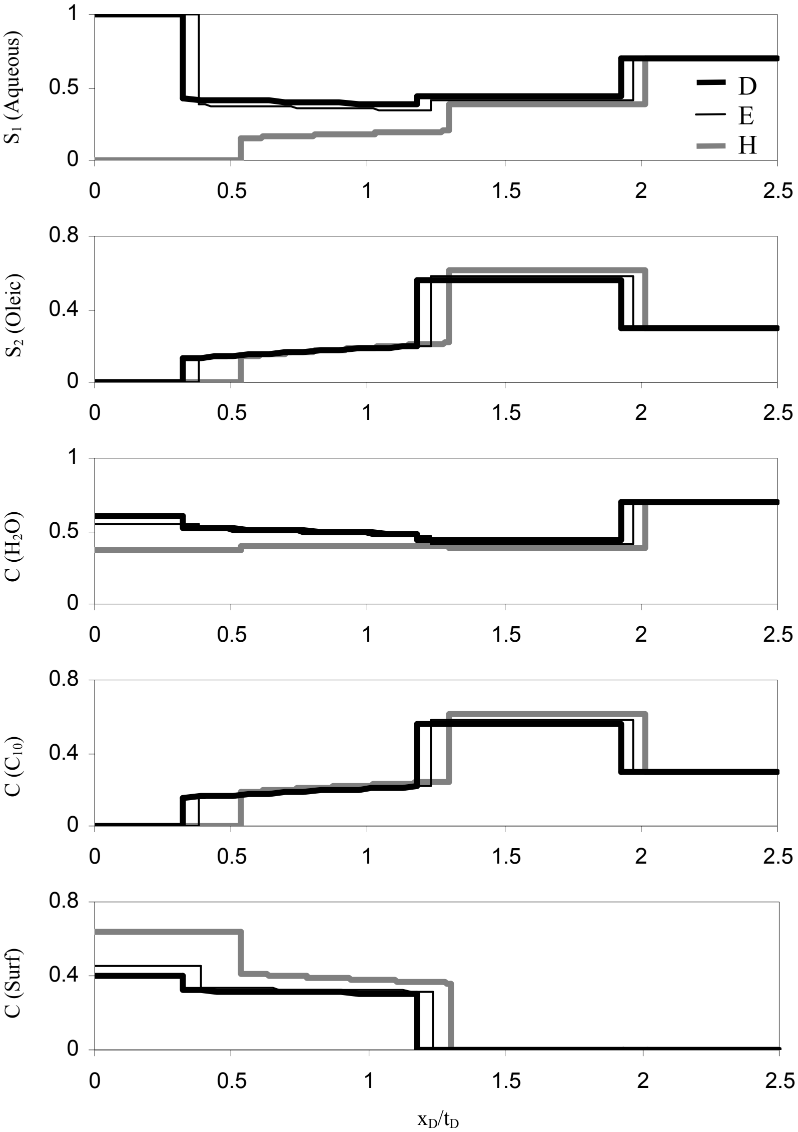

Figure 4.13 Compositions and phase saturations as a function of dimensionless velocity for injection compositions D, E, and H using the MHE conservation law. D and E are type 2 composition routes. H is a type 3c composition route.

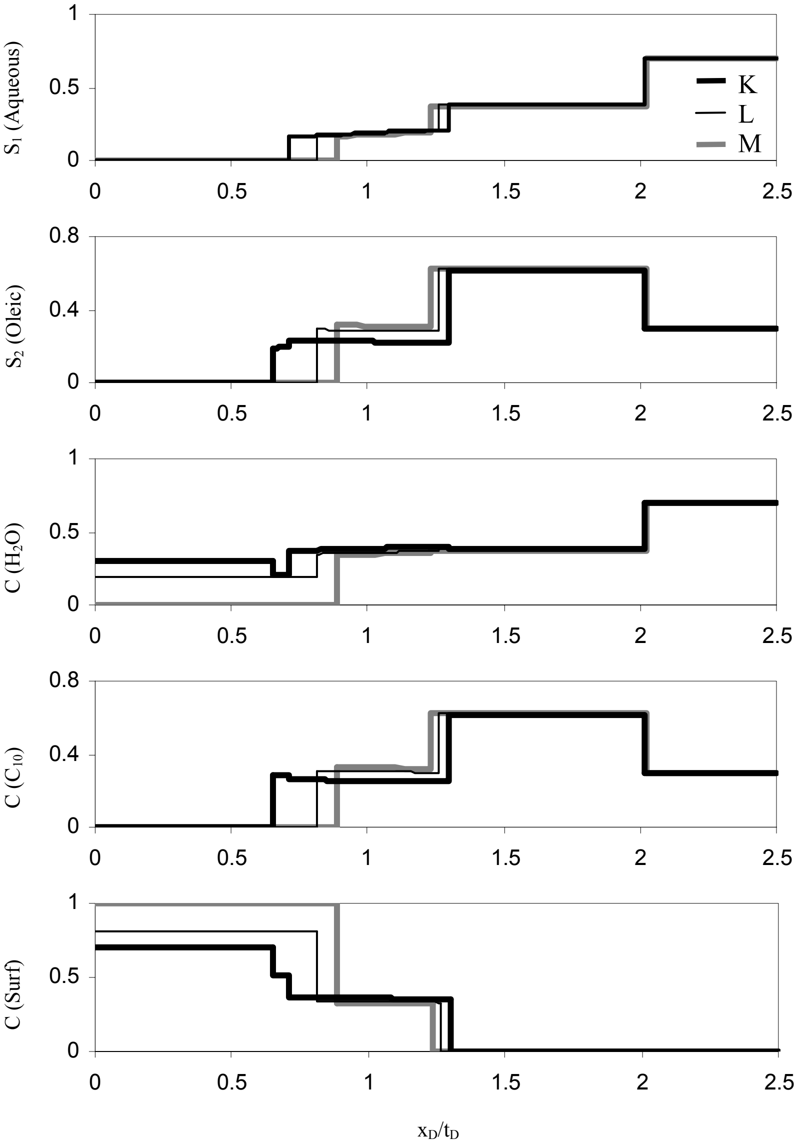

Figure 4.14 Compositions and phase saturations as a function of dimensionless velocity for injection compositions K-M using the MHE conservation law. K is a type 3d composition route. L and M are type 2 composition routes.

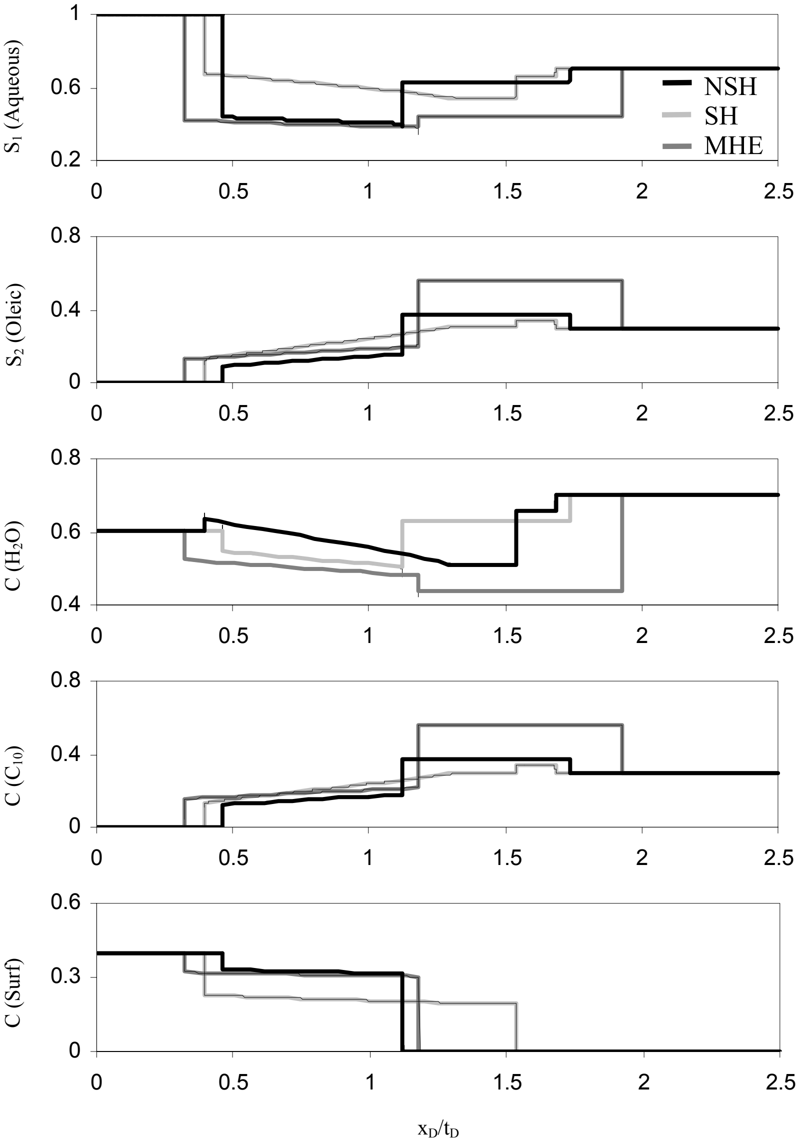

Figure 4.15 Composition and saturations as a function of dimensionless velocity for injection of composition D for each of the three relative permeability models. Simulated routes are thin lines and MOC routes are thick lines.

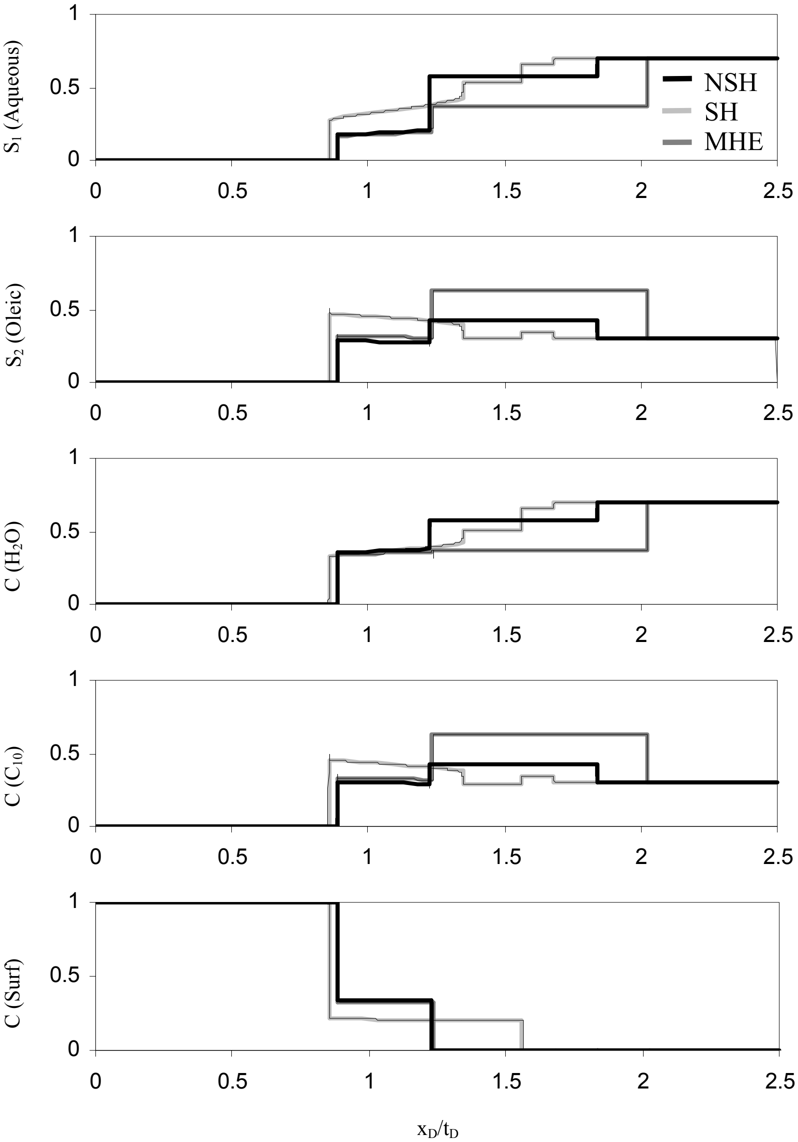

Figure 4.16 Composition and saturations as a function of dimensionless velocity for injection of composition M for each of the three relative permeability models. Simulated routes are thin lines and MOC routes are thick lines.

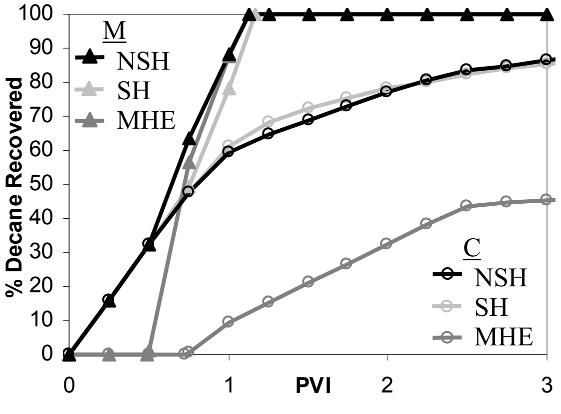

Figure 4.17 Percent decane recovered by volume as a function of PVI for injection compositions C and M.

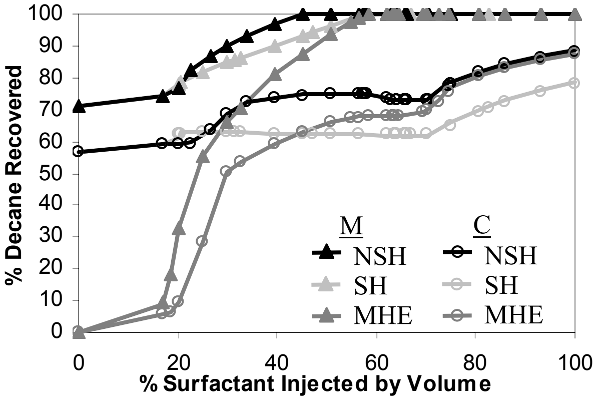

Figure 4.18 Cumulative decane recovery by volume percent after 1.0 PVI and 2.0 PVI as a function of percent surfactant injected by volume. Simulated recoveries are symbols and analytical recoveries are lines.

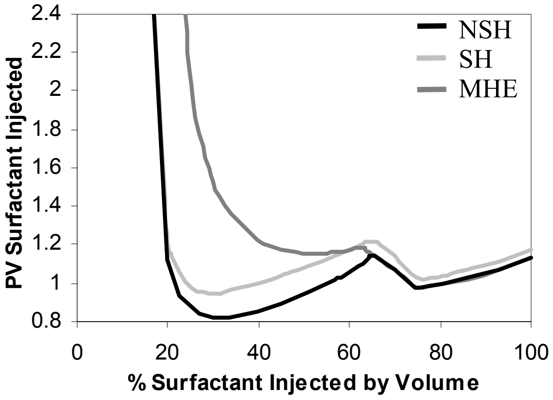

Figure 4.19 Total PV of surfactant necessary to achieve 100% removal of decane as a function of surfactant concentration in injection fluid.

Chapter 5 Dispersion in Three-Phase Partially Miscible Flow

In this chapter core flood effluent data are compared to MOC routes and profiles in order verify that the mathematical model captures the features of the core flood displacements. The effect of numerical dispersion on simulated three-phase composition routes, profiles, and recoveries is also studied. Numerical solutions are compared to MOC solutions and core flood effluents.

In any physical process some level of dispersion is present. In two-phase miscible gas injection numerical dispersion is typically used to model the effects of physical dispersion. It has been shown that even a small amount of dispersion causes two-phase flow in multi-component MCM displacements (Johns *et al.*, 1992). Walsh and Orr (1990) showed that the sensitivity to dispersion was determined by the size and shape of the two-phase region in MCM vaporizing drives in ternary systems. In quaternary C/V simulations dispersion causes partially miscible displacements to deviate from the true horizontal and vertical surfaces and enter deeper into the two-phase region (Johns *et al.,* 1999). Moreover, in MCM flow the sensitivity to dispersion and the amount of two-phase flow (and hence reduction in recovery) is dependent on the drive mechanism as well as the size and shape of the two-phase region (Johns *et al.,* 1999). Johns et al (2002) show that recoveries can be reduced by as much as 20% at the MME in a 12-component system.

In three-phase immiscible flow, there is some uncertainty as to whether it is possible to model physical dispersion using numerical dispersion. In three-phase flow the form of the diffusion tensor may determine the correct composition route, in which case using numerical dispersion could lead to incorrect routes (Marchesin *et al*., 1997). However, Marchesin *et al*. (1999) show that simulated and MOC solutions give similar composition routes and recoveries for three-phase immiscible WAG injection.

Both MOC and simulated solutions have been shown to accurately model three-phase immiscible flow experiments. Siddiqui *et al.* (1996) match MOC composition profiles and recoveries to core flood data accurately for three-phase immiscible flow. Hicks and Grader (1996) compared simulated and core flood composition routes and recoveries and obtained an excellent match.

For simulations of CO_2 injection in which three-phase partially miscible flow occurs, it has been shown that increasing numerical dispersion causes MCM composition routes to enter the three-phase region. Greater levels of dispersion cause the route to enter the three-phase region more deeply (Gardner *et al*., 1979). This result is directly analogous to the results of simulation of two-phase partially miscible flow. Giordano and Salter (1984) compared simulated, MOC, and core flood composition routes and profiles in a three-phase partially miscible system. Their results showed that numerical dispersion spreads shock fronts like in two-phase flow. Simulated routes otherwise matched the MOC solution they examined.

In this chapter the results from twelve core flood experiments are compared with analytical effluent routes and profiles for a partially miscible three-phase system. It is demonstrated that the zero dispersion limit of the simulated one-dimensional flow problems approaches the MOC composition routes. The effect of numerical dispersion on composition routes and recoveries is studied. MOC and core flood routes are also compared with simulations to assess whether the numerical dispersion accurately models the physical dispersion.

5.1 COMPARISON OF CORE FLOOD AND ANALYTICAL SOLUTION EFFLUENTS

Cinar and Orr (2004) performed two series of core floods on the NBA/water/C_{16} ternary system that was used in Chapter 3. The first series of experiments is the injection of C_{16} into eight glass bead packs, each of which contains a uniform mixture of NBA and water. The initial compositions are labeled A_1-A_8 and are outlined in Table 5.1. The second series of experiments is the constant injection of water and NBA into four cores initially saturated with C_{16}. The injection compositions are labeled B_1-B_4 and are outlined in Table 5.2.

The core floods were done using vertical glass bead packs with 37% porosity and a permeability of 33 Darcy. The cores were 34.8 cm long and 2.5 cm in diameter and the volumetric flow rates are between 2 and 3.11cm^3/s. Cinar and Orr (2004) estimate a Peclet number of 175 for the displacements based on the glass bead pack dispersivity experiments of Batycky (1994). Relatively high interfacial tensions were measured on the oleic/water and water/alcohol edges of the three-phase region, 2.5 mN/m and 2.3 mN/m, respectively. Low interfacial tensions of 0.24 mN/m were measured on the alcohol/oleic phase boundary of the three-phase region.

The phase behavior used in the MOC solutions and simulations is based on Pongpitak (1980) and is outlined in Table 2.1. The component densities and viscosities of each phase are outlined in Table 5.3. The pure component viscosities and densities are from Cinar and Orr (2004) and are slightly different than the parameters from the Chemical Properties Handbook (Yaws, 1999) and Pongpitak (1980) that were used in Chapters 2 and 3 because of experimental error.

The relative permeability model parameters are also shown in Table 5.3. The alcohol- and aqueous-phase relative permeabilities are based on two-phase water/NBA relative permeability measurements by Cinar and Orr (2004). The oleic-phase relative permeability is assumed to be the same as the alcohol-phase relative permeability since both phases are non-wetting and have similar interfacial tensions with the aqueous phase. The alcohol and oleic phase residual saturations are a function of all three phase saturations. In this case there are two α defined as

$$\alpha_2 = \frac{S_1(1-S_3)}{S_1+S_3} \qquad \alpha_3 = \frac{S_1(1-S_2)}{S_1+S_2} \tag{5.1}$$

and

$$
\begin{aligned}
S_{r2} &= \alpha_2 S_{r21} + (1-\alpha_2) S_{r23} \\
S_{r3} &= \alpha_3 S_{r31} + (1-\alpha_3) S_{r32}.
\end{aligned}
\tag{5.2}
$$

Otherwise the relative permeability functions have the same form as those detailed in Chapter 2. The three-phase residuals of the oleic and alcohol phases go to zero on the boundary of the oil/alcohol two-phase region to account for the low interfacial tension between the alcohol and oleic phases in this two-phase region. Changing interfacial tension was not considered in Chapters 2 and 3. Despite the interdependence of the relative permeabilities, there do not appear to be any elliptic characteristics in the three-phase region for this choice of parameters.

The measured effluent compositions are the overall fractional flows (F_j) of each component in Eqs. 2.6, not the overall compositions present (C_j). Reasonable in situ compositions could not be computed from the effluent data for some data points. Thus, the measured effluents and the overall composition fractional flows (F_j) in the MOC routes are compared directly in Figs. 6.1-6.24.

5.1.1 Injection of C_{16} into Water/NBA Saturated Cores

Cinar and Orr's (2004) first series of experiments was the injection of pure C_{16} into cores saturated with varying amounts of NBA and water. The initial compositions are A_1-A_8 and are outlined in Table 5.1. For this series of solutions the injection composition is held constant while the initial composition is varied, opposite the scenario studied in Chapters 3 and 4.

5.1.1.1 MOC Solutions for A_1-A_8

The MOC solution is constructed for each of the injection and initial compositions outlined in Table 5.1 and pure C_{16} injection. The key compositions in the MOC composition routes and profiles are given in Tables 5.4-5.7 and are shown in Figs. 5.1-5.16. All of the composition routes that enter the three-phase region are type 4 composition routes as described in Chapter 3.

Initial composition A_1 results in a type 1 composition route shown in Figs. 5.1 and 5.2 since both the initial and injection compositions are on tie-line extensions of the same two-phase region. Initial composition A_2 has the first route with three-phase flow and results in a composition route that takes a fast path with very little alcohol phase present as shown in Table 5.4 and Figs. 5.3 and 5.4. The route from A_2 has a tangent shock directly from the initial composition to the fast path with no leading two-phase flow, but has a small region of trailing two-phase flow before the shock to the injection composition.

For initial compositions with more NBA than A_2 the composition routes follow fast paths with increasing amounts of alcohol phase. For the initial composition that is 83.43% water and 16.57% NBA the tangent shock from the initial composition is to the fast path through the umbilic point. Initial compositions with more NBA, such as A_3-A_7, result in composition routes that shock or spread down the initial composition tie-line path before taking a tangent shock to this fast path. The routes from A_3-A_7 are shown in Tables 5.5-5.7 and Figs. 5.5-5.14. The leading spreading wave or shocks in the displacements from

A_3-A_7 are constructed and evolve exactly the same as the leading edge of the two-phase displacements in Chapter 6.

For the initial composition of 28.56% water and 71.44% NBA the route has a tangent shock directly from the initial composition to the fast path through the umbilic point. The routes from initial compositions with more NBA, such as A_8, cannot shock to the fast path through the umbilic point and instead tangent shock directly to a different fast path in the three-phase region. The route from A_8 is shown in Tables 5.7 and Figs. 5.15-5.16.

Initial compositions with more NBA than A_8 approach miscibility in much the same way as in the changing injection composition problem in Chapter 3. For initial compositions on the extension of a tie line in the C_{16}/NBA two-phase region the composition route has a tangent shock along the tie line, then shocks between the initial composition tie line and the tie line on the boundary of the three-phase region. There is either a constant state or a spreading wave on the boundary tie line until it is possible to shock to the injection composition tie line on the water/C_{16} boundary of the ternary diagram. The route from the initial composition on the extension of the tie line through the critical point has MCM flow for pure C_{16} injection, the same as in Chapter 3.

5.1.1.2 Comparison of MOC and Core Flood Routes and Profiles

The MOC route for initial composition A_1 matches the effluent composition and profiles very closely, as shown in Figs. 5.1 and 5.2. The MOC and core flood effluent routes are very different for initial composition A_2, as shown in Fig. 5.3. However, the MOC route captures the leading shock velocity in the displacement accurately, and the profiles are qualitatively similar.

Between A_2 (87% water by volume) and the initial composition that is 83% water the composition route changes very quickly with NBA enrichment. The composition route takes fast paths with larger alcohol phase saturations until the fast path through the umbilic point is reached. Since the composition routes in this region are highly sensitive to changes in initial composition, the difference between the MOC composition route and the core flood are likely caused by small errors in the parameters used in the MOC solution. This also explains why the leading shock velocity is accurately captured, even though the composition routes are dissimilar.

Initial compositions on the water/NBA axis of the ternary diagram with between 29% and 83% water by volume result in composition routes that have a shock along the initial composition tie line, then shock to the umbilic fast path for the parameters chosen. The MOC routes from initial compositions A_3-A_7 take the fast path through the umbilic point through the three-phase region as shown in Figs. 5.3-5.14. The core flood routes from initial compositions A_2-A_7 take this fast path through the three-phase region of composition space, though MOC theory predicted a very different route for A_2 as previously discussed. The MOC and effluent routes for A_3-A_7 are in remarkably good agreement.

The leading shock travels faster and the trailing shock travels slower in the core flood profiles than in MOC profiles. The discrepancy between MOC and core flood shock velocities is discussed further in section 5.1.4.

The effluent and MOC composition routes from A_8 both take a fast path through the three-phase region that has very little aqueous phase and are in good agreement. As with the routes from A_3-A_7, the effluent leading shock arrives earlier and the trailing shock arrives later than the MOC solution predicts.

5.1.2 Injection of Water/NBA Mixtures into a C_{16} Saturated Core

In the second series of experiments by Cinar and Orr (2004) mixtures of water and NBA were injected into cores saturated with pure C_{16}. The initial compositions are B_1-B_4 and are outlined in Table 5.2. For this series of experiments the initial composition is held constant while the injection composition is varied, identical to the scenario studied in Chapters 3 and 4.

5.1.2.1 MOC Solutions for B_1-B_4

Route construction is identical to the routes in Chapter 3 for all of these composition routes. The new parameters alter the composition routes slightly and route type changes at slightly different injection compositions. The MOC composition routes are outlined in Tables 5.8 and 5.9 and are shown in Figs. 5.17-5.24.

5.1.2.2 Comparison of MOC and Core Flood Routes and Profiles

The MOC effluent route for injection composition B_1 matches the core flood effluent route qualitatively, as shown in Fig. 5.17. For this injection composition the MOC theory predicts earlier water breakthrough than observed in the core floods as shown in Fig. 5.18. This is opposite the scenario seen in experiments A_3-A_7 where the MOC predicted a slower leading shock than observed in the core floods.

The MOC and effluent composition routes match extremely well for injection composition B_2, as shown in Fig. 5.19. The profiles in Fig. 5.20 show that the MOC route captures the leading shock along the initial composition tie line and the shock into the three-phase region accurately. Both the velocity and the change in composition across the shocks are correct. The small change in composition across the trailing shock makes it difficult to see if the MOC route captures this shock.

The MOC and effluent composition routes are very different for injection composition B_3, as shown in Fig. 5.21. The MOC composition route is a type 4 route and takes a fast path with small aqueous phase saturation through the three-phase region, while the core flood route takes a type 2 route similar to the route for injection composition B_2. Nevertheless, the MOC route captures the leading shock velocity in the displacement very accurately in the profiles in Fig. 5.22, though the profiles are not similar otherwise.

In Chapter 3 it was shown that the composition routes for injection compositions between 46% and 39% water by volume are highly sensitive to changes in injection composition. Hence the difference between the MOC composition route and the core flood are likely the cause of small errors in the parameters used in the MOC solution. This also explains why the leading shock velocity is accurately captured, even though the composition routes are dissimilar.

A similar result was observed for injection of C_{16} into a core with initial composition A_2.

The MOC effluent route matches the core flood route for injection composition B_4 as shown in Fig. 5.23. Both effluents take type 4 routes with very small aqueous phase saturation through the three-phase region. In Fig. 5.24 the profiles show that the MOC theory predicted a faster leading shock than the experimental result. A similar result was observed for injection compositions B_1 and B_3.

5.1.3 The Effect of Gravity

Cinar and Orr (2004) ran all of their core floods vertically, but in the MOC solutions gravity was neglected. In order to verify that gravity has little effect on the MOC composition routes and profiles, the MOC solution for experiment A_4 is found including gravity. When gravity is included in the three-phase partially immiscible flow equations the fractional flow of phases 1 and 3 are (Guzman, 1995)

$$\begin{aligned} f_1 &= \frac{\lambda_1}{\lambda_1+\lambda_2+\lambda_3}\left(1+N_3k_{r3}+N_1\mu_1\left(\lambda_2+\lambda_3\right)\right) \\ f_3 &= \frac{\lambda_3}{\lambda_1+\lambda_2+\lambda_3}\left(1-N_1k_{r1}-N_3\mu_3\left(\lambda_1+\lambda_1\right)\right) \end{aligned} \tag{5.3}$$

where the gravity numbers N_1 and N_3 are

$$N_1 = \frac{(\varphi_1 - \varphi_2)}{u\mu_1} kg \frac{\partial z}{\partial x} \quad \text{and} \quad N_3 = \frac{(\varphi_2 - \varphi_3)}{u\mu_3} kg \frac{\partial z}{\partial x}. \tag{5.4}$$

The total permeability is k, the gravity constant is g, the mass density of phase j is φ_j, and z is the direction of gravity. The phase densities are found from the pure component densities by $\varphi_j = \varphi_1 c_{1j} + \varphi_2 c_{2j} + \varphi_3 c_{3j}$. In the two-phase regions Eq. (5.3) simplifies to

$$f_1 = \frac{\lambda_1}{\lambda_1 + \lambda_2}\left(1 + N_1 \mu_1 \lambda_2\right), \tag{5.5}$$

which is identical to the two-phase fractional flow equation in Lake (1989).

The core flood effluent route and the profile for experiment A_4 are shown in Figs. 5.7 and 5.8. The pure component mass densities were measured to be 0.997, 0.772, and 0.807g/cm^3 for the water, C_{16} and NBA, respectively. For experiment A_4 the flow rate was 2cm^3/s.

For the water/C_{16}/NBA ternary system the gravity numbers in the three-phase region are $N_1 = 1.239\text{e-}4$ and $N_3 = 1.076\text{e-}5$ for a vertical experiment ($\partial z/\partial x = -1$). In the two-phase region the gravity number is dependent on phase compositions, but has similar magnitude. The reason the gravity numbers are so small is that all three phases are liquid and have similar densities. Figures 5.25-5.26 show the composition routes and profiles for the MOC solution with and without gravity. The maximum difference in saturations and velocities in the composition routes are on the order of 10^{-5}, so on Figs. 5.25-5.26 the two solutions are indistinguishable. Thus, neglecting gravity had little effect on the MOC solutions.

5.1.4 The Difference in MOC and Core Flood Shock Velocity

Recall from section 5.1.2.2 that the core floods in which C_{16} was injected into a core saturated with a two-phase water/NBA mixture showed much earlier breakthrough of C_{16} than was predicted by the MOC solutions, as shown in Figs 5.1-5.16. In section 5.1.3.2 three of the four core floods in which water and NBA were injected in to a core saturated with C_{16} had later breakthrough of water and NBA than was predicted by the MOC solutions, as shown in Figs 5.17-5.24.

The relative permeability parameters in Table 5.3 are based on two-component water/NBA measured relative permeabilities and were not fit to the core flood data. Thus, there is clearly some error in the parameters chosen. However, it is difficult to tell how changing the relative permeability parameters would affect the composition routes. It is also possible that the true relative permeabilities experience hysteresis, and that no single set of parameters exists that can accurately model both injection of C_{16} into water/NBA mixtures and injection of water/NBA mixtures into C_{16}.

The difference between the predicted and core flood shock velocities in both sets of experiments may be caused by of the assumption of no volume change on mixing in the MOC solutions. If components in this ternary system have a volume increase on mixing then the three-phase compositions will take up more space in the core than was assumed in the construction of MOC solutions.

This would cause composition routes to stay in the three-phase region longer on profiles. Alternately, if water and NBA have a loss of volume on mixing (as is typical for short chain alcohols and water), compositions in this two-phase region would take up less space in the core than assumed. As a consequence when C_{16} is injected water and NBA will be displaced faster than predicted by the MOC solutions. Conversely, when water and NBA are injected the oleic phase will be displaced slower than predicted by the MOC solutions.

It is also possible that the difference between the observed and MOC shock velocities is caused by dispersion in the core floods. In two-phase MCM flow dispersion causes the composition route to enter more deeply into the two-phase region. As a consequence, the leading shock speeds up and the trailing shock slows down (Johns *et al.*, 1999). Though most of the core floods are not near miscibility, it is possible that dispersion has a similar effect in three-phase flow.

5.2 NUMERICAL DISPERSION

The effect of numerical dispersion on composition routes and recoveries was briefly discussed in Chapters 3 and 4. For all of the simulations in this research a finite difference simulator with single point upstream-weighting is used. The simulator is explicit in time. The simulator approximates Eqs. 2.6 as

$$\begin{aligned} C_1^{j+1} &= C_1^j - (\Delta t_D / \Delta x_D)(F_1^i - F_1^{i-1}) \\ C_2^{j+1} &= C_2^j - (\Delta t_D / \Delta x_D)(F_2^i - F_2^{i-1}) \\ C_3^{j+1} &= 1.0 - C_1^{j+1} - C_2^{j+1} \end{aligned} \tag{5.6}$$

where *j* is the time step, and *i* is distance step. In general it is necessary to have CFL number $v_{max}\Delta t_D/\Delta x_D<0.5$ in order for the simulation to be stable (Guzman, 1995). In each of the simulations here, $\Delta t_D/\Delta x_D=0.08$ and the fastest wave $v_{max}<2.5$ so all simulations are stable.

Lantz (1971) showed that for explicit finite difference methods the numerical diffusion for a miscible one-dimensional displacement is given by $(\Delta x_D - \Delta t_D)/2$ and that for a fully immiscible two-phase displacement by

$$D=\frac{1}{2}\frac{df_1}{dS_1}\left(\Delta x_D-\frac{df_1}{dS_1}\Delta t_D\right). \tag{5.7}$$

An analysis similar to that of Lantz (1971) on the one-dimensional three-phase immiscible flow equations is shown in Appendix D and gives the dispersion as

$$D=\frac{1}{2}\begin{pmatrix} \frac{\partial f_1}{\partial S_1}\left[\Delta x_D-\frac{\partial f_1}{\partial S_1}\Delta t_D\right] & \Delta x_D\frac{\partial f_1}{\partial S_2} \\ \Delta x_D\frac{\partial f_2}{\partial S_1} & \frac{\partial f_2}{\partial S_2}\left[\Delta x_D-\frac{\partial f_2}{\partial S_2}\Delta t_D\right] \end{pmatrix}. \tag{5.8}$$

in three-phase immiscible simulations. When the fractional flow derivatives are approximately 1.0 the Peclet number due to numerical dispersion is

$$D=\frac{\Delta x_D-\Delta t_D}{2}\begin{pmatrix} 1 & 0 \\ 0 & 1 \end{pmatrix}. \tag{5.9}$$

Eq. (5.9) will be used to estimate the numerical dispersion in simulations. The grid block size is varied to introduce various levels of numerical dispersion for all of the simulations shown, while Δt_D=0.08Δx_D is fixed to ensure stability.

5.2.1 Effect of Numerical Dispersion on Partially Miscible Flow

Figures 5.27 and 5.28 compare analytical and simulated routes and profiles from injection of pure C_{16} into a core saturated with composition A_6. The simulations shown are N_{Pe}=1600 which minimizes numerical dispersion, N_{Pe}=175 which represents the amount of dispersion that Cinar and Orr (2004) estimated in their core floods, and N_{Pe}=16 which represents the amount of dispersion that could be expected at the field scale. At all three levels of dispersion shocks into and out of the three-phase region are dispersed, but there is little deviation from the spreading waves in the analytical composition route as shown on Fig. 5.27. Figure 5.28 shows that the high level of dispersion for the simulation with N_{Pe}=16 spreads the profile substantially, but the shock fronts are preserved for the other two simulations.

The recoveries of the NBA and water components are only slightly effected by dispersion for N_{Pe}=1600 and N_{Pe}=175 as shown on Fig. 5.29. At N_{Pe}=16 the recovery of both components is reduced from the analytical recoveries. NBA recovery is reduced between 0.75 and 1.5 PVI, and approaches the analytical recovery for longer times. Water recovery is only slightly reduced after breakthrough of the oil, but it never approaches the analytical recovery value for times less than 3 PVI.

It is possible for numerical dispersion to cause the simulated route to tend toward another route type for composition routes that are near the transition between route types. This was seen for injection composition I in Chapter 3 and injection composition D when the mass-balance equation was NSH in Chapter 4. The composition route from D is revisited here in order to demonstrate how various levels of numerical dispersion cause the simulated routes to diverge from the MOC routes.

Several simulated composition routes and profiles for injection composition D in the water/surfactant/alcohol system from Chapter 5 are shown in Figs. 5.30 and 5.31. This composition route is much more sensitive to dispersion than the previous example, so a much larger Peclet number is used to minimize dispersion. The simulations shown are N_{Pe}=18,000 which minimizes numerical dispersion, N_{Pe}=175 which represents laboratory scale dispersion, and N_{Pe}=16 which represents field scale dispersion.

As shown in Fig. 5.1, the composition route from injection composition D shocks directly to the initial composition tie line. The route from injection composition C shocks from the slow path to the boundary of the three-phase region and then takes a non-tie-line path to the initial composition tie line. The transition between these two routes is near D and as a consequence all of the simulated solutions tend toward routes that take a non-tie-line path through the water/decane two-phase region.

In the simulation with N_{Pe}=16 the shock out of the three-phase region is so dispersed that the composition route travels directly from the slow path to the initial composition. At this level of dispersion no decane bank is formed as shown on the profiles in Fig. 5.31. For N_{Pe}=16 the simulated route also takes a slow path with less water than the MOC solution. Figure 5.32 shows the water profile for the velocities 0.4 to 1.2 in order to detail the disparity in the profiles.

When the Peclet number is increased to 175, the composition route is on the non-tie-line path for a dimensionless velocity range of x_D/t_D=1.12 to 1.38, causing the profiles to show a dip in the profile not experienced by the MOC solution as shown on Fig. 5.32. The simulated route also tends toward higher water saturation as it passes through the water/surfactant two-phase region. This causes an additional spike at x_D/t_D=0.46. The MOC route shocks over the water/surfactant two-phase region, but the route from the simulation is still drawn toward the critical point of the two-phase region.

At N_{Pe}=18,000 the composition route is on the non-tie-line path for a dimensionless velocity range of x_D/t_D=1.120 to 1.124. Nonetheless these points result in a small spike in the profiles. At this level of dispersion the simulated route has a very slight tendency towards larger water saturations at the trailing edge of the displacement. It is clear that the simulated route is converging toward the MOC route as Peclet number goes to infinity, but that some anomalies in profiles will persist as long as any dispersion is present. A similar analysis of injection composition I from Chapter 3 shows an identical result.

The recovery of decane is not effected by dispersion for N_{Pe}=18,000 as shown on Fig. 5.33. In the simulation with N_{Pe}=175 recovery is marginally reduced between 1 and 2 PVI. At N_{Pe}=16 decane recovery is substantially reduced from the analytical recoveries after 0.5 PVI but approaches to the analytical recovery by 3 PVI.

In both of the above examples as the Peclet number increases the simulated routes, profiles, and recoveries all converge to the analytical solutions, thus verifying that the analytical routes are the zero-dispersion limit of the simulated displacement. The composition route and recovery from injection composition D in Chapter 4 is much more sensitive to dispersion than the composition route and recovery from injection of pure C_{16} into a core saturated with composition A_6.

5.2.2 The Effect of Numerical Dispersion on Recovery

Figure 5.34 shows the effect of numerical dispersion on C_{16} recoveries for the ternary system and parameters in Chapter 3. As shown on Fig. 5.35 the composition routes most sensitive to dispersion for N_{Pe}=16 occur near the onset of miscibility. This is an expected result since the MCM routes experience only one and two-phase flow and two-phase partially miscible displacements are very sensitive to dispersion near miscibility. After MCM is achieved, the recovery from the simulations continues to improve throughout the MCM and FCM composition routes. Improvement in recovery with over-enrichment is also observed in two-phase multi-component displacements.

Figures 5.36-5.38 show the effect of numerical dispersion on decane recoveries for all three sets of relative permeability parameters considered in Chapter 4. The decane recovery for all three conservation laws is more sensitive to dispersion than the C_{16} recoveries for the water/C_{16}/NBA ternary system as shown in Figs. 5.35 and 5.39. The NSH and MHE conservation law decane recoveries are more sensitive to dispersion than the recovery for the SH conservation law for most injection compositions as shown in Fig. 5.39. For the all three types of mass-balance equation type 2 composition routes are sensitive to dispersion. It is not clear why type 2 composition routes in this system are sensitive to dispersion, since the type 2 routes for the ternary system in Chapter 3 were not sensitive to dispersion.

Simulated recoveries with a large percent of surfactant injection by volume are sensitive to dispersion for all three conservation laws. For the NSH and MHE conservation laws injection compositions rich in surfactant are type 2 routes and for the SH conservation law these are type 3 routes. This is analogous to the increased sensitivity to dispersion that occurs as miscibility is approached for the water/C_{16}/NBA system.

5.3 COMPARISON OF SIMULATED AND CORE FLOOD COMPOSITION ROUTES AND PROFILES

Of particular interest in this section is whether numerical and physical dispersion cause the composition routes and profiles to diverge from the analytical solutions in the same way. Injection of composition A_1 into pure C_{16} is a two-phase displacement. As shown on Fig. 5.40 the core flood effluents traverse the two-phase region on the mixing line connecting the initial and injection compositions. This indicates a high level of dispersion in the displacement and matches the simulation with N_{Pe}=16. Conversely, the composition profiles in Fig. 5.41 show that shocks in composition in the core flood are substantially sharper than the shocks for the simulated displacement with N_{Pe}=16. The shocks in the core flood profile are slightly more spread out than the simulation with N_{Pe}=175 indicating a Peclet number on the order of 100. Clearly the numerical dispersion in simulations does not accurately reflect the true physical dispersion in the core flood for this composition route.

In Figs. 5.42-5.43 the composition route and profile from simulations and the core flood for initial composition A_6 are compared with the MOC composition route and profiles. In the composition route in Fig 5.42 both of the simulated routes closely match the effluent route. On the profiles in Fig. 5.43 the spreading of the shock fronts in the effluent compositions is somewhat more dispersed than the simulation with N_{Pe}=175, but not nearly as spread out as the simulation with N_{Pe}=16. A simulation with a Peclet number on the order of 100 captures the true level of dispersion of the core flood. The analyses of core floods A_3-A_7 have a similar result.

For injection of composition B_2 into pure C_{16} (Figs. 5.44-5.45) the core flood effluent composition route has a level of dispersion close to the simulated route with N_{Pe}=16. The composition profile also shows that shocks are much more spread out than the simulation with N_{Pe}=175, but the level of dispersion is still lower than N_{Pe}=16. As with core flood A_1, the numerical dispersion in the simulations does not reproduce the spreading of the shock fronts in the core flood.

5.4 CONCLUSIONS

Analytical, experimental and simulated composition routes and profiles were compared for a three-component system where three-phase partially miscible flow occurs. Simulated and analytical recoveries were compared for two different three-phase partially miscible ternary systems and the sensitivity of different composition routes and recoveries was studied. The convergence of simulated routes to MOC routes was demonstrated. The key conclusions are:

- Ten of the twelve MOC composition routes match the experimental effluent compositions well. The MOC composition routes were very sensitive to changes in boundary conditions near both A_3 and B_2 so that small errors in relative permeability parameters likely caused the difference in the composition routes.
- The MOC solutions capture core flood effluent profiles well. However for initial compositions A_3-A_8 the MOC theory predicted slower leading shocks than the experimental results showed. Conversely, for injection compositions B_1 B_3, and B_4 the MOC theory predicted slightly faster leading shocks than were experimentally observed. This may be caused by the assumption of no volume change on mixing, no dispersion, or errors in parameters in the MOC solution.

- Near transitional routes numerical dispersion may cause simulated routes to tend toward a route type different from the true MOC route, however as dispersion is minimized the simulated routes converge to MOC solutions.
- The MOC composition routes are the zero dispersion limits of the simulated displacements, indicating unique solutions have been found.
- When miscibility is possible oil recovery is most sensitive to dispersion near the MME (or MMP) in the ternary system in Chapter 3.
- In the ternary system in Chapter 4 type 2 routes are the most sensitive to dispersion when the NSH and MHE models apply. When the SH model applies type 2 routes and type 3 routes near 100% surfactant injection are the most sensitive to dispersion.
- The type of mass-balance equation affects the sensitivity of recoveries to dispersion. For most injection compositions the MHE conservation law contaminant recovery is the most sensitive to dispersion and the contaminant recovery from the SH conservation law is the least sensitive for the parameters studied.
- The sensitivity of composition routes and recoveries to numerical dispersion is dependent on the ternary system. Routes and recoveries in the water/decane/surfactant system from Chapter 4 were much more sensitive to dispersion than in the water/C_{16}/NBA system from Chapter 3.
- Numerical dispersion can be used to model the dispersion in the composition routes for core floods A_3-A_7. However, numerical dispersion

in simulated composition routes does not accurately represent the spreading of the shocks in core floods A_1 and B_2.

	Volume Fraction		
Experiment Initial Composition	H_2O	C_{16}	NBA
A_1^*	0.91	0.00	0.09
A_2	0.87	0.00	0.13
A_3	0.51	0.00	0.49
A_4	0.46	0.00	0.54
A_5	0.45	0.00	0.55
A_6	0.44	0.00	0.56
A_7	0.39	0.00	0.61
A_8	0.18	0.00	0.82

Table 5.1 Initial compositions for experiments A_1-A_8. All injection compositions are pure C_{16}. *In MOC and simulated solutions (0.9127, 0.0000, 0.0873) is used so that the displacement from A_1 does not enter the three-phase region.

	Volume Fraction		
Experiment Injection Composition	H_2O	C_{16}	NBA
B_1	0.91	0.00	0.09
B_2	0.51	0.00	0.49
B_3	0.40	0.00	0.60
B_4	0.18	0.00	0.82

Table 5.2 Injections compositions for experiments B_1-B_4. All initial compositions are pure C_{16}.

	C_1 Water	C_2 C_{16}	C_3 NBA
Density, ρ_i (g/cm^3)	0.997	0.772	0.807
Viscosity, μ_i (cp)	0.927	3.231	2.792
	S_1	S_2	S_3
S_{rj1}	*	0.05	0.05
S_{rj2}	0.10	*	0.00
S_{rj2}	0.10	0.00	*
k_{rj}	0.86	0.90	1.00
n_j	2.00	2.00	2.00

Table 5.3 Component densities and viscosities and relative permeability parameters of each phase (Cinar and Orr, 2004).

	Volume Fraction			Phase Saturations				
Label on Figures	H_2O	C_{16}	NBA	S_1	S_2	S_3	Dimensionless Velocity	Phases present
Initial Composition A_1								
J.C.	0.0000	1.0000	0.0000	0.0000	1.0000	0.0000	0.0000-0.0050	1
	0.1010	0.8990	0.0000	0.1006	0.8994	0.0000	0.0050(s)	2
	0.1582	0.8418	0.0000	0.1578	0.8422	0.0000	0.5738-1.0574(i)	2
	0.1937	0.6827	0.1237	0.2064	0.7936	0.0000	1.0574(s)	2
	0.2042	0.6727	0.1231	0.2180	0.7820	0.0000	1.1957	2
A_1	0.9128	0.0000	0.0872	1.0000	0.0000	0.0000	1.1957	1
Initial Composition A_2								
J.C.	0.0000	1.0000	0.0000	0.0000	1.0000	0.0000	0.000-0.0050	1
	0.1010	0.8990	0.0000	0.8994	0.1006	0.0000	0.0050(s)	2
	0.1423	0.8577	0.0000	0.8581	0.1419	0.0000	0.3978-0.8132	2
	0.1729	0.6563	0.1708	0.1750	0.7474	0.0775	0.8132(s)	3
	0.2035	0.6267	0.1697	0.2087	0.7130	0.0783	1.2718	3
A_2	0.8700	0.0000	0.1300	0.9419	0.0000	0.0580	1.2718	2

Table 5.4 Composition routes and velocities for the composition routes for pure C_{16} injection into initial compositions A_1 and A_2. (s) denotes the start of a spreading wave, (i) denotes the start of an indifferent wave.

	Volume Fraction			Phase Saturations				
Label on Figures	H_2O	C_{16}	NBA	S_1	S_2	S_3	Dimensionless Velocity	Phases present
Initial Composition A_3								
J.C.	0.0000	1.0000	0.0000	0.0000	1.0000	0.0000	0.0000-0.0050	1
	0.1010	0.8990	0.0000	0.1006	0.8994	0.0000	0.0050(s)	2
	0.1349	0.8651	0.0000	0.1345	0.8655	0.0000	0.3206-0.7566	2
	0.1636	0.6262	0.2102	0.1575	0.6995	0.1430	0.7566(s)	3
	0.1925	0.5604	0.2471	0.1824	0.6101	0.2075	1.3301	3
	0.4372	0.0000	0.5628	0.3552	0.0000	0.6448	1.3301-2.2349(s)	2
	0.4772	0.0000	0.5228	0.4094	0.0000	0.5906	2.4532	2
A_3	0.5100	0.0000	0.4900	0.4539	0.0000	0.5461	2.4532	2
Initial Composition A_4								
J.C.	0.0000	1.0000	0.0000	0.0000	1.0000	0.0000	0.0000-0.0050	1
	0.1010	0.8990	0.0000	0.1006	0.8994	0.0000	0.0050(s)	2
	0.1349	0.8651	0.0000	0.1345	0.8655	0.0000	0.3206-0.7566	2
	0.1636	0.6262	0.2102	0.1575	0.6995	0.1430	0.7566(s)	3
	0.1925	0.5604	0.2471	0.1824	0.6101	0.2075	1.3301	3
	0.4372	0.0000	0.5628	0.3552	0.0000	0.6448	1.3301-2.2349(s)	2
A_4	0.4600	0.0000	0.5400	0.3861	0.0000	0.6139	2.3925	2

Table 5.5 Composition routes and velocities for the composition routes for pure C_{16} injection into initial compositions A_3 and A_4. (s) denotes the start of a spreading wave, (i) denotes the start of an indifferent wave.

Label on Figures	H_2O	C_{16}	NBA	S_1	S_2	S_3	Dimensionless Velocity	Phases present
Initial Composition A_5								
J.C.	0.0000	1.0000	0.0000	0.0000	1.0000	0.0000	0.0000-0.0050	1
	0.1010	0.8990	0.0000	0.1006	0.8994	0.0000	0.0050(s)	2
	0.1349	0.8651	0.0000	0.1345	0.8655	0.0000	0.3206-0.7566	2
	0.1636	0.6262	0.2102	0.1575	0.6995	0.1430	0.7566(s)	3
	0.1925	0.5604	0.2471	0.1824	0.6101	0.2075	1.3301	3
	0.4372	0.0000	0.5628	0.3552	0.0000	0.6448	1.3301-2.2349(s)	2
A_5	0.4500	0.0000	0.5500	0.3725	0.0000	0.6275	2.3337	2
Initial Composition A_6								
J.C.	0.0000	1.0000	0.0000	0.0000	1.0000	0.0000	0.0000-0.0050	1
	0.1010	0.8990	0.0000	0.1006	0.8994	0.0000	0.0050(s)	2
	0.1349	0.8651	0.0000	0.1345	0.8655	0.0000	0.3206-0.7566	2
	0.1636	0.6262	0.2102	0.1575	0.6995	0.1430	0.7566(s)	3
	0.1925	0.5604	0.2471	0.1824	0.6101	0.2075	1.3301	3
	0.4372	0.0000	0.5628	0.3552	0.0000	0.6448	1.3301-2.2349(s)	2
A_6	0.4400	0.0000	0.5600	0.3589	0.0000	0.6411	2.2585	2

Table 5.6 Composition routes and velocities for the composition routes for pure C_{16} injection into initial compositions A_5 and A_6. (s) denotes the start of a spreading wave, (i) denotes the start of an indifferent wave.

Label on Figures	H_2O	C_{16}	NBA	S_1	S_2	S_3	Dimensionless Velocity	Phases present
Initial Composition A_7								
J.C.	0.0000	1.0000	0.0000	0.0000	1.0000	0.0000	0.0000-0.0050	1
	0.1010	0.8990	0.0000	0.1006	0.8994	0.0000	0.0050(s)	2
	0.1349	0.8651	0.0000	0.1345	0.8655	0.0000	0.3206-0.7566	2
	0.1636	0.6262	0.2102	0.1575	0.6995	0.1430	0.7566(s)	3
	0.1925	0.5604	0.2471	0.1824	0.6101	0.2075	1.3301	3
	0.4372	0.0000	0.5628	0.3552	0.0000	0.6448	1.3301-2.0231(s)	2
A_7	0.3900	0.0000	0.6100	0.2911	0.0000	0.7089	2.0231	2
Initial Composition A_8								
J.C.	0.0000	1.0000	0.0000	0.0000	1.0000	0.0000	0.0000-0.0343	1
	0.0146	0.9854	0.0000	0.0141	0.9859	0.0000	0.03423-0.6870	2
	0.0314	0.7284	0.2403	0.0073	0.1823	0.8104	0.6870(s)	3
	0.0393	0.6734	0.2873	0.0073	0.2621	0.7306	1.1476	3
A_8	0.1753	0.0000	0.8247	0.0000	0.0000	1.0000	1.1476	2

Table 5.7 Composition routes and velocities for the composition routes for pure C_{16} injection into initial compositions A_7 and A_8. (s) denotes the start of a spreading wave, (i) denotes the start of an indifferent wave.

Label on Figures	H_2O	C_{16}	NBA	S_1	S_2	S_3	Dimensionless Velocity	Phases present
Injection Composition B_1								
B_1	0.9128	0.0000	0.0872	1.0000	0.0000	0.0000	0.0000(s)	1-2
	0.6015	0.2956	0.1030	0.6564	0.3436	0.0000	0.8888(i)	2
	0.5370	0.4630	0.0000	0.5368	0.4632	0.0000	0.8888-1.4340	2
I.C.	0.0000	1.0000	0.0000	0.0000	1.0000	0.0000	1.4340	1
Injection Composition B_2								
B_2	0.5100	0.0000	0.4900	0.4539	0.0000	0.5461	0.0000-0.5521	2
	0.4115	0.1936	0.3949	0.3946	0.1304	0.4750	0.5521(s)	3
	0.3876	0.2449	0.3675	0.3736	0.1997	0.4268	1.0003	3
	0.4179	0.5821	0.0000	0.4177	0.5823	0.0000	1.0003-1.2354	2
I.C.	0.0000	1.0000	0.0000	0.0000	1.0000	0.0000	1.2354	1

Table 5.8 Composition routes and velocities for the composition routes for injection of compositions B_1 and B_2 into C_{16} saturated cores. (s) denotes the start of a spreading wave, (i) denotes the start of an indifferent wave.

Label on Figures	H_2O	C_{16}	NBA	S_1	S_2	S_3	Dimensionless Velocity	Phases present
Injection Composition B_3								
B_3	0.4000	0.0000	0.6000	0.3047	0.0000	0.6953	0.0000-0.6470	2
	0.1989	0.0000	0.8011	0.0320	0.0000	0.9680	0.6470-0.6727	2
	0.0873	0.3155	0.5972	0.0026	0.2098	0.7876	0.6727(s)	3
	0.0780	0.3801	0.5419	0.0026	0.3036	0.6938	1.1753	3
I.C.	0.0000	1.0000	0.0000	0.0000	1.0000	0.0000	1.1753	1
Injection Composition B_4								
B_4	0.1753	0.0000	0.8247	0.0000	0.0000	1.0000	0.0000	1
	0.1989	0.0000	0.8011	0.0320	0.0000	0.9680	0.0000-0.6727	2
	0.0873	0.3155	0.5972	0.0026	0.2098	0.7876	0.6727(s)	3
	0.0780	0.3801	0.5419	0.0026	0.3036	0.6938	1.1753	3
I.C.	0.0000	1.0000	0.0000	0.0000	1.0000	0.0000	1.1753	1

Table 5.9 Composition routes and velocities for the composition routes for injection of compositions B_3 and B_4 into C_{16} saturated cores. (s) denotes the start of a spreading wave, (i) denotes the start of an indifferent wave.

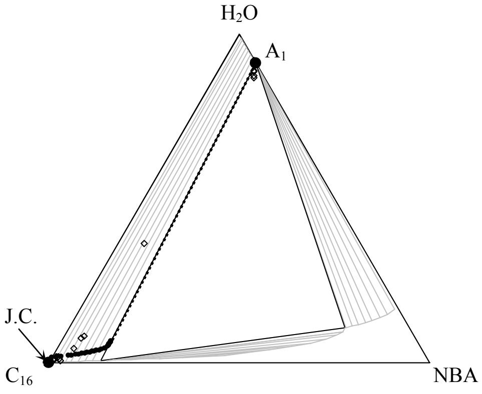

Figure 5.1 Effluent composition paths from MOC and core flood experiments for initial composition A_1 and pure C_{16} injection (J.C.). Spreading waves in the MOC solution are solid lines and shocks are dotted lines. Core flood effluents are diamonds.

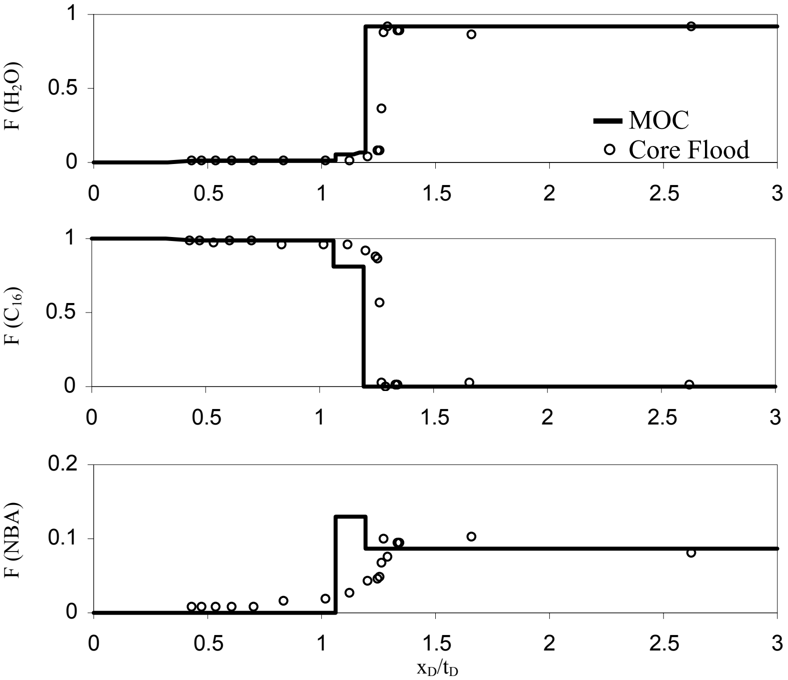

Figure 5.2 Comparison of MOC and core flood effluent profiles for pure C_{16} injection into initial composition A_1.

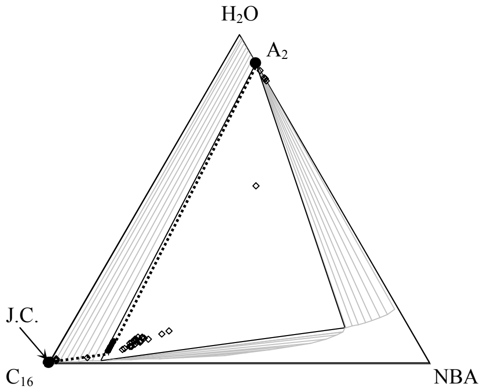

Figure 5.3 Effluent composition paths from MOC and core flood experiments for initial composition A_2 and pure C_{16} injection (J.C.). Spreading waves in the MOC solution are solid lines and shocks are dotted lines. Core flood effluents are diamonds.

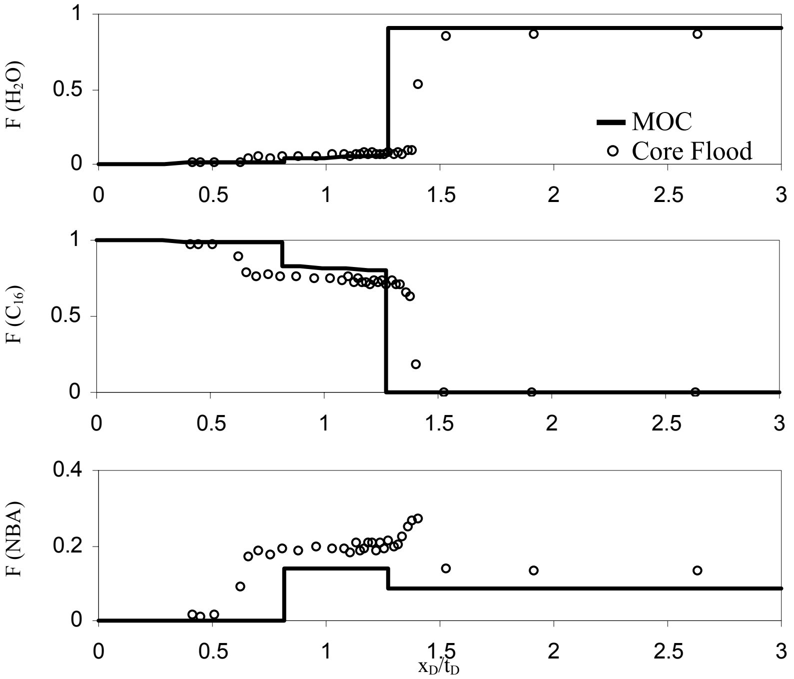

Figure 5.4 Comparison of MOC and core flood effluent profiles for pure C_{16} injection into initial composition A_2.

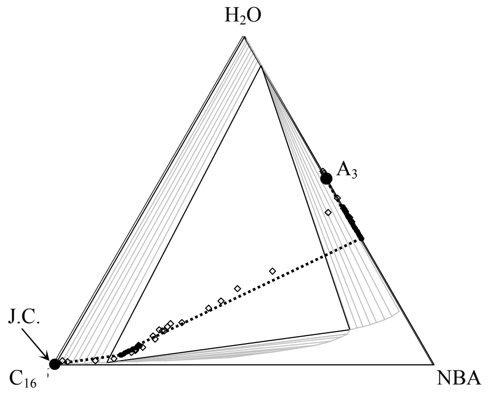

Figure 5.5 Effluent composition paths from MOC and core flood experiments for initial composition A_3 and pure C_{16} injection (J.C.). Spreading waves in the MOC solution are solid lines and shocks are dotted lines. Core flood effluents are diamonds.

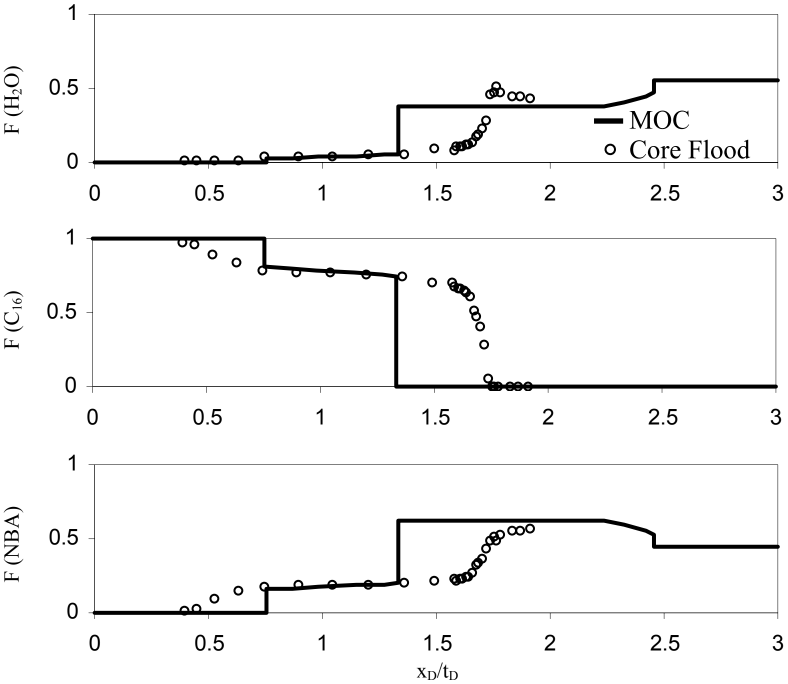

Figure 5.6 Comparison of MOC and core flood effluent profiles for pure C_{16} injection into initial composition A_3.

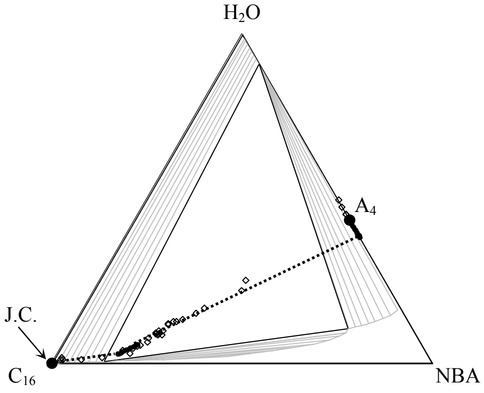

Figure 5.7 Effluent composition paths from MOC and core flood experiments for initial composition A_4 and pure C_{16} injection (J.C.). Spreading waves in the MOC solution are solid lines and shocks are dotted lines. Core flood effluents are diamonds.

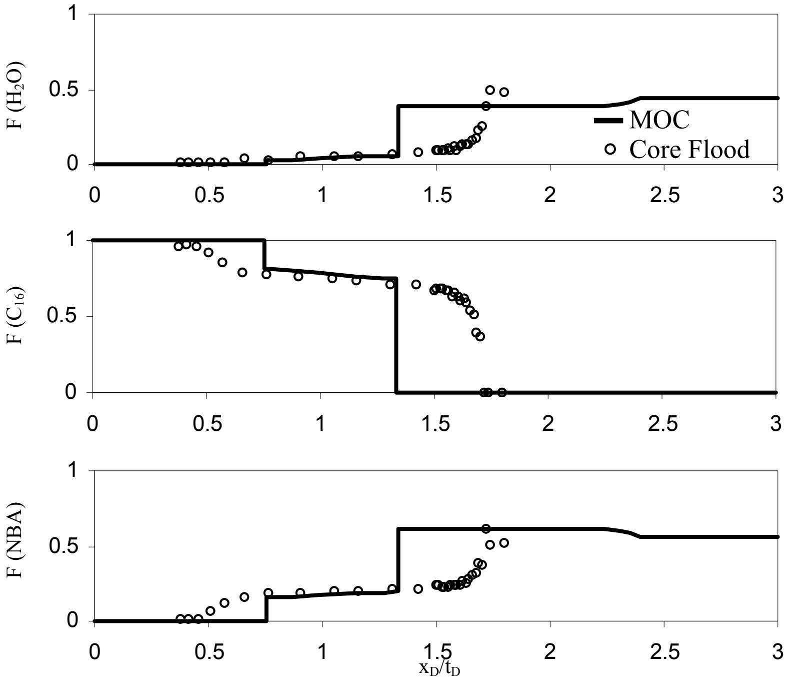

Figure 5.8 Comparison of MOC and core flood effluent profiles for pure C_{16} injection into initial composition A_4.

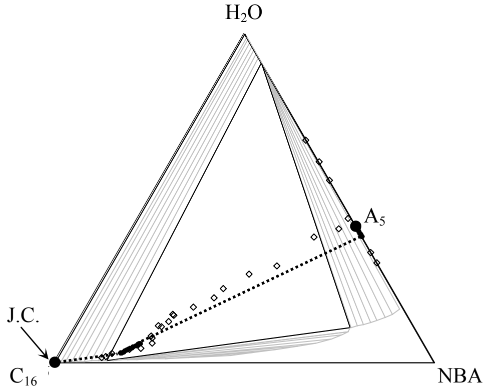

Figure 5.9 Effluent composition paths from MOC and core flood experiments for initial composition A_5 and pure C_{16} injection (J.C.). Spreading waves in the MOC solution are solid lines and shocks are dotted lines. Core flood effluents are diamonds.

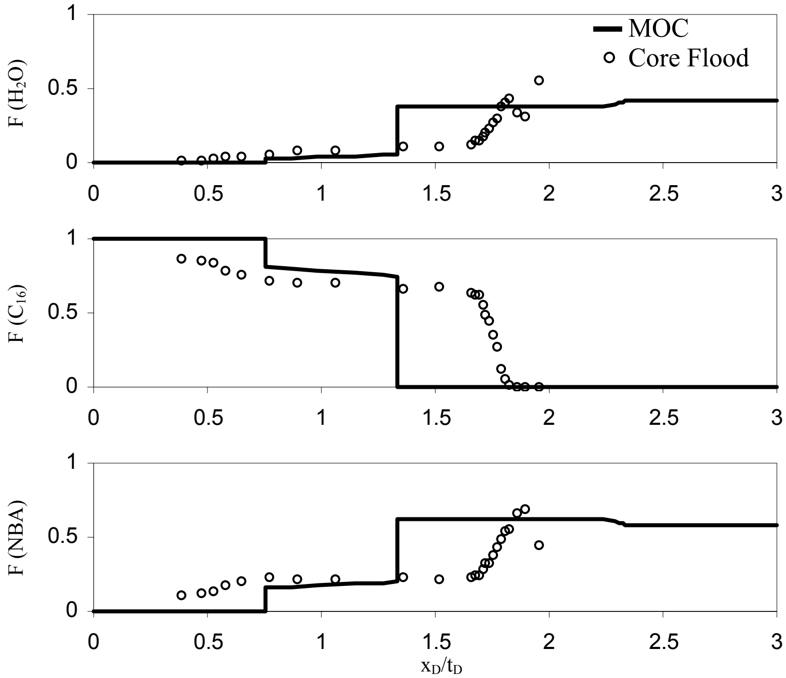

Figure 5.10 Comparison of MOC and core flood effluent profiles for pure C_{16} injection into initial composition A_5.

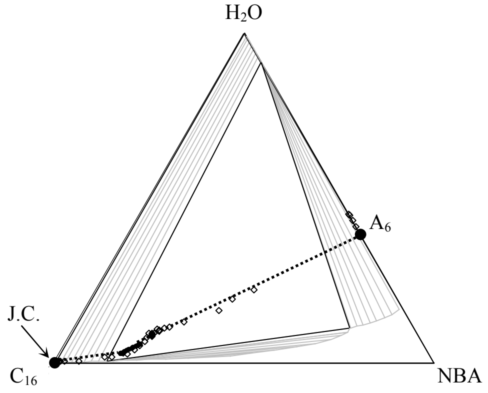

Figure 5.11 Effluent composition paths from MOC and core flood experiments for initial composition A_6 and pure C_{16} injection (J.C.). Spreading waves in the MOC solution are solid lines and shocks are dotted lines. Core flood effluents are diamonds.

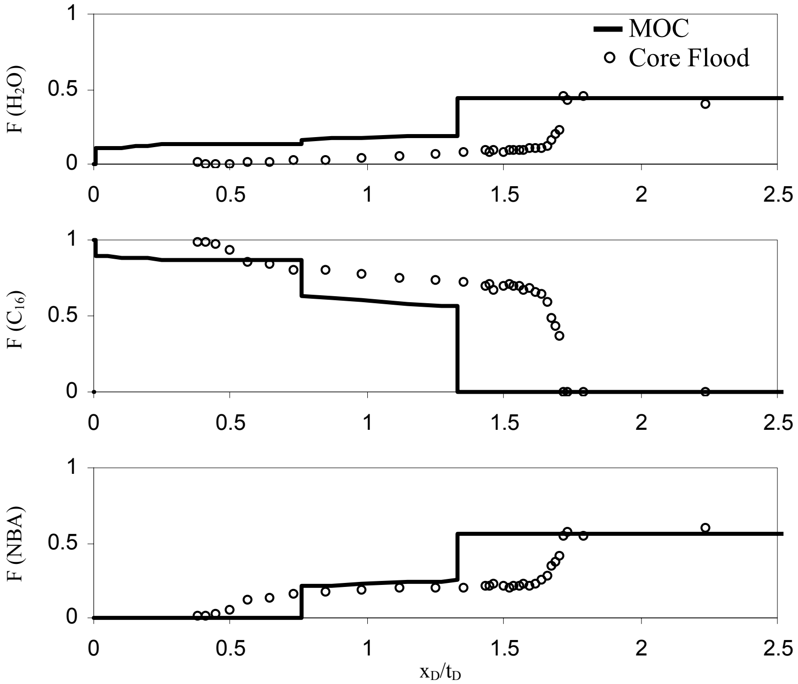

Figure 5.12 Comparison of MOC and core flood effluent profiles for pure C_{16} injection into initial composition A_6.

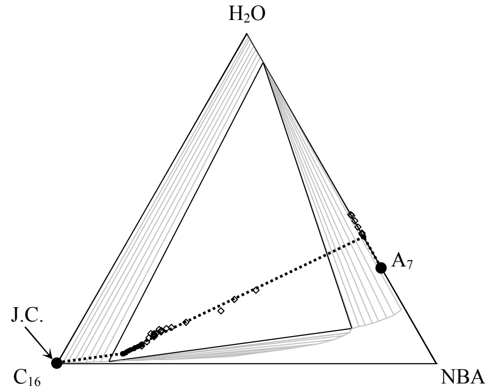

Figure 5.13 Effluent composition paths from MOC and core flood experiments for initial composition A_7 and pure C_{16} injection (J.C.). Spreading waves in the MOC solution are solid lines and shocks are dotted lines. Core flood effluents are diamonds.

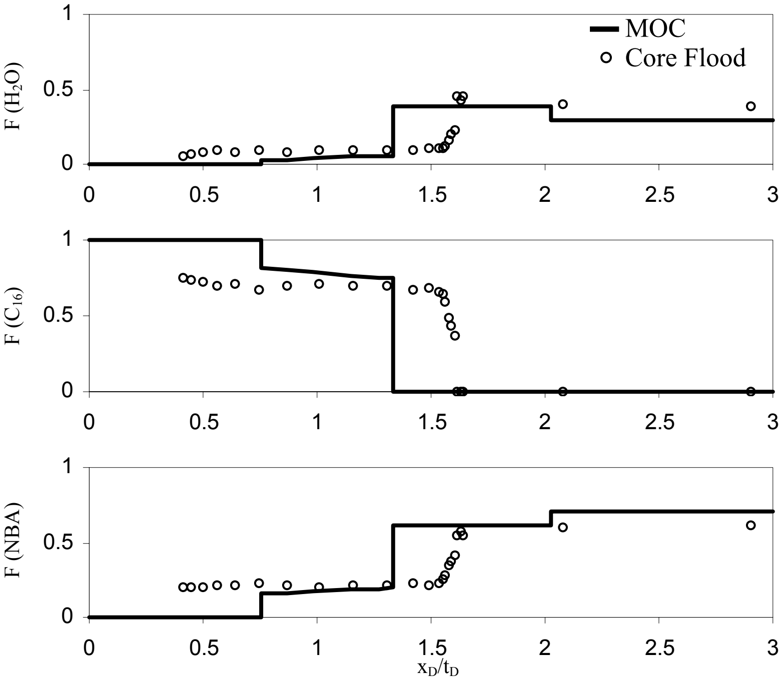

Figure 5.14 Comparison of MOC and core flood effluent profiles for pure C_{16} injection into initial composition A_7.

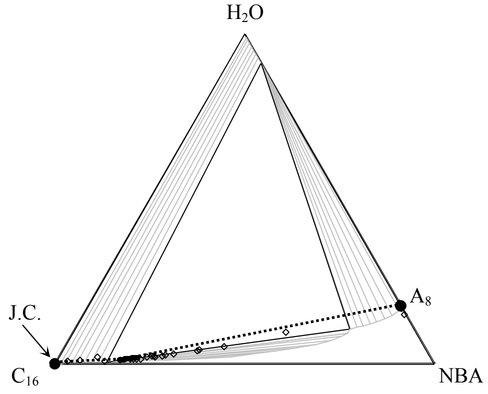

Figure 5.15 Effluent composition paths from MOC and core flood experiments for initial composition A_8 and pure C_{16} injection (J.C.). Spreading waves in the MOC solution are solid lines and shocks are dotted lines. Core flood effluents are diamonds.

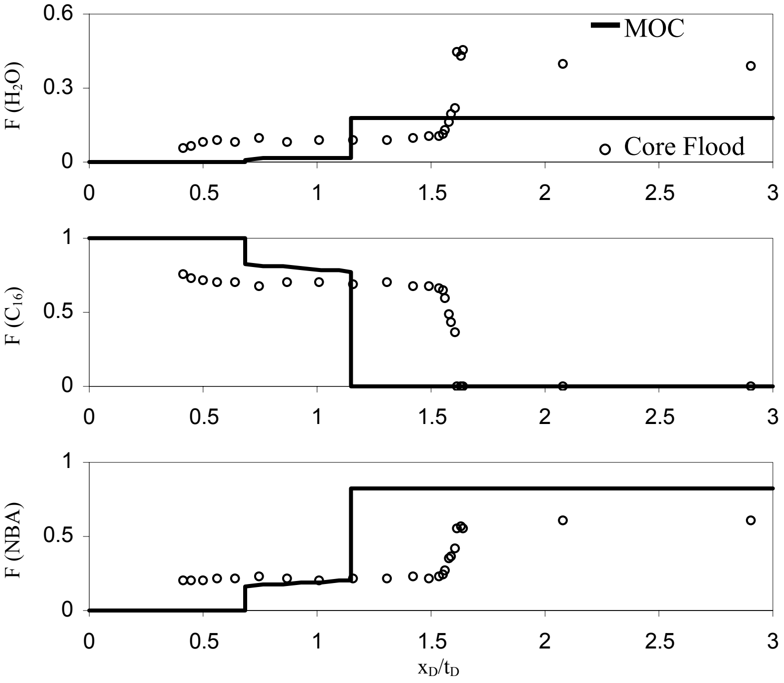

Figure 5.16 Comparison of MOC and core flood effluent profiles for pure C_{16} injection into initial composition A_8.

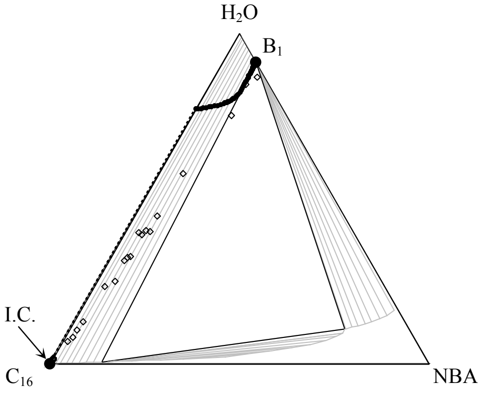

Figure 5.17 Effluent composition paths from MOC and core flood experiments for a pure C_{16} initial composition (I.C.) and injection composition B_1. Spreading waves in the MOC solution are solid lines and shocks are dotted lines. Core flood effluents are diamonds.

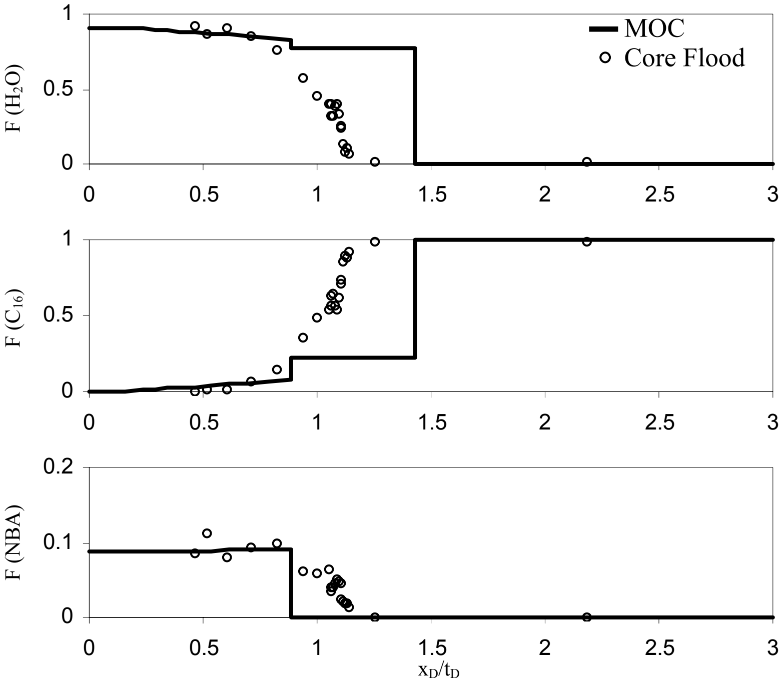

Figure 5.18 Comparison of MOC and core flood effluent profiles for injection of composition B_1 into a pure C_{16} initial composition.

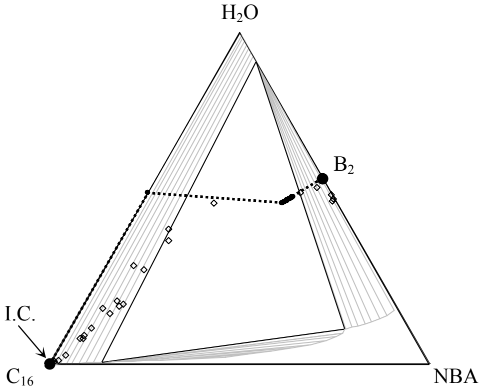

Figure 5.19 Effluent composition paths from MOC and core flood experiments for a pure C_{16} initial composition (I.C.) and injection composition B_2. Spreading waves in the MOC solution are solid lines and shocks are dotted lines. Core flood effluents are diamonds.

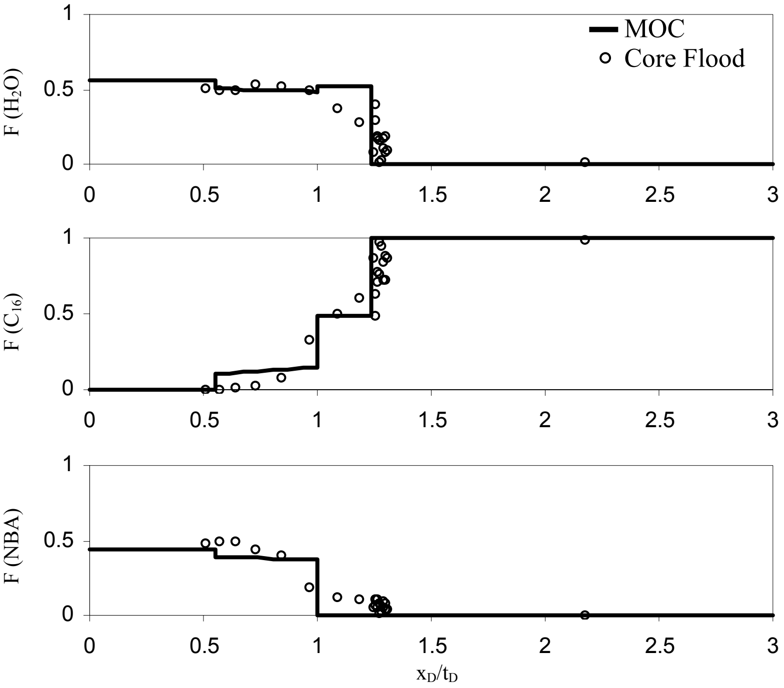

Figure 5.20 Comparison of MOC and core flood effluent profiles for injection of composition B_2 into a pure C_{16} initial composition.

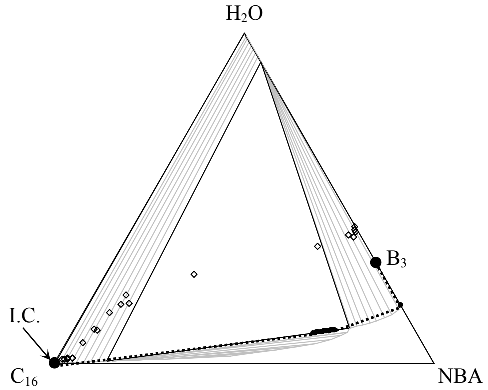

Figure 5.21 Effluent composition paths from MOC and core flood experiments for a pure C_{16} initial composition (I.C.) and injection composition B_3. Spreading waves in the MOC solution are solid lines and shocks are dotted lines. Core flood effluents are diamonds.

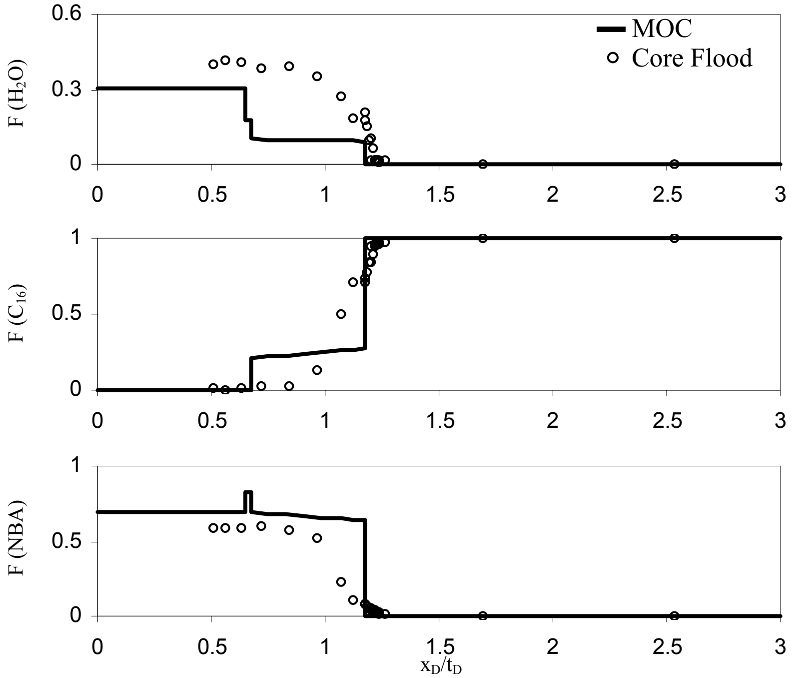

Figure 5.22 Comparison of MOC and core flood effluent profiles for injection of composition B_3 into a pure C_{16} initial composition.

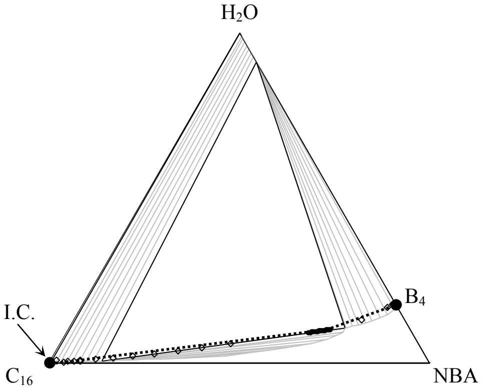

Figure 5.23 Effluent composition paths from MOC and core flood experiments for a pure C_{16} initial composition (I.C.) and injection composition B_4. Spreading waves in the MOC solution are solid lines and shocks are dotted lines. Core flood effluents are diamonds.

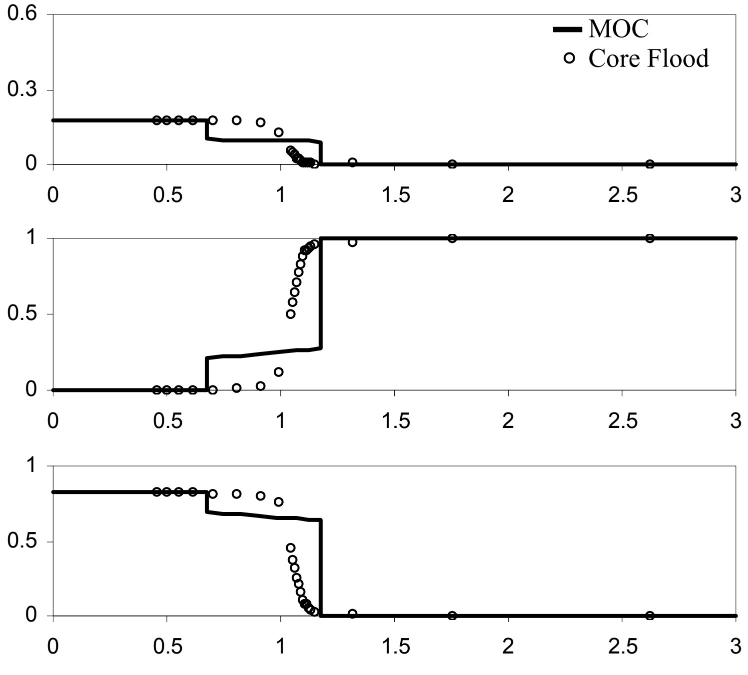

Figure 5.24 Comparison of MOC and core flood effluent profiles for injection of composition B_4 into a pure C_{16} initial composition.

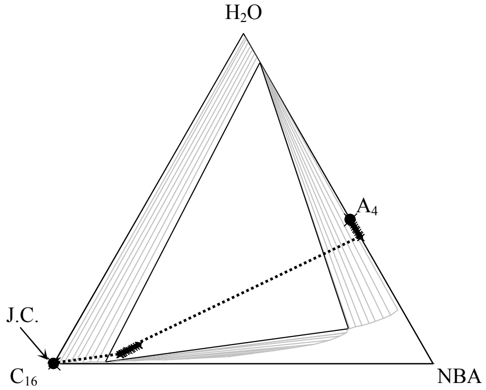

Figure 5.25 Effluent composition paths from MOC solutions with and without gravity for initial composition A_4 and pure C_{16} injection (J.C.). Shocks are dotted lines. Solutions neglecting gravity are solid circles, solutions including gravity are denoted by Xs.

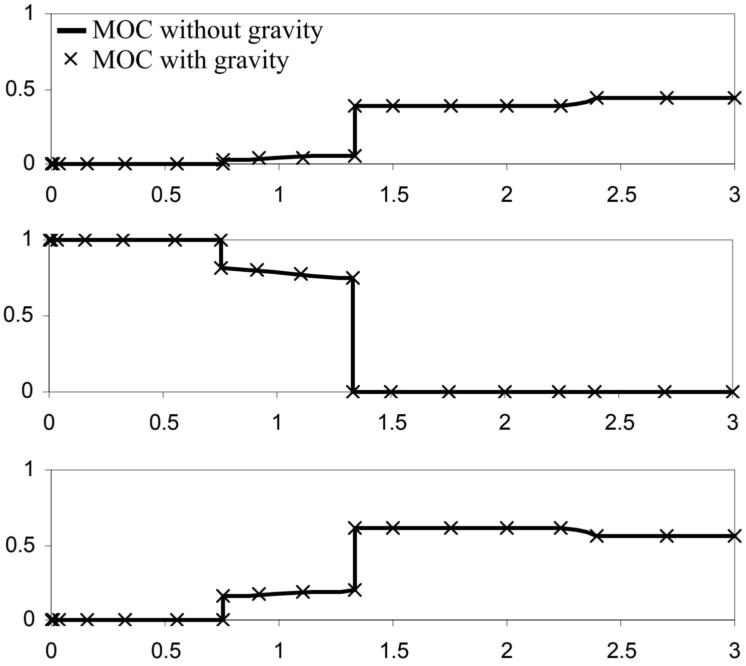

Figure 5.26 Comparison of MOC effluent profiles with and without gravity for pure C_{16} injection into initial composition A_4.

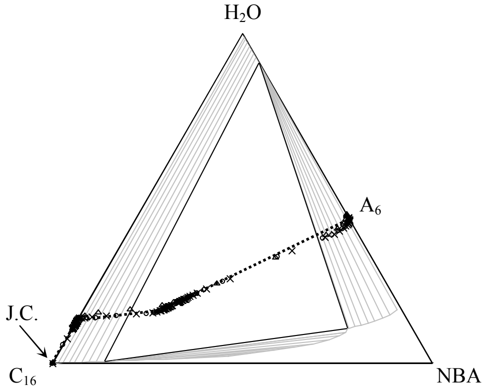

Figure 5.27 Composition paths from MOC and simulations for initial composition A_6 and pure C_{16} injection (J.C.). Spreading waves in the MOC solution are solid lines and shocks are dotted lines. The simulations shown are N_{Pe}= 1600 (denoted by o), N_{Pe}= 175 (denoted by x), and N_{Pe}= 16 (denoted by triangles).

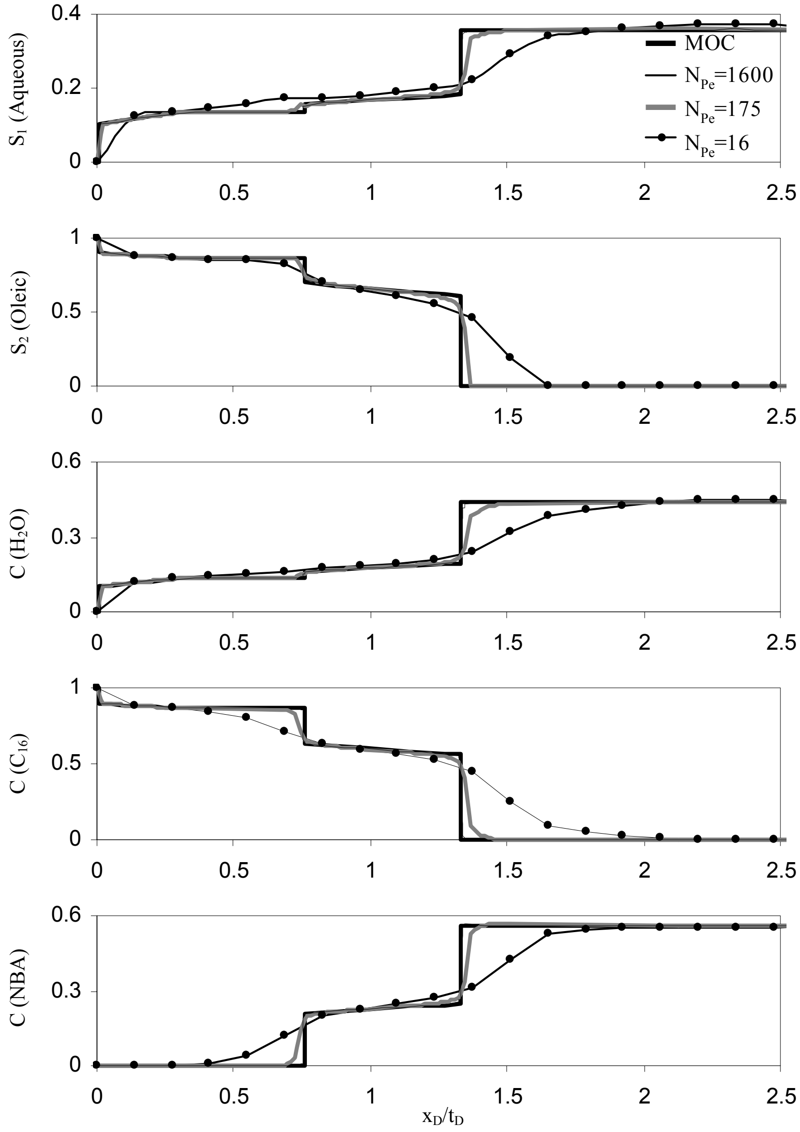

Figure 5.28 MOC and simulated profiles for initial composition A_6 and pure C_{16} injection.

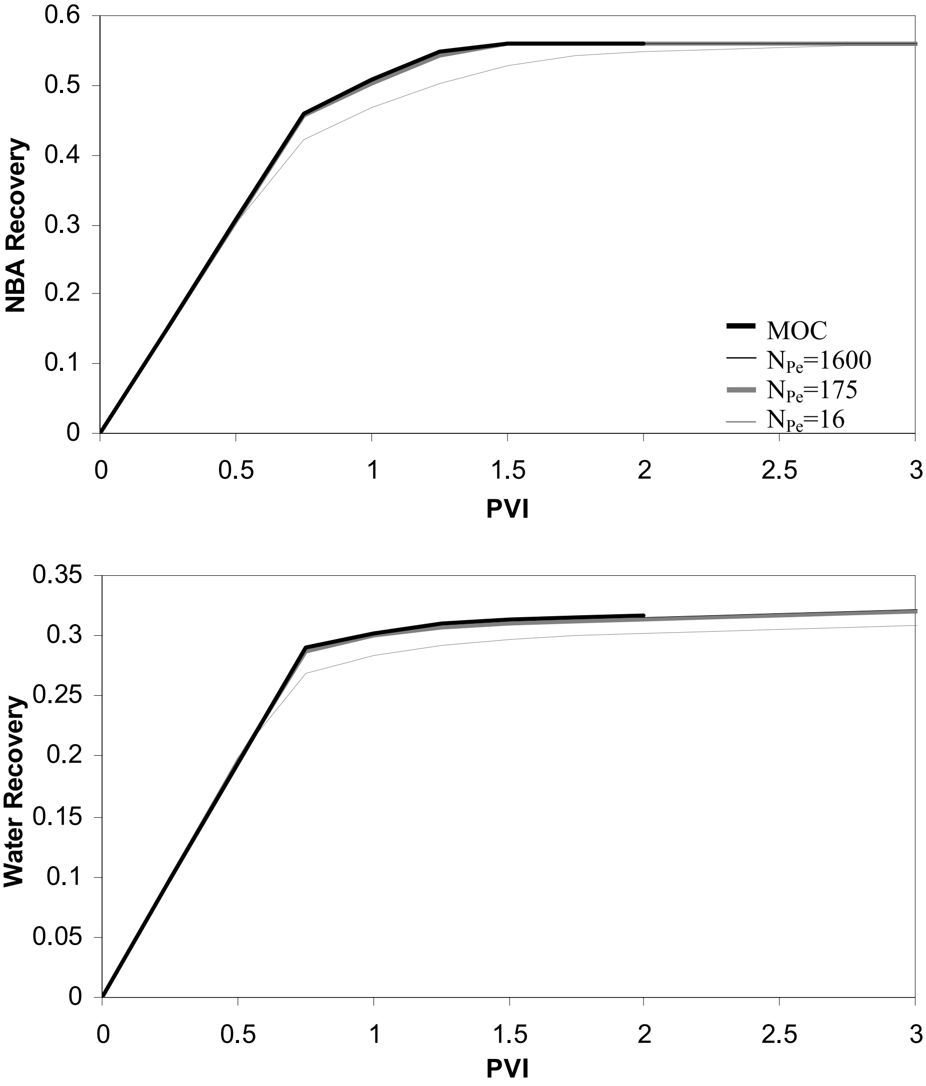

Figure 5.29 Recovery curves in volume fraction for NBA (top) and water (bottom) for initial composition A_6 and pure C_{16} injection.

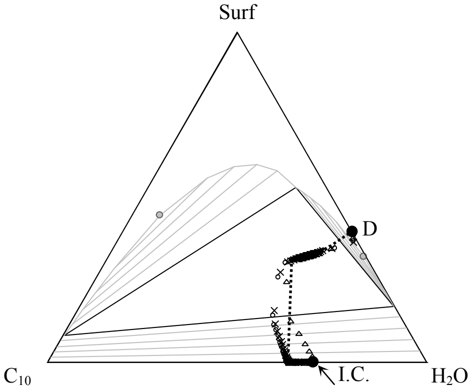

Figure 5.30 Comparison of MOC and simulated composition for the ternary system from Chapter 4 and the NSH conservation law. Injection composition D and an initial composition of 70% water and 30% decane are used. Spreading waves in the MOC solution are solid lines and shocks are dotted lines. The simulations shown are N_{Pe}= 18,000 (denoted by o), N_{Pe}= 175 (denoted by x), and N_{Pe}= 16 (denoted by triangles).

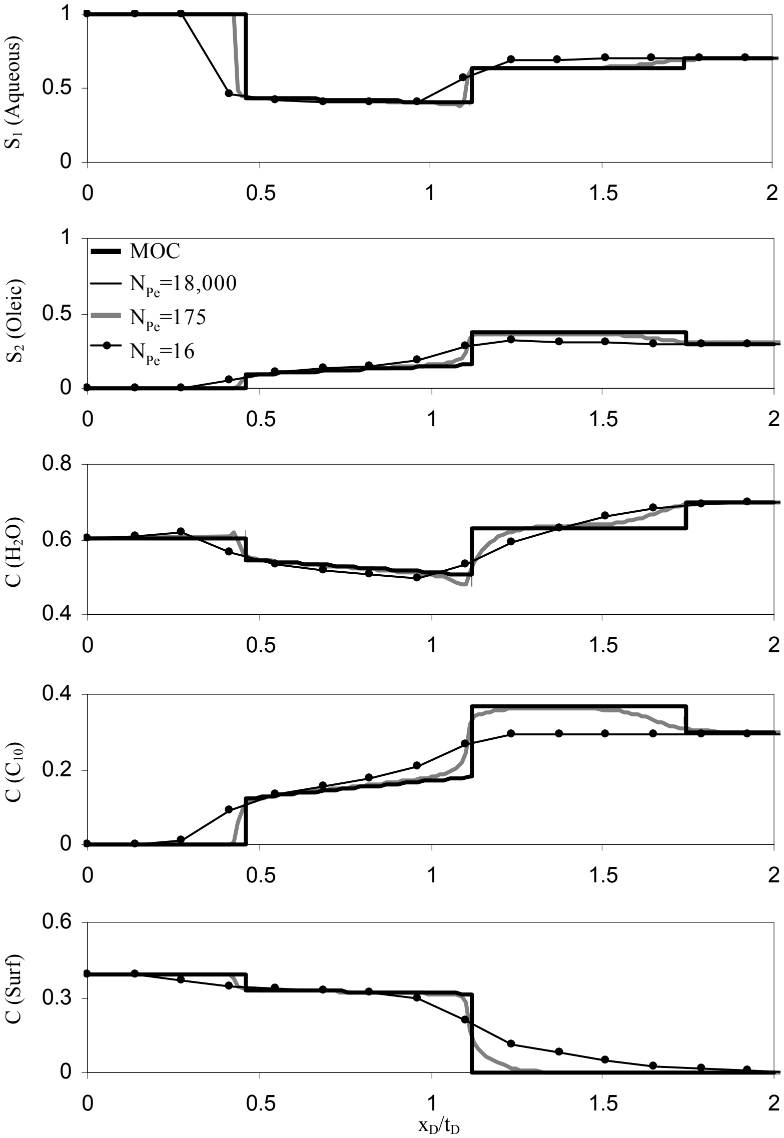

Figure 5.31 MOC and simulated profiles for the ternary system from Chapter 4 and the NSH conservation law. Injection composition D and an initial composition of 70% water and 30% decane are used.

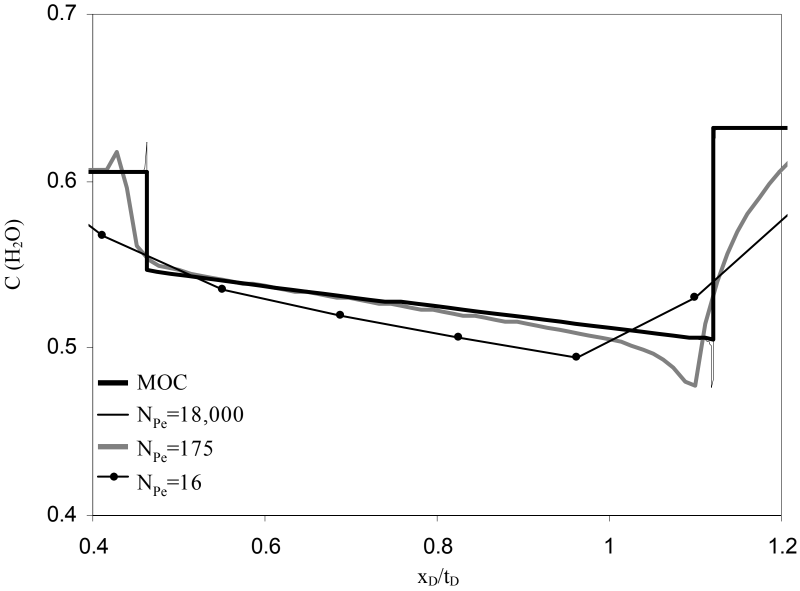

Figure 5.32 Detail of MOC and simulated water profiles for the ternary system from Chapter 4 and the NSH conservation law. Injection composition D and an initial composition of 70% water and 30% decane are used.

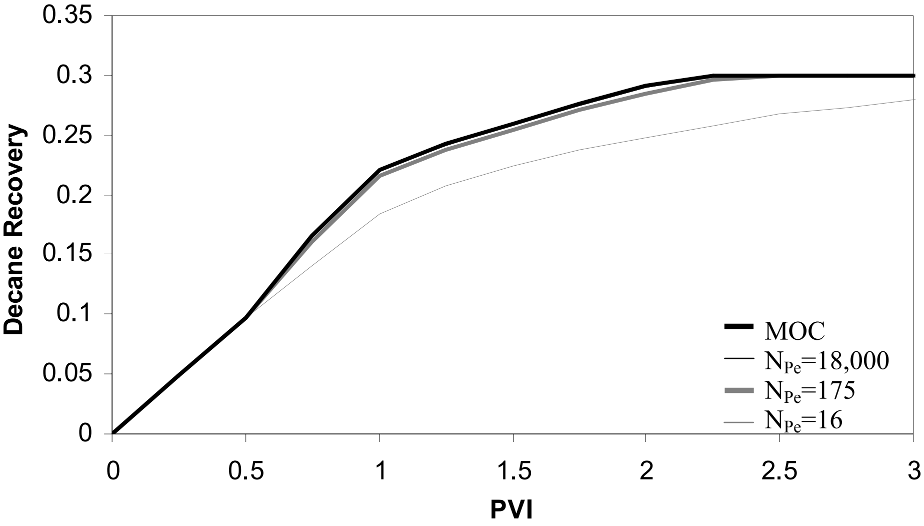

Figure 5.33 Recovery curves of decane in volume fractions for the ternary system from Chapter 4 and the NSH conservation law. Injection composition D and an initial composition of 70% water and 30% decane are used.

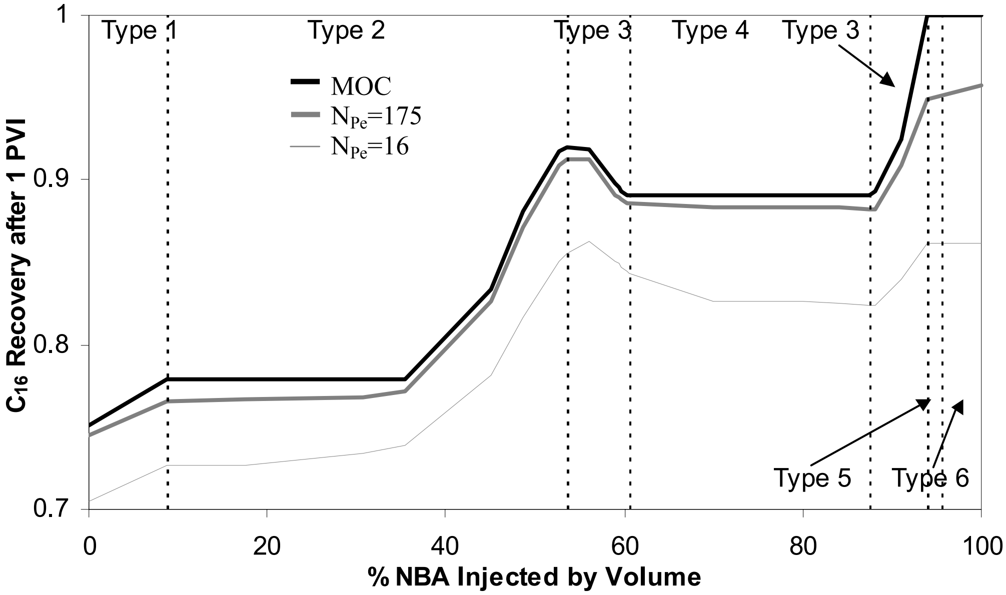

Figure 5.34 Cumulative C_{16} recovery after 1 PVI as a function of percent NBA injected by volume for the ternary system and parameters in Chapter 3. Changes in route types are denoted by dotted lines.

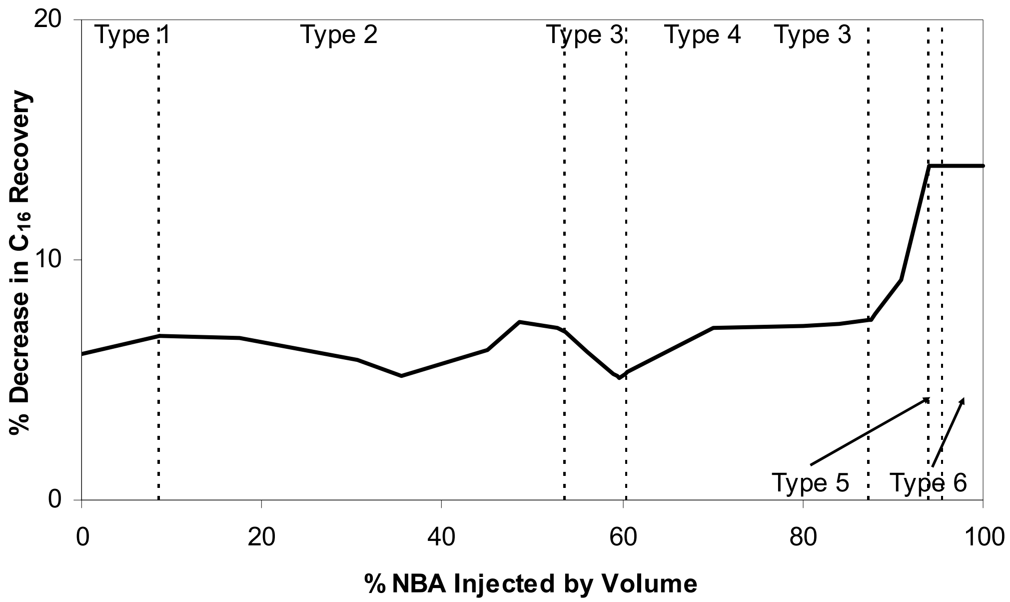

Figure 5.35 Change in C_{16} recovery as a function of percent NBA injected by volume for simulations with N_{Pe}=16 and the ternary system and parameters in Chapter 3. Changes in route types are denoted by dotted lines.

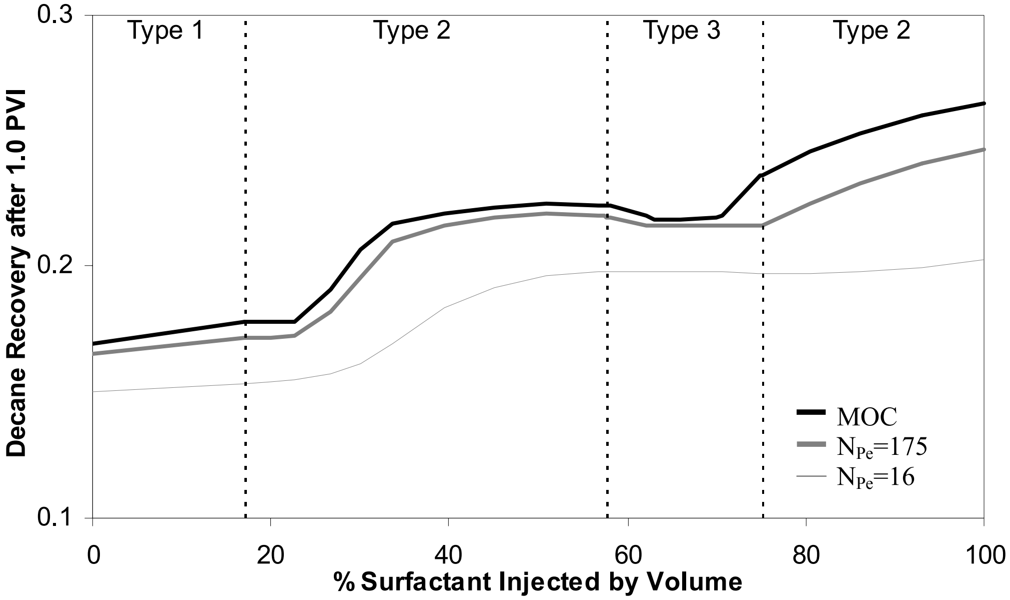

Figure 5.36 Cumulative decane recovery after 1 PVI as a function of percent surfactant injected by volume for the ternary system and NSH model parameters in Chapter 4. Changes in route types are denoted by dotted lines.

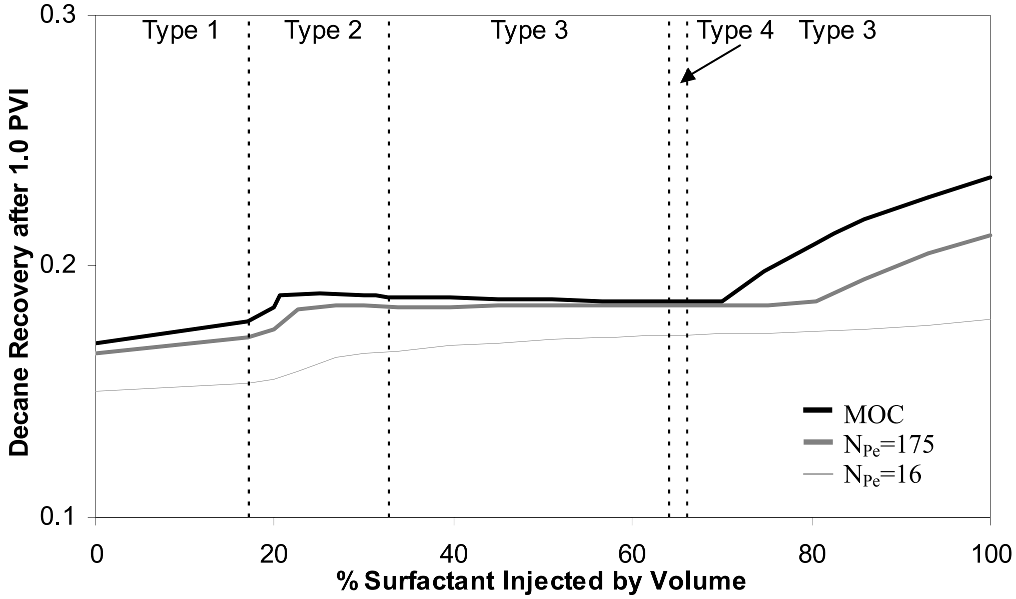

Figure 5.37 Cumulative decane recovery after 1 PVI as a function of percent surfactant injected by volume for the ternary system and SH model parameters in Chapter 4. Changes in route types are denoted by dotted lines.

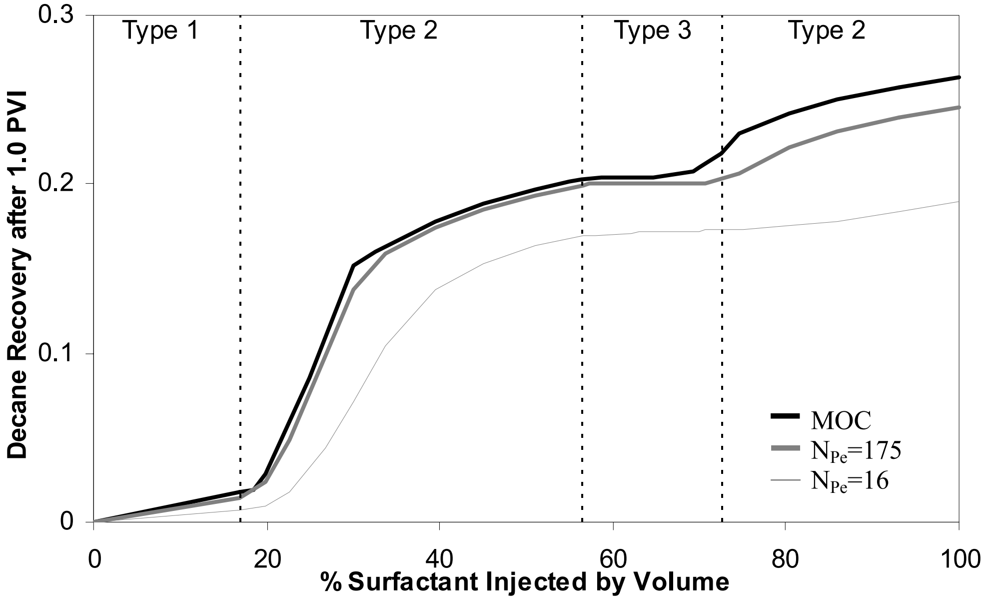

Figure 5.38 Cumulative decane recovery after 1 PVI as a function of percent surfactant injected by volume for the ternary system and MHE model parameters in Chapter 4. Changes in route types are denoted by dotted lines.

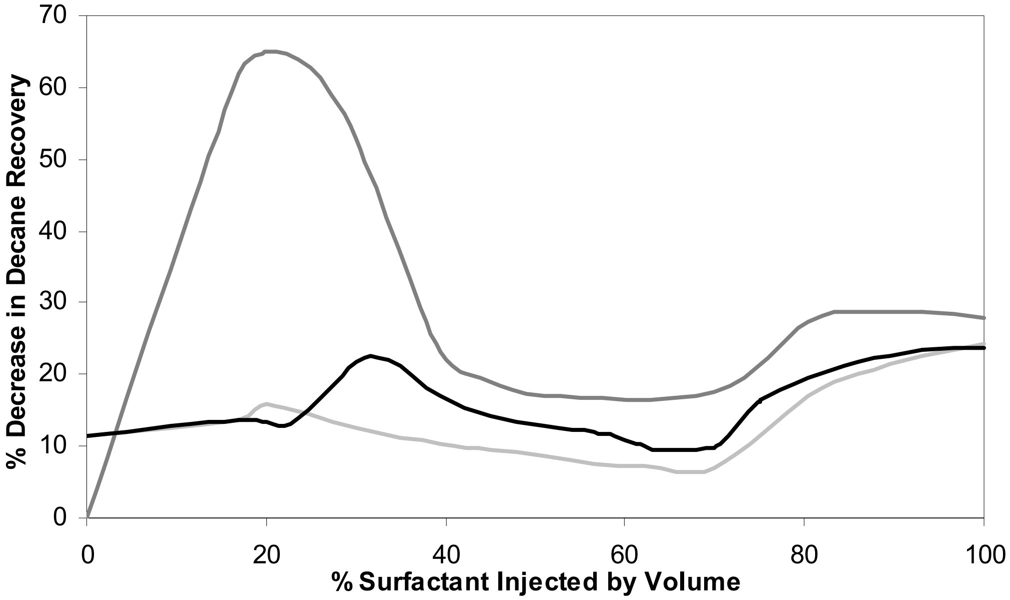

Figure 5.39 Change in decane recovery as a function of percent surfactant injected by volume for simulations with N_{Pe}=16 and the ternary system and parameters in Chapter 4 for all three relative permeability models considered.

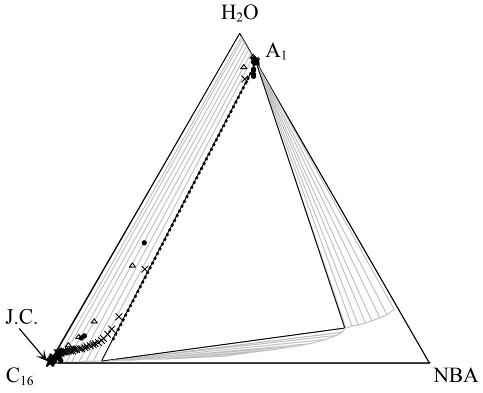

Figure 5.40 Effluent composition paths from core floods and simulations for initial composition A_1 and pure C_{16} injection (J.C.). Core flood effluents are solid circles, simulations shown are N_{Pe}= 175 (denoted by x), and N_{Pe}= 16 (denoted by triangles).

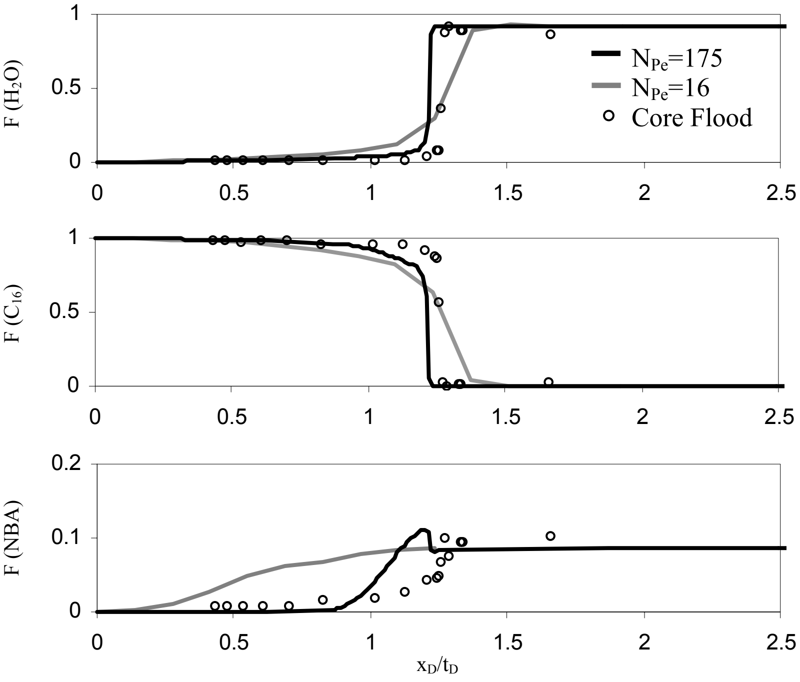

Figure 5.41 Effluent composition profiles from core floods and simulations for initial composition A_1 and pure C_{16} injection.

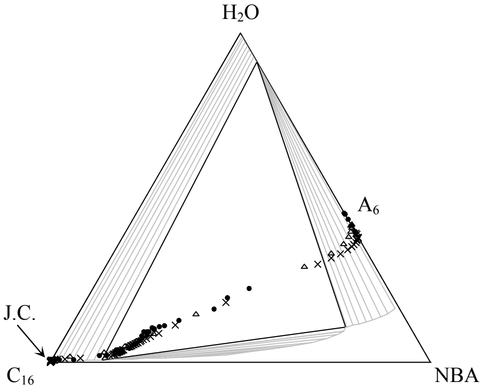

Figure 5.42 Effluent composition paths from core floods and simulations for initial composition A_6 and pure C_{16} injection (J.C.). Core flood effluents are solid circles, simulations shown are N_{Pe}= 175 (denoted by x), and N_{Pe}= 16 (denoted by triangles).

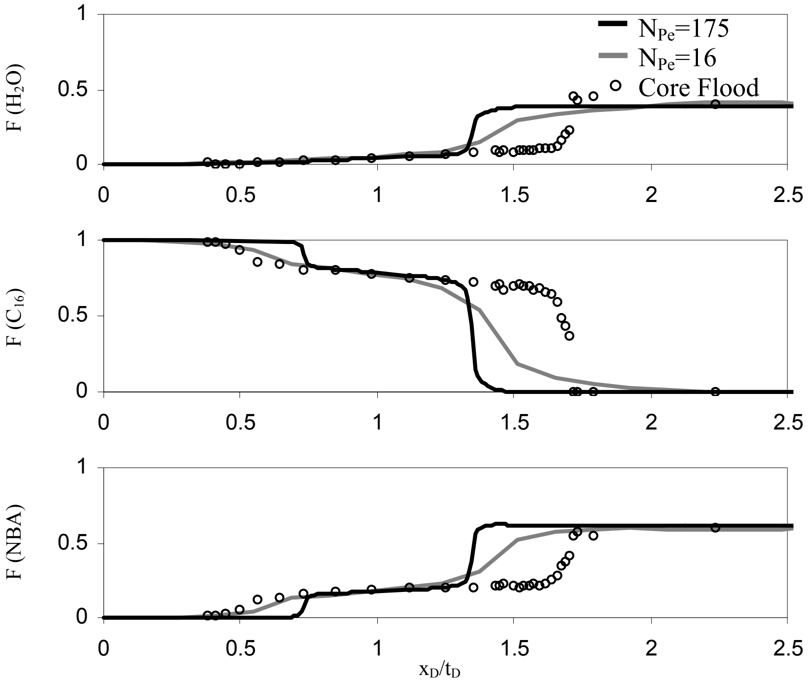

Figure 5.43 Core flood and simulated effluent profiles for initial composition A_6 and pure C_{16} injection.

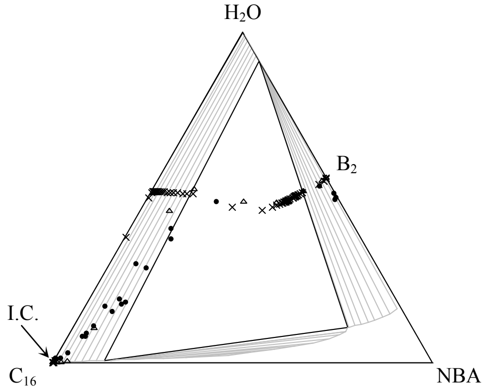

Figure 5.44 Effluent composition paths for core floods and simulations for injection of composition B_2 into a C_{16} saturated core (I.C.). Core flood effluents are solid circles, simulations shown are N_{Pe}= 175 (denoted by x), and N_{Pe}= 16 (denoted by triangles).

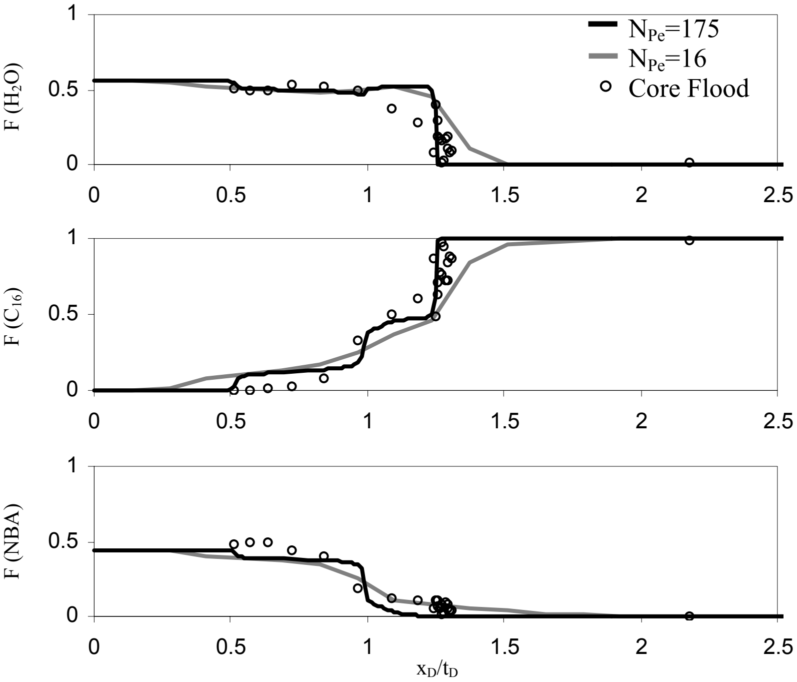

Figure 5.45 Core flood and simulated effluent profiles for core floods and simulations for injection of composition B_2 into a C_{16} saturated core.

Chapter 6 Recovery in Two-Phase Partially Miscible Displacements with Two-Phase Initial Compositions

The goal of this chapter is to explore the ramifications of leading condensate or gas banks on recovery in MCM floods with two-phase initial conditions. Three-phase flow is not considered in this chapter. Reservoir fluids often consist of an aqueous phase and several hydrocarbon phases as a result of water injection and naturally occurring or evolved gas caps. The effect on recovery of two hydrocarbon phases in situ at the beginning of MCM displacements has not been considered in detail in theoretical or experimental research.

In some reservoirs, the capillary transition zone can be very long, especially if permeability is low. The capillary transition zone can also be a significant concern in reservoirs with thin producing intervals (Albrechtsen *et al.*, 2001). Two-phase reservoir fluids also occur as a result of compositional grading in the vertical direction (Riemens *et al.*, 1988; Schulte, 1980; Whitson and Belery, 1994). The effect of compositional gradient on MMP and MME has been studied recently by Hoier and Whitson (2000) and Hoier *et al*. (2004). They observed the presence of condensate banks in simulations of MCM displacements on graded reservoirs. Development of miscibility in displacements of two hydrocarbon phases, however, has not received significant attention.

Jessen and Orr (2003) recently developed MOC solutions for partially miscible C/V displacements and purely vaporizing drives in gas condensate reservoirs with two-phase initial conditions. They showed that in purely vaporizing drives the displacement of two-phase reservoir fluids at the MMP is piston-like. The tie line that extends through the reservoir fluid (called the oil tie line) controls the development of miscibility. The reservoir fluid becomes single phase at the MMP, where the oil tie line intersects the critical locus. Thus, vaporizing drives at the MMP are always displacements of single-phase hydrocarbon fluids. Piston-like flow develops and the volume of oil recovered is approximately equal to the volume of gas injected.

For C/V drives, however, the crossover tie line controls the development of miscibility (Yuan, 2003). For such cases, the reservoir fluid may remain a two-phase fluid as the gas enrichment or pressure is increased. Jessen and Orr (2003) found the MMP for four- and twelve-component C/V displacements, but did not examine the composition and saturation profiles and their effect on recovery. They did observe the presence of a condensate bank, but again its impact on recovery was not discussed. In a related paper, Seto *et al.* (2003) performed streamline simulations using MOC for two-phase initial conditions in condensate reservoirs, however MCM flow again was not considered.

Bedrikovetsky (1993) and Bedrikovetsky *et al.* (1996) discuss construction of composition routes for miscible displacement of two-phase compositions and the resulting composition profiles. The resulting displacements are termed quasi-piston-like because of the condensate or gas bank ahead of the miscible front. The impact of condensate banks on oil recovery, however, is only briefly discussed. Lake (1989) also discusses MCM flow with two-phase initial conditions in three-component micellar-polymer flooding systems. Composition and saturation profiles are given, but the effect on miscible gas flood recovery is not discussed.

In this chapter, the composition routes and profiles for quasi-piston-like condensing drives of two-phase oil/gas initial compositions in a ternary system are constructed. The effect of quasi-piston-like flow on recovery efficiency in the condensing drives is examined. We also show that the existence of quasi-piston-like displacements of two-phase reservoir fluids under MCM conditions is not limited to condensing drives, but applies to C/V drives with four or more components.

6.1 TERNARY CONDENSING DRIVE

In this section, the MOC composition routes for the displacement of mixtures of CH_4 and C_{10} by injection of gases ranging from pure CH_4 to CO_2/CH_4 mixtures beyond the MME are calculated. The relative permeability model is

$$k_{rj} = k_{rj}^{o}\left[\left(S_j - S_{jr}\right)/\left(1 - S_{1r} - S_{2r}\right)\right]^{n_j} . \tag{6.1}$$

The non-wetting (gaseous) and wetting (oleic) phases are assumed to have residual saturations of S_{rg}=0.03 and S_{ro}=0.1 respectively. Both phases have Corey-exponents of n_j=2.0 and endpoint relative permeability of k_{rj}=1.0. The phase behavior of the ternary $CO_2/CH_4/C_{10}$ system at 160°F and 2320 psia is modeled using the Peng-Robinson equation of state (PREOS) (Sandler, 1999).

Component critical properties and acentric factors are taken from the Chemical Properties Handbook (Yaws, 1999) and shown in Table 6.1 along with binary interaction parameters. The viscosity of each phase is computed with the Lohrenz-Bray-Clark correlation (Lohrenz *et al.*, 1964).

Paths through composition space for this ternary system are constructed as outlined in Chapter 2 and are shown in Fig. 6.1. The key initial fluid compositions ($I_1 – I_5$) considered in the displacements that follow are also shown. Composition I_2 lies on the equal-velocity curve, where the phase velocities are equal.

Lake (1989) details the construction of composition routes for two-phase partially miscible flow in ternary systems. Johns (1992) discusses the construction of composition routes for single-phase boundary conditions for ternary, quaternary, and multi-component systems in detail. Johns (1992) construction method is based on finding key tie lines of the displacement route and applies to most two-phase initial composition problems directly. For initial compositions with high gas saturation the method must be modified, as outlined in this chapter.

6.1.1 Initial Reservoir Fluid with Small Gas Saturation

Consider the displacement of initial composition I_1, which corresponds to a gas saturation of 1% (see Fig. 6.2), by six different injection gas compositions varying from pure CH_4 injection to the MME. Construction of the composition routes for this initial composition is the same as discussed in Lake (1989).

Composition routes and profiles for these injection gases are shown in Figs. 6.2-6.3. All key compositions, saturations, and velocities for these routes are outlined in Table 6.2.

A two-component displacement along the CH_4/C_{10} axis of the ternary diagram occurs when I_1 is displaced by J_1. For that displacement, a trailing tangent shock occurs from J_1 to d_1, followed by a spreading wave from d_1 to c_1. The leading downstream shock is a tangent shock from c_1 to I_1.

With injection composition J_2 there is a trailing tangent shock from J_2 to e_2, followed by a spreading wave from e_2 to d_2. Composition d_2 is found by constructing a tangent shock from the intersection point of the oil and gas tie lines at $(C_{CO2}, C_{CH4}, C_{C10}) = (0.0000, -1.8205, 1.8205)$ to the injection gas tie line as shown in Fig. 6.4. Composition c_2 is found so that the shock velocity from c_2 to d_2 is equal to the tangent shock velocity from d_2 to the intersection point of the oil and gas tie lines. There is a constant state at c_2, followed by a leading shock to I_1. Each of the subsequent displacements with injection gases J_3-J_5 has composition routes constructed in this way.

Composition J_6 is the thermodynamic MME for two-phase initial fluid compositions along the CH_4/C_{10} axis because J_6 lies on the limiting tie line at the critical point. The composition route at the MME shocks from J_6 to the critical point, followed by a shock down the non-tie-line path to I_2, the equal velocity point. Each of these shocks has a dimensionless velocity of one. However, there is a final leading shock from I_2 to I_1 with dimensionless velocity greater than 1.0, in this case 1.078. The non-unity velocity results in a leading CH_4 bank on the composition profile in Fig. 6.3. The methane bank displaces C_{10} faster than piston-like flow. Thus, for small initial gas saturations such as composition I_1 C_{10} recovery is marginally enhanced. This is not the case for most two-phase initial gas saturations.

The physical explanation for the marginally enhanced recovery of C_{10} is related to the interplay of relative permeability and phase behavior. The initial fluid is at gas saturation less than the gas phase residual, so that the gas-phase relative permeability is zero, while the oil-phase relative permeability is large. Thus, early in the flood only the oil phase of the initial fluid is produced. The methane bank develops because methane, which prefers the vapor phase, is restricted from flowing to the production well. In general, relative permeability effects will cause enhanced production of C_{10} for any composition richer in C_{10} than composition I_2, the equal-phase velocity point.

6.1.2 Initial Reservoir Fluid with Intermediate Gas Saturation

The enhanced production of C_{10} only occurs for gas saturations below that of the equal-phase velocity point I_2. For example, consider the displacement of initial composition I_4, which corresponds to a gas saturation of 30% (see Figs. 6.5-6.6), by the injection gas compositions J_1-J_6 discussed in the previous section. All composition routes for the displacement of I_4 are outlined in Table 6.3.

A two-component displacement occurs when I_4 is displaced by J_1. For that displacement, a trailing tangent shock occurs from J_1 to d_1, followed by a spreading wave from d_1 to I_4. There is no leading shock in the displacement.

When I_4 is displaced by injection composition J_2, the composition route taken by the displacement is identical to the route of I_1 from J_2 to c_2 as shown on Fig. 6.4. The leading shock in the route is from c_2 to I_4, resulting in the development of a C_{10} bank. The displacement of I_4 by gas compositions J_3 and J_4 results in the same type of route as that with injection gas J_2.

As the injection composition is enriched to near-miscibility at J_5 the shock from d_5 (on the gas tie line) to the oil tie line intersects the oil tie line at c_5 as shown on Fig. 6.7. For the parameters chosen, the maximum tie-line velocity occurs at I_3, a larger methane composition than the equal velocity point I_2, as shown in Fig. 6.6. This allows for the route to take a spreading wave from c_5 to b_5, followed by a tangent shock from b_5 to I_4. In general, initial reservoir compositions between I_3 (S_g=0.2111) and S_g=0.4147 have both a spreading wave and a tangent shock along the tie line as part of their near-miscible and MCM routes.

The MCM composition route from J_6 is exactly the same as the route for I_1 up to I_2, the equal-phase velocity point. At I_2 there is a constant state followed by a spreading wave to b_5. Finally, there is a tangent shock from b_5 to I_4. The non-unity velocity tangent shock and wave from I_2 result in a leading C_{10} bank, as shown in Fig. 6.6. Thus, the recovery of C_{10} is delayed because of preferential flow of the gas phase ahead of the miscible front. In general, for any initial composition greater in methane than I_2 the gas phase velocity is greater than the liquid phase velocity, resulting in poorer C_{10} recovery for injection times less than 1.0 PVI.

6.1.3 Initial Reservoir Fluid with Large Gas Saturation

Consider the displacement of initial composition I_5, where S_g=0.80 by the same six injection compositions as for initial reservoir fluids I_1 and I_4. Composition routes and profiles are shown in Figs. 6.8 and 6.9. All composition routes from I_5 are given in Table 6.4.

The displacement of I_5 by pure methane (injection composition J_1) results in a slow non-tangent shock along the CH_4/C_{10} tie line from J_1 to I_5. The solution contains only one shock because a tangent shock to the initial fluid composition is not possible.

Next, consider the displacement of initial fluid I_5 by injection composition J_2. Injection composition J_2 results in a composition route for which the tangent-shock route construction outlined in the previous sections fails to provide a legal composition route; the leading shock from c_2 to I_5 shown in Fig. 6.4 would be slower than the shock from c_2 to d_2. Thus, the shock from the oil tie line to the gas tie line must be slower than the shock given by the tangent shock construction. The correct route shocks directly from the initial composition to the gas tie line. The velocity of the shock between the tie lines is found by constructing the non-tangent shock from the intersection point of the initial oil and gas tie lines to I_5 as shown in Fig. 6.4. Composition f_2 on the gas tie line is given by the intersection of the shock and the fractional flow curve along the tie line. As shown on Fig. 6.4, there are two possible compositions, f_2 and f_2* on the gas tie line that allow for the correct shock velocity. The composition f_2* can be eliminated because a shock to f_2* would result in a path that violates the entropy constraint. Finally, there is a constant state at f_2, followed by the leading shock to I_5.

Injection composition J_3 results in the same path type as J_2. However the shock from I_5 to the injection gas tie line is nearly tangent to the gas tie line for this enrichment. Enrichment past J_3 will result in composition routes that are able to satisfy the velocity constraint with tangent-shock routes. Injection compositions J_4-J_5 have the same routes as the displacements of fluid I_1 and I_4 except that the leading shock results in a CH_4 bank rather than a C_{10} bank. When multi-contact miscibility is reached at J_6, the leading shock velocity is 1.299, which indicates MCM flow is quasi-piston-like and recovery is significantly delayed for this reservoir fluid.

6.1.4 MCM Composition Routes

MCM flow is quasi-piston-like for reservoir fluids with initial gas saturations on either side of the equal velocity point I_2. In the case of gas saturations smaller than I_2 there is a leading gas bank that slightly increases oil recovery for injection times less than one PVI. For initial gas saturations greater than I_2 there is a leading oil bank that can substantially delay recovery of C_{10}. If the initial oil composition is exactly I_2, flow is genuinely piston-like. Thus, the choice of relative permeability model affects the MCM oil recovery for injection times smaller than 1.0 PVI.

MCM flow occurs in the ternary diagram of Fig. 6.1 for any injection gas composition between 100% CO_2 and J_6 at 79.04% CO_2. Figure 6.10 gives the composition profiles for the displacement of initial compositions I_1-I_5 by pure CO_2. Table 6.5 summarizes the dimensionless leading shock or wave velocities for the MCM composition routes from I_1-I_5. All MCM composition routes are the same as the routes from injection composition J_6 outlined in the previous sections as shown on Fig. 6.1.

For initial gas saturations smaller than I_2 the MCM routes have a leading shock down the oil tie line to I_2. As the initial fluid composition approaches I_2, the composition of the leading shock approaches I_2, and piston-like flow is obtained. Composition routes from initial gas saturations greater than I_2 will have a spreading wave down the tie-line path as explained previously.

Initial composition I_3 is an example of this type of route. I_3 corresponds to the initial gas phase saturation where the tie-line velocity reaches its maximum, and so this route has the longest possible spreading wave. Initial fluid compositions with gas saturations greater than I_3 will have routes with a leading shock and spreading wave. An example of this is reservoir fluid I_4 and was discussed in the previous section. The displacement of initial composition I_5, which corresponds to an initial gas saturation of 80%, contains only a leading shock.

6.1.5 Condensing Drive Recovery

Figure 6.11 shows the recovery of C_{10} for MCM displacements of various initial fluid compositions by any MCM injection gas composition along the CO_2/CH_4 axis (J_6 to pure CO_2). As shown, C_{10} recovery is significantly delayed by fractional flow effects ahead of the miscible front for all initial fluid compositions with gas saturations greater than that at I_2, that is, for I_3-I_5. C_{10} recovery is delayed the most at gas saturations 5-10% below S_g=1-S_{ro}. For reservoir fluids with initial gas saturations smaller than I_2, C_{10} recovery is increased over piston-like flow. C_{10} recovery is enhanced the most when the gas saturation is just above the residual saturation. Reservoir fluids at the boundary of the two-phase region (dew-point and bubble-point curves) or at I_2 give piston-like flow at all injection times, i.e. a straight line on Fig. 6.11. For cases in which recovery is delayed, the recovery increases rapidly to 100% by 1.0 PVI.

Figure 6.12 shows the cumulative recovery of C_{10} for MCM flow at various injection times as a function of initial gas saturation. As is shown, there is a large delay in recovery, especially for gas saturations near 0.80. The recovery is very sensitive to initial gas saturation below the oleic phase residual and increases rapidly to piston-like flow as the initial reservoir composition approaches the dew-point curve. Initial compositions on the dew-point curve are first contact miscible (FCM) with injection gas compositions on the CH_4/CO_2 axis.

6.2 QUATERNARY C/V DRIVE

The existence of a leading gas bank during MCM flow is not unique to purely condensing drives. C/V drives may also exhibit this behavior when two hydrocarbon phases are present in situ. We consider here quaternary displacements that are similar to the ternary ones of Fig. 6.1. The phase behavior is modeled with the PREOS (Sandler, 1999) and parameters as are outlined in

Table 6.1 (Yaws, 1999). The viscosity of each phase is again computed with Lohrenz-Bray-Clark correlation (Lohrenz *et al.*, 1964). Figure 6.13 shows the phase behavior for the $CO_2/CH_4/C_4/C_{10}$ quaternary displacements considered at 160°F and 1600 psia.

6.2.1 Composition Routes

In quaternary C/V displacements, the crossover tie line controls the development of miscibility. Thus, displacements by CO_2 injection of any initial reservoir fluid on the oil tie line shown in Fig. 6.13 will be MCM. This is because the crossover tie line for these displacements is the limiting tie line at the critical point on the $CO_2/C_4/C_{10}$ face of the diagram (Johns, 1992).

The composition routes for initial fluid compositions I_1-I_5 on the oil tie line are given in Fig. 6.13. Key compositions and leading wave/shock velocities are given in Table 6.6. All routes have a shock with dimensionless velocity 1.0 from the injection composition of pure CO_2 to the critical point on the $CO_2/C_4/C_{10}$ face. The composition routes then shock, again with unit velocity, from the critical point to the equal-velocity point I_2 on the $CH_4/C_4/C_{10}$ face. From I_2 the composition routes have a shock and/or spreading wave along the oil tie line to the initial reservoir fluid composition.

Each MCM displacement I_1-I_5 is constructed analogously to the displacement from the three-component initial condition with the same initial reservoir fluid label. The composition profiles in Fig. 6.14 show that flow is quasi-piston-like for displacement of I_1 and I_3-I_5, while for the equal-velocity point, I_2 the displacement piston-like.

6.2.2 C/V Drive Recovery

Figures 6.15 and 6.16 show C_4 and C_{10} production as a function of PVI for displacements of several initial reservoir compositions by CO_2 injection. Figures 6.17 and 6.18 show the cumulative fractional recovery of C_4 and C_{10} at four times as a function of initial gas saturation.

The recovery of C_4 is enhanced by a leading gas-phase bank and reduced by a leading condensate bank, but the effects are not as significant as C_{10}. This is because C_4 partitions more evenly between the two phases than C_{10}, though C_4 still preferentially partitions into the oleic phase. The recovery trend of C_{10} is nearly identical to the ternary condensing floods. C_{10} recovery is substantially delayed by formation of a condensate bank for large initial gas saturation and marginally enhanced by a gas bank for low initial gas saturation of the reservoir fluid.

6.3 CONCLUSIONS

Analytical solutions were built for a variety of MCM and partially miscible displacements where the initial reservoir fluid contains two hydrocarbon phases. The analytical solutions and theory give the following conclusions for both ternary condensing and quaternary C/V drive recoveries:

- Recovery of intermediate and heavy components under MCM injection conditions is delayed when the reservoir fluid has initial gas saturations greater than the gas saturation at the equal-phase velocity point. That is, recovery is delayed when the gas phase in the initial reservoir fluid flows preferentially compared to its oil phase.
- Recovery of intermediate and heavy hydrocarbons is enhanced when the oil phase flows preferentially.
- MCM flow for injection times less than 1.0 PVI is dependent on the relative permeability curves. This is because the relative permeability curves determine which phase flows preferentially.
- Recovery for all MCM displacements is 100% at 1.0 PVI, but the delay in recovery prior to this time could impact the economics of the project.
- A delay in recovery will also likely occur when a mobile aqueous phase is present. This indicates that gas should be injected as a primary oil recovery method rather than after a water flood.

Component	Mol Wt.	P_c (psia)	T_c (^{o}F)	V_c $\left(\frac{\text{ft}^3}{\text{lb-mol}}\right)$	ω
CO_2	44.01	1071.0	87.90	1.5060	0.2250
CH_4	16.04	667.8	-116.63	1.5899	0.0104
C_4	58.12	550.7	305.65	4.0828	0.2010
C_{10}	142.29	305.7	652.10	9.6610	0.4900
Binary interaction parameters	ρ_i $\left(\frac{\text{lb-mol}}{\text{ft}^3}\right)$	CO_2	CH_4	C_4	C_{10}
CO_2	0.4237	0.0000	0.1000	0.1257	0.0942
CH_4	0.2726		0.0000	0.0270	0.0420
C_4	0.5859			0.0000	0.0080
C_{10}	0.3041				0.0000

Table 6.1 Critical properties, acentric factors and binary interaction coefficients used in three- and four-component displacements.

Label on Figures	S_g	Volume Fractions			Dimensionless Velocity
		CO_2	C_1	C_{10}	
J_1	1.0000	0.0000	1.0000	0.0000	0.0000-0.0606
d_1	0.7819	0.0000	0.8884	0.1116	0.0606
c_1	0.3334	0.0000	0.6696	0.3304	2.1475
I_1	0.0100	0.5119	0.0000	0.4881	2.1475
J_2	1.0000	0.1764	0.8236	0.0000	0.0000-0.1003
e_2	0.7815	0.1702	0.7307	0.0991	0.1003
d_2	0.4994	0.1629	0.6202	0.2170	1.0592
c_2	0.2896	0.0000	0.6483	0.3517	1.0592-2.1072
I_1	0.0100	0.5119	0.0000	0.4881	2.1072
J_3	1.0000	0.3750	0.6250	0.0000	0.0000-0.1774
e_3	0.7769	0.3585	0.5532	0.0884	0.1774
d_3^*	0.5613	0.3448	0.4935	0.1617	1.0578
c_3^*	0.2342	0.0000	0.6213	0.3787	1.0578-1.9055
I_1	0.0100	0.5119	0.0000	0.4881	1.9055
J_4	1.0000	0.5586	0.4414	0.0000	0.0000-0.3182
e_4	0.7659	0.5299	0.3887	0.0815	0.3182
d_4^*	0.6210	0.5167	0.3645	0.1188	1.0470
c_4^*	0.1981	0.0000	0.6036	0.3964	1.0470-1.6616
I_1	0.0100	0.5119	0.0000	0.4881	1.6616
J_5	1.0000	0.7661	0.2339	0.0000	0.0000-0.7854
e_5	0.7197	0.7122	0.1998	0.0880	0.7854
d_5	0.6858	0.7104	0.1987	0.0909	1.0166
c_5	0.1554	0.0000	0.5828	0.4172	1.0166-1.2630
I_1	0.0100	0.5119	0.0000	0.4881	1.2630
J_6	1.0000	0.7904	0.2096	0.0000	0.0000-1.0000
Critical Pt.	1.0000	0.7262	0.1745	0.0994	1.0000
I_2	0.1384	0.0000	0.5745	0.4255	1.0000
I_1	0.0100	0.5119	0.0000	0.4881	1.0000

Table 6.2 Compositions and their velocities for ternary partially miscible composition routes with initial composition I_1 (S_g=0.01) and injection gas compositions J_1-J_6. *not labeled in figures

Label on Figures	S_g	Volume Fractions			Dimensionless Velocity
		CO_2	C_1	C_{10}	
J_1	1.0000	0.0000	1.0000	0.0000	0.0000-0.0606
d_1	0.7819	0.0000	0.8884	0.1116	0.0606
I_4	0.3000	0.0000	0.6533	0.3467	2.5402
J_2	1.0000	0.1764	0.8236	0.0000	0.0000-0.1003
e_2	0.7815	0.1702	0.7307	0.0991	0.1003
d_2	0.4994	0.1629	0.6202	0.2170	1.0592
c_2	0.2896	0.0000	0.6483	0.3517	1.0592-2.5993
I_4	0.3000	0.0000	0.6533	0.3467	2.5993
J_3	1.0000	0.3750	0.6250	0.0000	0.0000-0.1774
e_3	0.7769	0.3585	0.5532	0.0884	0.1774
d_3^*	0.5613	0.3448	0.4935	0.1617	1.0578
c_3^*	0.2342	0.0000	0.6213	0.3787	1.0578-2.8724
I_4	0.3000	0.0000	0.6533	0.3467	2.8724
J_4	1.0000	0.5586	0.4414	0.0000	0.0000-0.3182
e_4	0.7659	0.5299	0.3887	0.0815	0.3182
d_4^*	0.6210	0.5167	0.3645	0.1188	1.0470
c_4^*	0.1981	0.0000	0.6036	0.3964	1.0470-2.9794
I_4	0.3000	0.0000	0.6533	0.3467	2.9794
J_5	1.0000	0.7661	0.2339	0.0000	0.0000-0.7854
e_5^*	0.7197	0.7122	0.1998	0.0880	0.7854
d_5^*	0.6858	0.7104	0.1987	0.0909	1.0166
c_5^*	0.1554	0.0000	0.5828	0.4172	1.0166-2.7935
b_5^*	0.1727	0.0000	0.5913	0.4087	3.0035
I_4	0.3000	0.0000	0.6533	0.3467	3.0035
J_6	1.0000	0.7904	0.2096	0.0000	0.0000-1.0000
Critical Pt.	1.0000	0.7262	0.1745	0.0994	1.0000
I_2	0.1384	0.0000	0.5745	0.4255	1.0000-2.5132
b_5	0.1727	0.0000	0.5913	0.4087	3.0035
I_4	0.3000	0.0000	0.6533	0.3467	3.0035

Table 6.3 Compositions and their velocities for ternary partially miscible composition routes with initial composition I_4 (S_g=0.3) and injection gas compositions J_1-J_6. *not labeled in figures

Label on Figures	S_g	Volume Fractions			Dimensionless Velocity
		CO_2	C_1	C_{10}	
J_1	1.0000	0.0000	1.0000	0.0000	0.0000-0.0613
I_5	0.8000	0.0000	0.8972	0.1028	0.0613
J_2	1.0000	0.1764	0.8236	0.0000	0.0000-0.1003
e_2	0.7815	0.1702	0.7307	0.0991	0.1003
f_2	0.7621	0.1697	0.7231	0.1072	0.1257-1.0355
I_5	0.8000	0.0000	0.8972	0.1028	1.0355
J_3	1.0000	0.3750	0.6250	0.0000	0.0000-0.1774
e_3	0.7769	0.3585	0.5532	0.0884	0.1774
f_3	0.6806	0.3524	0.5265	0.1211	0.4509-1.0507
I_5	0.8000	0.0000	0.8972	0.1028	1.0507
J_4	1.0000	0.5586	0.4414	0.0000	0.0000-0.3182
e_4	0.7659	0.5299	0.3887	0.0815	0.3182
d_4	0.6210	0.5167	0.3645	0.1188	1.0470
c_4^*	0.1981	0.0000	0.6036	0.3964	1.0470-1.1378
I_5	0.8000	0.0000	0.8972	0.1028	1.1387
J_5	1.0000	0.7661	0.2339	0.0000	0.0000-0.7854
e_5	0.7197	0.7122	0.1998	0.0880	0.7854
d_5	0.6858	0.7104	0.1987	0.0909	1.0166
c_5	0.1554	0.0000	0.5828	0.4172	1.0166-1.2632
I_5	0.8000	0.0000	0.8972	0.1028	1.2632
J_6	1.0000	0.7904	0.2096	0.0000	0.0000-1.0000
Critical Pt.	1.0000	0.7262	0.1745	0.0994	1.0000
I_2	0.1384	0.0000	0.5745	0.4255	1.0000
I_5	0.8000	0.0000	0.8972	0.1028	1.0000

Table 6.4 Compositions and their velocities for ternary partially miscible composition routes with initial composition I_5 (S_g=0.8) and injection gas compositions J_1-J_6. *not labeled in figures

Label on Figures	S_g	Volume Fractions			Dimensionless Velocity
		CO_2	C_1	C_{10}	
Critical Pt.		0.1745	0.7261	0.0994	1.0000
I_1	0.0100	0.0000	0.5119	0.4881	1.0779
	0.1000	0.0000	0.5558	0.4442	2.1136
I_2	0.1384	0.0000	0.5745	0.4255	1.0000
I_3	0.2111	0.0000	0.6100	0.3900	3.1892
I_4	0.3000	0.0000	0.6533	0.3467	3.0035
	0.6000	0.0000	0.7997	0.2003	1.7934
I_5	0.8000	0.0000	0.8972	0.1028	1.2991
	0.9500	0.0000	0.9703	0.0297	1.0616

Table 6.5 Leading shock/wave velocities for ternary MCM displacement of several initial gas saturations.

Label on Figures	S_g	Volume Fractions				Dimensionless Velocity
		C_1	CO_2	C_4	C_{10}	
Critical Pt.		0.0000	0.8633	0.0784	0.0583	1.0000
Critical Pt.		0.5735	0.2154	0.2111	0.0000	1.0000
I_1	0.0500	0.4893	0.0000	0.1741	0.3366	1.5475
I_2	0.1327	0.5299	0.0000	0.1626	0.3076	1.0000
I_3	0.2048	0.5652	0.0000	0.1525	0.2823	3.2596
I_4	0.3000	0.6119	0.0000	0.1393	0.2488	3.0365
	0.6000	0.7590	0.0000	0.0975	0.1435	1.7888
I_5	0.8000	0.8571	0.0000	0.0697	0.0732	1.2968
	0.9000	0.9061	0.0000	0.0558	0.0381	1.1303

Table 6.6 Leading shock/wave velocities for quaternary MCM displacement of several initial gas saturations.

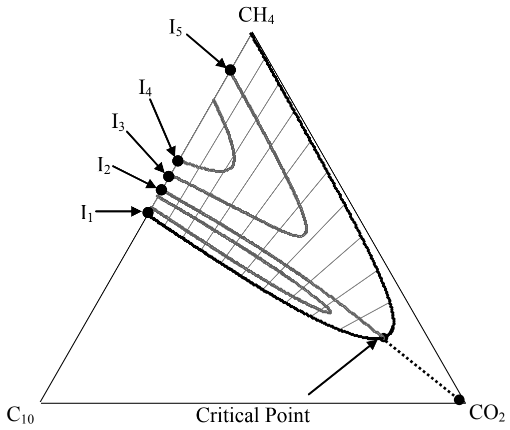

Figure 6.1 Tie-line and non-tie-line paths in ternary composition space. Composition I_2 is an equal velocity point and I_3 is at the maximum tie-line velocity point on the C_1/C_{10} tie line.

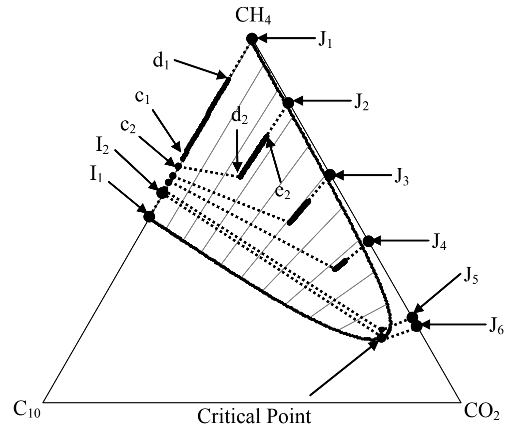

Figure 6.2 Composition routes for partially miscible displacements of initial composition I_1 (S_g=0.01) by various injection gases. The first MCM displacement occurs at the MME; injection gas J_6. Dotted lines indicate shocks and solid lines indicate spreading waves.

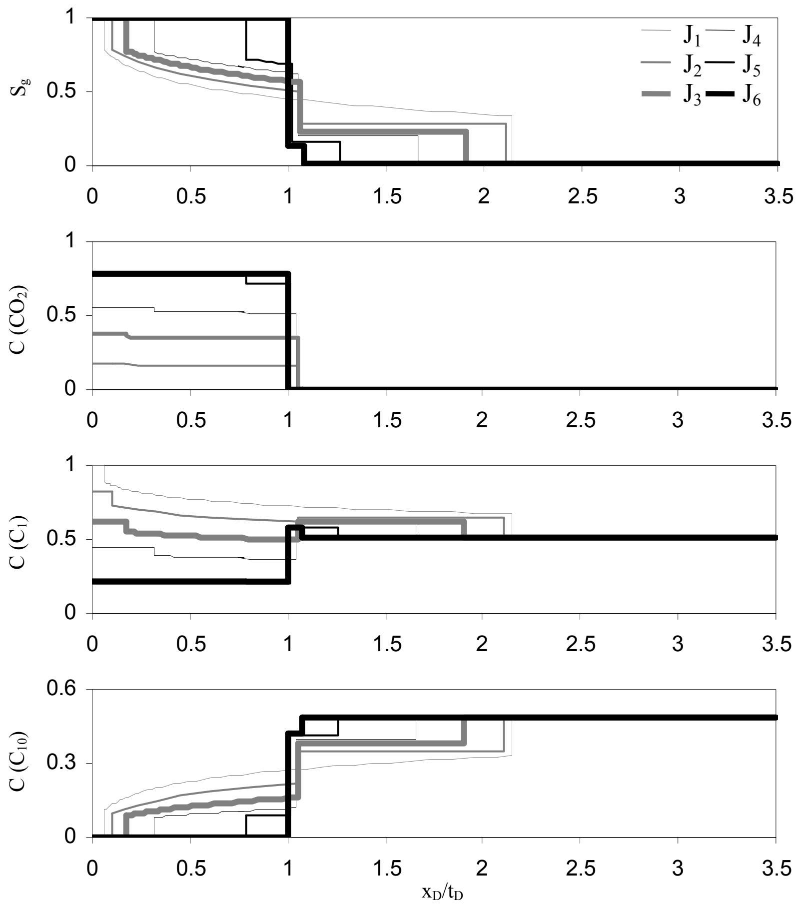

Figure 6.3 Composition and saturation profiles as a function of dimensionless velocity for the partially miscible displacements of initial composition I_1 (S_g=0.01) by various injection gases. Composition J_6 is the MME.

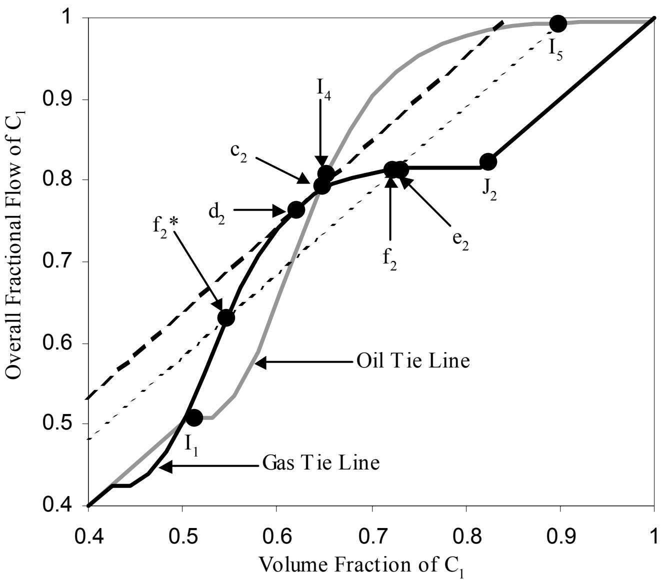

Figure 6.4 Fractional flow curves for the initial oil and injection gas tie lines. The injection gas tie line extends through injection gas J_2. The dashed line shows the shock from the intersection point of the two tie lines and tangent to the injection gas tie line. The non-tangent shock that occurs between the oil and gas tie lines for initial composition I_5 is the dotted line.

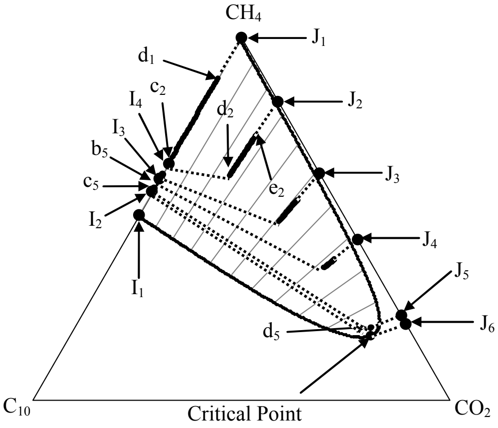

Figure 6.5 Composition routes for partially miscible displacements of initial composition I_4 (S_g=0.30) by various injection gas compositions. The first MCM displacement occurs at the MME; injection gas J_6. Dotted lines indicate shocks and solid lines indicate spreading waves.

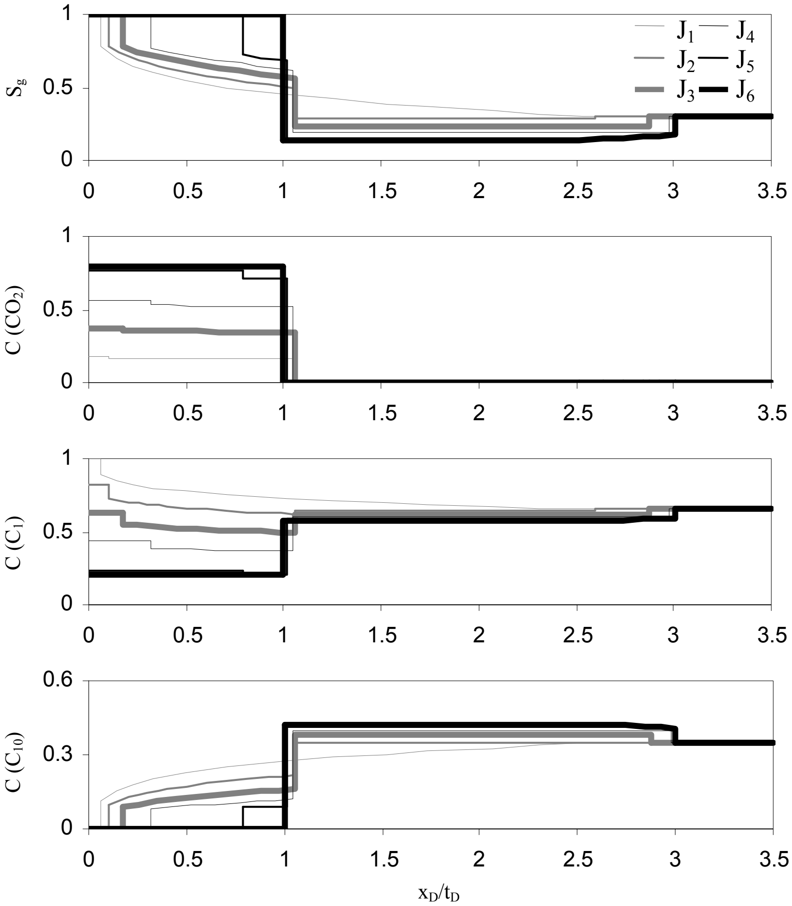

Figure 6.6 Composition and saturation profiles as a function of the dimensionless velocity for displacements of initial composition I_4 (S_g=0.30) by various injection gases. J_6 is at the MME.

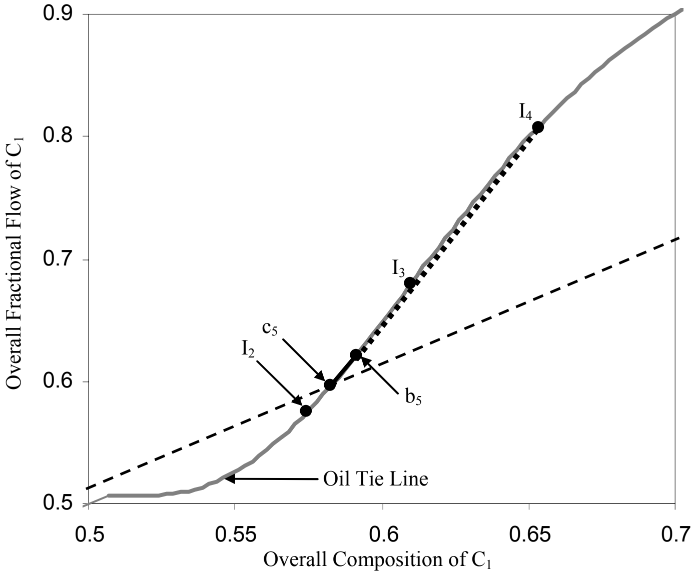

Figure 6.7 Fractional flow curve for initial reservoir compositions that are mixtures of C_{10} and CH_4. The dashed line is the shock (tangent to the oil tie line) from the intersection of the oil and injection gas tie lines for J_5. The tangent shock down the oil tie line is the dotted line.

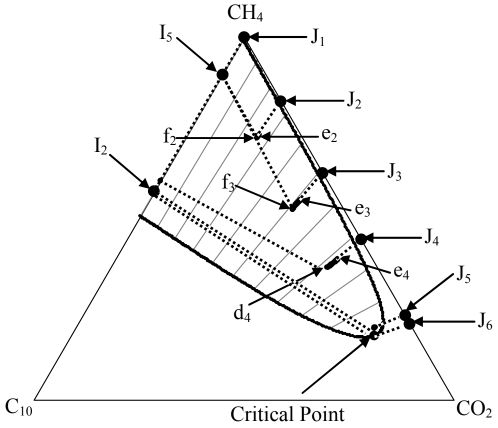

Figure 6.8 Composition routes for partially miscible displacements of initial composition I_5 (S_g=0.80) by various injection gas compositions. The first MCM displacement occurs at the MME; injection gas J_6. Dotted lines indicate shocks and solid lines indicate spreading waves.

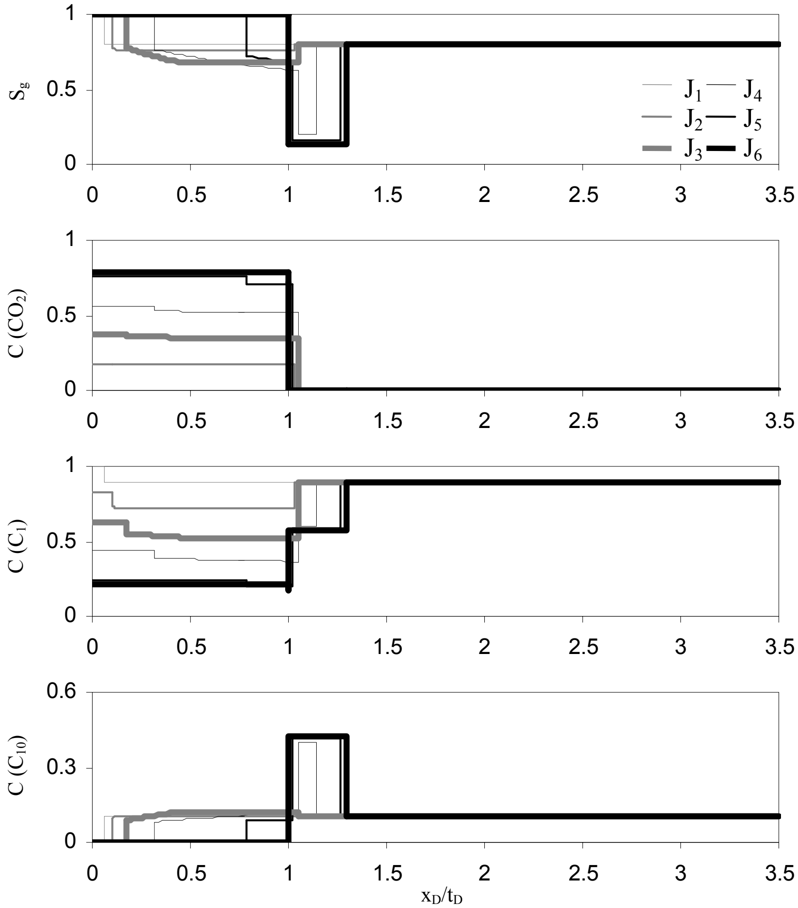

Figure 6.9 Composition and saturation profiles as a function of the dimensionless velocity for displacements of initial composition I_5 (S_g=0.80) by various injection gases. J_6 is at the MME.

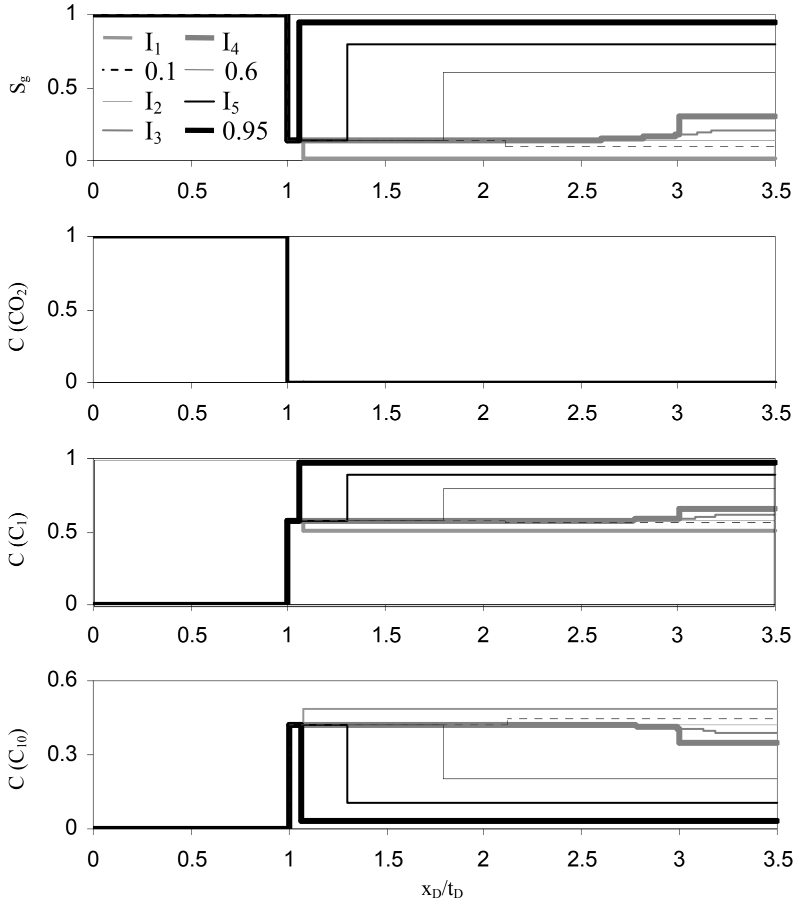

Figure 6.10 Profiles of gas saturation and CO_2, C_1 and C_{10} composition volume fractions for MCM ternary condensing drives of several two-phase initial reservoir compositions. The route from I_2 is at the equal velocity point and has a piston-like displacement.

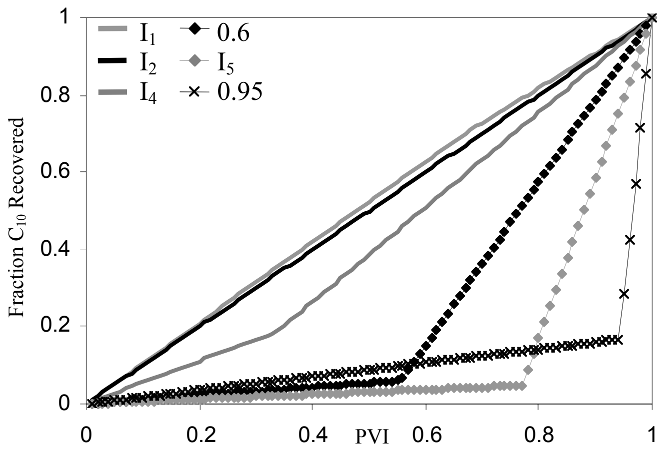

Figure 6.11 Fraction of C_{10} recovered in ternary MCM displacements as a function of PVI for several initial gas saturations. I_2 is a piston-like displacement because I_2 corresponds to the equal-velocity point.

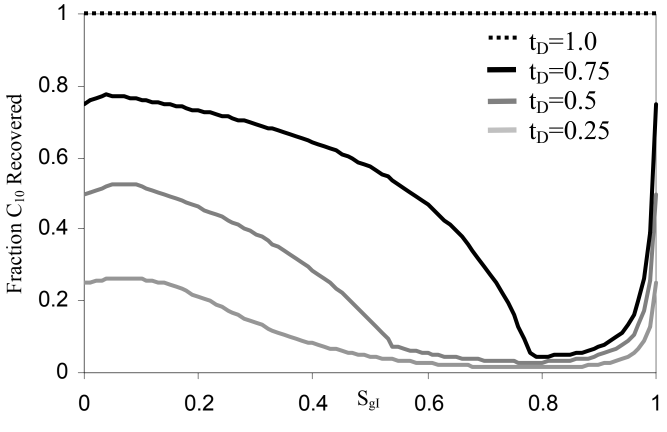

Figure 6.12 Fraction of C_{10} recovered in ternary MCM condensing drive displacements as a function of initial gas saturation for four dimensionless times. Recoveries are piston-like when initial gas saturation is zero, the equal velocity point, or one. Recovery for all displacements is 100% at 1.0 PVI.

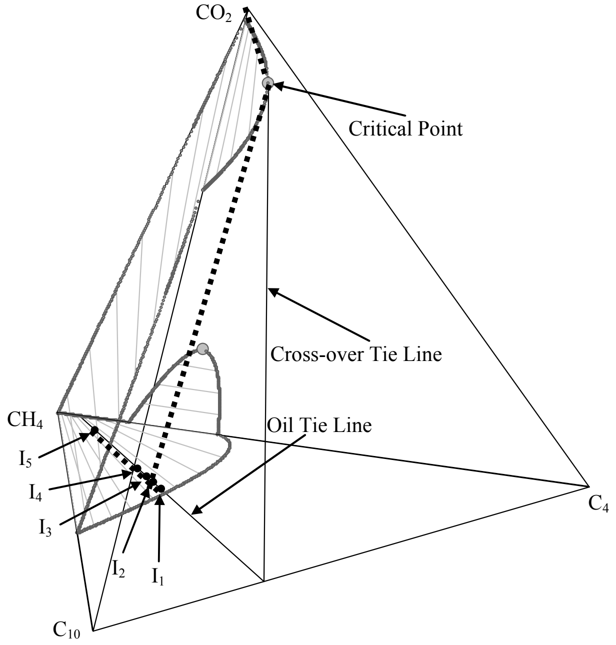

Figure 6.13 Composition routes of MCM displacements by pure CO$_2$. Shocks are shown as dotted lines.

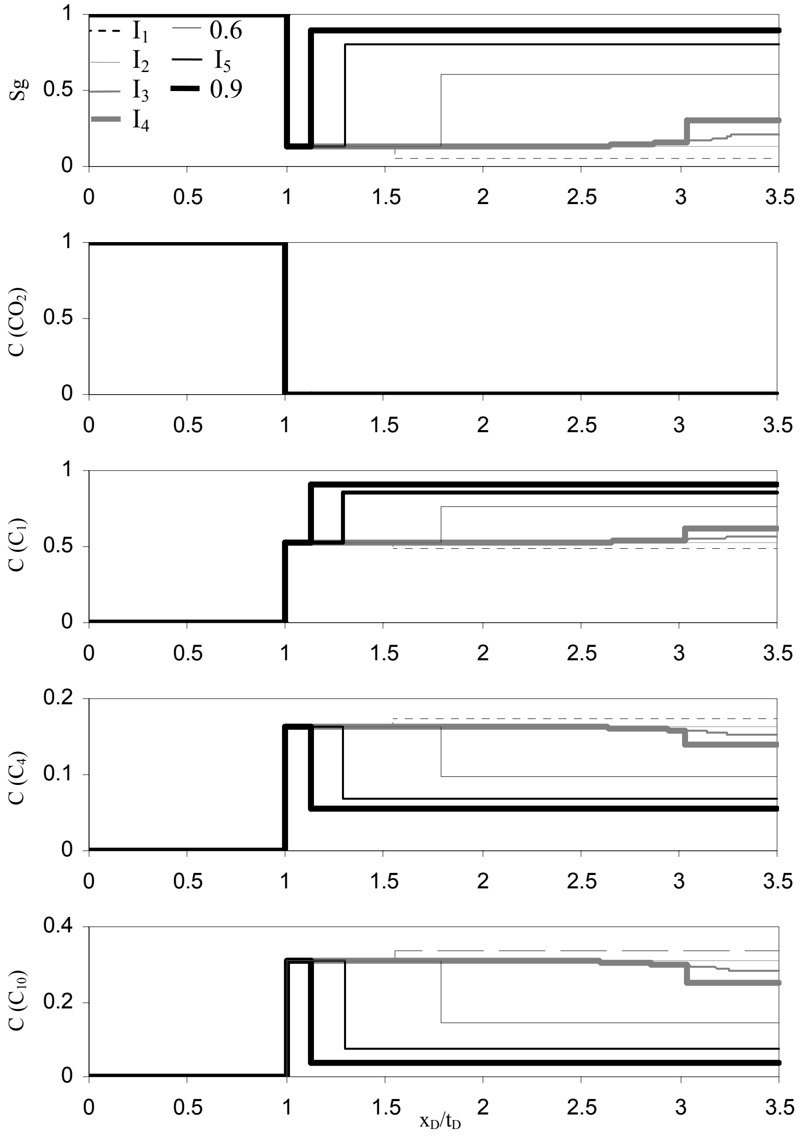

Figure 6.14 Profiles of gas saturation and CO_2, C_1, C_4, and C_{10} composition volume fractions for MCM quaternary C/V drives of several two-phase initial reservoir compositions. The black dashed line is for I_2, the equal velocity point, which has a piston-like displacement.

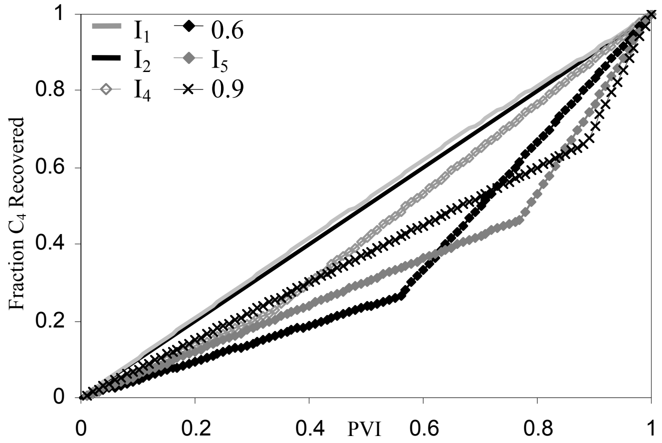

Figure 6.15 Fraction of C_4 recovered in quaternary MCM displacements as a function of PVI for several initial gas saturations. I_2 is a piston-like displacement because I_2 corresponds to the equal-velocity point.

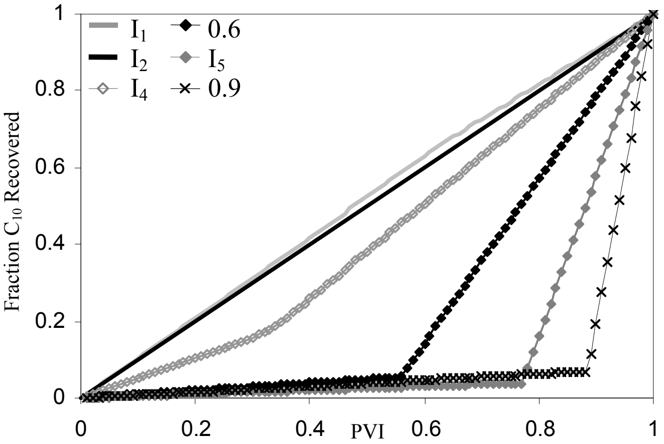

Figure 6.16 Fraction of C_{10} recovered in quaternary MCM displacements as a function of PVI for several initial gas saturations. I_2 is a piston-like displacement because I_2 corresponds to the equal-velocity point.

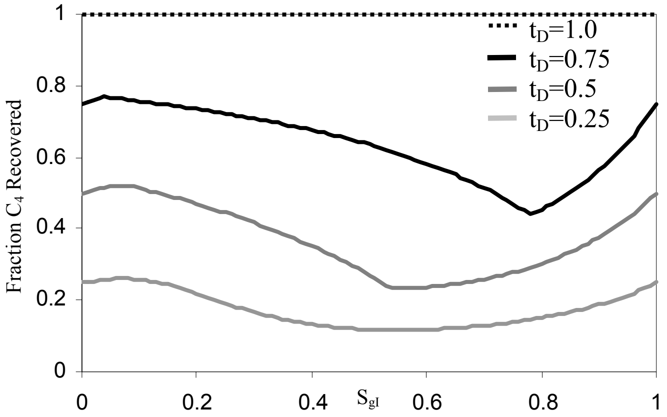

Figure 6.17 Fraction of C_4 recovered in quaternary MCM C/V drive displacements as a function of initial gas saturation for four dimensionless times. Recoveries are piston-like when initial gas saturation is zero, the equal velocity point, or one. Recovery for all displacements is 100% at 1.0 PVI.

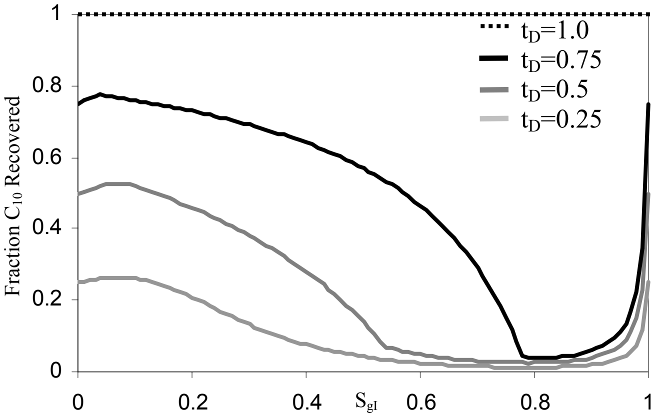

Figure 6.18 Fraction of C_{10} recovered in quaternary MCM C/V drive displacements as a function of initial gas saturation for four dimensionless times. Recoveries are piston-like when initial gas saturation is zero, the equal velocity point, or one. Recovery for all displacements is 100% at 1.0 PVI.

Chapter 7 Conclusions and Future Work

The theory and methodology for finding unique analytical solutions for three-phase, three component partially miscible flow using the method of characteristics has been developed. The effect of three-phase flow and choice of three-phase parameters on hydrocarbon and hydrocarbon contaminant recovery has been examined. Solutions were constructed for Riemann problems in which the injection and initial compositions are one or two phases. The implications of two-phase initial reservoir compositions on the development of miscibility were discussed for systems that form two or three flowing phases. Analytical solutions were also shown to model simulations and core floods with reasonable accuracy.

7.1 KEY CONCLUSIONS

7.1.1 MOC in Three-Phase Partially Miscible Flow

- Analytical composition routes exist and are unique for the three-phase partially miscible ternary systems studied, even when the conservation law is of mixed hyperbolic and elliptic type.
- Recovery may decline with surfactant or alcohol enrichment for a range of injection compositions. The decline is caused by the leading shock wave speeding up when constant states occur in the three-phase region. A decline in recovery occurred in both ternary systems studied. Only the relative permeability model that accounted for the mobilization of the

oleic phase did not experience a decline in recovery with surfactant enrichment.

- Miscibility is developed at the critical point of the alcohol/oleic two-phase region and along the boundary of the three-phase region for a single-phase initial reservoir composition in three-phase partially miscible systems.
- In three-phase partially miscible systems, miscibility is not developed for any injection composition when two phases are initially present in situ. This is a substantial divergence from previous theory developed for flow that is limited to two phases.
- Flow resistance is increased significantly when three-phase flow occurs.
- Relative permeability curves substantially affect the composition route and hence oleic phase recovery. The optimal surfactant concentration to minimize total surfactant volume injected is significantly impacted by the three-phase relative permeability model.

7.1.2 Dispersion in Three-Phase Partially Miscible Flow

- Ten of the twelve MOC solutions match experimental core flood effluent compositions and profiles well. The MOC composition routes were very sensitive to changes in boundary conditions near both of the composition routes that did not match; suggesting that small errors in relative permeability parameters likely caused the difference in the composition routes.

- The MOC composition routes are the zero-dispersion limits of the simulated displacements. This implies that the physically correct, unique solutions have been found. Near transitional routes numerical dispersion may cause simulated routes to diverge from MOC routes at shock fronts, but as dispersion is minimized the simulated routes converge to MOC solutions.
- Oil recovery is most sensitive to dispersion near the MME in the example system in Chapter 3. There is no general trend connecting composition route type and sensitivity to dispersion for the partially-miscible route types.
- Relative permeabilities affect the sensitivity of recoveries to dispersion in the water/decane/surfactant ternary system from Chapter 4. The sensitivity of composition routes and recoveries to numerical dispersion may also be dependent on the ternary system: the ternary system studied in Chapter 4 was more sensitive to dispersion than the ternary system studied in Chapter 3 for the relative permeability parameters studied.
- Comparison of core flood effluent composition routes and profiles with simulated results indicates that numerical dispersion may not accurately model the spreading of the shock fronts in the composition profiles in ternary systems that can form three flowing phases.

7.1.3 Two-Phase MCM Flow with Two-Phase Initial Compositions

- Two-phase partially miscible systems with an arbitrary number of components have quasi-piston-like displacement under condensing or C/V drive when two hydrocarbon phases are initially present in situ. The development of miscibility is the same as for single-phase initial compositions.
- In two-phase partially miscible systems, MCM flow for injection times less than 1.0 PVI is dependent on the relative permeability curves. Recovery of heavy hydrocarbons may be substantially delayed because of the formation of an oil bank ahead of the miscible front.

7.2 FUTURE WORK

- Explore the existence and uniqueness of composition routes for different relative permeability curves. In this work all three types of conservation law were shown to have unique solutions with extended-Corey relative curves and the parameters shown. Other relative permeability models or parameters may result in multiple interior umbilic points or large elliptic regions. Composition routes may not be unique for other models, particularly if one of the boundary conditions is in or near an elliptic region in three-phases.
- Include surfactant adsorption in method of characteristics solutions. Surfactants typically adsorb onto reservoir rocks in real three-phase partially miscible displacements. It is possible to develop an eigenvalue

problem for three-phase partially miscible flow in which the adsorption of one or more components is included. Solution of a three-phase flow problem including adsorption has never been attempted.

- Consider the four-component three-phase partially miscible flow problem. In two-phase flow four components are necessary to capture all of the possible drive mechanisms. It follows that in three-phase partially miscible flow at least four components will be necessary to capture all of the features of a displacement.
- Compare core flood effluent routes with the results of one-dimensional compositional simulations in which the physical dispersion term is included in the mass-balance equations.
- Develop a compositional simulator in which analytical solutions are used along streamlines. Such a simulator would be orders of magnitude faster than simulations using finite element or finite difference methods.

Appendix A Derivation of MOC Solution Derivation

In this section the solution to the characteristic problem is derived in detail. In the two- and three-phase regions flow is governed by the mass balance equations given by Eq. (2.1):

$$\left(\frac{\partial C_i}{\partial t_D}\right)_{x_D}+\left(\frac{\partial F_i}{\partial x_D}\right)_{t_D}=0 \quad i=1,...,3 \tag{A.1}$$

This can be re-written as

$$\left(\frac{\partial C_i}{\partial t_D}\right)_{x_D}+\left(\frac{\partial F_i}{\partial C}\right)\left(\frac{\partial C}{\partial x_D}\right)_{t_D}=0 \quad i=1,\ 2,\ 3. \tag{A.2}$$

Eq. (A.2) is over-determined since $\sum_{i=1}^{n_c} C_i=\sum_{i=1}^{n_c} F_i=1$. Choosing components 1 and 3 as the independent variables Eq. (A.2) becomes

$$\begin{aligned}&\left(\frac{\partial C_1}{\partial t_D}\right)_{x_D}+\left(\frac{\partial F_1}{\partial C_1}\right)\left(\frac{\partial C_1}{\partial x_D}\right)_{t_D}+\left(\frac{\partial F_1}{\partial C_3}\right)\left(\frac{\partial C_3}{\partial x_D}\right)_{t_D}=0\\&\left(\frac{\partial C_3}{\partial t_D}\right)_{x_D}+\left(\frac{\partial F_3}{\partial C_1}\right)\left(\frac{\partial C_1}{\partial x_D}\right)_{t_D}+\left(\frac{\partial F_3}{\partial C_3}\right)\left(\frac{\partial C_3}{\partial x_D}\right)_{t_D}=0.\end{aligned} \tag{A.3}$$

Eq. (A.3) can be re-written as the eigenvalue problem

$$\begin{pmatrix} C_{1t_D} \\ C_{3t_D} \end{pmatrix} + \begin{pmatrix} F_{11} & F_{13} \\ F_{31} & F_{33} \end{pmatrix} \begin{pmatrix} C_{1x_D} \\ C_{3x_D} \end{pmatrix} = \begin{pmatrix} 0 \\ 0 \end{pmatrix} \tag{A.4}$$

where $C_{it_D}=\partial C_i/\partial t_D$, $C_{ix_D}=\partial C_i/\partial x_D$ and $F_{ij}=\partial F_i/\partial C_j$. The eigenvalues (or characteristic directions) of Eq. (A.4) are

$$\frac{dx_D}{dt_D} = \tfrac{1}{2}\left[\left(F_{11}+F_{33}\right) \pm \sqrt{\left(F_{11}+F_{33}\right)^2 + 4\left(F_{13}F_{31} - F_{11}F_{33}\right)}\right] \tag{A.5}$$

which simplifies to

$$\lambda_{\pm} = \frac{dx_D}{dt_D} = \tfrac{1}{2}\left[\left(F_{11}+F_{33}\right) \pm \sqrt{\left(F_{11}-F_{33}\right)^2 + 4F_{13}F_{31}}\right] \tag{A.6}$$

Substitution of Eq. (A.6) into Eq. (A.3) gives the characteristic curves as

$$\frac{dC_3}{dC_1} = \frac{\lambda_{\pm} - F_{11}}{F_{13}} \text{ or } \frac{dC_1}{dC_3} = \frac{\lambda_{\pm} - F_{33}}{F_{31}} \tag{A.7}$$

which are shown in Eq. 2.13.

Appendix B Equivalence of Saturation and Composition Mass Balance Equations in Three-Phase Region

In this appendix it is shown that the system of equations given by Eq. (2.6) is equivalent to the system given by Eq. (2.15). First writing the equation for some component i in terms of S_j and f_j

$$\left(\frac{\partial(c_{i1}S_1+c_{i2}S_2+c_{i2}S_2)}{\partial t_D}\right)_{x_D}+\left(\frac{\partial(c_{i1}f_1+c_{i2}f_2+c_{i2}f_2)}{\partial x_D}\right)_{t_D}=0 \qquad \text{(B.1)}$$

which can be multiplied out to

$$c_{i1}\left[\left(\frac{\partial S_1}{\partial t_D}\right)_{x_D}+\left(\frac{\partial f_1}{\partial x_D}\right)_{t_D}\right]+c_{i2}\left[\left(\frac{\partial S_2}{\partial t_D}\right)_{x_D}+\left(\frac{\partial f_2}{\partial x_D}\right)_{t_D}\right]+c_{i3}\left[\left(\frac{\partial S_3}{\partial t_D}\right)_{x_D}+\left(\frac{\partial f_3}{\partial x_D}\right)_{t_D}\right]=0 \quad \text{(B.2)}$$

using the auxiliary relations $\sum_{j=1}^{3}S_j=1,\ \sum_{j=1}^{3}f_j=1$ to write only in terms of phases one and three

$$\left(c_{i1}-c_{i2}\right)\left[\left(\frac{\partial S_1}{\partial t_D}\right)_{x_D}+\left(\frac{\partial f_1}{\partial x_D}\right)_{t_D}\right]+\left(c_{i3}-c_{i2}\right)\left[\left(\frac{\partial S_3}{\partial t_D}\right)_{x_D}+\left(\frac{\partial f_3}{\partial x_D}\right)_{t_D}\right]=0 \quad i=1,\ 2,\ 3 \quad \text{(B.3)}$$

using the additional auxiliary relation $\sum_{i=1}^{3} C_{ij} = 1$ it can be shown that only two of these equations are independent. Components 1 and 3 are chosen as the independent variables. Writing the two remaining equations in matrix form

$$\begin{pmatrix} [c_{11} - c_{12}] & [c_{13} - c_{12}] \\ [c_{31} - c_{32}] & [c_{33} - c_{32}] \end{pmatrix} \begin{pmatrix} \left(\partial S_1 / \partial t_D\right)_{x_D} + \left(\partial f_1 / \partial x_D\right)_{t_D} \\ \left(\partial S_3 / \partial t_D\right)_{x_D} + \left(\partial f_3 / \partial x_D\right)_{t_D} \end{pmatrix} = \begin{pmatrix} 0 \\ 0 \end{pmatrix}. \tag{B.4}$$

If the C matrix is non-singular, the only possible solution to this equation is for the vector of partial derivatives to be zero. Decomposing the C matrix into the two matrices

$$\begin{pmatrix} [c_{11} - c_{12}] & [c_{13} - c_{12}] \\ [c_{31} - c_{32}] & [c_{33} - c_{32}] \end{pmatrix} = \begin{pmatrix} c_{11} & c_{13} \\ c_{31} & c_{33} \end{pmatrix} + \begin{pmatrix} c_{12} & c_{12} \\ c_{32} & c_{32} \end{pmatrix} \tag{B.5}$$

the determinant of C, $\det(C) = \det(A) + \det(B) = c_{11}c_{33} - c_{13}c_{31} + 0$ can be forced to be non-zero with the simple and logical constraints that $c_{11} > c_{31}$ and $c_{33} > c_{13}$. Therefore the matrix is non-singular and the vector of partial derivatives must be zero. This proves that the system of equations

$$\left(\frac{\partial S_j}{\partial t_D}\right)_{x_D} + \left(\frac{\partial f_j}{\partial x_D}\right)_{t_D} = 0 \quad j = 1,\ 3 \tag{B.6}$$

is sufficient to describe Eq. (2.6) in the three-phase region. The characteristic problem given by Eq. (B.6) can be derived by the method introduced in Appendix A. The eigenvalues are

$$\lambda_{\pm} = \frac{1}{2}\left[(f_{11} + f_{33}) \pm \sqrt{(f_{11} - f_{33})^2 + 4 f_{13} f_{31}} \right] \tag{B.7}$$

and the corresponding equivalent eigenvectors are

$$\frac{dS_3}{dS_1} = \frac{\lambda_{\pm} - f_{11}}{f_{13}} \text{ or } \frac{dS_1}{dS_3} = \frac{\lambda_{\pm} - f_{33}}{f_{31}}. \tag{B.8}$$

Appendix C Shock Jump Condition in Three-Phase Residual Region

In this section we prove that it is impossible to satisfy the shock jump conditions for compositions not on the same fast path and below the residual saturation of the same phase. The jump conditions from Eq. (2.16) written in terms of phase saturations are

$$\Lambda = \frac{\left[c_{i1}f_1 + c_{i2}f_2 + c_{i3}(1 - f_1 - f_2)\right]^d - \left[c_{i1}f_1 + c_{i2}f_2 + c_{i3}(1 - f_1 - f_2)\right]^u}{\left[c_{i1}S_1 + c_{i2}S_2 + c_{i3}(1 - S_1 - S_2)\right]^d - \left[c_{i1}S_1 + c_{i2}S_2 + c_{i3}(1 - S_1 - S_2)\right]^u} \quad \text{(C.1)}$$

for *i*=1 or 2 Without loss of generality we assume that phase one is below its residual saturation on both sides of the shock ($f_1=0$). Equation (C.1) can be rearranged to

$$\Lambda = \frac{(c_{i2} - c_{i3})(f_2^d - f_2^u)}{(c_{i1} - c_{i3})(S_1^d - S_1^u) + (c_{i2} - c_{i3})(S_2^d - S_2^u)},\ i = 1 \text{ or } 2\,. \quad \text{(C.2)}$$

Because c_{ij} are fixed in the three-phase region we make the following definitions:

$$\begin{aligned}\alpha_i &= c_{i2} - c_{i3}\\ \beta_i &= c_{i1} - c_{i3}\\ y &= S_2^d - S_2^u\\ z &= S_1^d - S_1^u\\ x(y) &= f_2^d - f_2^u\end{aligned} \tag{C.3}$$

so that Λ_1- $\Lambda_2 = 0$ from Eqs. (C.2) becomes

$$\alpha_1\beta_2 z - \alpha_2\beta_1 z = 0\,. \tag{C.4}$$

The parameter z is not equal to zero when the shock is between two fast paths and therefore,

$$\frac{\alpha_1}{\beta_1} = \frac{\alpha_2}{\beta_2} \;\Rightarrow\; \frac{c_{12} - c_{13}}{c_{11} - c_{13}} = \frac{c_{22} - c_{23}}{c_{21} - c_{23}}\;. \tag{C.5}$$

Clearly there are very few three-phase regions for which Eq. (C.5) holds. Thus, the only shocks that can take place between two compositions in the residual region of the tie triangle are shocks down a fast path in that region.

Appendix D Derivation of Three-Phase Numerical Dispersion

In this appendix the local truncation error, or numerical dispersion associated with a first order finite difference scheme that is explicit in time is derived for immiscible three-phase flow. The simulator iterates on the equations

$$\begin{aligned}\frac{S_1^{j+1}-S_1^{j}}{\Delta t_D}&=\frac{f_1^{i}-f_1^{i-1}}{\Delta x_D}\\ \frac{S_2^{j+1}-S_2^{j}}{\Delta t_D}&=\frac{f_2^{i}-f_2^{i-1}}{\Delta x_D}\end{aligned} \tag{D.1}$$

to approximate the original partial differential equations

$$\begin{aligned}\frac{\partial S_1}{\partial t_D}&=-\left[\frac{\partial f_1}{\partial S_1}\frac{\partial S_1}{\partial x_D}+\frac{\partial f_1}{\partial S_2}\frac{\partial S_2}{\partial x_D}\right]\\ \frac{\partial S_2}{\partial t_D}&=-\left[\frac{\partial f_2}{\partial S_1}\frac{\partial S_1}{\partial x_D}+\frac{\partial f_2}{\partial S_2}\frac{\partial S_2}{\partial x_D}\right].\end{aligned} \tag{D.2}$$

Eq. (D.1) is equivalent to Eqs. 5.3 in the three-phase region since all three phases behave immiscibly.

According to Taylor's theorem

$$\frac{f_1^i - f_1^{i-1}}{\Delta x_D} = \frac{\partial f_1}{\partial S_1}\frac{\partial S_1}{\partial x_D} + \frac{\partial f_1}{\partial S_2}\frac{\partial S_2}{\partial x_D} - \frac{\Delta x_D}{2}\left[\frac{\partial^2 f_1}{\partial S_1^2}\left(\frac{\partial S_1}{\partial x_D}\right)^2 + \frac{\partial f_1}{\partial S_1}\frac{\partial^2 S_1}{\partial x_D^2} + \frac{\partial^2 f_1}{\partial S_2^2}\left(\frac{\partial S_2}{\partial x_D}\right)^2 + \frac{\partial f_1}{\partial S_2}\frac{\partial^2 S_2}{\partial x_D^2}\right] + \ldots \tag{D.3}$$

and

$$\frac{S_1^i - S_1^{i-1}}{\Delta t_D} = \frac{\partial S_1}{\partial t_D} + \frac{\Delta t_D}{2}\frac{\partial^2 S_1}{\partial t_D^2} + \ldots \tag{D.4}$$

for phase 1. Assuming that the second derivatives of the fractional flows are negligible and substituting (D.3) and (D.4) into Eq. (D.1) gives

$$\frac{\partial S_1}{\partial t_D} = -\left[\frac{\partial f_1}{\partial S_1}\frac{\partial S_1}{\partial x_D} + \frac{\partial f_1}{\partial S_2}\frac{\partial S_2}{\partial x_D}\right] + \frac{\Delta x_D}{2}\left[\frac{\partial f_1}{\partial S_1}\frac{\partial^2 S_1}{\partial x_D^2} + \frac{\partial f_1}{\partial S_2}\frac{\partial^2 S_2}{\partial x_D^2}\right] - \frac{\Delta t_D}{2}\frac{\partial^2 S_1}{\partial t_D^2} \tag{D.5}$$

as the equation the simulator is solving for phase 1. It is necessary to eliminate the derivative with respect to time in order to have a meaningful truncation error. Taking the derivative of the first Eq. (D.2) with respect to time gives

$$\frac{\partial^2 S_1}{\partial t_D^2} = -\left[\frac{\partial f_1}{\partial S_1}\frac{\partial^2 S_1}{\partial x_D \partial t_D} + \frac{\partial f_1}{\partial S_2}\frac{\partial S_2}{\partial x_D \partial t_D}\right]. \tag{D.6}$$

In order to eliminate the two cross-partial derivatives terms we take the space derivative of both Eqs. (D.2)

$$\begin{aligned} \frac{\partial^2 S_1}{\partial x_D \partial t_D} &= -\left[\frac{\partial f_1}{\partial S_1} \frac{\partial^2 S_1}{\partial x_D^2} + \frac{\partial f_1}{\partial S_2} \frac{\partial^2 S_2}{\partial x_D^2} \right] \\ \frac{\partial^2 S_2}{\partial x_D \partial t_D} &= -\left[\frac{\partial f_2}{\partial S_1} \frac{\partial^2 S_1}{\partial x_D^2} + \frac{\partial f_2}{\partial S_2} \frac{\partial^2 S_2}{\partial x_D^2} \right]. \end{aligned} \tag{D.7}$$

In Eqs. (D.6) and (D.7) the terms including second derivatives of the fractional flows are neglected. Substitution of Eqs. (D.7) into (D.6) gives

$$\frac{\partial^2 S_1}{\partial t_D^2} = \left[\frac{\partial f_1}{\partial S_1} \left(\frac{\partial f_1}{\partial S_1} \frac{\partial^2 S_1}{\partial x_D^2} + \frac{\partial f_1}{\partial S_2} \frac{\partial^2 S_2}{\partial x_D^2} \right) + \frac{\partial f_1}{\partial S_2} \left(\frac{\partial f_2}{\partial S_1} \frac{\partial^2 S_1}{\partial x_D^2} + \frac{\partial f_2}{\partial S_2} \frac{\partial^2 S_2}{\partial x_D^2} \right) \right]. \tag{D.8}$$

Finally, Eq. (D.8) is substituted into (D.5), which after some rearrangement is

$$\begin{aligned} &\frac{\partial S_1}{\partial t_D} = -\left[\frac{\partial f_1}{\partial S_1} \frac{\partial S_1}{\partial x_D} + \frac{\partial f_1}{\partial S_2} \frac{\partial S_2}{\partial x_D} \right] + \\ &\frac{1}{2} \partial f_1 / dS_1 \left[\Delta x_D - \partial f_1 / dS_1 \, \Delta t_D \right] \partial^2 S_1 / dx_D^2 + \\ &\frac{1}{2} \partial f_1 / dS_2 \left[\Delta x_D - \partial f_2 / dS_1 \, \Delta t_D \right] \partial^2 S_2 / dx_D^2 - \\ &\frac{\Delta t_D}{2} \partial f_1 / dS_2 \, \partial f_2 / dS_1 \left[\partial^2 S_1 / dx_D^2 + \partial^2 S_2 / dx_D^2 \right]. \end{aligned} \tag{D.9}$$

Thus the dispersion term in the equation for phase 1 is

$$\begin{aligned}D_1 &= \frac{1}{2}\partial f_1/dS_1\left[\Delta x_D - \partial f_1/dS_1\,\Delta t_D\right]\partial^2 S_1/dx_D^2 + \\ &\frac{1}{2}\partial f_1/dS_2\left[\Delta x_D - \partial f_2/dS_1\,\Delta t_D\right]\partial^2 S_2/dx_D^2 - \\ &\frac{\Delta t_D}{2}\partial f_1/dS_2\,\partial f_2/dS_1\left[\partial^2 S_1/dx_D^2 + \partial^2 S_2/dx_D^2\right].\end{aligned} \tag{D.10}$$

In order to ensure numerical stability Δt_D is an order of magnitude smaller than Δx_D in all simulations in this research. The derivatives $\partial f_1/\partial S_2$ and $\partial f_2/\partial S_1$ are also typically small so all terms containing $\Delta t_D\, \partial f_1/\partial S_2\, \partial f_2/\partial S_1$ are dropped. The third term in Eq. (D.9) is eliminated and the numerical dispersion for phase 1 is

$$\begin{aligned}D_1 &= \frac{1}{2}\partial f_1/dS_1\left[\Delta x_D - \partial f_1/dS_1\,\Delta t_D\right]\partial^2 S_1/dx_D^2 + \\ &\frac{\Delta x_D}{2}\partial f_1/dS_2\,\partial^2 S_2/dx_D^2.\end{aligned} \tag{D.11}$$

Similarly, the numerical dispersion for phase 2 is

$$\begin{aligned}D_2 &= \frac{\Delta x_D}{2}\partial f_2/dS_1\,\partial^2 S_1/dx_D^2 + \\ &\frac{1}{2}\partial f_2/dS_2\left[\Delta x_D - \partial f_2/dS_2\,\Delta t_D\right]\partial^2 S_2/dx_D^2.\end{aligned} \tag{D.12}$$

Thus the equations solved by three-phase simulator are

$$\begin{pmatrix} \dfrac{\partial S_1}{\partial t_D} \\ \dfrac{\partial S_2}{\partial t_D} \end{pmatrix} = \begin{pmatrix} \dfrac{\partial f_1}{\partial S_1} & \dfrac{\partial f_1}{\partial S_2} \\ \dfrac{\partial f_2}{\partial S_1} & \dfrac{\partial f_2}{\partial S_2} \end{pmatrix} \begin{pmatrix} \dfrac{\partial S_1}{\partial x} \\ \dfrac{\partial S_2}{\partial x_D} \end{pmatrix} +$$

$$\frac{1}{2} \begin{pmatrix} \dfrac{\partial f_1}{\partial S_1}\left[\Delta x_D - \dfrac{\partial f_1}{\partial S_1}\Delta t_D\right] & \Delta x_D \dfrac{\partial f_1}{\partial S_2} \\ \Delta x_D \dfrac{\partial f_2}{\partial S_1} & \dfrac{\partial f_2}{\partial S_2}\left[\Delta x_D - \dfrac{\partial f_2}{\partial S_2}\Delta t_D\right] \end{pmatrix} \begin{pmatrix} \dfrac{\partial^2 S_1}{\partial x_D^2} \\ \dfrac{\partial^2 S_2}{\partial x_D^2} \end{pmatrix}. \tag{D.13}$$

and the numerical dispersion tensor is given by

$$D = \frac{1}{2} \begin{pmatrix} \dfrac{\partial f_1}{\partial S_1}\left[\Delta x_D - \dfrac{\partial f_1}{\partial S_1}\Delta t_D\right] & \Delta x_D \dfrac{\partial f_1}{\partial S_2} \\ \Delta x_D \dfrac{\partial f_2}{\partial S_1} & \dfrac{\partial f_2}{\partial S_2}\left[\Delta x_D - \dfrac{\partial f_2}{\partial S_2}\Delta t_D\right] \end{pmatrix}. \tag{D.14}$$

Nomenclature

C_i	overall volume fraction of component i
c_{ij}	volume fraction of component i in phase j.
F_i	overall fractional flow of component i.
F_{ij}	derivative of F_i with respect to component j.
f_j	fractional flow of phase j.
f_{jk}	derivative of f_j with respect to phase k.
g	gravity constant.
i	component.
j	phase.
k	total permeability.
k_{rj}	relative permeability of phase j.
k_{rj}^{o}	endpoint permeability of phase j.
K_{ij}	the dispersion tensor.
L	length of the porous medium.
n_c	number of components.
n_p	number of phases.
n_j	exponent in Corey-type relative permeability model.
N_1	gravity number of phase 1.
N_3	gravity number of phase 3.
N_{Pe}	Peclet number.
r_{ij}	rate of reactions in which component j is created or destroyed.

S_j	saturation of phase *j*.
S_j^*	normalized saturation of phase *j*.
S_{rj}	residual saturation of phase *j*.
S_{rjk}	residual saturation of phase *j* in the presence of phase *k*.
t_D	dimensionless time, pore volumes injected.
u	total velocity.
u_j	velocity of phase *j*.
V	total volume of surfactant injection necessary for 100% recovery
x	distance along porous medium, ft.
x_D	dimensionless distance.
x_{ij}	mole fraction of component *i* in the j^{th} phase.
x_{is}	mole fraction of component *i* in the solid phase.
z	height.
α_j	weighting function for three-phase relative permeability parameters
$\eta_{+/-}^{u/d}$	equilibria of a shock at the upstream (*u*) or downstream (*d*) composition with respect to the fast (+) or slow (-) eigenvalue.
φ_j	mass density of phase *j*.
λ_j	mobility of phase *j*.
Λ	dimensionless shock velocity.
$\lambda_{+/-}$	characteristic velocity of three-phase compositions.
$\lambda_{t/nt}$	characteristic velocity of two-phase compositions.
ϕ	porosity.
μ_j	viscosity of phase *j*, cp.

ρ_j	molar density of phase *j*.
ρ_s	density of solid phase.
ρ_i°	pure component density.

Bibliography

Albrechtsen, T, Andersen, S. J., Dons, T., Engstrom, F., Jorgensen, O., Sorensen, F. W.: “Halfdan: Developing Non-Structurally Trapped Oil in North Sea Chalk,” SPE 71322 presented at the SPE ATCE, New Orleans, LA (2001).

Azevedo, A.V. Marchesin, D.: “Multiple Viscous Solutions for Systems of Conservation Laws,” Trans. of Amer. *Math. Soc.*, (1995) 47, 3061-3077.

Azevedo, A.V. Marchesin, D. Plohr, B. Zumbrun, K.: “Bifurcation of Nonclassical Viscous Shock Profiles from the Constant State,” *Comm. Math. Phys*. (1999) 202, 267-290.

Azevedo, A.V. Marchesin, D. Plohr, B. Zumbrun, K.: “Capillary instability in models for three-phase flow.” *ZAMP* (2002) 713-746.

Azevedo, A.V. Marchesin, D. Plohr, B. Zumbrun, K.: “Nonuniqueness of Solutions Riemann Problems” *ZAMP* (1996) 47, 977-998.

Baker, L. E., “Three-Phase Relative Permeability Correlations,” SPE 17369 presented at the SPE/DOE EOR Symposium, Tulsa, OK (1988).

Baran, J.R., Pope, G.A., Wade, W.H., Weerasooriya, V.: “Phase Behavior of Water/Perchloroethylene/Anionic Surfactant Systems,” *Langmuir* (1994) 10, 1146-1150.

Baran, J. R., Pope, G. A., and Wade, W. H., “Microemulsion Formation with Chlorinated Hydrocarbons of Differing Polarity, “ *Env. Sci. and Tech*. (1994) 1361-1366.

Batycky, R. P.: *Experimental Verification of MOC Theory for Three and Four Component Systems*, MS Thesis, Stanford University, Stanford, CA (1994).

Bedrikovetsky, P.: *Mathematical Theory of Oil and Gas Recovery*, Petroleum Engineering and Development Studies, Vol. 4, Kluwer Academic Pub. 1993.

Bedrikovetsky, P., Andrade, G.M., Ferreira, L.E.A., and Menezes, G.L.: "Optimization of Tertiary Water-Alternate-CO_2 Injection," SPE 36133 presented at the SPE 4th Latin American and Caribbean Conference, Port of Spain, Trinidad and Tobago (1996).

Bell, J.B., Trangenstein, J.A., Shubin, G.R.: "Conservation Laws of Mixed Type Decribing Three-Phase Flow in Porous Media," *SIAM J. Appl. Math.* (1986) 46, 1000-1017.

Blunt, M. J.: "An Empirical Model for Three-Phase Relative Permeability," *SPE J.*, SPE 67950 (2000) 5, 435-445.

Bruining, J. and van Duijn, C. J.: "Uniqueness Conditions in a Hyperbolic Model for Oil Recovery by Steamdrive," *Comp. Geosciences*, (2000) 4, 65-98.

Bruining, J., Marchesin, D., and van Duijn, C. J.: "Steam Injection into Water-Saturated Porous Rock," *Comp. and Appl. Math.* (2003) 22, 359-395.

Bruining, J. and Marchesin, D.: "Analysis of Nitrogen and Steam Injection in a Porous Medium with Water," personal communication with J. Bruining, (2004).

Bruining, J., Marchesin, D., and Schecter, S.: "Steam Condensation Waves in Water-Saturated Porous Rock," personal communication with J. Bruining, (2004).

Buckley, S. E., and Leverett, M.C.: "Mechanism of Fluid Displacement in Sands," *Trans. AIME* (1941) 146, 107-116.

Burden, R. L., and Faires, J. D.: *Numerical Analysis*, Brooks/Cole Pub., sixth edition (1997).

Cinar, Y. and Orr, F. M. Jr.: "Experimental Investigation of Three-Phase Flow with Composition Variation," personal communication with Y. Cinar, used with permission (2004).

Cinar, Y. and Orr, F. M. Jr.: "Measurement of Three-Phase Relative Permeability with IFT Variation," SPE 89419 presented at the SPE/DOE IOR Conference, Tulsa, OK, (2004).

Cinar, Y., Marquez, S., and Orr F. M. Jr.: "Effect of IFT variation and Wettability on Three-Phase Relative Permeability," SPE 90572 presented at the SPE ATCE, Houston, TX (2004).

Corey, A. T., Rathjens, C. H., Henderson, J. H., and Wyllie M. R. J.: "Three-Phase Relative Permeability," *JPT*, (1956) 63-65.

Coutinho, J. A. P., Jorgensen, M., Stenby, E.H.: "Predictions of Three-Phase Regions in CO_2-oil Mixtures," *J. of Pet. Sci. and Eng.*, (1995) 12, 201-208.

Creek, J. L. and Sheffield, J. M.: "Phase Behavior, Fluid Properties, and Displacement Characteristics of Permian Basin Reservoir Fluid/CO_2 Systems," *SPERE*, SPE 20188 (1993) 34-42.

Delshad, M., Pope, G. A.: "Comparison of Three-Phase Oil Relative Permeability Models," *Trans. in Porous Media*, (1989) 4, 59-83.

Delshad, M., Pope, G. A.: "A Compositional Simulator for Modeling Surfactant Enhanced Aquifer Remediation, 1 Formulation," *J. of Contam Hyd.* (1996) 23, 303-327.

Delshad, M., Delshad, M., Pope, G. A., Lake, L.W.: "Two- and Three-Phase Relative Permeabilities of Micellar Fluids," *SPE Formation Evaluation*, SPE 13581 (1987) 327-337.

DiCarlo, D. A., Sahni, A., Blunt, M. J.: "Three-Phase Relative Permeability of Water-Wet, Oil-Wet and Mixed-Wet Sandpacks," *SPEJ*, SPE 60767 (2000) 5, 82-91.

Dindoruk, B., Johns, R. T., and Orr, F. M.: "Analytical Solution for Four Component Gas Displacements with Volume Change on Mixing," Proceedings of the Third European Conference on the Mathematics of Oil Recovery, Delft, the Netherlands, 149-157 (1992).

Dria, D. E., Pope, G. A., and Sepehrnoori, K.: "Three-Phase Gas/Oil/Brine Relative Permeabilities Measured Under CO_2 Flooding Conditions," *SPERE*, SPE 20184 (1993) 143-150.

Dwarakanath, V, and Pope, G. A.: "Surfactant Phase Behavior with Field Degreasing Solvent," *Env. Sci. Tech.,* (2000) 4842-4848.

Dwarakanath, V.: *Characterizaion and Remediation of Aquifers Contaminated by Nonaqueous Phase Liquids Using Partitioning Tracers and Surfactants.* PhD dissertation, University of Texas, Austin, May 1997.

Dwarakanath, V, Kostarelos, K., Pope, G. A., Shotts, D., Wade W. H.: "Anionic Surfactant Remediation of Soil Columns Contaminated by Nonaqueous Phase Liquids," *J. Contam. Hydrol*., (1999) 38, 465-488.

Falls, A.H. and Schulte, W.M.: "Theory of Three-Component, Three-Phase Displacement in Porous Media." *SPERE*, SPE 19387 (1992a) 377-384.

Falls, A.H. and Schulte, W.M.: "Features of Three-Component, Three-Phase Displacement in Porous Media." *SPERE*, SPE 19678 (1992b) 426-432.

Falta, R. W.: "Modeling Sub-Grid-Block-Scale Dense Nonaqueous Phase Liquid (DNAPL) Pool Dissolution Using a Dual-Domain Approach," *Water Resources Research*, (2003) 39, 1360.

Fanchi, J.R.: "Effect of Complex Fluid Phase Behavior on CO_2 Flood Simulation," SPE 16711 presented at the SPE ATCE, Dallas, TX (1987).

Fayers, F. J.: "Extension of Stone's Method I and Conditions for Real Characteristics in Three-Phase Flow," SPE 16965 presented at the SPE ATCE, Dallas, TX (1987).

Fayers, F. J. and Matthews, J. D.: "Evaluation of Normalized Stone's Methods for Estimating Three-Phase Relative Permeabilities," *SPE J*., SPE 11277 (1984) 224-232.

Fayers, F. J. and Perrine, R. L.: "Mathematical Description of Detergent Flooding in Oil Reservoirs," *Trans. AIME*, (1959) 216, 277-283.

Fountain, J. C., Starr, R. C., Middleton, T., Beikirch, M. Taylor, C., and Hodge, D.: "A Controlled Field Test of Surfactant-Enhanced Aquifer Remediation," *Ground Water* (1996) 34, 910-916.

Gardner, J. W., Orr, F. M., Patel, P. D: "The Effect of Phase Behavior on CO_2 Flood Displacement Efficiency." SPE 8367 presented at the SPE ATCE, Las Vegas, NV, (1979).

Giordano, R. M., Salter, S. J.: "Comparison of Simulation and Experiments for Compositionally Well-Defined Corefloods." SPE 12697 presented at the SPE/DOE EOR Symposium, Tulsa, OK, (1984).

González, M., and Araujo, M.: "Use of the Method of Characteristics to Study Three-Phase Flow." SPE 75168 presented at the SPE/DOE IOR Symposium, Tulsa, OK, (2002).

Greenberg, M. D.: *Foundations of Applied Mathematics*, Prentice Hall, Englewood Cliffs, NJ (1998).

Gupta, D. K. and Mohanty K. K.: "A Laboratory Study of Surfactant Flushing of DNAPL in the Presence of Macroemulsion," *Env. Sci. Tech.* (2001) 35, 2836-2843.

Guzman, R. E.: *Mathematics of Three-Phase Flow*, PhD Dissertation, Stanford University, Stanford, CA (1995).

Guzman, R. E. Giordano, D., Fayers F. J., Aziz, K., and Godi, A.: "Three-Phase Flow in Field Scale Simulation of Gas and WAG Injections," SPE 28897 presented at the SPE European Petroleum Conference, London, U. K. (1994).

Hadamard, J. S.: *Lectures on Cauchy's Problem in Linear Partial Differential Equations*, Dover Pub., New York, NY (1952).

Helfferich, F.G.: "Generalized Welge Construction for Two-Phase Flow in Porous Media in Systems with Limited Miscibility," SPE 9730 presented at the SPE ATCE, New Orleans, LA (1982).

Helfferich, F.G.: "General Theory of Multi-component, Multiphase Displacement," SPE 8372 presented at the SPE ATCE (1979).

Henry R.L. and Metcalfe, R.S.: "Multiple-Phase generation During Carbon Dioxide Flooding," *SPE J*, SPE 8812 (1983) 595-601.

Hicks, P.J. and Grader, A. S.: "Simulation of Three-Phase Displacement Experiment," *Trans. in Porous Media*, (1996) 24, 221-245.

Hirasaki, G.J.: "Application of the Theory of Multicomponent, Multiphase Displacement to Three-Component, Two-Phase Surfactant Flooding," *SPEJ*, (1981) 191-204.

Hoier, L., Cheng, N., and Whitson, C.H.: "Miscible Gas Injection in Undersaturated gas-Oil Systems," SPE 90379 presented at the SPE ATCE, Houston, TX (2004).

Hoier, L., Whitson, C. H.: "Miscibility Variation in Compositionally Grading Reservoirs," *SPEREE*, SPE 69840, 36-43 (2000).

Holden, L.: "On the Strict Hyperbolicity of the Buckley-Leverett Equations for Three-Phase Flow in a Porous Media," *SIAM J. Appl. Math.*, (1990) 50, 667-682.

Isaacson, E., Marchesin, D., Plohr, B.: "Transitional Waves for Conservation Laws." *SIAM J. Math. Anal.* (1990) 21, 837-866.

Isaacson, E., Marchesin, D., Plohr, B., Temple, J.B.: "Multiphase Flow Models with Singular Riemann Problems." *Mat. Aplic. Comp,.* (1992) V, 11, 147-166.

Jabbour, C., Quintard, M., Bertin, H., and Robin, M.: "Oil Recovery by Steam Injection: Three-Phase Flow Effects," *J. Pet. Sci. and Eng.*, (1996) 16, 109-130.

Jayanti, S. Britton, L. N., Dwarakanath, V., and Pope, G. A.: "Laboratory Evaluation of Custom-Designed Surfactants to Remediate NAPL Source Zones," *Env. Sci. Tech*. (2002) 5491-5497.

Jessen, K., Orr, F. M. Jr.: "Gas Cycling and the Development of Miscibility in Condensate Reservoirs," SPE 84070 presented at the SPE ATCE, CO (2003).

Jessen, K., Wang, Y., Ermakov, P., Zhu, Ji., and Orr, F. M. Jr.: "Fast, Approximate Solutions for 1D Multicomponent Gas Injection Problems." SPE 56608 presented at the SPE ATCE, Houston, TX (1999).

Johns, R. T.: *Analytical Theory of Multicomponent Gas Drives with Two-Phase Mass Transfer*, PhD Dissertation, Stanford University, Stanford, CA (1992).

Johns, R. T., Fayers, J. F., and Orr, F. M.: "Effect of gas Enrichment and Dispersion on Nearly Miscible Displacements in Condensing/Vaporizing Drives," SPE 24938 presented at the SPE ATCE, Washington, DC, (1992).

Johns, R. T., Sah, P, Solano, R.: "Effect of Dispersion on Local Displacement Efficiency for Multicomponent Enriched-Gas Floods Above the Minimum Miscibility Enrichment," *SPEREE* (2002) 5, 4-10.

Johns, R. T., Sah, P, and Subramanian, S.: "Effect of Gas Enrichment Above the MME on Oil Recovery in Enriched-Gas Floods," SPE 56826 presented at the SPE ATCE, Houston, TX, (1999).

Johns, R. T., Yuan, H., Dindoruk, B.: "Quantification of Displacement Mechanisms in Multicomponent Gasfloods," *SPEJ*, (2004) 314-321.

Johnson, E. F., Bossler, D. P. and Naumann, V. O.: "Calculation of Relative Permeability from Displacement Experiments," *Trans. AIME*, (1959) 216, 370-372.

Juanes, R., Patzek, T. W.: "Three-Phase Displacement Theory: An Improved Description of Relative Permeabilities." SPE 77539 presented at the SPE ATCE, San Antonio, TX, (2002).

Juanes, R., Patzek, T. W.: "Relative Permeabilities in Co-Current Three-Phase Displacements with Gravity." SPE 83445 presented at the SPE Western Regional/AAPG Pacific Section Joint Meeting, Long Beach, CA (2003).

Juanes, R., Patzek, T. W.: "Multiscale Numerical Modeling of Three-Phase Flow." SPE 84369 presented at the SPE ATCE, Denver, CO (2003).

Kilpatrick, P.K., Gorman, C.A., Davis, H.T., Scriven, L.E., Miller, W.G.: "Patterns of Phase Behavior in Ternary Ethoxylated Alcohol-n-Alkane-Water Mixtures." *J of Phys. Chem*. (1986) 90, 5292-5299.

Kvanik, B. A., Skauge, A., Matre, B. and Kolltveit, K.: "Three-Phase Microemulsion Relative Permeabilities: Experimental and Theoretical Consideration," *J. of Pet. Sci. and Eng*. (1992) 7, 105-116.

Lake, L.W.: *Enhanced Oil Recovery*, first edition, Prentice Hall, Upper Saddle River, N.J. (1989).

Lake, L.W.: *Numerical Simulation of Reservoirs*, course notes, University of Texas at Austin. (Sp. 2002).

Lantz, R. B.: "Quantitative Evaluation of Numerical Diffusion (Truncation Error)," *SPE J*, (1971) 315-320.

Larsen, L. L.: *Prediction of Phase Behavior of CO_2-Hydrocarbon Mixtures*. MS Thesis, New Mexico Institute of Mining and Technology, Socorro, NM (1984)

Larson, L. L., Silva, M. K., Taylor, M. A., and Orr, F. M.: "Temperature Dependence of L1/L2/V behavior in CO2/Hydrocarbon Systems," *SPERE*, (1989) 105-113.

Larson, R. G.: "The Influence of Phase Behavior on Surfactant Flooding," *SPE J.*, SPE 6774 (1979) 411-422.

Larson, R. G. and Hirasaki, G. J.: "Analysis of the Physical Mechanisms in Surfactant Flooding," *SPE J*, SPE 6003 (1978) 42-58.

Lax, P. D.: "Hyperbolic Systems of Conservation Laws II," *Comm. On Pure and App. Math.* (1957) 10, 537-566.

Leverett, M. C. and Lewis, W. B.: "Steady Flow of Gas-oil-water Mixtures through Unconsolidated sands," *Trans. AIME* (1941) 142, 107-116.

Liu, T. P.: "The Riemann Problem for General 2x2 Conservation Laws," *Trans. Amer. Math. Soc.* (1974) 199, 89-112.

Lohrenz, J., Bray, B. G., Clark, C. R.: "Calculating Viscosities of Reservoir Fluids from their Composisitons,"SPE ATCE, Houston, TX (1964).

Marchesin, D., Plohr, B., Schecter, S.: "Wave Structure in WAG Recovery" SPE 56480 presented at the SPE ATCE, Houston, TX (1999).

Marchesin, D., Plohr, B., Schecter, S.: "An Organizing Center for Wave Bifurication in Multiphase Flow Models." *SIAM J. Appl. Math.* (1997) 57, 1189-1215.

Martel, R., Gélinas, P. J.: "Surfactant Solutions Developed for NAPL Recovery in Contaminated Aquifers," *Ground Water* (1996) 34, 143-154.

Merrill, R.C. Luks, K.D., Kohn, J.P.: "Three-Phase Liquid-Liquid-Vapor Equlibria in the Methane + n-Pentane + n-Octane, Methane + n-Hexane + n-Octane, and Methane + n-Hexane + Carbon Dioxide Systems," *J of Chem. Eng. Data*, (1983) 28, 210-215.

Miller, C. T., Christakos, G., Imhoff, P. T. McBride, J. F., Pedit, J. A., Trangenstein, J. A.: "Multiphase Flow and Transport Modeling in Heterogeneous Porous Media: Challenges and Approaches." *Adv. in Water Resources* (1998) 21, 77-120.

Moulds, T. P., McGuire, P. L., Jerauld, G. R., Lee, S. T., and Solano, R.: "Pt. McIntyre: A Case Study of Gas Enrichment Above MME," SPE 84185 presented at the SPE ATCE, Denver, CO (2003).

Negahban, S., Willhite, G. P., Walas, S. M., and Michnick, M. J.: "Three-Liquid-Phase Equilibria of Ternary and Quaternary Mixture, Water/n-Decane/2-Butyloxyethanol and Water/n-Octane/1-Propanol/Sodium Chlorite-Experimental Measurements and Their Correlation with the UNIQUAC Model," *Fluid Phase Equilibria* (1986) 32, 49-61.

Nghiem, L. X. and Li, Y. K.: "Effect of Phase Behavior on CO2 Displacement Efficiency at Low Temperatures: Model Studies with an Equation of State," *SPERE*, SPE 13116 (1986) 414-422.

Orr, F.M. Jr.: "Simulation of the One-Dimensional Convection of Four-Phase, Four-Component Mixtures," Report 80-3, New Mexico Petroleum Recovery Research Center, Socorro, NM, (1980).

Orr, F. M. Jr. and Jensen, C. M.: "Interpretation of Pressure-Composition Phase Diagrams for CO_2/Crude Oil Systems," *SPE J*, SPE 11125 (1984) 485-497.

Orr, F. M. Jr., Yu, A. D., and Lien, C. L.: "Phase Behavior of CO_2 and Crude Oil in Low Temperature Reservoirs," SPE 8813 presented at the SPE/DOE EOR Symposium, Tulsa, OK (1980).

Pires, A. P., Bedrikovetsky, P. G., and Shapiro, A. A.: "Analytical Models for 1-D Gas Flooding: Splitting between Hydrodynamics and Thermodynamics," SPE 89441 presented at the SPE/DOE IOR Symposium, Tulsa, OK (2004).

Pires, A. P., Bedrikovetsky, P. G., and Shapiro A.A.: "Analytical Modeling for Two-Phase EOR Processes: Splitting Between Hydrodynamics and Thermodynamics," SPE 89919 presented at the SPE ATCE, Houston, TX (2004).

Pongpitak, S.: *Interaction of Phase Behavior with Multiphase Flow in Porous Media*, Master's Thesis, New Mexico Institute of Mining and Technology, Socorro, New Mexico. (1980).

Pope, G. A.: "The Application of Fractional Flow Theory to Enhanced Oil Recovery," *SPEJ*, SPE 7660 (1980) 191-205.

Riemens, W. G., Schulte, A. M., de Jong, L. N. J.: "Birba Field PVT Variations Along the Hydocarbon Column and Confirmatory Field Tests," *JPT*, SPE 13719, 83-88 (1988).

Rossen, W. R. and Bruining, J.: "Foam Displacements with Multiple Steady States," SPE 89397 presented at the SPE/DOE IOR Symposium, Tulsa, OK (2004).

Sahni, A., Guzman, R., Blunt, M.: "Theoretical Analysis of Three Phase Flow Experiments in Porous Media." SPE 36664 presented at the SPE ATCE, Denver, CO (1996).

Sandler, S.: *Chemical and Engineering Thermo-dynamics*, third edition, John Wiley and Sons, Inc. (1999).

Saraf, D. N., Batycky, J.P, Jackson, C.H., and Fischer, D.B.: "An Experimental Investigation of Three-Phase Flow of Water-Oil-Gas Mixtures Through Water-Wet Sandstones," SPE 10761 presented at the SPE California Regional Meeting, San Francisco, CA (1982).

Saraf, D. N. and Fatt. I.: "Three-Phase Relative Permeability Measurement Using a Nuclear Magnetic Resonance Technique for Estimating Fluid Saturation," *SPEJ*, SPE 1760 (1967) 235-242.

Schecter, S., Marchesin, D., and Plohr, B. J.: "Structurally Stable Riemann Solutions." *J. of Diff. Eq.* (1996) 126, 303-354.

Schulte, A.M.: " Compositional Variations Within a Hydrocarbon Column Due to Gravity." SPE 9235 presented at the SPE ATCE, Dallas TX (1980).

Seto, C. J., Jessen, K., Orr F. M. Jr.: "Compositional Streamline Simulation of Field Scale Condensate Vaporization by Gas Injection," SPE 79690 presented at the SPE Reservoir Simulation Symposium, Houston, TX (2003).

Shearer, M. and Trangenstein, J.A.: "Loss of Real Characteristics for Models of Three-Phase Flow in a Porous Medium," *Trans. in Porous Media*, (1989) 4, 499-525.

Shotts, Douglas Robert: *Surfactant Remediation of Soils Contaminated Solvents,* Master's Thesis, University of Texas at Austin, Austin, TX, (1996).

Siddiqui, S., Hicks, P. J., Grader, A. S.: "Verification of Buckley-Leverett Three-Phase Theory Using Computerized Tomography," *J. of Pet Sci. and Eng.* (1996) 15, 1-21.

Sleep, B. E.: "A Method of Characteristics Model for Equation of State Compostional Simulation of Organic Compounds in Groundwater," *J. Contam. Hydrol.* (1995) 17, 189-212.

Spiteri, E. and Juanes, R.: "Impact of Relative Permeability Hysteresis on the Numerical Simulation of WAG Injection," SPE 89921 presented at the SPE ATCE, Houston, TX (2004).

Stone, H. L.: "Probability Model for Estimating Three-Phase Relative Permeability," *J Pet. Tech*., SPE 2116, (1970) 22.

Stone, H. L.: "Estimation of Three-Phase Relative Permeability and Residual Oil Data," *J. Can. Pet. Soc.*, (1973) 53-61.

Strauss, W. A.: *Partial Differential Equations: An Introduction*, John Wiley and Sons, Inc., New York, NY (1992).

Svirsky, D. S., van Dijke, M. I. J., and Sorbie, K. S.: "Prediction of Three-Phase Relative Permeabilities Using a Pore-Scale Network Model Anchored to Two-Phase Data," SPE 89992 presented at the SPE ATCE, Houston, TX (2004).

Trangenstein, J. A. and Bell, J. B.: "Mathematical Structure of Compositional Reservoir Simulation," *SIAM J. Sci. Stat. Comput*., (1989) 10, 817-845.

Trangenstein, J. A.: "Three-Phase Flow with Gravity," *Contemp. Math*. (1989) 100, 147-159.

Turek, E. A., Metcalfe, R. S., Fishback, R. E.: "Phase Behavior of Several CO_2/West-Texas-Reservoir-Oil Systems," *SPERE*, SPE 13117 (1988) 505-516.

Turek, E. A., Metcalfe, R. S., Yarborough, L., and Robinson, R. L.: "Phase Equilibria in Carbon Dioxide-Multicomponent Hydrocarbon Systems: Experimental Data sand an Improved Prediction Technique," SPE 9231 presented at the SPE ATCE, Dallas, TX (1980).

Wachman, C.: "A Mathematical Theory for the Displacement of Oil and Water by Alcohol," *SPE J* (1964) 250-266.

Walsh, B. W., and Orr. F. M. Jr.: "Prediction of Miscible Flood Performance: Tthe Effect of Dispersion on Composition Paths in Ternary Systems," *In Situ*, (1990) 14, 19-47.

Wang, Y., *Analytical Calculation of Minimum Miscibility Pressure*, PhD Dissertation, Stanford University, Palo Alto, CA (1998).

Whitson, C. H., Belery, P.: "Compositional Gradients in Petroleum Reservoirs," SPE28000 presented at the U. of Tulsa Centennial Petroleum Eng. Symposium, Tulsa, OK, Aug (1994).

Wingard, J. S. and Orr, F. M.: "An Analytical Solution for Steam/Oil/Water Displacements," SPE 19667 presented at the SPE ATCE, San Antonio, TX (1989).

Winsor, P. A.: *Solvent Properties of Amphiphilic Compounds*, Butterworths Scientific Publications, London, U. K. (1954).

Yaws, C. L.: (Ed.) *Chemical Properties Handbook*, McGraw-Hill (1999).

Yuan, H. and Johns, R. T.: "Simplified Method for Calculation of Minimum Miscibility Pressure or Enrichment," SPE 77381 presented at the SPE ATCE, San Antonio, TX (2002).

Yuan, H.: *Application of Miscibility Calculations to Gas Floods*, PhD Dissertation, University of Texas at Austin, Austin, TX (2003).

Zanotti, F., de Notaristefani, C., Gardini, L.: "Sharpening Behavior of Chemical Flooding," *SPE J*, SPE 11809 (1983).

Vita

Tara Catherine LaForce was born on April 4, 1978 in Aurora, CO, the daughter of Robert Francis LaForce and Beverly Ann LaForce. After graduating as valedictorian from Gateway High School in Aurora, CO, in 1996, she entered Colorado State University in Ft. Collins, CO. She received the degree of Bachelor of Science in Mathematics cum laude in 1999. In 2000 she entered the Computational and Applied Mathematics program at the University of Texas at Austin. She received a Masters of Science degree in Computational and Applied Mathematics and entered the Department of Petroleum and Geosystems Engineering at the University of Texas at Austin in 2002. Thus far she has presented two SPE papers and contributed a chapter to a SIAM book on bio-terrorism. She was awarded the Thrust 2000 Fellowship in 2002-2005.

Permanent Address: 20588 E. Shefield Ct.
Parker, CO 80138

This dissertation was typed by Tara LaForce.